

**ULTRAFAST LASER INDUCED THERMO-ELASTO-VISCO-
PLASTODYNAMICS IN SINGLE CRYSTALLINE SILICON**

A Dissertation

by

XUELE QI

Submitted to the Office of Graduate Studies of
Texas A&M University
in partial fulfillment of the requirements for the degree of

DOCTOR OF PHILOSOPHY

December 2009

Major Subject: Mechanical Engineering

**ULTRAFAST LASER INDUCED THERMO-ELASTO-VISCO-
PLASTODYNAMICS IN SINGLE CRYSTALLINE SILICON**

A Dissertation

by

XUELE QI

Submitted to the Office of Graduate Studies of
Texas A&M University
in partial fulfillment of the requirements for the degree of

DOCTOR OF PHILOSOPHY

Approved by:

Chair of Committee,	Chii-Der S. Suh
Committee Members,	Gary Fry
	Hung-Jue Sue
	Jyhwen Wang
Head of Department,	Dennis O'Neal

December 2009

Major Subject: Mechanical Engineering

ABSTRACT

Ultrafast Laser Induced Thermo-Elasto-Visco-Plastodynamics in Single Crystalline Silicon. (December 2009)

Xuele Qi, B.S., Tsinghua University, Beijing, China;

M.S., Tsinghua University, Beijing, China

Chair of Advisory Committee: Dr. Chii-Der S. Suh

A comprehensive model for describing the fundamental mechanism dictating the interaction of ultrafast laser pulse with single crystalline silicon wafer is formulated. The need for establishing the feasibility of employing lasers of subpicosecond pulse width in Laser Induced Stress Waves Thermometry (LISWT) for single crystalline silicon processing motivated the work. The model formulation developed is of a hyperbolic type capable of characterizing non-thermal melting and thermo-elasto-viscoplastic deformation as functions of laser input parameters and ambient temperature. A plastic constitutive law is followed to describe the complex elasto-viscoplastic responses in silicon undergoing Rapid Thermal Processing (RTP) annealing at elevated temperatures. A system of nine first-order hyperbolic equations applicable to describing 3-D elasto-viscoplastic wave motions in silicon is developed. The group velocities of certain selected frequency components are shown to be viable thermal indicators, thus establishing the feasibility of exploiting nanosecond laser induced propagating stress waves for the high-resolution thermal profiling of silicon wafers.

Femtosecond laser induced transport dynamics in silicon is formulated based on the relaxation-time approximation of the Boltzmann equation. Temperature-dependent multi-phonons, free-carrier absorptions, and the recombination and impact ionization processes governing the laser model and carrier numbers are considered using a set of balance equations. The balance equation of lattice energy and equations of motion of both parabolic and hyperbolic types are derived to describe the complex thermo-elasto-plastodynamic behaviors of the material in response to ultrafast laser pulsing. The solution strategy implemented includes a multi-time scale axisymmetric model of finite geometry and a staggered-grid finite difference scheme that allows both velocity and stress be simultaneously determined without having to solve for displacements. Transport phenomena initiated by femtosecond pulses including the spatial and temporal evolutions of electron and lattice temperatures, along with electron-hole carrier density, are found to be functions of laser fluence and pulse width. The femtosecond laser heating model that admits hyperbolic energy transport is shown to remedy the dilemma that thermal disturbances propagate with infinite speed. Non-thermal melting fluence is examined favorably against published experimental data. That it is feasible to explore femtosecond laser induced displacement and stress components for 1K resolution thermal profiling is one of the conclusions reached.

ACKNOWLEDGEMENTS

I would like to express my deepest gratitude to my academic advisor, Dr. Chii-Der S. Suh, who provided me with sustaining guidance and necessary financial support throughout my doctoral career at Texas A&M University. His encouragement and direction led me into the most wonderful life of research. His attitude of seriousness toward science and truth will benefit me throughout my life. I am also grateful to my dissertation committee members, Drs. Gary Fry, Hung-Jue Sue and Jyhwen Wang, for their invaluable advice and support.

I wish to thank my beloved wife, Jing. My research and dissertation would not be finished without her love and patience. Finally, lots of thanks go to my parents for their love and encouragement for all these years.

NOMENCLATURE

C_{e-h}	Electron-hole pairs specific heat
C_l	Lattice specific heat
D_0	Ambipolar diffusion coefficient
E	Young's modulus
E_d	Demmer field
E_g	Band-gap energy
E_c	Energy of conduction-band
E_v	Energy of valence-band
F	Fermi-Dirac integral
f	Dislocation density related coefficient
G	Pair generation rate
G_s	Shear modulus
$h\nu$	Photon energy
I	Laser intensity
J	Carrier current
k_B	Boltzmann constant
L_U	Energy loss term due to energy exchange
L_M	Energy loss term due to mechanical wave

n	Carrier density
N_m	Dislocation density
Q_c	Seebeck coefficient
q	Charge
R	Pair recombination rate
r	Radius in cylindrical coordinates
r_s	Laser spot size
S_U	Energy source term
S_{ij}	Deviatoric stress tensor
T_e	Electron temperature
T_l	Lattice temperature
T_0	Ambient temperature
t	Time variable
t_{eq}	Thermal equilibrium time
t_p	Pulse duration
t_1	Thermal-mechanical relaxation time
t_2	Thermal relaxation time
U	Total energy of electron-hole pairs
u	Displacement in r-direction
V_0	Dislocation velocity coefficient

W	Energy current
w	Displacement in z-direction
z	Depth in cylindrical coordinates
α	One-photon absorption coefficient
α'	Thermal expansion coefficient
β	Two- photon absorption coefficient
β_d	Dislocation interaction parameter
Γ	Reflectivity
γ	Auger recombination coefficient
ε	Strain
η_c	Reduced Fermi level
Θ	Free carrier absorption area
θ	Angle in cylindrical coordinates
θ_i	Impact ionization coefficient
θ_l	Lattice temperature increase
κ	Thermal conductivity
λ	Lamé constants
μ	Lamé constants
μ_c^0	Mobility of electrons
ν	Poisson's ratio

π_c	Peltier coefficient
ρ	Mass density
σ	Stress
σ_c	Electron conductivity
τ_e	Relaxation time
Φ	Laser fluence
ψ_c	Fermi level

TABLE OF CONTENTS

		Page
ABSTRACT		iii
ACKNOWLEDGEMENTS		v
NOMENCLATURE.....		vi
TABLE OF CONTENTS		x
LIST OF FIGURES.....		xiii
LIST OF TABLES		xix
 CHAPTER		
I	INTRODUCTION.....	1
	1.1 Overview	1
	1.2 Laser Induced Stress Wave Thermometry	2
	1.3 Ultrafast Laser Induced Transport Dynamics in Silicon.....	6
	1.4 Research Objective.....	11
	1.5 Dissertation Outline.....	14
II	SOLUTION STRATEGY FOR STUDYING ELASTO-VISCO- PLASTODYNAMICAL RESPONSES OF SINGLE CRYSTALLINE SILICON	15
	2.1 Constitutive Law	15
	2.2 Elasto-Viscoplastic Wave Formulation.....	18
	2.3 Computational Model.....	22
	2.3.1 Finite Difference Model	27
	2.3.2 Boundary Conditions, Temporal and Spatial Discretization	32
	2.4 Summary	33
III	NANOSECOND LASER INDUCED STRESS WAVE THERMOMETRY FOR SILICON PROCESSING	35
	3.1 Waveforms and Gabor Wavelet Transform	35

CHAPTER	Page
3.2 Thermal Effect on Group Velocity.....	41
3.3 Thermal Effect on Wave Attenuation	50
3.4 Thermal and Geometric Effects on Wave Dispersion.....	56
3.5 Summary	59
 IV FEMTOSECOND LASER INDUCED TRANSPORT DYNAMICS IN SEMICONDUCTORS	 61
4.1 Relaxation-Time Approximation of Boltzmann Equation	61
4.1.1 Macroscopic Electrical Current of the Carriers.....	65
4.1.2 Macroscopic Energy Current of the Carriers	70
4.2 Carrier Number Balance Equation and Laser Model.....	73
4.3 Carrier Energy Balance Equation.....	77
4.4 Summary	77
 V PARABOLIC THERMO-ELASTODYNAMICS FOR SILICON MATERIALS SUBJECTED TO ULTRAFAST LASER HEATING.	 79
5.1 Classical Thermoelasticity	79
5.2 Lattice Energy Balance Equation and Equations of Motion	80
5.3 Computational Model.....	82
5.3.1 Geometric Model.....	82
5.3.2 Multi-Time Scale Time Integration Scheme	85
5.3.3 Staggered Grid Finite Difference Model.....	88
5.3.4 Initial and Boundary Conditions	93
5.4 Results	96
5.4.1 Carrier and Lattice Temperatures.....	96
5.4.2 Carrier Density	105
5.4.3 Displacement and Velocity Fields.....	109
5.4.4 Thermal Stress Waves.....	113
5.4.5 Power Density and Effect of Laser Fluence.....	119
5.5 Summary	127
 VI GENERALIZED THERMO-ELASTODYNAMICS FOR SILICON MATERIALS SUBJECTED TO ULTRAFAST LASER HEATING.	 128
6.1 Generalized Thermoelasticity	128
6.2 Lattice Energy Balance Equation and Equations of Motion	129
6.3 Computational Model.....	131
6.4 Results	136
6.4.1 Carrier Density and Model Validation	136
6.4.2 Lattice Temperature and Heat Flux.....	140

CHAPTER	Page
6.4.3 Displacement and Velocity Fields.....	143
6.4.4 Thermal Stress Waves.....	148
6.5 Damage Evaluation	150
6.5.1 Power Density	150
6.5.2 Accumulated Damage Evaluation.....	152
6.6 Summary	163
 VII GENERALIZED THERMO-ELASTO-VISCO-PLASTODYNAMICS FOR SILICON MATERIALS SUBJECTED TO ULTRAFAST LASER HEATING	164
7.1 Lattice Energy Balance Equation and Equations of Motion	165
7.2 Computational Model.....	167
7.3 Results	172
7.3.1 Temperature Increment of Lattice Temperature	172
7.3.2 Displacement Fields as Temperature Indicators	174
7.3.3 Stress Fields as Temperature Indicators.....	183
7.4 Summary	191
 VIII CONCLUSIONS	192
 REFERENCES.....	197
 VITA	207

LIST OF FIGURES

FIGURE	Page
2.1 Configuration of 3-D model domain for solving wave equation	23
2.2 Temporal distribution Gaussian function $F(t)$ of stress wave input function.....	25
2.3 Spatial distribution Gaussian function $G(x_1, x_2)$ of stress wave input function.....	26
2.4 Finite difference model with staggered grids.....	28
3.1 (a) Numerical waveforms acquired at sampling points A (5mm) and B (7mm) at 200°C in 0.5mm thick wafer; (b) Experimental waveform acquired in 4" wafer of 0.5mm thickness at a 10mm sampling point.....	36
3.2 GWT of waveforms obtained at sampling point A at 1000°C (wafer thickness: 0.5mm).....	39
3.3 GWT of waveforms obtained at sampling point B at 1000°C (wafer thickness: 0.5mm).....	40
3.4 Top view of GWT of waveforms obtained at sampling point A at 1000°C (wafer thickness: 0.5mm).....	42
3.5 Top view of GWT of waveforms obtained at sampling point B at 1000°C (wafer thickness: 0.5mm).....	43
3.6 Group velocities vs. frequency (low frequency components) at five selected temperatures (wafer thickness: 0.5mm)	45
3.7 Group velocities vs. temperature of three selected low frequencies (wafer thickness: 0.5mm).....	46
3.8 Group velocities vs. frequency (high frequency components) at five selected temperatures (wafer thickness: 0.5mm)	48
3.9 Group velocities vs. temperature of three selected high frequencies (wafer thickness: 0.5mm).....	49

FIGURE	Page
3.10 Attenuation factor vs. frequency (low frequency components) at five selected temperatures (wafer thickness: 0.5mm)	51
3.11 Attenuation factor vs. temperature of three selected low frequencies (wafer thickness: 0.5mm).....	52
3.12 Attenuation factor vs. frequency (high frequency components) at five selected temperatures (wafer thickness: 0.5mm)	54
3.13 Attenuation factor vs. temperature of three selected high frequencies (wafer thickness: 0.5mm).....	55
3.14 Group velocities vs. wafer thickness at 600°C wafer temperature for three selected high frequencies	57
3.15 Group velocities vs. wafer thickness at 600°C wafer temperature for three selected low frequencies.....	58
4.1 Electrical current in spherical coordinates	66
4.2 Time evolution of laser intensity on top surface of silicon	75
4.3 Spatial distribution of laser intensity along thickness direction of silicon.	76
5.1 Axisymmetric model in cylindrical coordinates	83
5.2 Time evolutions of electron (T_e) and lattice (T_l) temperature (pulse duration 500fs, spot size 10 μ m, laser fluence 0.005J/cm ²)	87
5.3 Finite difference model with staggered grids.....	89
5.4 Electron temperature distribution in silicon wafer irradiated by ultrafast laser (pulse duration 500fs, spot size 10 μ m, laser fluence 0.005J/cm ²)....	97
5.5 Lattice temperature distribution in silicon wafer irradiated by ultrafast laser (pulse duration 500fs, spot size 10 μ m, laser fluence 0.005J/cm ²)....	99
5.6 Time evolution of electron and lattice temperatures (pulse duration 500fs, spot size 10 μ m, laser fluence 0.005J/cm ²)	100
5.7 Time evolution of electron and lattice temperatures (pulse duration 500fs, spot size 10 μ m, laser fluence 0.015J/cm ²)	103

FIGURE	Page
5.8 Time evolution of electron and lattice temperatures (pulse duration 500fs, spot size 10 μ m, laser fluence 0.15J/cm ²)	104
5.9 Time evolution of carrier density (pulse duration 500fs, spot size 10 μ m, laser fluence 0.005J/cm ²)	106
5.10 Time evolution of carrier density (pulse duration 500fs, spot size 10 μ m, laser fluence 0.015J/cm ²)	107
5.11 Time evolution of carrier density (pulse duration 500fs, spot size 10 μ m, laser fluence 0.15J/cm ²)	108
5.12 Displacement profiles of silicon wafer irradiated by ultrafast laser at two different times (pulse duration 500fs, spot size 10 μ m, laser fluence 0.005J/cm ²)	110
5.13 Laser induced nodal motion of silicon wafer (pulse duration 500fs, spot size 10 μ m, laser fluence 0.005J/cm ²)	112
5.14 Velocity profiles of silicon wafer irradiated by ultrafast laser at two different times (pulse duration 500fs, spot size 10 μ m, laser fluence 0.005J/cm ²)	114
5.15 Stress distributions of silicon wafer irradiated by ultrafast laser at two different times (pulse duration 500fs, spot size 10 μ m, laser fluence 0.005J/cm ²)	116
5.16 Waveforms obtained at sampling locations A and B (pulse duration 500fs, spot size 10 μ m, laser fluence 0.005J/cm ²)	117
5.17 GWT of waveforms acquired at sampling locations (a) A and (b) B (pulse duration 500fs, spot size 10 μ m, laser fluence 0.005J/cm ²)	118
5.18 Power density of σ_{zz} at t = 5ns (pulse duration 500fs, spot size 10 μ m, laser fluence 0.005J/cm ²)	121
5.19 Power density of σ_{rz} at t = 5ns (pulse duration 500fs, spot size 10 μ m, laser fluence 0.005J/cm ²)	122
5.20 Power density of σ_{rr} at t = 5ns (pulse duration 500fs, spot size 10 μ m, laser fluence 0.005J/cm ²)	123

FIGURE	Page
5.21 Power density of σ_{rr} at $t = 10\text{ns}$ (pulse duration 500fs, spot size $10\mu\text{m}$, laser fluence $0.005\text{J}/\text{cm}^2$)	124
5.22 w displacement profile at $t = 10\text{ns}$ for higher laser fluence (pulse duration 500fs, spot size $10\mu\text{m}$, laser fluence $0.015\text{J}/\text{cm}^2$)	125
5.23 σ_{zz} stress profile at $t = 10\text{ns}$ for higher laser fluence (pulse duration 500fs, spot size $10\mu\text{m}$, laser fluence $0.015\text{J}/\text{cm}^2$)	126
6.1 Time evolution of carrier density subject to four laser fluences (laser pulse duration 500fs, spot size $10\mu\text{m}$)	138
6.2 Comparison of computed non-thermal melting thresholds with experimental data	139
6.3 Distribution of lattice temperature oscillation θ_l at 10ns (pulse duration 500fs, spot size $10\mu\text{m}$, laser fluence $0.005\text{J}/\text{cm}^2$)	141
6.4 Distribution of heat flux components (a) q_z and (b) q_r at $t = 10\text{ns}$ (pulse duration 500fs, spot size $10\mu\text{m}$, laser fluence $0.005\text{J}/\text{cm}^2$)	142
6.5 Displacement components w and u at two different times (pulse duration 500fs, spot size $10\mu\text{m}$, laser fluence $0.005\text{J}/\text{cm}^2$)	144
6.6 Laser induced nodal motions at 10ns (pulse duration 500fs, spot size $10\mu\text{m}$, laser fluence $0.005\text{J}/\text{cm}^2$)	146
6.7 Profiles of velocity components at two different times (pulse duration 500fs, spot size $10\mu\text{m}$, laser fluence $0.005\text{J}/\text{cm}^2$)	147
6.8 Distributions of stress component at 10ns (pulse duration 500fs, spot size $10\mu\text{m}$, laser fluence $0.005\text{J}/\text{cm}^2$)	149
6.9 Distributions of power density components at 10ns (pulse duration 500fs, spot size $10\mu\text{m}$, laser fluence $0.005\text{J}/\text{cm}^2$)	151
6.10 Sampling locations from which power density waves are acquired	155
6.11 Time histories of power density at 8 sampling locations (pulse duration 500fs, spot size $10\mu\text{m}$, laser fluence $0.005\text{J}/\text{cm}^2$)	156

FIGURE	Page
6.12 Time-frequency distribution of power density wave acquired at location 1 (a) 2D view (b) 3D view (pulse duration 500fs, spot size 10 μ m, laser fluence 0.005J/cm ²)	158
6.13 Power density vs. time-frequency at sampling location 1 (pulse duration 500fs, spot size 10 μ m, laser fluence 0.015J/cm ²)	159
6.14 Total accumulated damage at sampling location 1 within 10ns (pulse duration 500fs, spot size 10 μ m, laser fluence 0.015J/cm ²)	162
7.1 Temperature increment of lattice temperature at 10ns corresponding to four different ambient temperatures: 300K, 600K, 800K and 1100K (pulse duration 500fs, spot size 10 μ m, laser fluence 0.005J/cm ²)	173
7.2 Displacement fields at 10ns corresponding to two different ambient temperatures: 300K and 1100K (pulse duration 500fs, spot size 10 μ m, laser fluence 0.005J/cm ²)	175
7.3 Comparison of nodal motions at 10ns corresponding to two different ambient temperatures: 300K and 1100K (pulse duration 500fs, spot size 10 μ m, laser fluence 0.005J/cm ²)	177
7.4 Displacement w vs temperature at 10ns with fitting error; sampling location: $z=0$, $r=4\mu$ m (pulse duration 500fs, spot size 10 μ m, laser fluence 0.005J/cm ²)	179
7.5 Displacement u vs temperature at 10ns with fitting error; sampling location: $z=0$, $r=4\mu$ m (pulse duration 500fs, spot size 10 μ m, laser fluence 0.005J/cm ²)	181
7.6 Using displacements w and u to differentiate 1K temperature (pulse duration 500fs, spot size 10 μ m, laser fluence 0.005J/cm ²)	182
7.7 Stress fields at 10ns corresponding to two different ambient temperatures: 300K and 1100K (pulse duration 500fs, spot size 10 μ m, laser fluence 0.005J/cm ²)	184
7.8 Waveforms obtained at sampling locations 1 and 2 corresponding to two different ambient temperatures: (a) 300K and (b) 1100K (pulse duration 500fs, spot size 10 μ m, laser fluence 0.005J/cm ²)	185

FIGURE	Page
7.9 GWT of waveforms obtained at sampling locations 1 and 2 corresponding to two different ambient temperatures: 300K and 1100K (pulse duration 500fs, spot size 10 μ m, laser fluence 0.005J/cm ²)	187
7.10 Stress σ_{rr} vs temperature at 10ns with fitting error; sampling location: z=0, r=4 μ m (pulse duration 500fs, spot size 10 μ m, laser fluence 0.005J/cm ²)	189
7.11 Using stress component σ_{rr} to differentiate 1K temperature (pulse duration 500fs, spot size 10 μ m, laser fluence 0.005J/cm ²)	190

LIST OF TABLES

TABLE	Page
2.1 Material constants in Haasen-Sumino model.....	17
5.1 Laser optical properties	93
5.2 Material properties for silicon	94
6.1 Relaxation times	132

CHAPTER I

INTRODUCTION

1.1 Overview

Laser technology began moving into the sub-picoseconds time regime in the early 70s. Ultrashort laser micromachining of materials has been the focus of scientific research for many years because of a large number of advantages in comparison with long pulses [1-3]. The benefit provided by the brief heating time on the order of femtoseconds also enables precision control over the spread of the heat affected zone.

Laser melting of single crystalline semiconductors, silicon in particular, has become the subject of many recent investigations [4-6]. Laser micromachining including microdrilling, microcutting and micromilling, and optical lithography are accomplished by employing high fluence laser pulses [7, 8]. The use of low fluence ultrafast pulses on the other hand is secure enough to initiate high frequency propagating stress waves that could potentially be explored to characterize the elastic and thermal properties of thin films deposited in the material without inducing any physical damage. These waves are usually dispersive and broad band in frequency, and thus contain plenty of variables which are sensitive enough to resolve defects [9] and to profile thermal distribution with high resolution [10]. The Laser Induced Stress Waves Thermometry (LISWT) [11, 12] employed the nanosecond laser induced stress waves in real-time as thermometric probes for the precision profiling of the thermal state of silicon substrates

This dissertation follows the style of *Journal of Thermal Stresses*.

as they undergo rapid annealing processing. This technique was experimentally demonstrated for feasibility for measuring temperatures up to 600°C with $\pm 1^\circ\text{C}$ thermal resolution. Due to the aforementioned advantages of ultrafast lasers over nanosecond lasers, utilizing femtosecond laser in LISWT was considered. However, the fundamentals addressing the thermomechanical responses of silicon subject to ultrafast laser interrogation were not completely understood or established.

The research is aimed to formulate a comprehensive model for describing the fundamental mechanism of interaction between ultrafast laser pulse and single crystalline silicon. The model considers multi-dimensionality, generalized thermoelasticity, thermo-mechanical coupling and elasto-viscoplastic deformation. The various thermomechanical responses of a silicon wafer excited by a femtosecond pulsed laser are investigated in this dissertation. A literature review of relevancy and interest to this research including LISWT and ultrafast laser-induced transport dynamics in silicon is presented, followed by a statement of the research objective.

1.2 Laser Induced Stress Wave Thermometry

During the thermal annealing of silicon wafers, proper thermal control in real-time is required to ensure fabrication quality. It is therefore essential to knowing the thermal state of the substrate being processed at all time. As feature size smaller than 90nm is becoming dominant, non-contact, in-situ thermometry capable of $\pm 1^\circ\text{C}$ thermal resolution over the range from room temperature to 1,000°C is called for [13]. Of the handful of temperature diagnostics explored, Degertekin et al. [14, 15] employed contact

transducers along with a tomographic reconstruction technique to profile wafer temperature distribution, while Schietinger et al. [16] developed a non-contact ripple technology based on the stray radiation and emissivity effect. The lightpipe radiation thermometers (LPRTs) and cable-less LPRTs (CLRTs) studied by Tsai et al. [17, 18] offered better emissivity control whose thermal uncertainty was as low as $\pm 2^\circ\text{C}$. However, these methods all fall short of meeting the needed thermal resolution as the emissivity of silicon wafer subject to rapid annealing is not sensitive enough to differentiate slightly differing surface condition and dopant content. An alternative non-contact, emissivity-independent technique of desired temperature resolution is therefore needed.

Recognizing the dependency of wave dispersion on simultaneous temperature-thickness variation, Suh and co-workers [11, 12] exploited laser-generated ultrasonic guided waves [19] to the successful interrogation of silicon wafers for thermal information. Applicable to silicon wafers undergoing RTP, their methodology of thermal diagnostics, named Laser-Induced Stress Wave Thermometry (LISWT), was experimentally demonstrated for feasibility for temperatures up to 600°C . As silicon wafers no longer behave elastically, but rather elasto-viscoplastically, subject to temperature higher than 600°C , to cover the whole temperature range required by RTP, the physics behind elasto-viscoplastic wave propagation in single crystalline silicon thin structures at elevated temperature has to be understood.

While extensive theoretical and experimental works can be found in the field of elasticity [20, 21], works on plastic wave propagation in silicon were rare. There are

two key issues need be resolved before an elasto-viscoplastic wave propagation model can be developed. The first one concerns the kinematics of elastic-plastic deformation. It is common that the total strain is determined as the sum of the elastic strain and plastic strain. Valid assumptions must be made to justify the simple summation operation so as to clarify the associated kinematical implications. The framework on elasto-plastic deformation as presented in [20] assumed a fictitious elastically deformed state between the undeformed state and the elasto-plastic state in order to calculate the displacement gradients and strains. A mathematically rigorous procedure was then followed for obtaining the elasto-plastic kinematics. The second one is the constitutive law of silicon materials. All reviewed papers on plastic wave propagation adopted a fairly simple linear-elastic-perfect-plastic (LEPP) material model, which is not a true representation of the silicon material property at elevated temperature. Alexander and Haasen [22] were among the few who first proposed a constitutive law of single crystalline structure that was later refined by Suezava et al [23] and subsequently named as the Haasen-Sumino model. Tsai et al [24-26] generalized the model and developed a 3D formulation that was supported by experimental results. Tsai's model, which was derived from uniaxial tensile data, is modified and adopted for the investigation reported herein.

Mathematically, classic wave equations are second-order hyperbolic equations of displacement or stress. In this investigation, due to the complexity of the constitutive law, it is impossible to derive a second-order hyperbolic equation in terms of either displacement or stress component. Instead a first-order hyperbolic equation system is followed in which three velocity components and six stress components are the

dependent variables. Given its inherent complexity, it is difficult to obtain the analytical solutions to the first-order hyperbolic system. Finite difference is a typical method commonly used for investigating wave motions [27-29]. As a strong form solution, finite difference is a straightforward approach to time-integrating differential equations. The major drawback of finite difference, however, is its numerical dispersion [30]. This disadvantage prevents it from accurately predicting long distance wave propagation. In this dissertation, the staggered grid finite difference method [31, 32] is employed to numerically determine the velocity and stress fields in response to various temperature input. In this investigation, stresses are located at the center of the finite-difference elements, while velocities are positioned at the midpoints on the surface. There are two major advantages. First, initial and boundary conditions are specified in terms of the dependent variables alone. No derivatives of the dependent variables are involved. Second, stresses and velocities are the direct solution output. Note that in the displacement formulation, further calculations are needed to approximate stress components and in the stress formulation, numerical integrations are required to obtain displacements. Reducing the number of numerical differentiation or integration can minimize errors. This is also a welcome feature in applications where stress or stress gradient is the primary variable of interest.

In LISWT where dispersive, elasto-viscoplastic waves of broad bandwidth are employed for thermal profiling, there are two key practical issues in implementation. One is data acquisition and the other is extraction of thermal information. Fast Fourier Transform (FFT) is the popular tool in signal processing. However, it is not effective for

this investigation because it only provides spectral information. FFT is usually applied to time-invariant signals whose spectral structure does not change with time. As an alternative to FFT, Gabor Wavelet Transform (GWT) has been shown to provide simultaneous time-frequency resolution optimal for processing dispersive waves in beams and silicon wafers [10, 33]. This doctoral research adopts GWT as the feature extraction tool for the determination of temperature dependence of group velocity and wave attenuation for selected frequency components.

1.3 Ultrafast Laser Induced Transport Dynamics in Silicon

Micro-machining and -fabrication of materials using sub-picoseconds or femtoseconds ultrafast lasers have several prominent advantages over coherent optical source of long pulses [7-8, 34-35]. Given their low input energy, high power output and limited spread of the heat affected zone, pulsed lasers of ultra-short rise time allows precise control over the generation of extremely small features. Laser melting of single crystalline semiconductors, silicon in particular, has become the subject of many recent investigations [4-6]. Silicon processing using low fluence, ultra-short pulses generates no plasma and inflicts no damage to the material [9, 36]. The use of ultrafast pulsed lasers with such non-damaging fluence is sufficient to generate high frequency propagating stress waves that can be explored for many types of applications including non-destructive evaluation (NDE). Moreover, defects, material properties such as density and elastic constants, substrate thickness, residual stresses, bonding integrity, and surface roughness may all be measured using laser induced stress waves. The stress

waves can also be employed in real-time as thermometric probes for the precision thermal profiling of silicon substrates as they undergo rapid annealing process [10, 11]. In order to effectively apply ultrafast lasers to the fabrication and processing of semiconductor, it is necessary to establish the knowledge base essential for correlating ultrafast laser pulsing with the irradiated response of semiconductor materials.

Although experiments with ultrashort laser pulses of various fluences are plenty [1-3, 37-38], publications of the fundamentals addressing the thermomechanical responses of silicon subject to ultrafast laser interrogation are rare. Unlike traditional thermal melting, the mechanism dictating non-thermal melting must be explained in the views of quantum mechanics. When a semiconductor is irradiated by ultrafast lasers, a large number of electrons are excited with high temperature and jump from the valence band into the conduction band. The energy absorbed by electrons is a function of the difference between the photon energy ($h\nu$) and band-gap energy (E_g). When $h\nu > E_g$, electrons jump from the valence band into the conduction band and electron-hole pairs are subsequently created through either the one-photon or two-photon absorption mechanism. As a result, the initial kinetic energy of the electron-hole pairs is either $(h\nu - E_g)$ or $(2h\nu - E_g)$. As time elapses, a portion of the carriers (electrons and holes) would recombine and more new pairs would be generated through impact ionization. Recombination and impact ionization are the two opposite processes competing to balance the total number of carriers. As soon as the carrier density reaches a threshold, the silicon material begins undergoing non-thermal melting [39]. H.M. van Driel [40] was among the few who first proposed a self-consistent model based on the

relaxation-time approximation of the Boltzmann equation. The model, which included plasma degeneracy effects, was used to obtain the spatial and temporal evolution of the lattice temperature along with the carrier density and temperature. The laser duration utilized in the model was 20ps. Chen et al. [41] extended van Driel's model by reducing a rate equation that modeled the carrier density and introduced a laser model for expressing the laser intensity. They also developed a one-dimensional numerical model with finite difference method applicable to problems involving subpicoseconds or femtosecond lasers. However, there are few drawbacks pertaining to van Driel's and Chen's models as follows,

- (1) Ultrafast laser heating is one of multiphysics involving both electron-lattice interaction and thermal-mechanical coupling. With the governing equations describing only the total energy transfer in the form of heat and completely void of thermal-mechanical coupling and the equation of lattice motion, van Driel and Chen's do not take into account the mechanical response. If the objective is to explore the various dynamical behaviors initiated by rapid laser heating, the evolution of the induced mechanical field in space needs be considered.
- (2) The one-dimensional models formulated by van Driel and Chen are not applicable to describing temperature distributions in time and space, nor particle velocity or thermal stress, in both the thickness and radial directions. Considering multi-dimensionality is critical to the understanding of heating mechanisms.

- (3) Constrained by the extremely small time steps as required for properly time-integrating ultrashort laser pulses, the response time frame considered by van Driel and Chen using their models covers only up to a few picoseconds. To investigate the implications of ultrafast laser heating of single crystalline silicon, whose thermal-mechanical relaxation time is on the order of 10^{-13} seconds [42], it is necessary that the integration time window be wider than a few hundreds or even thousands picoseconds to be considered sufficient.
- (4) For a heat-conducting deformable body, the classical theory of thermoelasticity as van Driel and Chen used in their papers views heat propagation as a diffusion phenomenon because it incorporates a parabolic-type heat transport equation. The thermal distribution therefore travels with infinite speed and the thermoelastic responses are able to be observed instantaneously at any location in the entire model domain no matter how far it is away from the heat source. However, this prediction is physically unrealistic although it works well for problems where the duration of thermal shocks is as short as $1\mu\text{s}$ [43]. For modeling near-field, sub-nanosecond, especially sub-picosecond responses induced by laser pulses, generalized thermoelasticity has to be introduced.

The dissertation addresses the above comments with the formulation of a multi-time scale, multi-dimensional model that governs the transport dynamics in silicon wafer. The model introduces a term of energy loss to the generation of thermal-mechanical disturbances in the total energy balance equation. Mechanical responses,

such as lattice motions, are governed by the momentum equations. Assuming an axisymmetric volumetric laser heat source and neglecting material anisotropy, the model is reduced to a geometrically thin axisymmetric model in the cylindrical coordinates. Once the thermal equilibrium of electron and lattice is reached in the form of identical temperature, a multi-time scale scheme is then followed to rationally simplify the governing equations to allow for evolution time history as long as 10ns.

Due to the complexity of the model formulation, which is described by 17 coupled, time-dependent partial differential governing equations, closed-form solutions are beyond any tangible effort. A finite difference scheme with staggered grids is adopted as an alternative to attempting analytical solutions. Unlike the conventional finite difference method in which primary variables are evaluated at grid points, the staggered finite difference scheme defines velocities and the first order spatial derivative terms at locations midway between two consecutive grid points, and defines the shear stress at the center of each element. Compared with established methods of common, the staggered grid finite difference method can effectively suppress numerical oscillations [44, 45].

Non-thermal melting threshold is determined mainly by pulse duration and laser fluence. It is an important parameter for gauging the physical damage induced by ultrafast laser irradiation. When a semiconductor is irradiated by ultrafast laser pulses, a large number of electrons are excited from the valence band into the conduction band. As more and more covalent bonds are severed, lattices experience a dramatic reduction in shear strength and begin undergoing non-thermal melting [39] – a process unlike

regular thermal melting which usually is characterized by elevated temperature. Non-thermal melting generally occurs as immediate crystal disordering or material ablation. However, as ultrafast lasers also generate short-time scale shock waves of extremely high frequency, damages in the form of microcracking are probable. As detrimental as they are to the fabrication quality, damages of this kind nevertheless cannot be estimated by the non-thermal threshold. To address the need for being able to characterize this type of damage mode associated with the propagating stress waves, the accumulated damage evaluation algorithm introduced in Refs. 46 and 47 is adopted. The algorithm correlates in the qualitative sense short-time scale thermal stress waves excited by rapid thermal transient with various damage modes in a microelectronic packaging configuration. Such a correlation is possible through considering the oscillation of thermal stresses in time, which has the unit of power per unit volume, thus properly termed as power density. The concept of power density and its relation with low stress/high cycle fatigue is applied to investigate if ultrafast lasers induced thermal-mechanical wave motions are likely to initiate dynamic fatigue cracking in thin silicon section.

1.4 Research Objective

To explore the feasibility of Laser Induced Stress Waves Thermometry (LISWT) using ultrafast lasers, the mechanism dictating the interactions of ultrafast laser pulses with single crystalline silicon has to be established. The objective of this dissertation is to address the need for understanding the thermomechanical responses of single

crystalline silicon when irradiated by ultrafast lasers through developing a comprehensive physical model that incorporates hyperbolic thermal transport and considers the characteristics of non-thermal melting. Moreover, the model has to be extended for describing wave behaviors from being elastic to elasto-viscoplastic subject to the annealing temperature ranging from room temperature to exceeding 1,000K. To this end, several tasks are identified as follows:

- (1) Establish an axisymmetric model for describing complex laser-induced coupled thermal-mechanical responses;
- (2) Generate numerical results by building a staggered-grid finite difference model effective in solving boundary-value problems involving coupled PDEs;
- (3) Revise the mathematical and numerical model to consider hyperbolic heat transport and remedy the physically inadmissible infinite thermal speed resulted from the classical Fourier's Conduction Law;
- (4) Investigate the thermal equilibrium process of electrons and lattices;
- (5) Study non-thermal melting characteristics, and compare the melting threshold with the available experimental data in literature;
- (6) Finalize the model in (3) by considering the elasto-viscoplastic response of silicon at high temperature based on the kinematics of elasto-viscoplastic deformation;
- (7) Apply a viable multi-time scale integral algorithm to obtain numerical results up to at least several nanoseconds;

- (8) Investigate the distribution and propagation of laser induced mechanical waves, such as stresses and displacements;
- (9) Analyze the dispersive characteristics of laser induced mechanical waves by using wavelet time-frequency transformation;
- (10) Determine laser induced power density and heat flux to evaluate potential damages;
- (11) Compare thermomechanical responses 1) calculated by the elasto-viscoplastic and elastic models; 2) subject to different laser fluencies; and 3) at different ambient temperatures;
- (12) Identify parameters that are sensitive to temperature variation that can be used as thermal indicators.

1.5 Dissertation Outline

LISWT and ultrafast laser induced transport dynamics in silicon material along with the research objectives were discussed. In the remaining chapters, the dissertation is organized as follows. The constitutive law and elasto-viscoplastic wave formulation which govern the elasto-visco-plastodynamics of single crystalline silicon is reviewed in Chapter II. The feasibility study for LISWT by using nanosecond lasers are presented in Chapter III. Chapter IV derives the model formulation of the femtosecond laser induced transport dynamics in semiconductor materials. The near field thermal-mechanical responses and corresponding results calculated by classical thermo-elastodynamics, generalized thermo-elastodynamics, and generalized thermo-elasto-plastodynamics for silicon materials are discussed in Chapter V, Chapter VI and Chapter VII, respectively. Finally, some relevant remarks are made in the last chapter, Chapter VIII.

CHAPTER II

**SOLUTION STRATEGY FOR STUDYING ELASTO-VISCO-
PLASTODYNAMICAL RESPONSES OF SINGLE CRYSTALLINE SILICON**

2.1 Constitutive Law

According to the kinematics of elasto-plastic deformation eligible for considering small elastic deformation, the total strain rate of a body undergoing elasto-plastic deformation can be defined as the summation of the elastic strain rate and the plastic strain rate [25, 48] as

$$\dot{\epsilon}_{ij} = \dot{\epsilon}_{ij}^{(e)} + \dot{\epsilon}_{ij}^{(p)} \quad (2-1)$$

where $\dot{\epsilon}_{ij}^{(e)}$ is the elastic strain rate, $\dot{\epsilon}_{ij}^{(p)}$ is the plastic strain rate, and $\dot{\epsilon}_{ij}$ is the total strain rate which can be expressed alternatively as

$$\dot{\epsilon}_{ij} = \frac{1}{2} \left(\frac{\partial v_i}{\partial x_j} + \frac{\partial v_j}{\partial x_i} \right) \quad (2-2)$$

with v_i (or v_j) being the components of the total deformation rate and x_i (or x_j) being the components of the Cartesian coordinates.

Experiments have shown that single crystalline silicon behaves plastically at temperatures exceeding 600°C. As the governing constitutive law is rate dependent, plastic flow would become more prominent at even higher temperatures [49], at which silicon would behave like a viscoplastic material. The empirical constitutive law for silicon at elevated temperatures as described by the Haasen-Sumino model was derived

from studying the relation between plastic flow and dislocation density using uniaxial tension specimens. Dislocation density, which is the most important parameter dominating plastic deformation, was defined as the length of dislocations per unit volume in the crystal silicon. In the revised model by Tsai [24] that considers three-dimensional loading, the plastic strain rate can be expressed as a function of the deviatoric stress tensor as

$$\dot{\epsilon}_{ij}^{(p)} = f S_{ij} \quad (2-3)$$

where S_{ij} denotes the deviatoric stress tensor, and f is the dislocation density related coefficient defined as

$$f = \frac{b V_0 N_m (\sqrt{J_2} - D \sqrt{N_m} - \tau_d)^p}{\sqrt{J_2}} \quad (2-4)$$

Here N_m is the dislocation density, b is the magnitude of the Burgers vector, J_2 is the second invariant of the deviatoric stress tensor, τ_d is the back-stress due to the impurity concentration in the crystal, V_0 is the dislocated velocity coefficient

$$V_0 = \left(\frac{B_0}{\tau_0^p} \right) \exp\left(-\frac{Q}{k_B T_0}\right) \quad (2-5)$$

and $D = \frac{G_s b}{\beta_d}$, with B_0 being the dislocation mobility, τ_0 a material constant, Q the Peierls potential, T_0 the temperature, k_B the Boltzmann constant, G_s the shear modulus, and β_d a parameter characterizing the interaction between dislocations. The rate of the dislocation density is

$$\dot{N}_m = KV_0 N_m (\sqrt{J_2} - D\sqrt{N_m})^{p+\xi} \quad (2-6)$$

where K , p and ξ are material constants. Table 2.1 [26] tabulates the numeric values along with their units for the various material constants listed in Eqs. (2-4)-(2-6) that are used in the investigation.

Table 2.1 Material constants in Haasen-Sumino model

Parameters	Values
b	$3.8 \times 10^{-10} \text{m}$
B_0	$4.3 \times 10^4 \text{m/sec}$
τ_0	10^7N/m^2
Q	2.17eV
k_B	$8.617 \times 10^{-5} \text{eV/K}$
p	1.1
ξ	1.0
K	$3.1 \times 10^{-4} \text{m/N}$
β_d	3.3

2.2 Elasto-Viscoplastic Wave Formulation

The equation of motion can be derived by applying the principle of conservation of linear momentum,

$$\rho \dot{v}_j = \sigma_{ij,i} + q_j \quad (2-7)$$

where σ_{ij} is the stress tensor, q_j is the body force and ρ is the mass density. (Note that in this investigation $q_j = 0$ and $\rho = 2330 \text{ kg/m}^3$.) Thus, its component form can be expressed as

$$\rho \frac{\partial v_1}{\partial t} = \frac{\partial \sigma_{11}}{\partial x_1} + \frac{\partial \sigma_{21}}{\partial x_2} + \frac{\partial \sigma_{31}}{\partial x_3} \quad (2-8)$$

$$\rho \frac{\partial v_2}{\partial t} = \frac{\partial \sigma_{12}}{\partial x_1} + \frac{\partial \sigma_{22}}{\partial x_2} + \frac{\partial \sigma_{32}}{\partial x_3} \quad (2-9)$$

$$\rho \frac{\partial v_3}{\partial t} = \frac{\partial \sigma_{13}}{\partial x_1} + \frac{\partial \sigma_{23}}{\partial x_2} + \frac{\partial \sigma_{33}}{\partial x_3} \quad (2-10)$$

Typically of 0.5mm in thickness or less, single crystalline silicon wafers can be considered as orthotropic with the following constitutive Hooke's Law

$$\begin{bmatrix} \varepsilon_{11}^{(e)} \\ \varepsilon_{22}^{(e)} \\ \varepsilon_{33}^{(e)} \\ \varepsilon_{23}^{(e)} \\ \varepsilon_{13}^{(e)} \\ \varepsilon_{12}^{(e)} \end{bmatrix} = \begin{bmatrix} M_{11} & M_{12} & M_{13} & 0 & 0 & 0 \\ M_{21} & M_{22} & M_{23} & 0 & 0 & 0 \\ M_{31} & M_{32} & M_{33} & 0 & 0 & 0 \\ 0 & 0 & 0 & M_{44} & 0 & 0 \\ 0 & 0 & 0 & 0 & M_{55} & 0 \\ 0 & 0 & 0 & 0 & 0 & M_{66} \end{bmatrix} \begin{bmatrix} \sigma_{11} \\ \sigma_{22} \\ \sigma_{33} \\ \sigma_{23} \\ \sigma_{13} \\ \sigma_{12} \end{bmatrix} \quad (2-11)$$

with $M_{i,j}$ being the compliance matrix. Substituting Eqs. (2-2), (2-3) and (2-11) into Eq. (2-1), the following component forms are resulted

$$\frac{\partial v_1}{\partial x_1} = M_{11} \frac{\partial \sigma_{11}}{\partial t} + M_{12} \frac{\partial \sigma_{22}}{\partial t} + M_{13} \frac{\partial \sigma_{33}}{\partial t} + f \left(\sigma_{11} - \frac{\sigma_{11} + \sigma_{22} + \sigma_{33}}{3} \right) \quad (2-12)$$

$$\frac{\partial v_2}{\partial x_2} = M_{21} \frac{\partial \sigma_{11}}{\partial t} + M_{22} \frac{\partial \sigma_{22}}{\partial t} + M_{23} \frac{\partial \sigma_{33}}{\partial t} + f \left(\sigma_{22} - \frac{\sigma_{11} + \sigma_{22} + \sigma_{33}}{3} \right) \quad (2-13)$$

$$\frac{\partial v_3}{\partial x_3} = M_{31} \frac{\partial \sigma_{11}}{\partial t} + M_{32} \frac{\partial \sigma_{22}}{\partial t} + M_{33} \frac{\partial \sigma_{33}}{\partial t} + f \left(\sigma_{33} - \frac{\sigma_{11} + \sigma_{22} + \sigma_{33}}{3} \right) \quad (2-14)$$

$$\frac{\partial v_1}{\partial x_2} + \frac{\partial v_2}{\partial x_1} = 2M_{66} \frac{\partial \sigma_{12}}{\partial t} + 2f \sigma_{12} \quad (2-15)$$

$$\frac{\partial v_1}{\partial x_3} + \frac{\partial v_3}{\partial x_1} = 2M_{55} \frac{\partial \sigma_{13}}{\partial t} + 2f \sigma_{13} \quad (2-16)$$

$$\frac{\partial v_2}{\partial x_3} + \frac{\partial v_3}{\partial x_2} = 2M_{44} \frac{\partial \sigma_{23}}{\partial t} + 2f \sigma_{23} \quad (2-17)$$

With straightforward manipulations, it can be shown that Eqs. (2-8)-(2-17) together constitute a first-order hyperbolic equation system having the following matrix form,

$$\mathbf{A} \frac{\partial \mathbf{U}}{\partial t} + \mathbf{B} \frac{\partial \mathbf{U}}{\partial x_1} + \mathbf{C} \frac{\partial \mathbf{U}}{\partial x_2} + \mathbf{D} \frac{\partial \mathbf{U}}{\partial x_3} + \mathbf{E} = \mathbf{0} \quad (2-18)$$

where \mathbf{U} is the variable vector having three velocity components and six stress components as its entries

$$\mathbf{U} = \{v_1, v_2, v_3, \sigma_{11}, \sigma_{22}, \sigma_{33}, \sigma_{23}, \sigma_{13}, \sigma_{12}\}^T \quad (2-19)$$

For thin orthotropic silicon sections, the associated matrices \mathbf{A} , \mathbf{B} , \mathbf{C} , \mathbf{D} and vector \mathbf{E} are

$$\mathbf{D} = \begin{bmatrix} 0 & 0 & 0 & 0 & 0 & 0 & 0 & 1 & 0 \\ 0 & 0 & 0 & 0 & 0 & 0 & 1 & 0 & 0 \\ 0 & 0 & 0 & 0 & 0 & 1 & 0 & 0 & 0 \\ 0 & 0 & 0 & 0 & 0 & 0 & 0 & 0 & 0 \\ 0 & 0 & 0 & 0 & 0 & 0 & 0 & 0 & 0 \\ 0 & 0 & -1 & 0 & 0 & 0 & 0 & 0 & 0 \\ 0 & -1 & 0 & 0 & 0 & 0 & 0 & 0 & 0 \\ -1 & 0 & 0 & 0 & 0 & 0 & 0 & 0 & 0 \\ 0 & 0 & 0 & 0 & 0 & 0 & 0 & 0 & 0 \end{bmatrix} \quad (2-23)$$

$$\mathbf{E} = \begin{bmatrix} 0 & 0 & 0 & (\sigma_{11} - \frac{\sigma_{11} + \sigma_{22} + \sigma_{33}}{3})f & (\sigma_{22} - \frac{\sigma_{11} + \sigma_{22} + \sigma_{33}}{3})f & (\sigma_{33} - \frac{\sigma_{11} + \sigma_{22} + \sigma_{33}}{3})f & 2\sigma_{23}f & 2\sigma_{13}f & 2\sigma_{12}f \end{bmatrix}^T \quad (2-24)$$

Thus considering the kinematics of plastic deformation and the viscoplastic constitutive law of single crystalline silicon at elevated temperature, the first-order hyperbolic system of equations of stress and velocity is obtained. In addition to small deformation, it is assumed that the total strain rate is the sum of elastic strain rate and plastic strain rate, thus defining the kinematics of plastic deformation subject to the temperature range considered.

2.3 Computational Model

Due to the complexity of the constitutive law, it is difficult to find closed-form solutions to the system of equations that describe elasto-viscoplastic wave motions in silicon wafers. A finite difference scheme is introduced in the following for solving the equations numerically to obtain waveforms at selected locations in a 3-D model domain. Figure 2.1 shows the configuration of the 3-D model. The model is a square plate of $30\text{mm}\times 30\text{mm}\times 0.5\text{mm}$ in dimensions. Since the influence of wafer thickness on wave dispersion is significant, thus necessary to be investigated, the model thickness is considered as an important input parameter that needs be specified in all model runs. A point excitation is exerted at the center of the plate model. Two waveforms are obtained as output at the two sampling locations, A and B, that are 5mm and 7mm away from the excitation point, respectively.

In the model shown in Figure 2.1, a point source with a simultaneous temporal-spatial profile is introduced as the forcing function. The function is a stress rate term having a two-dimensional Gaussian function and an impulse function in time that

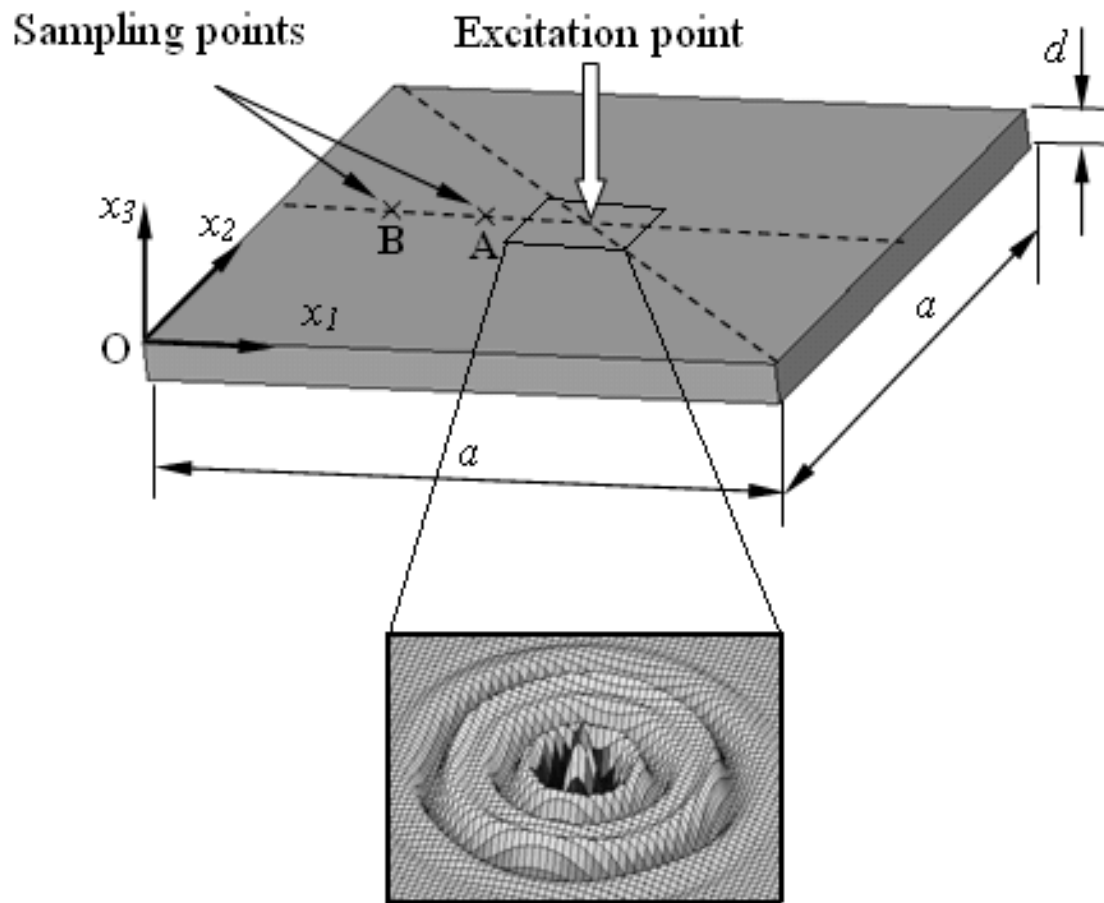


Figure 2.1 Configuration of 3-D model domain for solving wave equation

describes, respectively, the spatial and temporal distributions of the function as $g(x_1, x_2, t) = F(t)G(x_1, x_2)$, with $F(t)$ and $G(x_1, x_2)$ being defined explicitly as follows:

$$F(t) = \begin{cases} A_m \exp\left[-\frac{(t-3\sigma_i)^2}{2\sigma_i^2}\right] & (0 \leq t \leq T_i) \\ 0 & (t > T_i) \end{cases} \quad (2-25)$$

and

$$G(x_1, x_2) = \exp\left[-\frac{(x_1-X_1)^2 + (x_2-X_2)^2}{2\beta_s^2}\right] \quad (2-26)$$

where A_m is the amplitude of the impulse, T_i is the duration of the impulse (which is 20 nsec for the LISWT configuration reported in [10] and [50]), $\sigma_i = T_i / 6$ is a temporal parameter, (X_1, X_2) is the coordinates of the excitation located on the top surface, $\beta_s = d_s / 6$ is a spatial parameter that depends on the spot size, d_s . It should be noted that, because stress wave generation by laser impulse is a complex, coupled thermal-mechanical process that is beyond the scope of the dissertation, $g(x_1, x_2, t) = F(t)G(x_1, x_2)$ defined above is employed as an approximation to laser excitation. Figures 2.2 and 2.3 plot the two distribution functions that are incorporated into the computational model for the generation of Lamb guided waves in silicon thin plates.

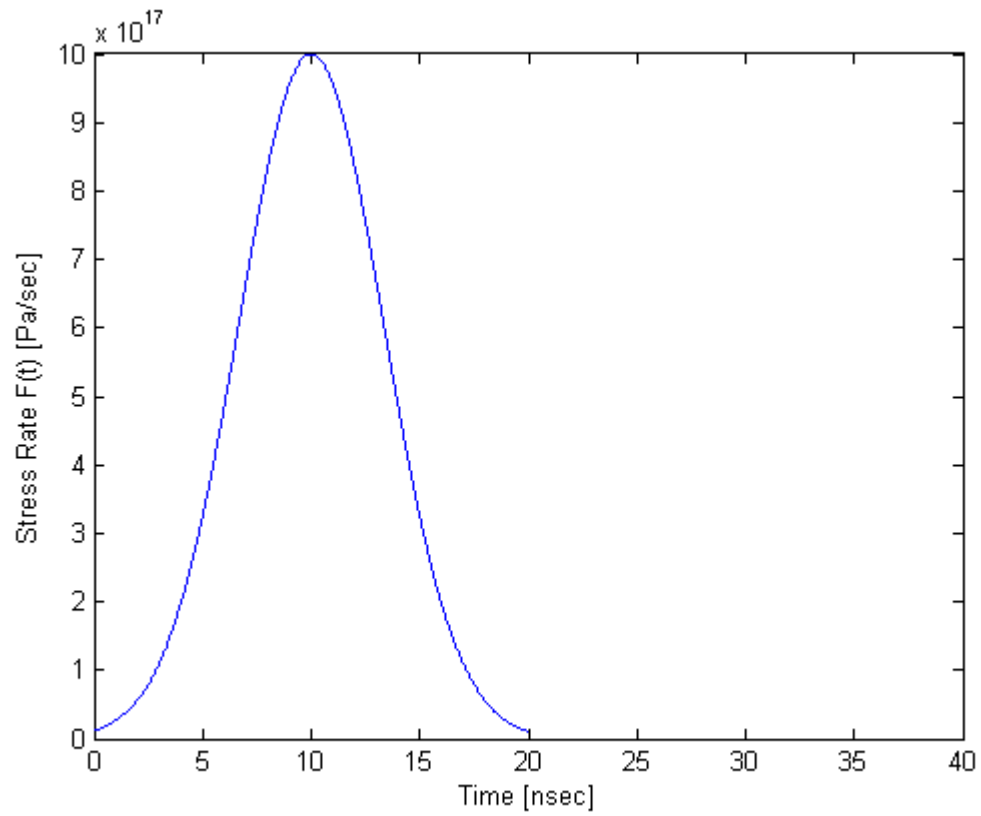


Figure 2.2 Temporal distribution Gaussian function $F(t)$ of stress wave input function

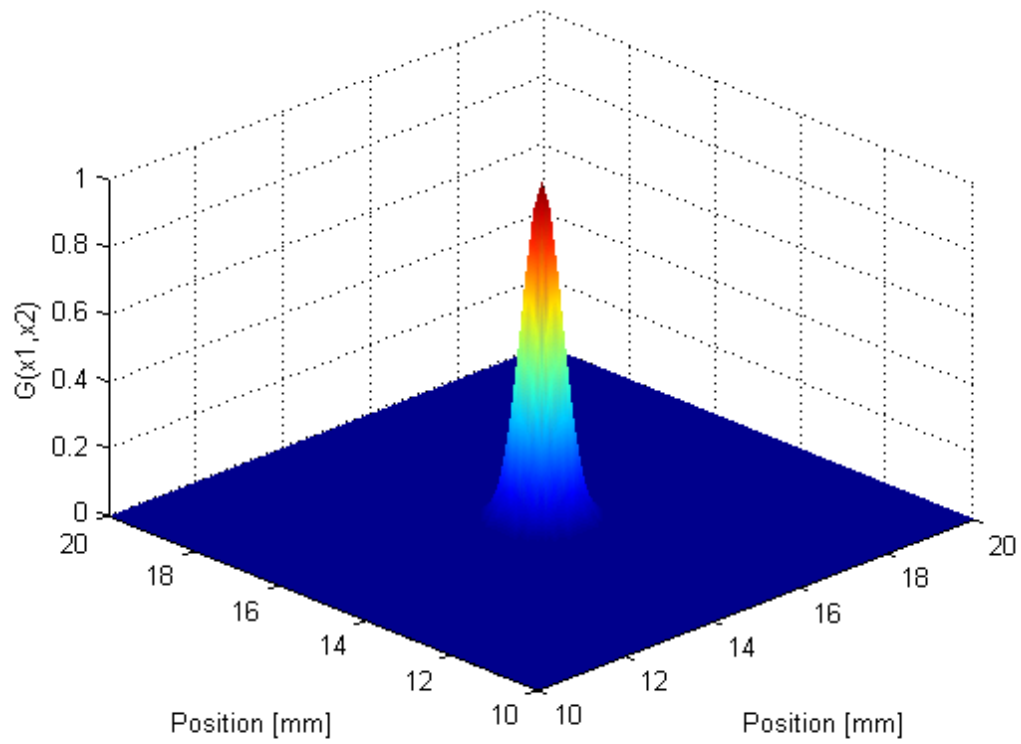


Figure 2.3 Spatial distribution Gaussian function $G(x_1, x_2)$ of stress wave input function

2.3.1 Finite Difference Model

The staggered-grid finite difference scheme is followed to define the unknown variables, stress and velocity components, at each grid point. Since the unknown variables in the governing equations are not defined at the same grid point, but instead they are halfway off according to their positions in the equation. Figure 2.4 shows the arrangement of unknown variables in one control volume in the finite difference mesh where the three normal stresses are defined at the center and the three shear stresses are at the midpoint of each side. The three velocity components $v_i (i = 1, 2, 3)$ are defined at the center of the six sides and aligned with the x_i -axis. With stress components being surrounded by velocity components, and vice versa, the scheme is thus called “staggered.”

As a type of orthotropic material, crystalline silicon has three orthogonal planes of symmetry. When the three coordinate axes are aligned with the three planes of symmetry, the stress components in the material can be expressed in terms of the strains following the Hook’s Law as

$$\begin{bmatrix} \sigma_{11} \\ \sigma_{22} \\ \sigma_{33} \\ \sigma_{23} \\ \sigma_{13} \\ \sigma_{12} \end{bmatrix} = \begin{bmatrix} C_{11} & C_{12} & C_{13} & 0 & 0 & 0 \\ C_{21} & C_{22} & C_{23} & 0 & 0 & 0 \\ C_{31} & C_{32} & C_{33} & 0 & 0 & 0 \\ 0 & 0 & 0 & C_{44} & 0 & 0 \\ 0 & 0 & 0 & 0 & C_{55} & 0 \\ 0 & 0 & 0 & 0 & 0 & C_{66} \end{bmatrix} \begin{bmatrix} \varepsilon_{11}^{(e)} \\ \varepsilon_{22}^{(e)} \\ \varepsilon_{33}^{(e)} \\ \varepsilon_{23}^{(e)} \\ \varepsilon_{13}^{(e)} \\ \varepsilon_{12}^{(e)} \end{bmatrix} \quad (2-27)$$

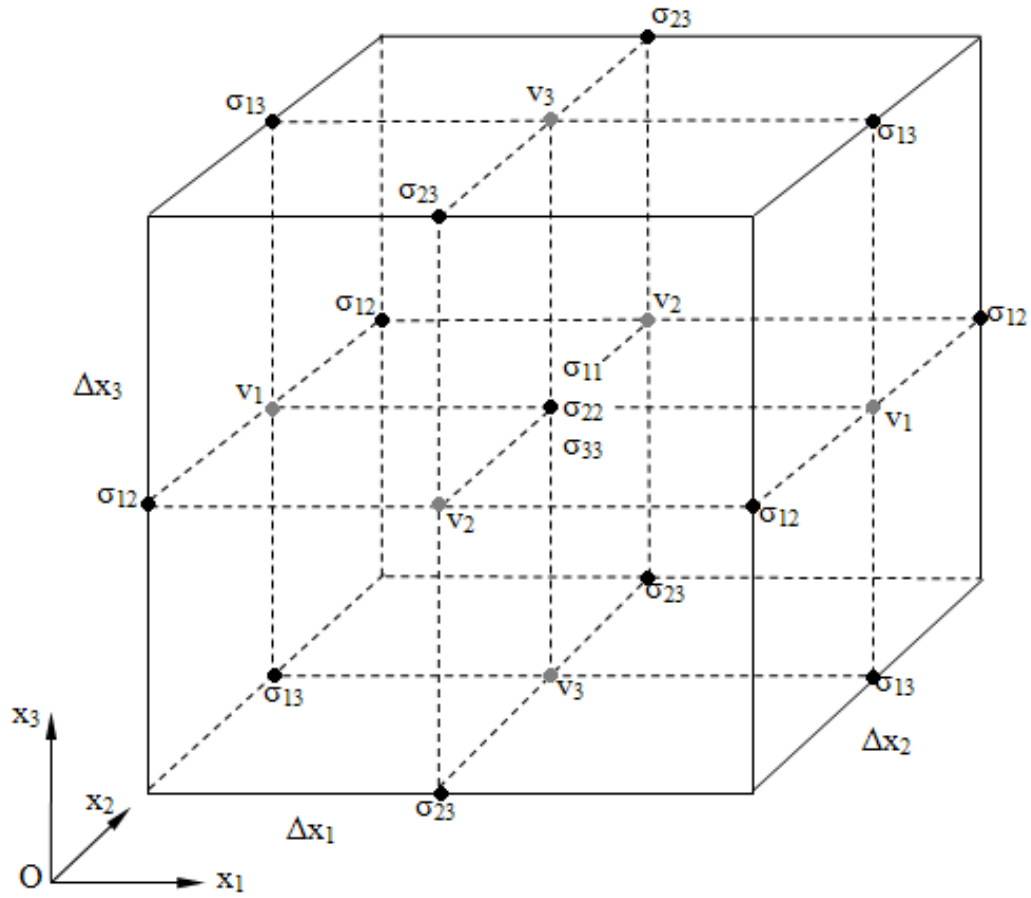


Figure 2.4 Finite difference model with staggered grids

Here C_{ij} is the stiffness matrix. Using the arrangement defined in Figure 2.4 and assuming a time step, Δt , along with 3 spatial discretizations, Δx_1 , Δx_2 , Δx_3 , the first-order hyperbolic equation system in Eq. (2-18) can be discretized into the following finite difference equations:

$$\begin{aligned}
& \sigma_{mm}^{(n+1)}\left(i + \frac{1}{2}, j + \frac{1}{2}, k + \frac{1}{2}\right) = \sigma_{mm}^{(n)}\left(i + \frac{1}{2}, j + \frac{1}{2}, k + \frac{1}{2}\right) \\
& + C_{m1} \frac{\Delta t}{\Delta x_1} \left(v_1^{(n+1/2)}\left(i + 1, j + \frac{1}{2}, k + \frac{1}{2}\right) - v_1^{(n+1/2)}\left(i, j + \frac{1}{2}, k + \frac{1}{2}\right)\right) \\
& + C_{m2} \frac{\Delta t}{\Delta x_2} \left(v_2^{(n+1/2)}\left(i + \frac{1}{2}, j + 1, k + \frac{1}{2}\right) - v_2^{(n+1/2)}\left(i + \frac{1}{2}, j, k + \frac{1}{2}\right)\right) \\
& + C_{m3} \frac{\Delta t}{\Delta x_3} \left(v_3^{(n+1/2)}\left(i + \frac{1}{2}, j + \frac{1}{2}, k + 1\right) - v_3^{(n+1/2)}\left(i + \frac{1}{2}, j + \frac{1}{2}, k\right)\right) \\
& - (C_{m1} \xi_{11}^{(n)}\left(i + \frac{1}{2}, j + \frac{1}{2}, k + \frac{1}{2}\right) + C_{m2} \xi_{22}^{(n)}\left(i + \frac{1}{2}, j + \frac{1}{2}, k + \frac{1}{2}\right) \\
& + C_{m3} \xi_{33}^{(n)}\left(i + \frac{1}{2}, j + \frac{1}{2}, k + \frac{1}{2}\right)) \Delta t \quad (m = 1, 2, 3)
\end{aligned} \tag{2-28}$$

$$\begin{aligned}
& \sigma_{23}^{(n+1)}\left(i + \frac{1}{2}, j, k\right) = \sigma_{23}^{(n)}\left(i + \frac{1}{2}, j, k\right) \\
& + \frac{C_{44}}{2} \frac{\Delta t}{\Delta x_3} \left(v_2^{(n+1/2)}\left(i + \frac{1}{2}, j, k + \frac{1}{2}\right) - v_2^{(n+1/2)}\left(i + \frac{1}{2}, j, k - 1\right)\right) \\
& + \frac{C_{44}}{2} \frac{\Delta t}{\Delta x_2} \left(v_3^{(n+1/2)}\left(i + \frac{1}{2}, j + \frac{1}{2}, k\right) - v_3^{(n+1/2)}\left(i + \frac{1}{2}, j - \frac{1}{2}, k\right)\right) \\
& - C_{44} \xi_{23}^{(n)}\left(i + \frac{1}{2}, j, k\right) \Delta t
\end{aligned} \tag{2-29}$$

$$\begin{aligned}
\sigma_{13}^{(n+1)}(i, j + \frac{1}{2}, k) &= \sigma_{13}^{(n)}(i, j + \frac{1}{2}, k) \\
&+ \frac{C_{55}}{2} \frac{\Delta t}{\Delta x_3} (v_1^{(n+1/2)}(i, j + \frac{1}{2}, k + \frac{1}{2}) - v_1^{(n+1/2)}(i, j - \frac{1}{2}, k + \frac{1}{2})) \\
&+ \frac{C_{55}}{2} \frac{\Delta t}{\Delta x_1} (v_3^{(n+1/2)}(i + \frac{1}{2}, j + \frac{1}{2}, k) - v_3^{(n+1/2)}(i - \frac{1}{2}, j + \frac{1}{2}, k)) \\
&- C_{55} \xi_{13}^{(n)}(i, j + \frac{1}{2}, k) \Delta t
\end{aligned} \tag{2-30}$$

$$\begin{aligned}
\sigma_{12}^{(n+1)}(i, j, k + \frac{1}{2}) &= \sigma_{12}^{(n)}(i, j, k + \frac{1}{2}) \\
&+ \frac{C_{66}}{2} \frac{\Delta t}{\Delta x_2} (v_1^{(n+1/2)}(i, j + \frac{1}{2}, k + \frac{1}{2}) - v_1^{(n+1/2)}(i, j - \frac{1}{2}, k + \frac{1}{2})) \\
&+ \frac{C_{66}}{2} \frac{\Delta t}{\Delta x_1} (v_2^{(n+1/2)}(i + \frac{1}{2}, j, k + \frac{1}{2}) - v_2^{(n+1/2)}(i - \frac{1}{2}, j, k + \frac{1}{2})) \\
&- C_{66} \xi_{12}^{(n)}(i, j, k + \frac{1}{2}) \Delta t
\end{aligned} \tag{2-31}$$

$$\begin{aligned}
v_1^{(n+1/2)}(i, j + \frac{1}{2}, k + \frac{1}{2}) &= v_1^{(n-1/2)}(i, j + \frac{1}{2}, k + \frac{1}{2}) \\
&+ \frac{\Delta t}{\rho \Delta x_1} (\sigma_{11}^{(n)}(i + \frac{1}{2}, j + \frac{1}{2}, k + \frac{1}{2}) - \sigma_{11}^{(n)}(i - \frac{1}{2}, j + \frac{1}{2}, k + \frac{1}{2})) \\
&+ \frac{\Delta t}{\rho \Delta x_2} (\sigma_{12}^{(n)}(i, j + 1, k + \frac{1}{2}) - \sigma_{12}^{(n)}(i, j, k + \frac{1}{2})) \\
&+ \frac{\Delta t}{\rho \Delta x_3} (\sigma_{13}^{(n)}(i, j + \frac{1}{2}, k + 1) - \sigma_{13}^{(n)}(i, j + \frac{1}{2}, k))
\end{aligned} \tag{2-32}$$

$$\begin{aligned}
v_2^{(n+1/2)}(i + \frac{1}{2}, j, k + \frac{1}{2}) &= v_2^{(n-1/2)}(i + \frac{1}{2}, j, k + \frac{1}{2}) \\
&+ \frac{\Delta t}{\rho \Delta x_1} (\sigma_{12}^{(n)}(i + 1, j, k + \frac{1}{2}) - \sigma_{12}^{(n)}(i, j, k + \frac{1}{2})) \\
&+ \frac{\Delta t}{\rho \Delta x_2} (\sigma_{22}^{(n)}(i + \frac{1}{2}, j + \frac{1}{2}, k + \frac{1}{2}) - \sigma_{22}^{(n)}(i + \frac{1}{2}, j - \frac{1}{2}, k + \frac{1}{2})) \\
&+ \frac{\Delta t}{\rho \Delta x_3} (\sigma_{32}^{(n)}(i + \frac{1}{2}, j, k + 1) - \sigma_{32}^{(n)}(i + \frac{1}{2}, j, k))
\end{aligned} \tag{2-33}$$

$$\begin{aligned}
v_3^{(n+1/2)}(i + \frac{1}{2}, j, k + \frac{1}{2}) &= v_3^{(n-1/2)}(i + \frac{1}{2}, j, k + \frac{1}{2}) \\
&+ \frac{\Delta t}{\rho \Delta x_1} (\sigma_{13}^{(n)}(i + 1, j + \frac{1}{2}, k) - \sigma_{13}^{(n)}(i, j + \frac{1}{2}, k)) \\
&+ \frac{\Delta t}{\rho \Delta x_2} (\sigma_{23}^{(n)}(i + \frac{1}{2}, j + 1, k) - \sigma_{23}^{(n)}(i + \frac{1}{2}, j, k)) \\
&+ \frac{\Delta t}{\rho \Delta x_3} (\sigma_{33}^{(n)}(i + \frac{1}{2}, j + \frac{1}{2}, k + \frac{1}{2}) - \sigma_{33}^{(n)}(i + \frac{1}{2}, j + \frac{1}{2}, k - \frac{1}{2}))
\end{aligned} \tag{2-34}$$

The above contains 9 discretized equations, with the superscripts denoting the index for time step, the “1/2” index indicating the “staggered” arrangement, and ξ_{ij} representing the plastic strain rate, $\dot{\epsilon}_{ij}^{(p)}$, which can be calculated using Eq. (2-3),

$$\xi_{ij}^{(n)} = f^{(n)} S_{ij}^{(n)}.$$

For cubic single crystalline silicon, only three independent elastic constants exist. These elastic constants in the stiffness matrix in Eq. (2-27) are found to be temperature-dependent as follows [50]:

$$C_{ij} = \begin{cases} 1.6564 \times 10^{11} \exp[-9.4 \times 10^{-5} (T - 298.15)] \text{ (Pa)} & (i = j = 1, 2, 3) \\ 0.6394 \times 10^{11} \exp[-9.8 \times 10^{-5} (T - 298.15)] \text{ (Pa)} & (i \neq j) \\ 0.7915 \times 10^{11} \exp[-8.3 \times 10^{-5} (T - 298.15)] \text{ (Pa)} & (i = j = 4, 5, 6) \end{cases} \quad (2-35)$$

Since the elastic constants in Eq. (2-35) and the plastic coefficient f in $\xi_{ij}^{(n)} = f^{(n)} S_{ij}^{(n)}$ are all functions of temperature from 23°C up to 1000°C, the stress and velocity variables in the discretized equations system are therefore temperature dependent. It should be noted that only wave motions along the [1 0 0] crystal lattice direction are acquired from the plate model. Extraction of thermal information from waves propagating along the particular crystal direction is discussed in the section that follows.

2.3.2 Boundary Conditions, Temporal and Spatial Discretization

The boundary conditions of the 3-D finite difference plate model are so defined that all four sides of the model are clamped, thus displacements along $x_1 = 0$, $x_1 = a$, $x_2 = 0$ and $x_2 = a$ are restrained. Moreover, at time $t = 0$, all initial values of the stress and velocity component are set to be zero. The explicit time integration method is followed for solving the 9 discretized nonlinear equations in Eqs. (2-28)-(2-34). The implicit method is not chosen for its costly overhead and the large number of iterations needed for solving the equations. However, the explicit method may become computationally unstable if the integration time step were not properly chosen. A proper time step is determined using the Courant condition to ensure solution convergence

$$\Delta t \leq \frac{1}{c_{\max} \sqrt{\frac{1}{\Delta x_1^2} + \frac{1}{\Delta x_2^2} + \frac{1}{\Delta x_3^2}}} \quad (2-36)$$

with c_{\max} being the maximum wave velocity that is equal to the longitudinal wave velocity in the silicon material as $c_{\max} = c_l = \sqrt{\frac{\lambda + 2\mu}{\rho}}$, where λ and μ are Lamé constants and ρ is the mass density. The longitudinal wave velocity is approximately $c_{\max} = 8000$ m/sec in single crystalline silicon. Spatial discretizations, Δx_1 , Δx_2 and Δx_3 , mainly depend on the mesh size. When element numbers in the 3-D plate domain are greater than $100 \times 100 \times 5$, results obtained in response to the range of temperature considered are seen to show negligible differences. Thus, no further mesh refinement is needed. With the particular mesh size, the maximum allowed time step according to Eq. (2-36) is found to be $\Delta t \leq 1.1 \times 10^{-8}$ sec. A much smaller time step, $\Delta t = 2$ nsec, is chosen to improve accuracy.

2.4 Summary

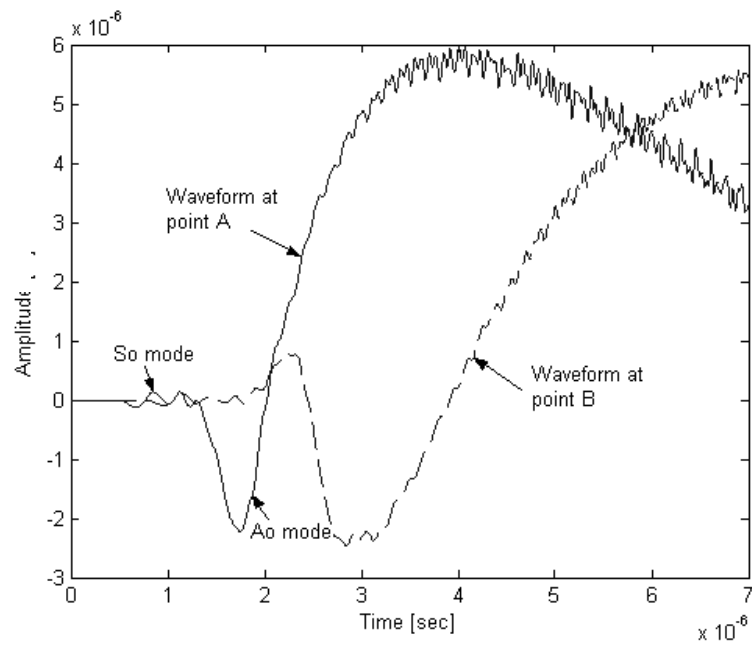
In this chapter, a unified plastic constitutive law, which accurately embodies the elasto-viscoplastic characteristics of silicon material at temperatures ranging from 23°C to exceeding 1000°C , along with the kinematics of elasto-plastic deformation were reviewed. A system of nine first-order hyperbolic equations applicable to describing 3-D elasto-viscoplastic wave motion in silicon wafer was developed. The advantage provided by the first-order hyperbolic system was of many folds. First it rendered

possible the incorporation of a complex constitutive law – one which conventional displacement or stress formulations cannot handle because elimination of unknowns is impossible with the complex constitutive law present. Secondly, it enabled velocity and stress as the dependent variables. In other words, unlike the conventional formulations where displacement was the unknown to be solved for, it provided a straightforward way to obtain information on both motion and force simultaneously. Finally this first-order system was readily discretized following the staggered grid method, so that solutions to the equation system as numerical waveforms could be obtained. Using the model it is possible to correlate temperature with the group velocity and attenuation of certain selected spectral components (thus temperature-dependent dispersion) over the targeted range of temperatures. In addition to understanding temperature influence on wave propagation in silicon, the influence of other parameters such as wafer thickness can also be studied. In Chapter III, numerical results will be presented and discussed to establish the feasibility of exploiting nanosecond laser induced propagating stress waves to the high resolution thermal profiling of silicon wafers undergoing rapid annealing.

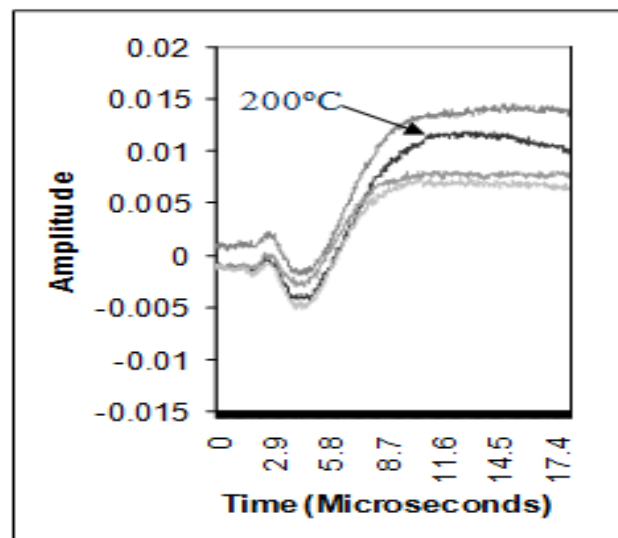
CHAPTER III
NANOSECOND LASER INDUCED STRESS WAVE
THERMOMETRY FOR SILICON PROCESSING

3.1 Waveforms and Gabor Wavelet Transform

Disturbances propagating in silicon wafer of finite thickness are bound by two traction-free surfaces. Such dynamic modes are called Lamb guided waves, which are dispersive with time-varying spectra. Figure 3.1 shows the Lamb waveforms acquired at locations A and B at 200°C (see Figure 2.1) using the 3-D finite difference computational model elaborated in Chapter II. The numerical waveforms agree well with the experimental observations made with 4"-diameter silicon wafers subject to thermal annealing reported in [10, 12, 51], thus validating the elasto-viscoplastic wave model along with the numerical procedures. The 7 μ s time window is adequate for thermal information to be fully resolved without being confounded by reflections from the boundary. For Lamb waveguide modes, only a finite number of symmetric and anti-symmetric modes are admissible for any selected frequency. S_0 and A_0 modes represent the lowest symmetric and anti-symmetric modes, respectively. It is evident from the waveforms that the Lamb guided waves are dispersive and broadband in frequency, making it difficult to determine the phase velocities of the different modes. In the followings, the group velocities of selected frequency components are calculated instead for the extraction of thermal information.



(a)



(b)

Figure 3.1 (a) Numerical waveforms acquired at sampling points A (5mm) and B (7mm) at 200°C in 0.5mm thick wafer; (b) Experimental waveform acquired in 4" wafer of 0.5mm thickness at a 10mm sampling point [12]

An appropriate signal processing tool must be adopted to identify the frequency characteristics of the waveforms. Fourier Transform (FT) has long been a widely used tool. But it cannot be applied to signals whose structure changes with time. This is due to the fact that FT uses a set of sinusoidal functions as the bases and assumes time-invariant spectral components of the signal. The transformed result contains only the frequency information. Unlike the Fourier Transform (FT), the Short-Time Fourier Transform (STFT) is a typical method used for time-frequency analysis of the dispersive waves. However, one of the major disadvantages of the STFT is the fixed time-frequency resolution [52], because its window function is fixed for all times and frequencies. Wavelet Transform (WT) is considered a preferred alternative signal processing tool for dispersive waves [33, 53]. In WT, a scaling parameter controls the frequency characteristics of the basis wavelet, and scaled wavelets are translated along the time dimension to calculate each wavelet coefficient corresponding to each particular time. The continuous WT is defined as follows:

$$W_f(a,b) = \frac{1}{\sqrt{a}} \int_{-\infty}^{\infty} \bar{\psi}\left(\frac{t-b}{a}\right) f(t) dt \quad (3-1)$$

where $\psi(t)$ is the basic wavelet function, a is the scaling parameter, and b is the shifting parameter. Assume that the basic wavelet function $\psi(t)$ is centered at $t=0$ with a width W and its Fourier Transform $\hat{\psi}(\omega)$ is centered at $\omega = \omega_0$ with a width \tilde{W} . Then $\psi(t-b)/a$ is centered at $t=b$ and its Fourier transform $a \exp(-ib\omega)\hat{\psi}(a\omega)$ is centered at $\omega = \omega_0/a$. Therefore a particular pair of (b,a) in the wavelet transform corresponds

to an area with a width aW along the time axis and a width \tilde{W}/a along the frequency axis. The area is centered at $(b, \omega_0/a)$ on the time-frequency plane [48].

Gabor Wavelet Transform (GWT) uses the Gabor function as the mother wavelet. Chui proved that according to the uncertainty principle, the Gabor function offers the smallest area of time-frequency window than any other function, and has high-resolution capabilities of both frequency and time [54]. The Gabor function can be expressed as a complex sinusoid modulated by a Gaussian function,

$$\psi_g(t) = \frac{1}{\sqrt[4]{\pi}} \sqrt{\frac{\omega_0}{\gamma}} \exp\left[-\frac{(\omega_0/\gamma)^2}{2} t^2 + i\omega_0 t\right] \quad (3-2)$$

The Fourier Transform of the Gabor function is

$$\hat{\psi}_g(\omega) = \frac{\sqrt{2\pi}}{\sqrt[4]{\pi}} \sqrt{\frac{\gamma}{\omega_0}} \exp\left[-\frac{(\omega_0/\gamma)^2}{2} (\omega - \omega_0)^2\right] \quad (3-3)$$

From Eq. (2-2), the Gabor function is a sinusoidal function modulated by an exponential function. Since it controls the width of the Gabor function, γ has an impact on the time-frequency resolution. Figures 3.2 and 3.3 show the GWT of the waveforms obtained at points A and B at 1000°C, respectively. It is seen that both waves are broadband up to several MHz's in spectrum, with the most energy carried by the 0-700 kHz components.

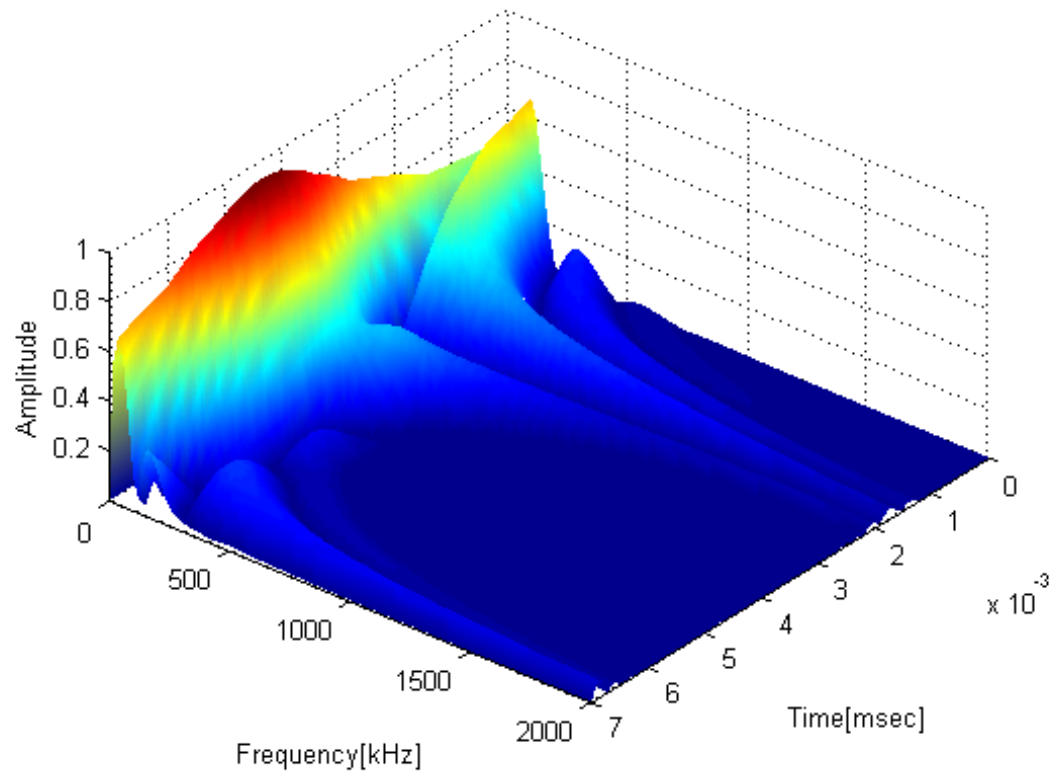


Figure 3.2 GWT of waveforms obtained at sampling point A at 1000°C (wafer thickness: 0.5mm)

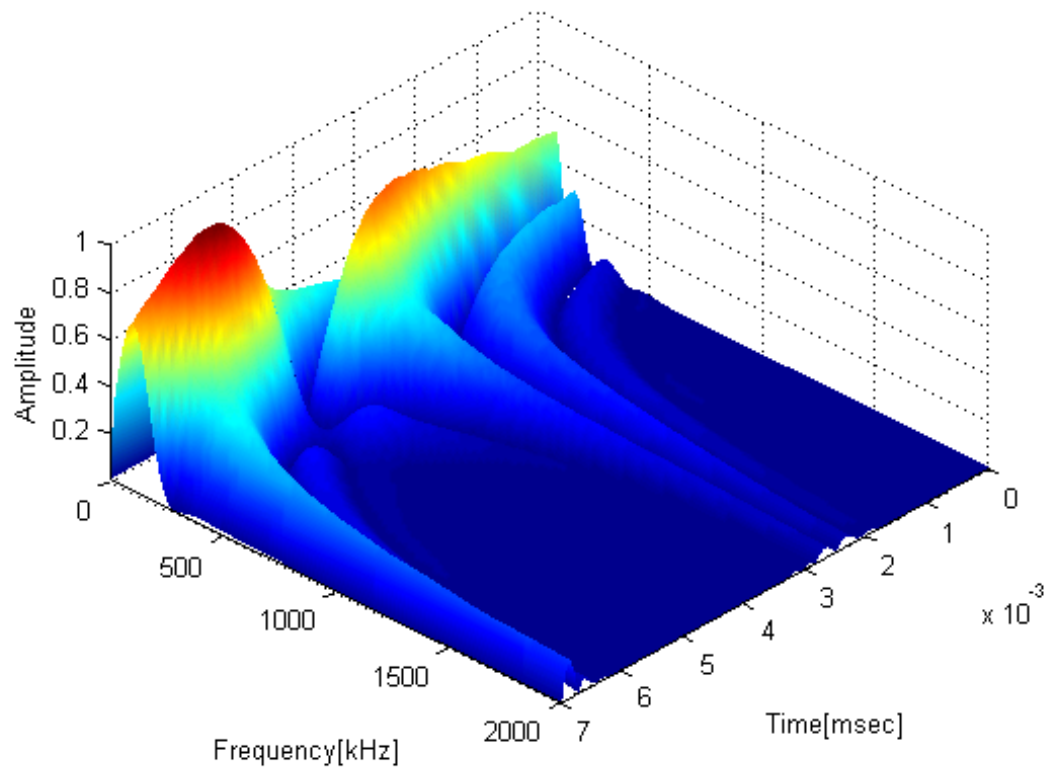


Figure 3.3 GWT of waveforms obtained at sampling point B at 1000°C (wafer thickness: 0.5mm)

3.2 Thermal Effect on Group Velocity

Though both are functions of frequency, phase velocity and group velocity are different for dispersive waves such as those seen in Figures 3.1, 3.2 and 3.3. This characteristic has a pronounced effect on the interpretation of the broadband waveforms observed in silicon wafers and, thus, the extraction of phase velocity. In the following a viable alternative is followed for the determination of dispersion information. By using GWT, the group velocity of individual frequency component, which is both frequency- and temperature-dependent, can be calculated as follows. Figures 3.4 and 3.5 show the top views of the two GWT found in Figures 3.2 and 3.3. For a particular frequency component, the time location corresponding to the maximum GWT magnitude indicates the arrival time of the frequency [33]. Designate T_a and T_b seen in Figures 3.4 and 3.5 as the arrival times of the particular frequency component f (600 kHz in this case) at points A and B, respectively. The travel time for this frequency component to reach point B from A is therefore

$$\Delta t(f) = T_b(f) - T_a(f) \quad (3-4)$$

The group velocity of component f can then be defined from the time-of-flight calculation as follow

$$v_g(f) = \frac{d}{\Delta t(f)} \quad (3-5)$$

where d is the distance between point A and B, which is 2mm in this investigation.

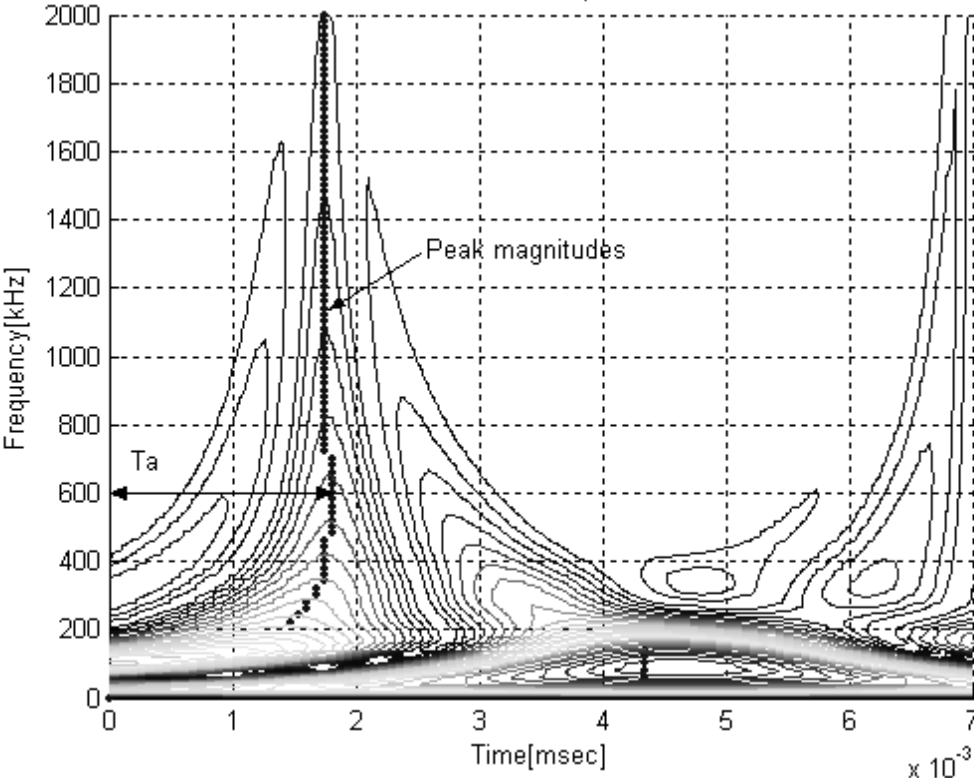


Figure 3.4 Top view of GWT of waveforms obtained at sampling point A at 1000°C
(wafer thickness: 0.5mm)

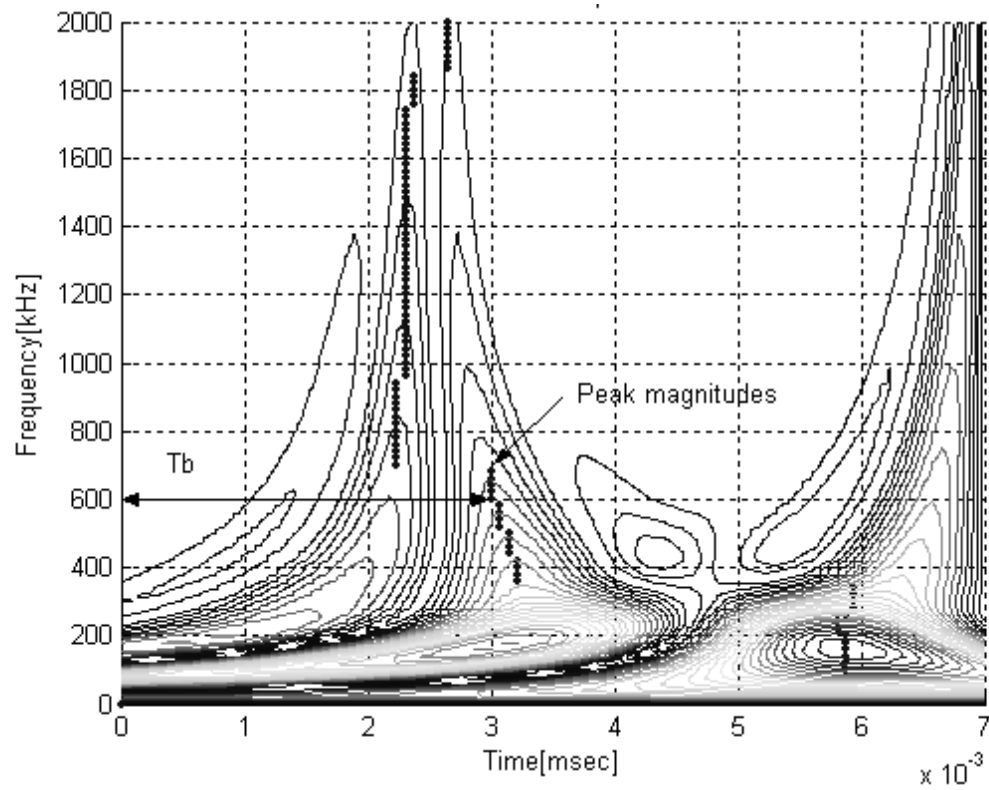


Figure 3.5 Top view of GWT of waveforms obtained at sampling point B at 1000°C

(wafer thickness: 0.5mm)

The GWT results in Figures 3.2 and 3.3 show that frequency components between 0-700 kHz are dominant within the time window considered. In the followings, two specific frequency ranges, namely, 0-100 kHz and 400-700kHz, are considered. It is noted that the two ranges of frequency correspond to the low frequency A_0 mode and high frequency S_0 mode, respectively, that are induced in a silicon wafer measured 0.5mm in thickness. Figure 3.6 shows the dispersion (group velocity as a function of frequency) in response to 5 different temperatures. It is seen that the group velocity of all the spectral components considered increases as frequency increases. For frequency components fall in the 30-to-70 kHz range, the group velocity drops almost linearly with the increasing temperature, indicating similar thermal resolution can be achieved using any frequency from within the range.

Figure 3.7 plots the dependency of group velocity on temperature ranging from 200°C to 1000°C for 3 selected frequencies: 30 kHz, 60 kHz and 90 kHz. All three lines in the figure are curve-fitted using third-order polynomials. The relationship between the group velocity and temperature, though nonlinear, is relatively well-defined for the two lower frequency components. Two observations can be made with regards to the figure: that it is in excellent agreement with the experimental results in References [10], [11] and [12] (which correspond to temperatures up to 600°C) and that the group velocity behaves almost linearly with respect to high temperatures that define the elasto-viscoplastic response of the silicon wafer.

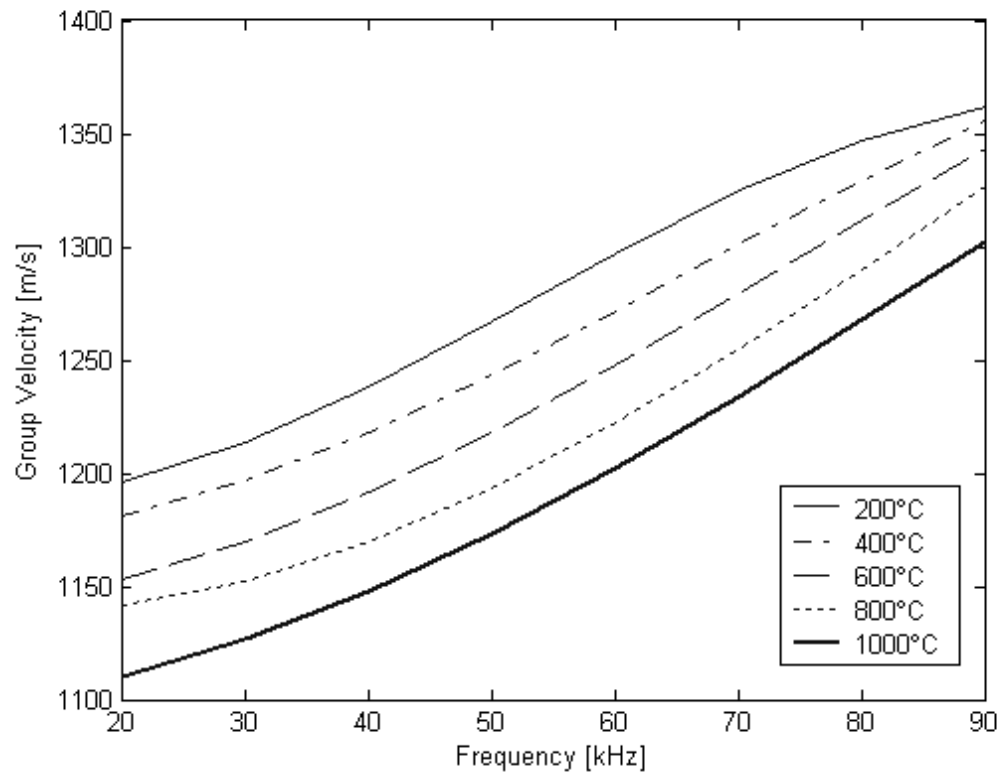


Figure 3.6 Group velocities vs. frequency (low frequency components) at five selected temperatures (wafer thickness: 0.5mm)

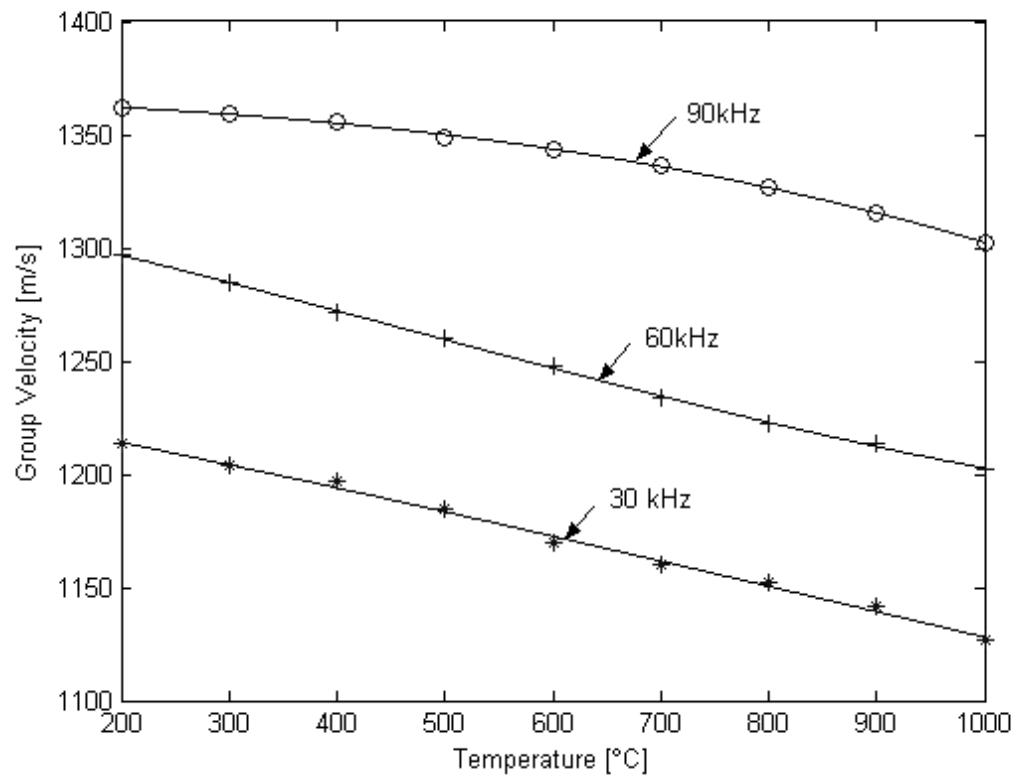


Figure 3.7 Group velocities vs. temperature of three selected low frequencies (wafer thickness: 0.5mm)

As in Figure 3.7, the spatial resolution provided by the 30 kHz and 60 kHz components for differentiating temperature variation with a $\pm 1^\circ\text{C}$ resolution is 0.12 m/s in group velocity. Such differentiating resolutions can be readily achieved using the established LISWT technique [10-12]. This well defined correlation between group velocity and temperature provides a straightforward approach for the extraction of desired thermal information. The group velocity-temperature curve for the 90 kHz frequency component is nonlinear, and the spatial and thermal resolution provided by the component is 75% less than the other two components for the 200-600°C temperature range. The 90 kHz component is therefore not preferred as an operating frequency for thermal measurement.

Similarly, Figure 3.8 shows the changes of group velocity with higher frequency components at various temperatures. It is seen that the frequencies between 450 to 650 kHz provide relatively better thermal resolution. The temperature dependence of group velocity for three selected frequency components is plotted in Figure 3.9. With the group velocity decreases by 0.16 m/s per degree Celsius ($^\circ\text{C}$), the figure shows a better thermal resolution than was seen in Figure 3.7. It is also seen that both spatial and thermal resolutions become better with increasing frequency. However, though providing a little better temperature resolution, the high frequency S_0 mode is less attractive than the low frequency A_0 mode [10] for the reasons that the symmetric S_0 mode is more difficult to generate and that it has a much smaller signal-to-noise ratio.

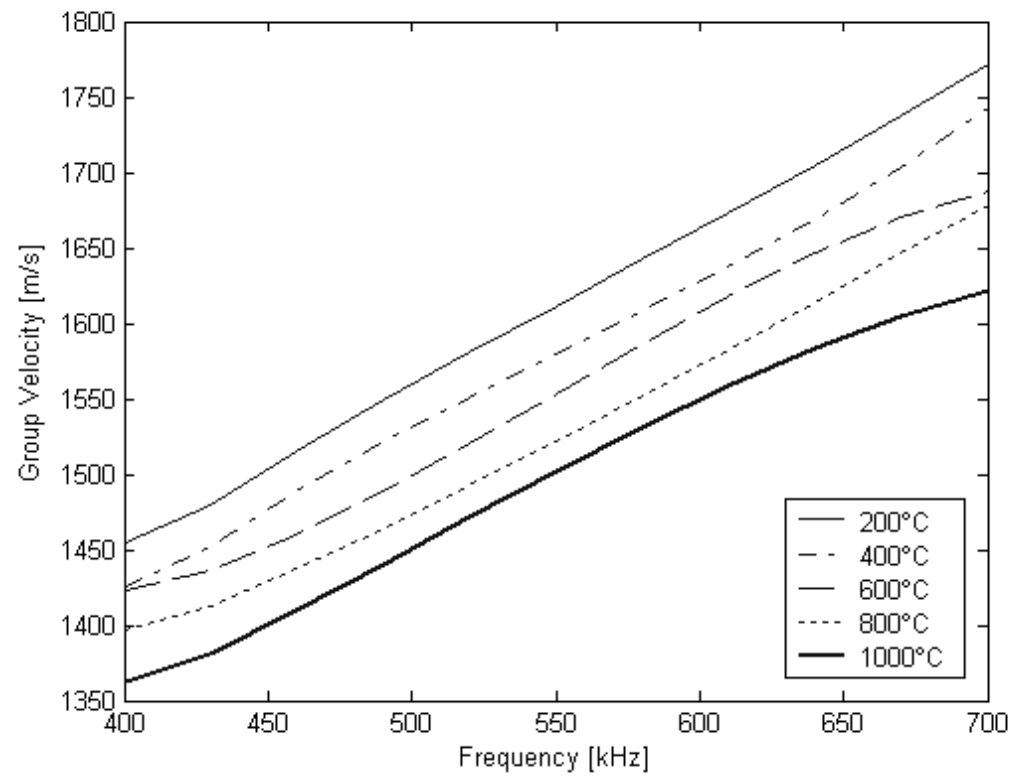


Figure 3.8 Group velocities vs. frequency (high frequency components) at five selected temperatures (wafer thickness: 0.5mm)

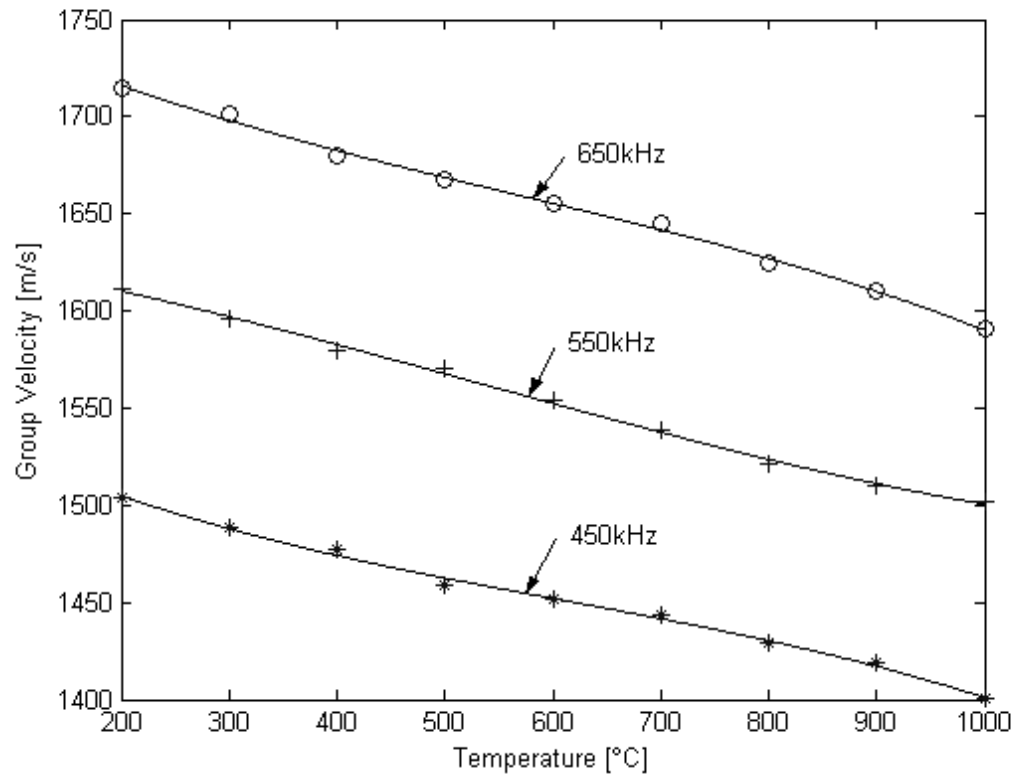


Figure 3.9 Group velocities vs. temperature of three selected high frequencies (wafer thickness: 0.5mm)

3.3 Thermal Effect on Wave Attenuation

Attenuation of elasto-viscoplastic waves in silicon wafer at annealing temperature is mainly caused by the viscous damping and plastic deformation in the material. As energy dissipates, wave amplitudes decrease. Attenuation in dispersive waves can be calculated as follows. Assume that $y_a(x_a, t)$ and $y_b(x_b, t)$ are the two waveforms acquired at two different locations in space, and $A_a(f)$ and $A_b(f)$ are the GWT projection of the two waveforms. An attenuation factor Q can be defined as follow to quantify the attenuation of a particular frequency component f ,

$$Q(f) = -20 \times \log\left[\frac{A_a(f)}{A_b(f)}\right] \quad (3-6)$$

The unit of the logarithmic operation Q is dB. Obviously Q is a function of frequency. Implicitly, since $A_a(f)$ and $A_b(f)$ are functions of locations x_a and x_b , respectively, Q is also a function of the distance between the two locations. Since temperature has an immediate impact on plastic constitutive law, wave attenuation is an indicative function for temperature variation.

Frequency- and temperature-dependent wave attenuation can also be exploited to establish thermal information. However, a relevant question to ask is if exploiting attenuation would provide the desired $\pm 1^\circ\text{C}$ resolution? Figure 3.10 shows the changes of attenuation factor with low frequency components at various temperatures. Unlike the case with group velocity, the differentiations between the five curves (which correspond to the 5 temperatures considered) decrease with increasing frequency,

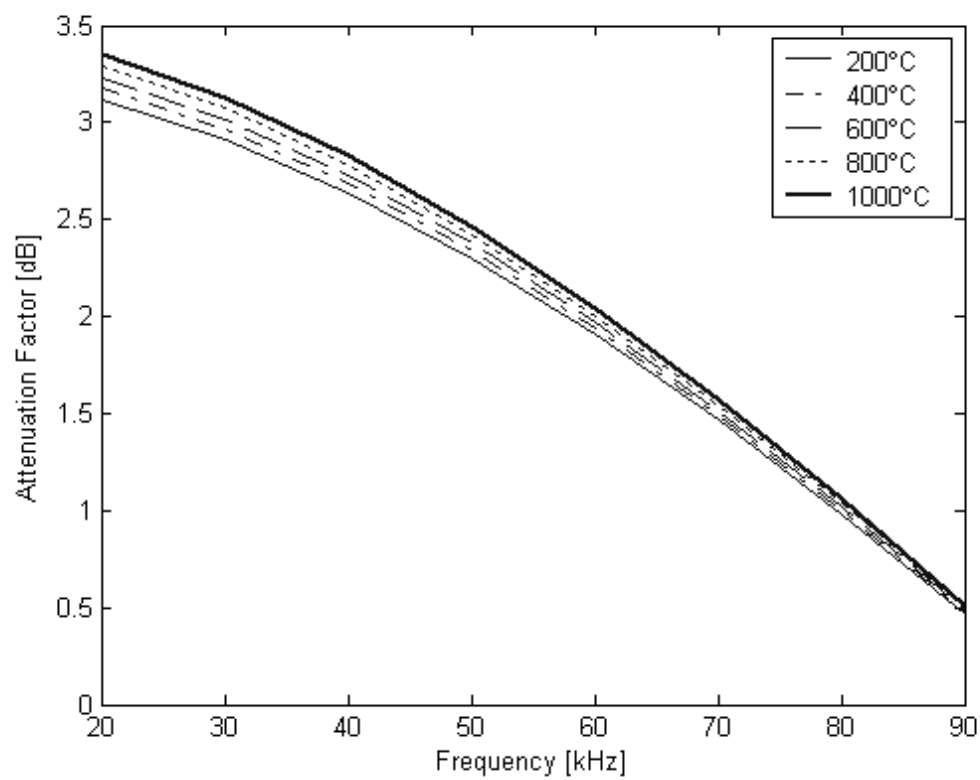


Figure 3.10 Attenuation factor vs. frequency (low frequency components) at five selected temperatures (wafer thickness: 0.5mm)

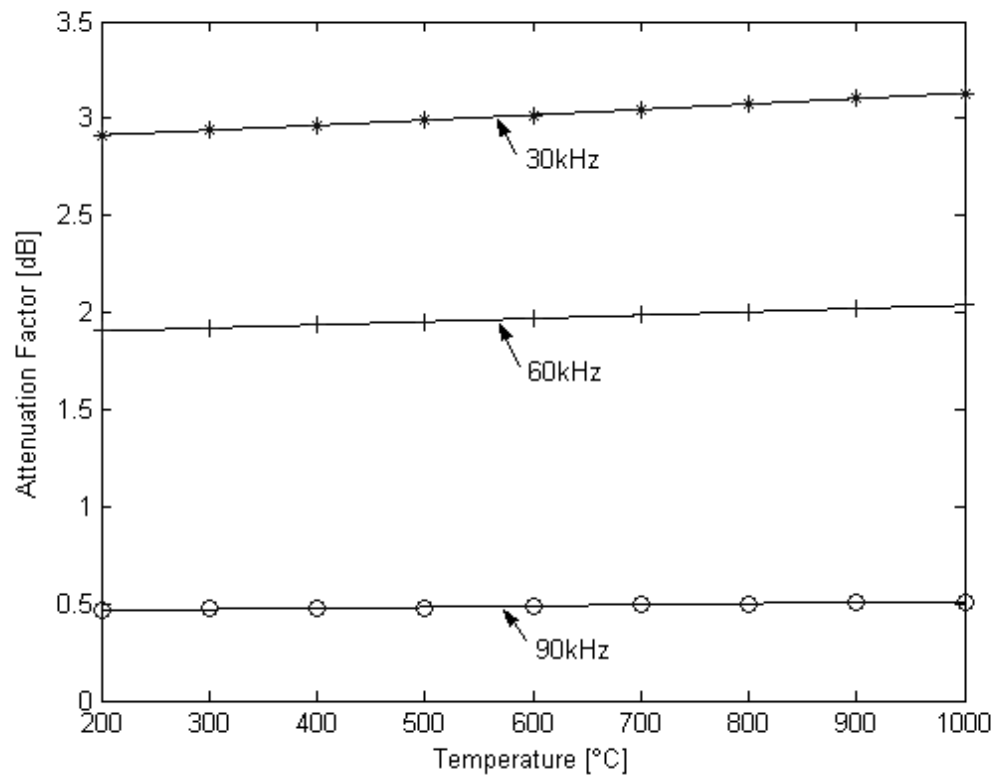


Figure 3.11 Attenuation factor vs. temperature of three selected low frequencies (wafer thickness: 0.5mm)

meaning that thermal resolution becomes worse as frequency increases. This can be observed further in Figure 3.11, where wave attenuation is plotted against temperature for three different frequency components. To differentiate temperature with a $\pm 1^\circ\text{C}$ resolution, the required changes in attenuation factor are roughly 3.1×10^{-4} dB, 1.5×10^{-4} dB and 0 dB for the 30 kHz, 60 kHz and 90 kHz components, respectively. These magnitudes are relatively difficult for LISWT to make out. However, the magnitude of the attenuation factor will increase when the distance d between sampling points A and B increases. Further analyses (not shown) indicate that the magnitude could increase as much as five times subject to an increase of d from 2 mm to 5 mm. Since such a spatial separation can be readily achieved in a 12"-diameter silicon wafer, it would be feasible to achieve the desired $\pm 1^\circ\text{C}$ thermal resolution should the 30 kHz frequency be selected.

Figure 3.12 shows the changes of attenuation factor with high frequency components in response to the same temperature range. All attenuation factors are seen to increase with increasing frequency, which is opposite to what was observed for the low frequency components in Figure 3.10. As seen in Figure 3.13, the magnitudes of these factors vary negligibly in the temperature range considered. It therefore can be concluded that the attenuation of frequency components that are in the range of 400-700 kHz is not a feasible temperature indicator.

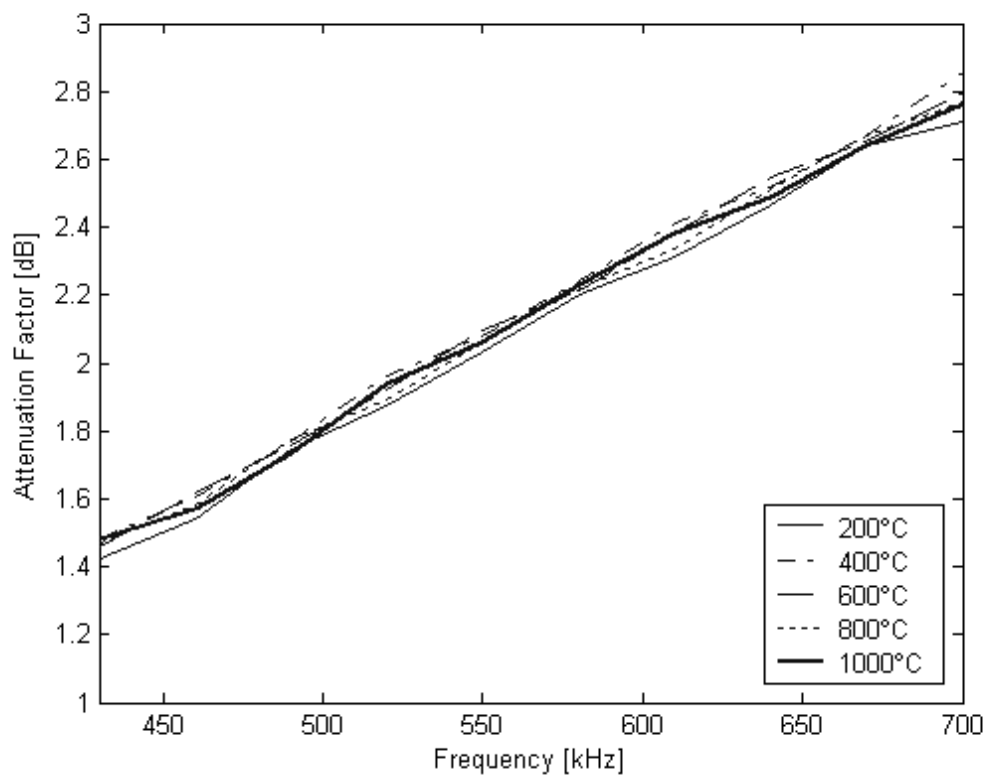


Figure 3.12 Attenuation factor vs. frequency (high frequency components) at five selected temperatures (wafer thickness: 0.5mm)

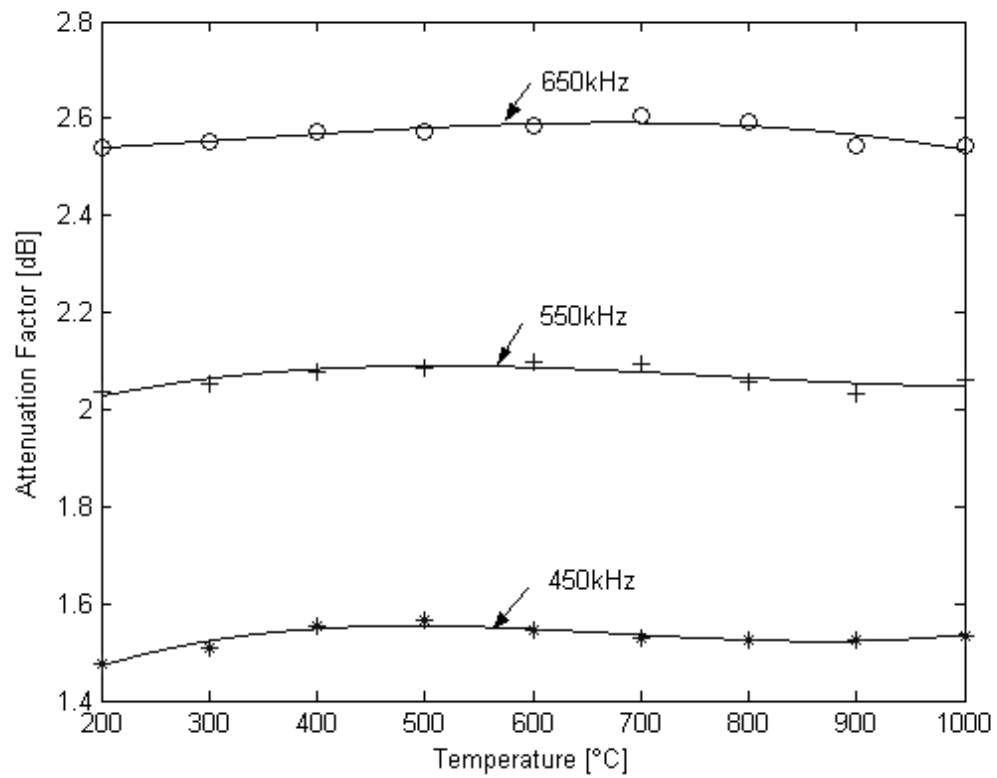


Figure 3.13 Attenuation factor vs. temperature of three selected high frequencies (wafer thickness: 0.5mm)

3.4 Thermal and Geometric Effects on Wave Dispersion

The group velocities for three selected high frequency components and low frequency components are plotted against wafer thickness in Figures 3.14 and 3.15 at 600°C processing temperature. The propagation path between sampling points A and B are set to be $d=5\text{mm}$. At the particular temperature, the dispersion curves of the three selected high frequency components in Figure 3.14 are all highly nonlinear with respect to thickness. The nonlinearity is seen to be significantly more prominent for thin wafers -- a typical property of the Lamb guided mode. As thickness increases to exceeding 0.5mm, the dispersions become well-behaved with increasing group velocity for all three components. Such an observation is also made with the three selected low frequency components in Figure 3.15, in which the group velocity associated with each component is seen to be increasing nonlinearly as the thickness is stepped up linearly from 0.5mm to 0.7mm. The impact of thickness on dispersion is evidently non-negligible. Further calculation shows that for any thermometry considered viable for discerning thickness changes as small as 0.1mm using high frequency components, it must be able to differentiate group velocity changes up to several hundreds meters per second. With the FTI (fiber-tip interferometer) broadband sensing configuration [10], LISWT meets the demanding requirement for spatial resolution. Given the non-negligible effect of wafer thickness on wave dispersion, wafer thickness needs be calibrated before thermal profiling is performed.

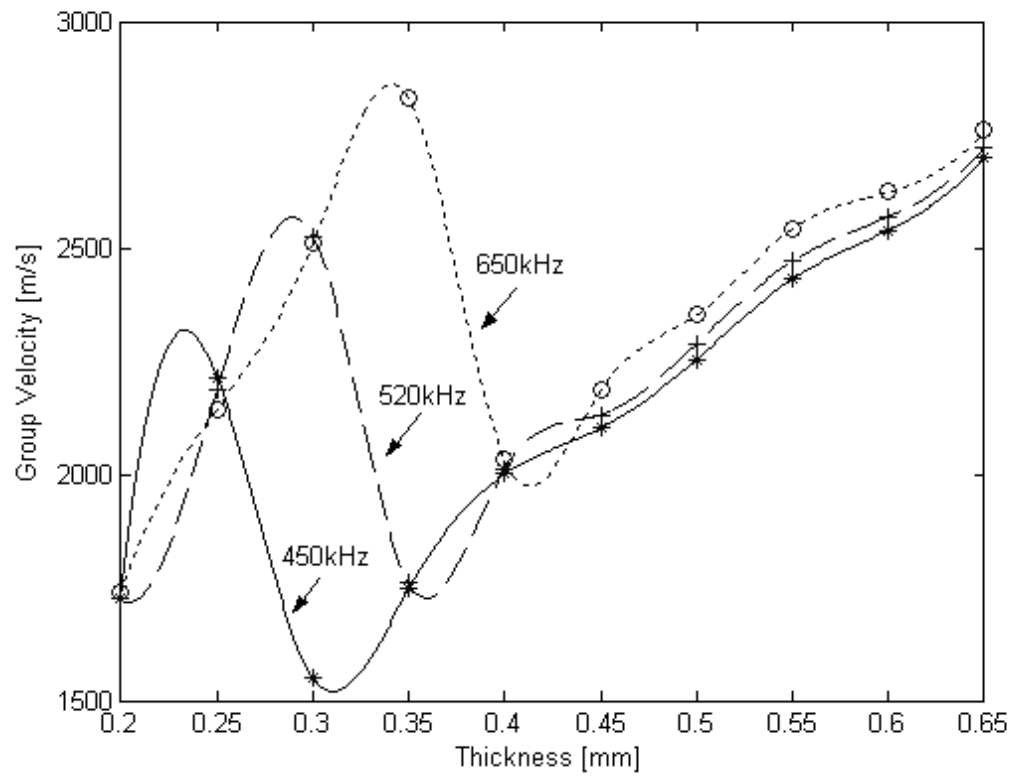


Figure 3.14 Group velocities vs. wafer thickness at 600°C wafer temperature for three selected high frequencies

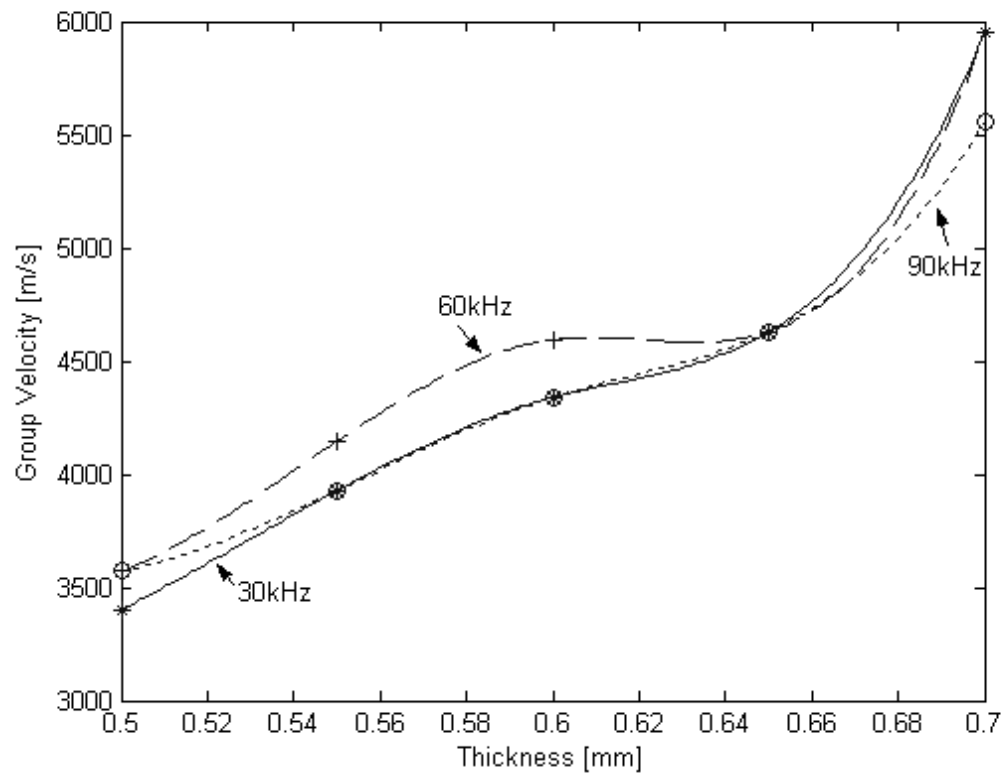


Figure 3.15 Group velocities vs. wafer thickness at 600°C wafer temperature for three selected low frequencies

From the results presented it can be concluded that temperature and wafer thickness both have a significant effect on wave dispersion. The impact of thermal variations is nonlinear. The nonlinearity becomes prominent at higher temperatures for high frequency components. And both the high and low frequencies considered for the study were relatively insensitive to the variations of attenuation factor subject to thermal increment. For every degree Celsius change of temperature, the corresponding change in attenuation factor is of the order of 10^{-4} dB or less using the low frequency components. However, attenuation factor can possibly be used as a thermal indicator if the propagation path between sampling points is properly set to allow for significant attenuation to be detected. The effect of thickness on dispersion is much more significant. Using the high frequency components, for every 0.1mm change in thickness, the orders of changes in group velocity are readily discernible by LISWT. The current LISWT setup is able to achieve such a spatial resolution through exploring wave attenuation and dispersion without the need for further enhancement.

3.5 Summary

The numerical results presented in the chapter were generated using the model formulated in Chapter II. The waveforms obtained at the two sampling points showed a good agreement with physical data reported in [11, 12]. The method for extracting thermal information, including the Gabor wavelet transform (GWT) and its application to calculate the frequency- and temperature-dependent group velocities and wave attenuations, was demonstrated.

The results showed that the group velocities for both of the frequency ranges, 30 kHz~70 kHz and 450 kHz~650 kHz, are both nonlinear functions of temperature and wafer thickness, and theoretically good enough to be used to achieve the temperature resolution of $\pm 1^\circ\text{C}$. It showed that the low frequency A_0 mode is easier to be generated and more accurate. The 30 kHz~70 kHz frequency region was thus recommended. The well defined correlation between group velocity and temperature provides a straightforward extraction of the desired thermal information for the temperature range considered. Also, once silicon wafer started behaving elasto-viscoplastically, the nonlinearity was more prominent at higher temperatures for high frequencies. Unlike the group velocity, the wave attenuation factor was found feasible only for achieving the desired temperature resolution in a relatively narrow frequency range around 30 kHz, which also requires an adequate distance between the two sampling points. For spectral components within the high frequency S_0 mode, the associated attenuation factors were too minuscule to be considered viable temperature indicators.

CHAPTER IV
FEMTOSECOND LASER INDUCED TRANSPORT DYNAMICS IN
SEMICONDUCTORS

4.1 Relaxation-Time Approximation of Boltzmann Equation

The Boltzmann equation describes the time evolution of the distribution function $f(\vec{x}, \vec{p}, t)$ of particles in a phase-space volume $d\vec{x}d\vec{p}$, where \vec{x} and \vec{p} are position and momentum, respectively. The number of particles in the volume is thus $f(\vec{x}, \vec{p}, t)d\vec{x}d\vec{p}$. Since collisions between particles do occur, the particle density in the phase-space volume, $d\vec{x}d\vec{p}$, varies, i.e.

$$\begin{aligned} & f\left(\vec{x} + \frac{\vec{p}}{m} dt, \vec{p} + \vec{F} dt, t + dt\right) d\vec{x}d\vec{p} - f(\vec{x}, \vec{p}, t) d\vec{x}d\vec{p} \\ &= \left. \frac{\partial f(\vec{x}, \vec{p}, t)}{\partial t} \right|_{coll} d\vec{x}d\vec{p} dt \end{aligned} \quad (4-1)$$

where m is the mass of the particles and \vec{F} is the external force field acting on the particles. Dividing Eq. (4-1) by $d\vec{x}d\vec{p}dt$ and taking the limit, the initial Boltzmann equation can be obtained as [55]

$$\frac{\partial f}{\partial t} + \frac{\partial f}{\partial \vec{x}} \cdot \frac{\vec{p}}{m} + \frac{\partial f}{\partial \vec{p}} \cdot \vec{F} = \left. \frac{\partial f}{\partial t} \right|_{coll} \quad (4-2)$$

With the relaxation-time approximation, the Boltzmann equation for carriers (electrons and holes) has the following form [56]

$$\frac{\partial f}{\partial t} + \nabla f \cdot \vec{v} + \frac{\partial f}{\partial \vec{p}} \cdot (q_c \vec{E}) = \frac{f_0 - f}{\tau} \quad (4-3)$$

where q_c equals to charge q , τ is the relaxation time, \vec{E} denotes electric field, and f_0 is the equilibrium distribution function. For steady-state scenarios, the temporal variation of the distribution function is negligible compared with the spatial variation and the deviation from the equilibrium distribution function f_0 is small. Thus $\frac{\partial f}{\partial t} \approx 0$ and $\nabla f \approx \nabla f_0$ can be assumed. Using the velocity vector $\vec{v} = \frac{\partial E}{\partial \vec{p}}$ where E is the energy

of the carrier, one has

$$\frac{\partial f}{\partial \vec{p}} \approx \frac{\partial f_0}{\partial \vec{p}} = \frac{\partial f_0}{\partial E} \frac{dE}{d\vec{p}} = \frac{\partial f_0}{\partial E} \vec{v} \quad (4-4)$$

Substituting Eq. (4-4) and above relations into Eq. (4-3), the relaxation time approximation of the Boltzmann equation for carriers can be rewritten as

$$(\nabla f_0 + q_c \vec{E} \frac{\partial f_0}{\partial E}) \cdot \vec{v} = \frac{f_0 - f}{\tau} \quad (4-5)$$

The corresponding Fermi-Dirac distribution function, shown in Eq. (4-6) [57], is a classical microscopic distribution function for the carriers in semiconductors

$$f_0 = \frac{1}{\exp(\eta_c) + 1} \quad (4-6)$$

The reduced Fermi level η_c and its corresponding forms for electrons and holes are given by

$$\eta_c = \frac{E - \psi_c}{k_B T_e} \quad (4-7)$$

$$\eta_e = \frac{\psi_e - E_c}{k_B T_e} \quad (4-8)$$

$$\eta_h = \frac{E_v - \psi_h}{k_B T_e} \quad (4-9)$$

where ψ_c is the Fermi level, T_e is the electron temperature, E_c and E_v are the energies of the conduction- and valence-band, respectively, and k_B is the Boltzmann constant.

From Eq. (4-7), we have

$$\frac{\partial f_0}{\partial E} = \frac{df_0}{d\eta_c} \frac{\partial \eta_c}{\partial E} = \frac{df_0}{d\eta_c} \frac{1}{k_B T_e} \quad (4-10)$$

$$\nabla f_0 = \frac{df_0}{d\eta_c} \nabla \eta_c = k_B T_e \frac{\partial f_0}{\partial E} \nabla \eta_c \quad (4-11)$$

$$\begin{aligned} \nabla \eta_c &= \frac{\nabla E - \nabla \psi_c}{k_B T_e} - \frac{E - \psi_c}{k_B T_e^2} \nabla T_e \\ &= -\frac{1}{k_B T_e} \nabla \psi_c - \frac{E - \psi_c}{k_B T_e^2} \nabla T_e \end{aligned} \quad (4-12)$$

Combining Eqs. (4-11) and (4-12),

$$\nabla f_0 = -\frac{\partial f_0}{\partial E} \left(\nabla \psi_c + \frac{E - \psi_c}{T_e} \nabla T_e \right) \quad (4-13)$$

and substituting Eq. (4-13) into Eq. (4-5), we have

$$\frac{\partial f_0}{\partial E} \left[-\nabla \psi_c - \frac{E - \psi_c}{T_e} \nabla T_e + q_c \vec{E} \right] \cdot \vec{v} = \frac{f_0 - f}{\tau} \quad (4-14)$$

Since there is no external electric field, i.e. $\vec{E} = 0$, considered in this investigation, Eq.

(4-14) can be expressed as

$$f = f_0 - \frac{\partial f_0}{\partial E} \left[-\nabla \psi_c - \frac{E - \psi_c}{T_e} \nabla T_e \right] \cdot \vec{v} \tau \quad (4-15)$$

It should be noted that the distribution function, Eq. (4-15), is a microscopic description. To generalize the microscopic description to be applicable to description at the macroscopic scale so that the distribution function can be properly integrated and the macroscopic electrical current flow (of carriers) can be obtained, certain assumptions need be made [57-58]:

- (1) The size of the volumetric domain within macroscopic transport phenomena is to be considered is large enough so that the statistical fluctuations of the dominant variables in the volume can be neglected.
- (2) The material is spatially homogeneous, thus the actual local distribution functions are not far off from the local equilibrium distribution functions. The local electron temperature and local Fermi levels of carriers can be defined in a small but macroscopic volume.
- (3) The particles of this volume are considered to be independent in the sense of the statistical and quantum mechanics, so that the overall distribution function of the volume can be expressed as a product of single particle distribution functions. The particles do not have to be bare particles, but may be quasi-particles whose total energy may include a self-energy component related to the interaction between bare particles in this volume. Thus, the energy of carriers which includes a band-gap component can vary with the carrier density and lattice temperature.

Based on the assumptions, the distribution function in Eq. (4-15) can be integrated over the entire control volume. The macroscopic electrical current which flows in and out of the volume can then be determined.

4.1.1 Macroscopic Electrical Current of the Carriers

The macroscopic electrical current of carriers is derived in a typical spherical coordinates system, shown in Figure 4.1. The electrons are located within an infinitesimal volume in the immediate proximity of the origin of the spherical coordinates with a distribution function f defined in Eq. (4-15). Therefore, the number of electrons with an energy between E and $E + dE$ is $fg(E)dE$, with $g(E)$ being the density-of-states function [56]

$$g(E) = \frac{1}{2\pi^2} \left(\frac{2m}{\hbar^2} \right)^{3/2} E^{1/2} \quad (4-16)$$

Since there is no electric field, these electrons are considered to have the same probability of moving toward any (θ, ϕ) direction in the spherical coordinates. The surface area of the sphere is $4\pi r^2$. The probability for an electron moving through a finite area $d\Omega = r^2 \sin\theta d\theta d\phi$ is hence $\frac{d\Omega}{4\pi r^2} = \frac{\sin\theta d\theta d\phi}{4\pi}$. For simplicity, the three electrical current components (j_x, j_y, j_z) are individually considered. As j_z is the electrons-generated electrical current along the Z -axis, the charge flux in the Z -direction produced by a charge moving through $d\Omega$ is $qv \cos\theta$, and the total electrical current produced by all electrons moving toward the entire sphere surrounding the infinitesimal volume can be determined as

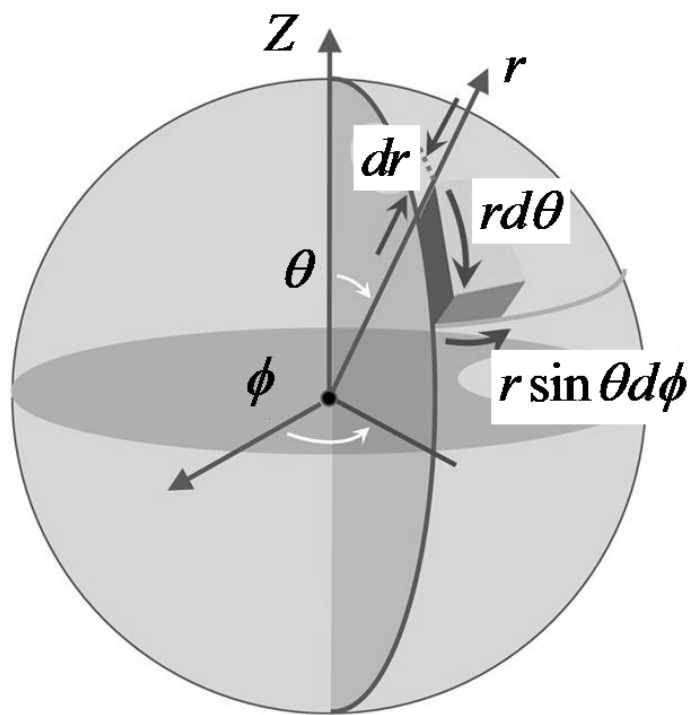


Figure 4.1 Electrical current in spherical coordinates

$$\begin{aligned}
j_z &= \iint_S \frac{\sin \theta d\theta d\phi}{4\pi} \int_{E=0}^{\infty} fg(E)(qv \cos \theta) dE \\
&= \frac{1}{4\pi} \int_{\phi=0}^{2\pi} d\phi \int_{\theta=0}^{\pi} \sin \theta \cos \theta d\theta \int_{E=0}^{\infty} fg(E)qv dE
\end{aligned} \tag{4-17}$$

In the Z direction, the distribution function, Eq. (4-15), can be rewritten as

$$f = f_0 - \frac{\partial f_0}{\partial E} \left[-\frac{d\psi_c}{dZ} - \frac{E - \psi_c}{T_e} \frac{dT_e}{dZ} \right] \tau v \cos \theta \tag{4-18}$$

Substitute Eq. (4-18) into Eq. (4-17), the electrical current can be obtained as

$$\begin{aligned}
j_z &= \frac{1}{4\pi} \int_{\phi=0}^{2\pi} d\phi \int_{\theta=0}^{\pi} \sin \theta \cos \theta d\theta \int_{E=0}^{\infty} f_0 g(E) q_c v dE \\
&+ \frac{1}{4\pi} \int_{\phi=0}^{2\pi} d\phi \int_{\theta=0}^{\pi} \sin \theta \cos^2 \theta d\theta \int_{E=0}^{\infty} \frac{\partial f_0}{\partial E} g(E) q_c \left(\frac{d\psi_c}{dZ} + \frac{E - \psi_c}{T_e} \frac{dT_e}{dZ} \right) \tau v^2 dE
\end{aligned} \tag{4-19}$$

Since the first term on the right hand side is zero, the second term yields

$$j_z = \frac{q_c}{3} \int_{E=0}^{\infty} \frac{\partial f_0}{\partial E} g(E) \left(\frac{d\psi_c}{dZ} + \frac{E - \psi_c}{T_e} \frac{dT_e}{dZ} \right) \tau v^2 dE \tag{4-20}$$

Because $E = \frac{1}{2}mv^2$, replacing v^2 in the above equation one has

$$j_z = \frac{2q_c}{3m} \int_{E=0}^{\infty} \frac{\partial f_0}{\partial E} g(E) \left(\frac{d\psi_c}{dZ} + \frac{E - \psi_c}{T_e} \frac{dT_e}{dZ} \right) \tau E dE \tag{4-21}$$

Consequently, one can obtain the electrical current equation as follows

$$j_z = L_{11} \left(\frac{1}{q_c} \frac{d\psi_c}{dZ} \right) + L_{12} \left(\frac{dT_e}{dZ} \right) \tag{4-22}$$

where

$$L_{11} = \frac{2q_c^2}{3m} \int_{E=0}^{\infty} \frac{\partial f_0}{\partial E} g(E) \tau E dE \tag{4-23}$$

$$L_{12} = \frac{2q_c}{3mT_e} \int_{E=0}^{\infty} \frac{\partial f_0}{\partial E} g(E)(E - \psi_c) \tau E dE \quad (4-24)$$

Introducing electron conductivity σ_c and Seebeck coefficient Q_c ,

$$\sigma_c = L_{11} = \frac{2q_c^2}{3m} \int_{E=0}^{\infty} \frac{\partial f_0}{\partial E} g(E) \tau E dE \quad (4-25)$$

$$Q_c = -\frac{L_{12}}{L_{11}} = -\frac{1}{q_c T_e} \frac{\int_{E=0}^{\infty} \frac{\partial f_0}{\partial E} g(E)(E - \psi_c) \tau E dE}{\int_{E=0}^{\infty} \frac{\partial f_0}{\partial E} g(E) \tau E dE} \quad (4-26)$$

$$= -\frac{1}{q_c T_e} \left(\frac{\int_{E=0}^{\infty} \frac{\partial f_0}{\partial E} g(E) \tau E^2 dE}{\int_{E=0}^{\infty} \frac{\partial f_0}{\partial E} g(E) \tau E dE} - \psi_c \right)$$

As a result, the electrical current equation in the Z direction is

$$j_z = \sigma_c \left(\frac{1}{q_c} \frac{d\psi_c}{dZ} \right) - \sigma_c Q_c \left(\frac{dT_e}{dZ} \right) \quad (4-27)$$

Combining all three current components, the final form of the electrical current of the carriers is expressed as

$$j_c = \frac{\sigma_c}{q_c} \nabla \psi_c - \sigma_c Q_c \nabla T_e \quad (4-28)$$

which is the same formula given in References [40] and [41].

In the case of ultrafast laser irradiation, both electrons and holes move together in the absence of external electric field. However, due to the difference in the mobility of electron and hole, the Dember field, E_d , has to be included in Eq. (4-28) for both the electron and hole currents. Therefore, Eq. (4-28) becomes

$$j_e = \frac{\sigma_e}{q} \nabla \psi_e - \sigma_e Q_e \nabla T_e + \sigma_e E_d \quad (4-29)$$

$$j_h = \frac{\sigma_h}{q} \nabla \psi_h - \sigma_h Q_h \nabla T_e + \sigma_h E_d \quad (4-30)$$

Because the two currents are approximately equal in magnitude and opposite in sign, i.e.

$j_e = -j_h$, the particle current for the electron and hole pairs is found from Eqs. (4-29)

and (4-30) to be

$$J = -\frac{j_e}{q} = \frac{j_h}{q} = \frac{1}{q^2} \frac{\sigma_e \sigma_h}{\sigma_e + \sigma_h} [\nabla(\psi_h - \psi_e) + q(Q_e + Q_h) \nabla T_e] \quad (4-31)$$

According to the equality of electron and hole densities, $n_e = n_h = n$, the definition of

local carrier density is [59]

$$n_c = 2 \left(\frac{mk_B T_e}{2\pi\hbar^2} \right)^{3/2} F_{1/2}(\eta_c) \quad (4-32)$$

where F_i is the Fermi-Dirac integral of order i , defined as follow

$$F_i(\eta_c) = \frac{1}{\Gamma(i+1)} \int_0^\infty \frac{E^i}{\exp(E - \eta_c) + 1} dE \quad (4-33)$$

Moreover, the relaxation time depends on the energy, and we can assume

$$\tau = \tau_0 E^r \quad (4-34)$$

where τ_0 is a constant independent of E , and $r = 0.5$ in this investigation [40]. Substitute

Eqs. (4-8), (4-9), (4-16), (4-25), (4-26), (4-32)-(4-34) into Eq. (4-31), one has

$$\begin{aligned}
J = & -D \left\{ \nabla n + \frac{n}{k_B T_e} \left[\frac{F_{1/2}(\eta_e)}{F_{-1/2}(\eta_e)} + \frac{F_{1/2}(\eta_h)}{F_{-1/2}(\eta_h)} \right]^{-1} \nabla E_g \right. \\
& \left. + \frac{n}{T_e} \left\{ \frac{2 \left[\frac{F_1(\eta_e)}{F_0(\eta_e)} + \frac{F_1(\eta_h)}{F_0(\eta_h)} \right]}{\left[\frac{F_{1/2}(\eta_e)}{F_{-1/2}(\eta_e)} + \frac{F_{1/2}(\eta_h)}{F_{-1/2}(\eta_h)} \right]} - \frac{3}{2} \right\} \nabla T_e \right\}
\end{aligned} \tag{4-35}$$

where $E_g = E_c - E_v$ is the band gap energy and coefficient D is defined as

$$D = \frac{1}{q} \frac{k_B T_e (\sigma_e \sigma_h)}{\sigma_e + \sigma_h} \left[\frac{F_{1/2}(\eta_e)}{F_{-1/2}(\eta_e)} + \frac{F_{1/2}(\eta_h)}{F_{-1/2}(\eta_h)} \right] \tag{4-36}$$

For a highly non-degenerate carrier distribution, the Fermi level $\psi_e (\psi_h)$ is considerably lower than E_c (higher than E_v), the reduced Fermi level $\eta_e (\eta_h)$ is, therefore, large and negative. The ratio of the Fermi-Dirac integral, $F_j(\eta_c) / F_i(\eta_c)$, approaches 1 for all i and j [40]. Thus, D approaches D_0 , which is the ambipolar diffusivity, and Eq. (4-35) can be simplified further as

$$J = -D_0 \left(\nabla n + \frac{n}{2k_B T_e} \nabla E_g + \frac{n}{2T_e} \nabla T_e \right) \tag{4-37}$$

4.1.2 Macroscopic Energy Current of the Carriers

The derivation of macroscopic energy current of carriers basically follows a similar procedure as deriving the electrical current. The energy flux in the Z direction produced by a charge moving through $d\Omega$ is $E v \cos \theta$, thus the total energy current produced by all electrons moving toward the entire sphere surrounding the infinitesimal volume can be determined as

$$\begin{aligned}
w_z &= \iint_S \frac{\sin \theta d\theta d\phi}{4\pi} \int_{E=0}^{\infty} f g(E) (E v \cos \theta) dE \\
&= \frac{1}{4\pi} \int_{\phi=0}^{2\pi} d\phi \int_{\theta=0}^{\pi} \sin \theta \cos \theta d\theta \int_{E=0}^{\infty} f g(E) E v dE
\end{aligned} \tag{4-38}$$

In the Z direction, substituting the distribution function in Eq. (4-18), Eq. (4-38)

becomes

$$\begin{aligned}
w_z &= \frac{1}{4\pi} \int_{\phi=0}^{2\pi} d\phi \int_{\theta=0}^{\pi} \sin \theta \cos \theta d\theta \int_{E=0}^{\infty} f_0 g(E) E v dE \\
&+ \frac{1}{4\pi} \int_{\phi=0}^{2\pi} d\phi \int_{\theta=0}^{\pi} \sin \theta \cos^2 \theta d\theta \int_{E=0}^{\infty} \frac{\partial f_0}{\partial E} g(E) E \left(\frac{d\psi_c}{dZ} + \frac{E - \psi_c}{T_e} \frac{dT_e}{dZ} \right) \tau v^2 dE
\end{aligned} \tag{4-39}$$

Drop the first term which equals zero, the second term yields

$$w_z = \frac{1}{3} \int_{E=0}^{\infty} \frac{\partial f_0}{\partial E} g(E) E \left(\frac{d\psi_c}{dZ} + \frac{E - \psi_c}{T_e} \frac{dT_e}{dZ} \right) \tau v^2 dE \tag{4-40}$$

Again substitute v^2 with $2E/m$ in the above equation

$$w_z = \frac{2}{3m} \int_{E=0}^{\infty} \frac{\partial f_0}{\partial E} g(E) \left(\frac{d\psi_c}{dZ} + \frac{E - \psi_c}{T_e} \frac{dT_e}{dZ} \right) \tau E^2 dE \tag{4-41}$$

Thus,

$$\begin{aligned}
w_z &= \frac{2}{3m} \int_{E=0}^{\infty} \frac{\partial f_0}{\partial E} g(E) \left(\frac{d\psi_c}{dZ} + \frac{E - \psi_c}{T_e} \frac{dT_e}{dZ} \right) \tau E^2 dE \\
&= \frac{2}{3m} \int_{E=0}^{\infty} \frac{\partial f_0}{\partial E} g(E) \left(\frac{d\psi_c}{dZ} + \frac{E - \psi_c}{T_e} \frac{dT_e}{dZ} \right) \tau E (E - \psi_c) dE \\
&+ \frac{2}{3m} \int_{E=0}^{\infty} \frac{\partial f_0}{\partial E} g(E) \left(\frac{d\psi_c}{dZ} + \frac{E - \psi_c}{T_e} \frac{dT_e}{dZ} \right) \tau E \psi_c dE \\
&= \frac{2}{3m} \int_{E=0}^{\infty} \frac{\partial f_0}{\partial E} g(E) \left(\frac{d\psi_c}{dZ} + \frac{E - \psi_c}{T_e} \frac{dT_e}{dZ} \right) \tau E (E - \psi_c) dE + \frac{\psi_c j_z}{q_c}
\end{aligned} \tag{4-42}$$

It is seen that the macroscopic energy current equation is a function of the electrical current j_c . The equation can be rewritten in the following form

$$w_z = L_{21} \left(\frac{1}{q_c} \frac{d\psi_c}{dZ} \right) + L_{22} \left(\frac{dT_e}{dZ} \right) + \frac{\psi_c j_z}{q_c} \quad (4-43)$$

where

$$L_{21} = \frac{2q_c}{3m} \int_{E=0}^{\infty} \frac{\partial f_0}{\partial E} g(E) \tau E (E - \psi_c) dE = L_{12} T_e \quad (4-44)$$

$$L_{22} = \frac{2}{3mT_e} \int_{E=0}^{\infty} \frac{\partial f_0}{\partial E} g(E) (E - \psi_c)^2 \tau E dE \quad (4-45)$$

From Eq. (4-22)

$$\frac{1}{q_c} \frac{d\psi_c}{dZ} = \frac{j_z}{L_{11}} - \frac{L_{12}}{L_{11}} \left(\frac{dT_e}{dZ} \right) \quad (4-46)$$

Substitute into Eq. (4-43), we have

$$w_z = \frac{L_{21}}{L_{11}} j_z + \frac{\psi_c j_z}{q_c} + \left(L_{22} - \frac{L_{21} L_{12}}{L_{11}} \right) \left(\frac{dT_e}{dZ} \right) \quad (4-47)$$

Introducing the Peltier coefficient, π_c , and thermal conductivity κ_c

$$\pi_c = T_e Q_c = T_e \left(-\frac{L_{12}}{L_{11}} \right) = -\frac{L_{21}}{L_{11}} \quad (4-48)$$

$$\kappa_c = L_{22} - \frac{L_{21} L_{12}}{L_{11}} = k_B^2 \sigma_c \frac{T_e}{q^2} \left[\frac{6F_2(\eta_c) F_0(\eta_c) - 4F_1(\eta_c)^2}{F_0(\eta_c)^2} \right] \quad (4-49)$$

Thus, the energy current in the Z direction can be expressed as

$$w_z = -\left(\pi_c - \frac{\psi_c}{q_c} \right) j_z + \kappa_c \left(\frac{dT_e}{dZ} \right) \quad (4-50)$$

Combining all three energy current components, the final form of the energy current that flows into the control volume is therefore

$$w_c = \left(\pi_c - \frac{\psi_c}{q_c}\right)j_c - \kappa_c \nabla T_e \quad (4-51)$$

which is the same equation found in Reference [41]. Therefore, the total energy current is equal to the summation of the energy currents of the electrons and holes. Combining Eqs. (4-8), (4-9), (4-16), (4-25), (4-26), (4-32)-(4-34), (4-48), (4-49) and (4-51), the total energy current can be determined as follow

$$W = w_e + w_h = (E_g + 4k_B T_e)J - (\kappa_e + \kappa_h)\nabla T_e \quad (4-52)$$

4.2 Carrier Number Balance Equation and Laser Model

The balance equation for the laser generated electron-hole pairs is

$$\frac{\partial n}{\partial t} + \nabla \cdot J = G - R \quad (4-53)$$

where G indicates the pair generation rate and R is the pair recombination rate. The recombination rate has taken into account the Auger recombination and impact ionization,

$$R = \gamma n^3 - \theta_i n \quad (4-54)$$

where γ is the Auger recombination coefficient and θ_i is the impact ionization coefficient.

The generation rate is obtained from the one-photon and two-photon absorption as

$$G = \frac{\alpha I(z, r, t)}{h\nu} + \frac{\beta I^2(z, r, t)}{2h\nu} \quad (4-55)$$

with I being the laser intensity, $h\nu$ the photon energy, α and β the one-photon and two-photon absorption coefficients, respectively. Substitute Eqs. (4-54) and (4-55) into (4-53)

$$\frac{\partial n}{\partial t} = \frac{\alpha I(z, r, t)}{h\nu} + \frac{\beta I^2(z, r, t)}{2h\nu} - (\gamma n^3 - \theta_i n) - \nabla \cdot J \quad (4-56)$$

Assume that the ultrafast laser beam is Gaussian in both time and space, then the laser intensity on the irradiated top surface of the silicon wafer is formulated as

$$I_0(r, t) = \sqrt{\frac{4 \log(2)}{\pi}} \frac{(1 - \Gamma)\Phi}{t_p} e^{[-(r/r_s)^2 - 4 \log(2)((t-3t_p)/t_p)^2]} \quad (4-57)$$

where t_p is the laser pulse duration, Γ is the reflectivity, Φ is the laser fluence, and r_s is the spot size.

The attenuation of the laser beam along the depth of the wafer is given as $\partial I / \partial z = -\alpha I - \beta I^2 - \Theta n I$ by the Beer-Lambert law, with Θ being the area of the free-carrier absorption. By integrating this equation, the laser intensity I in Eq. (4-57) can be determined as

$$I(z, r, t) = \frac{(\alpha + \Theta n) I_0 e^{-(\alpha + \Theta n)z}}{(\alpha + \Theta n) + \beta I_0 [1 - e^{1 - (\alpha + \Theta n)z}]} \quad (4-58)$$

The time evolution and spatial distribution of the laser intensity are given in Figures 4.2 and 4.3, respectively.

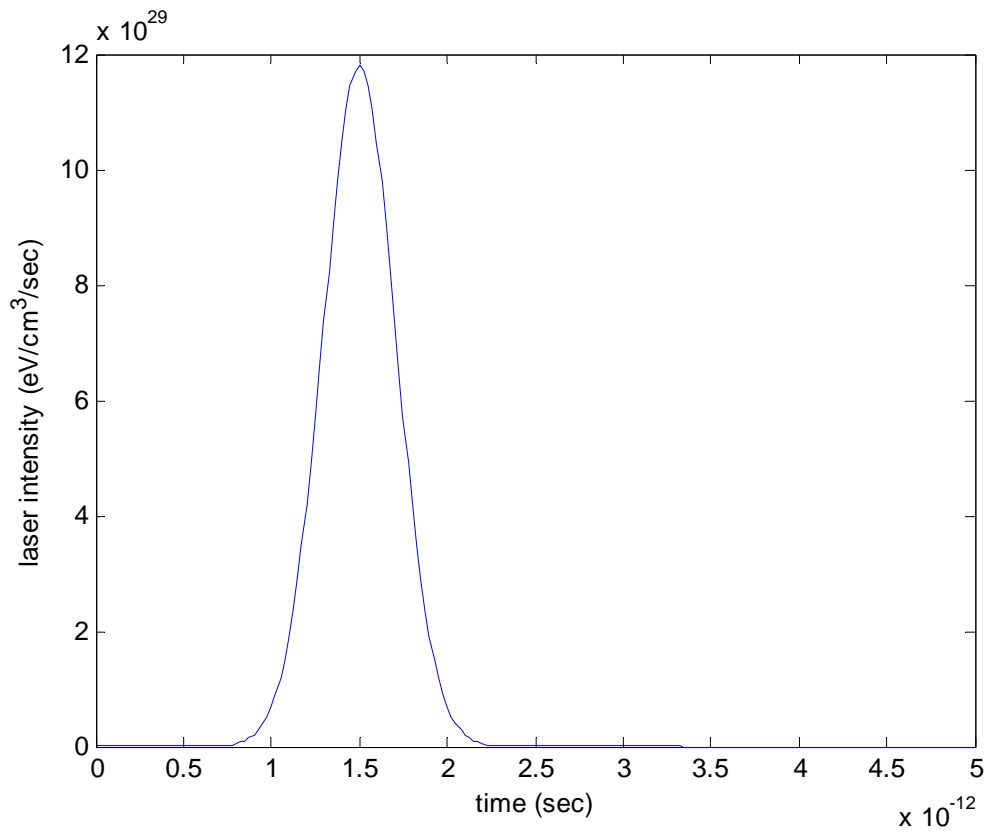


Figure 4.2 Time evolution of laser intensity on top surface of silicon

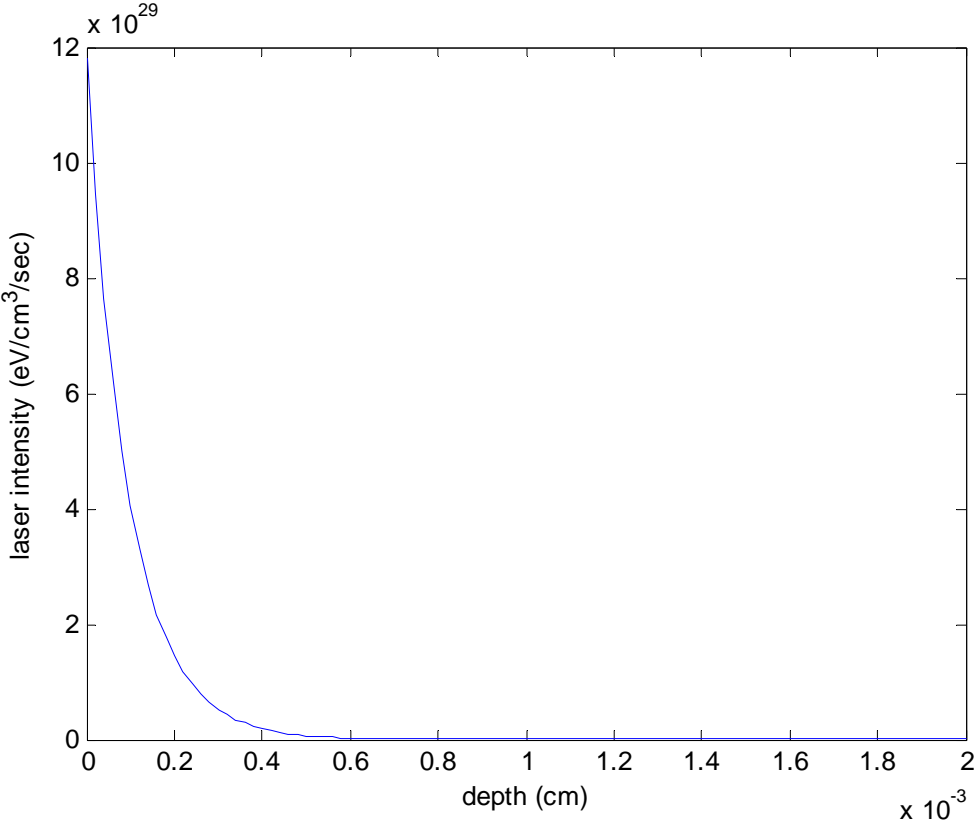


Figure 4.3 Spatial distribution of laser intensity along thickness direction of silicon

4.3 Carrier Energy Balance Equation

The total energy balance equation of the carrier is expressed as

$$\frac{\partial U}{\partial t} + \nabla \cdot W = S_U - L_U \quad (4-59)$$

where $U = nE_g + (3/2)nk_B T_e [F_{3/2}(\eta_e) / F_{1/2}(\eta_e) + F_{3/2}(\eta_h) / F_{1/2}(\eta_h)] = nE_g + 3nk_B T_e$ is the total energy of the electron-hole pairs that equals to the summation of the kinetic energy and band-gap energy per unit volume. $S_U = (\alpha + \Theta n)I + \beta I^2$ is the source term and $L_U = C_{e-h}(T_e - T_l) / \tau_e$ defines the loss term due to the energy exchange from carriers to lattice. Note that $C_{e-h} = 3nk_B$ is the specific heat of carriers, T_l is the lattice temperature, and τ_e is the thermal relaxation time between the carriers and lattice. Eq. (4-59) can then be rewritten as

$$\begin{aligned} C_{e-h} \frac{\partial T_e}{\partial t} = & (\alpha + \Theta n)I + \beta I^2 - \nabla \cdot W - \frac{C_{e-h}}{\tau_e} (T_e - T_l) \\ & - \frac{\partial n}{\partial t} (E_g + 3k_B T_e) - n \left(\frac{\partial E_g}{\partial T_l} \frac{\partial T_l}{\partial t} + \frac{\partial E_g}{\partial n} \frac{\partial n}{\partial t} \right) \end{aligned} \quad (4-60)$$

4.4 Summary

The transport dynamics in silicon was presented based on the relaxation-time approximation of the Boltzmann equation. The governing equations, including the macroscopic electrical current equation (Eq. 4-37), macroscopic energy current equation (Eq. 4-52), balance equation of carrier number (Eq. 4-56), and balance equation of carrier energy (Eq. 4-60), are summarized as follows

$$J = -D_0(\nabla n + \frac{n}{2k_B T_e} \nabla E_g + \frac{n}{2T_e} \nabla T_e) \quad (4-37)$$

$$W = w_e + w_h = (E_g + 4k_B T_e)J - (\kappa_e + \kappa_h)\nabla T_e \quad (4-52)$$

$$\frac{\partial n}{\partial t} = \frac{\alpha I(z, r, t)}{h\nu} + \frac{\beta I^2(z, r, t)}{2h\nu} - (\gamma n^3 - \theta_i n) - \nabla \cdot J \quad (4-56)$$

$$C_{e-h} \frac{\partial T_e}{\partial t} = (\alpha + \Theta n)I + \beta I^2 - \nabla \cdot W - \frac{C_{e-h}}{\tau_e} (T_e - T_l) - \frac{\partial n}{\partial t} (E_g + 3k_B T_e) - n \left(\frac{\partial E_g}{\partial T_l} \frac{\partial T_l}{\partial t} + \frac{\partial E_g}{\partial n} \frac{\partial n}{\partial t} \right) \quad (4-60)$$

The details as to how the governing equations were derived from the relaxation-time approximation of the Boltzmann equation were given. The key assumptions associated with generalizing the microscopic description to macroscopic description were also reviewed. Temperature-dependent multi-phonons, free-carrier absorptions, and the recombination and impact ionization processes were considered in the formulation. These equations constituted the fundamentals of femtosecond laser induced transport dynamics in semiconductor materials. The balance equation of lattice energy and equations of motion applicable to describing diffusion-type, parabolic thermo-elastodynamics, hyperbolic thermo-elastodynamics, and hyperbolic thermo-elastoplastodynamics for silicon materials are meticulously treated in Chapters V, VI and VII, respectively.

CHAPTER V

PARABOLIC THERMO-ELASTODYNAMICS FOR SILICON MATERIALS

SUBJECTED TO ULTRAFAST LASER HEATING

5.1 Classical Thermoelasticity

The thermoelastic theory formulated by M. C. Biot [60] describes the behavior of elastic bodies under the influence of nonuniform temperature fields. The constitutive equations, i.e. the equations characterizing the particular material, are temperature dependent and include a relation connecting the heat flux in the body with the local temperature gradient. The relation is known as the Fourier's Law in its simplest form, which determines the temperature distribution in the body [61]. In the absence of body force and heat source, the classical thermoelasticity comprises coupled equations of energy and motion [62]

$$\rho c_v \dot{T} + (3\lambda + 2\mu)\alpha' T \nabla \dot{\mathbf{U}} = \kappa \nabla^2 T \quad (5-1)$$

$$\mu \nabla^2 \mathbf{U} + (\lambda + \mu) \nabla \nabla \cdot \mathbf{U} - (3\lambda + 2\mu)\alpha' \nabla T = \rho \ddot{\mathbf{U}} \quad (5-2)$$

where \mathbf{U} represents the displacement fields, T is the temperature field, T_0 is the ambient temperature, κ is the lattice thermal conductivity, c_v denotes the specific heat, λ and μ are the Lamé constants, α' is the thermal expansion coefficient, and the overdot “.” denotes the derivative with respect to time.

With the introduction of the strain-rate term, it is seen from Eqs. (5-1) and (5-2) that the heat conduction equation is one of parabolic type, called the diffusion equation.

This theory predicts that if an elastic continuum is subjected to a thermal disturbance, the effect of the disturbance will be felt instantaneously at distances infinitely far away from the source [63].

5.2 Lattice Energy Balance Equation and Equations of Motion

According to Eq. (5-1), the energy balance equation of the lattice has the following expression

$$C_l \frac{\partial T_l}{\partial t} = \nabla \cdot (\kappa_l \nabla T_l) + L_U - L_M \quad (5-3)$$

where T_l is the lattice temperature field, κ_l is the lattice thermal conductivity, and C_l is the lattice specific heat. $L_U = C_{e-h}(T_e - T_l) / \tau_e$, defined in Eq. (4-59), is the energy transfer from the carriers to lattices. To account for thermomechanical responses, the two-step laser heating models found in Refs. [40-41] needs be extended to consider the coupling of thermal and mechanical fields. Since the energy transferred into the lattices induces steep thermal gradients, which then in turn initiate propagating stress waves, an energy term, L_M , is included into the lattice energy balance equation

$$L_M = (3\lambda + 2\mu)\alpha' T_l \dot{\varepsilon}_{kk} \quad (5-4)$$

Since silicon wafer is of a thin disk, thus it is intuitive to establish the governing equations in the cylindrical coordinates. This is further explained in the section on Geometric Model. In cylindrical coordinates the volumetric strain is $\varepsilon_{kk} = \varepsilon_{zz} + \varepsilon_{rr} + \varepsilon_{\theta\theta}$.

Thus Eq. (5-3) becomes

$$C_l \frac{\partial T_l}{\partial t} = \nabla \cdot (\kappa_l \nabla T_l) + \frac{C_{e-h}}{\tau_e} (T_e - T_l) - (3\lambda + 2\mu) \alpha' T_l \dot{\varepsilon}_{kk} \quad (5-5)$$

The corresponding equations of motion are therefore

$$\rho \ddot{u} = \sigma_{rr,r} + \sigma_{rz,z} + \frac{\sigma_{rr} - \sigma_{\theta\theta}}{r} \quad (5-6)$$

$$\rho \ddot{w} = \sigma_{rz,r} + \sigma_{zz,z} + \frac{\sigma_{rz}}{r} \quad (5-7)$$

where u and w are the displacement variables in the thickness and radial directions, respectively, and the three normal stresses, σ_{ii} ($i = r, z, \theta$), and the shear stress, σ_{rz} , are defined as

$$\sigma_{ii} = 2\mu \varepsilon_{ii} + \lambda \varepsilon_{kk} - (3\lambda + 2\mu) \alpha' (T_l - T_o) \quad (i = z, r, \theta) \quad (5-8)$$

$$\sigma_{rz} = 2\mu \varepsilon_{rz} \quad (5-9)$$

Thus, the equations of motion are of the same forms as those of classical thermoelasticity in Eq. (5-2). Lattice deformation of the silicon material can be elastic or plastic depending on the lattice and ambient temperatures [24]. At low ambient temperature, the absolute lattice temperatures induced by ultrafast laser pulse of the order of subpicoseconds or femtoseconds are effectively low in magnitude. Thus, elastic deformations are assumed for the lattices. The strain-displacement relations in the cylindrical coordinates are

$$\varepsilon_{rr} = \frac{\partial u}{\partial r} \quad (5-10)$$

$$\varepsilon_{zz} = \frac{\partial w}{\partial z} \quad (5-11)$$

$$\varepsilon_{\theta\theta} = \frac{u}{r} \quad (5-12)$$

$$\varepsilon_{rz} = \frac{1}{2} \left(\frac{\partial u}{\partial z} + \frac{\partial w}{\partial r} \right) \quad (5-13)$$

All of the governing equations for describing classical thermo-elastodynamics in silicon materials have been introduced. They include the macroscopic electrical current equation (Eq. 4-37), macroscopic energy current equation (Eq. 4-52), balance equation of carrier number (Eq. 4-56), balance equation of carrier energy (Eq. 4-60), balance equation of lattice energy (Eq. 5-5) and equations of motion (Eqs. 5-6 and 5-7).

5.3 Computational Model

5.3.1 Geometric Model

An axisymmetric model is developed for establishing the mechanisms governing the coupled thermal-mechanical behaviors in silicon subject to the exertion of femtosecond laser pulses along the thickness and radial directions. Since the heat affected zone and the thermal waves are not expected to go beyond a finite domain of 20 μm in thickness and 20 μm in radius in the first 10nsec, the axisymmetric thin section defined in the cylindrical coordinates and shown in Figure 5.1 is employed as the micro-scale geometric model for the present study. Assume axisymmetry for the volumetric laser heat source. Given the small wafer thickness and the brief time window within which laser heating is considered, the anisotropy of the single crystalline silicon material is also neglected. Thus the governing equations have no θ -dependent terms, and the model is fully defined by the 20 μm ×20 μm micron-scale section as seen in Figure 5.1.

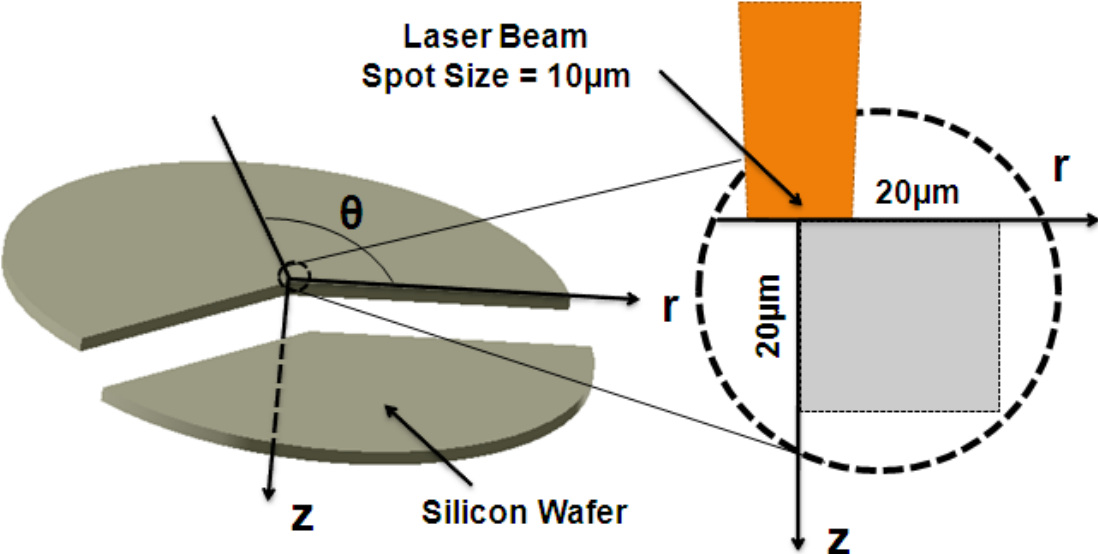


Figure 5.1 Axisymmetric model in cylindrical coordinates

The followings summarize all the relevant governing equations, Eqs. (4-37), (4-52), (4-56), (4-60) and (5-5), in the cylindrical coordinates

$$J_r = -D_0 \left[\frac{\partial n}{\partial r} + \frac{n}{2k_B T_e} \left(\frac{\partial E_g}{\partial T_l} \frac{\partial T_l}{\partial r} + \frac{\partial E_g}{\partial n} \frac{\partial n}{\partial r} \right) + \frac{n}{2T_e} \frac{\partial T_e}{\partial r} \right] \quad (5-14)$$

$$J_z = -D_0 \left[\frac{\partial n}{\partial z} + \frac{n}{2k_B T_e} \left(\frac{\partial E_g}{\partial T_l} \frac{\partial T_l}{\partial z} + \frac{\partial E_g}{\partial n} \frac{\partial n}{\partial z} \right) + \frac{n}{2T_e} \frac{\partial T_e}{\partial z} \right] \quad (5-15)$$

$$W_r = (E_g + 4k_B T_e) J_r - (\kappa_e + \kappa_h) \frac{\partial T_e}{\partial r} \quad (5-16)$$

$$W_z = (E_g + 4k_B T_e) J_z - (\kappa_e + \kappa_h) \frac{\partial T_e}{\partial z} \quad (5-17)$$

$$\frac{\partial n}{\partial t} = \frac{\alpha I(z, r, t)}{h\nu} + \frac{\beta I^2(z, r, t)}{2h\nu} - \gamma n^3 + \theta_i n - \frac{J_r}{r} - \frac{\partial J_r}{\partial r} - \frac{\partial J_z}{\partial z} \quad (5-18)$$

$$\begin{aligned} C_{e-h} \frac{\partial T_e}{\partial t} &= (\alpha + \Theta n) I(z, r, t) + \beta I^2(z, r, t) \\ &\quad - \frac{W_r}{r} - \frac{\partial W_r}{\partial r} - \frac{\partial W_z}{\partial z} - \frac{C_{e-h}}{\tau_e} (T_e - T_l) \\ &\quad - \frac{\partial n}{\partial t} (E_g + 3k_B T_e) - n \left(\frac{\partial E_g}{\partial T_l} \frac{\partial T_l}{\partial t} + \frac{\partial E_g}{\partial n} \frac{\partial n}{\partial t} \right) \end{aligned} \quad (5-19)$$

$$\begin{aligned} C_l \frac{\partial T_l}{\partial t} &= \frac{1}{r} \kappa_l \frac{\partial T_l}{\partial r} + \left(\frac{\partial T_l}{\partial r} \right)^2 \frac{\partial \kappa_l}{\partial T_l} + \kappa_l \frac{\partial^2 T_l}{\partial r^2} + \left(\frac{\partial T_l}{\partial z} \right)^2 \frac{\partial \kappa_l}{\partial T_l} + \kappa_l \frac{\partial^2 T_l}{\partial z^2} \\ &\quad + \frac{C_{e-h}}{\tau_e} (T_e - T_l) - (3\lambda + 2\mu) \alpha' T_l \dot{\epsilon}_{kk} \end{aligned} \quad (5-20)$$

Eqs. (5-14) – (5-20) together with the equations of motion found in Eqs. (5-6) – (5-13) constitute the computational model governing the thermo-elastodynamical behaviors of silicon wafer in response to femtosecond laser heating. There are 17 partial differential equations in the system, with Eq. 5-6 containing three components. Due to the

complexity of the equation system, it is difficult, if impossible, to obtain analytical solutions. Hence a numerical scheme has to be established.

5.3.2 Multi-Time Scale Time Integration Scheme

The interactions of materials with ultrafast laser pulses are typically characterized by motions on many time scales [64]. In the $10^{-15} \sim 10^{-13}$ sec pulse duration, for example, there is a fast time scale arising from the internal motion of the molecules and the heat transfer between electrons and photons (lattice). However, the time scale on which stress wave propagation is observed as one of the induced physical phenomena is several orders of magnitude greater at the nanoseconds range. To generate the time history of ultrafast laser heating in silicon, the time step used for numerical integration must stay below the shortest time scale present. Such a requirement necessarily takes a huge computational overhead to meet. An effective alternative to the Euler algorithm that is commonly utilized in multi-time scale problems [65, 66], the modified velocity-Verlet algorithm [67] is employed,

$$a(t + \Delta t) = a(t) + \Delta t \dot{a}(t) + \frac{1}{2} (\Delta t)^2 \ddot{a}(t) \quad (5-21)$$

$$\tilde{a}(t + \Delta t) = \dot{a}(t) + \lambda_i \Delta t \ddot{a}(t) \quad (5-22)$$

$$\ddot{a}(t + \Delta t) = \ddot{a}(a(t + \Delta t), \tilde{a}(t + \Delta t)) \quad (5-23)$$

$$\dot{a}(t + \Delta t) = \dot{a}(t) + \frac{1}{2} \Delta t (\ddot{a}(t) + \ddot{a}(t + \Delta t)) \quad (5-24)$$

with a being an arbitrary variable (such as the displacements in this study), $\lambda_i = 1/2$, \tilde{a} a predicted velocity in the integration process, and \dot{a} and \ddot{a} the velocity and

acceleration, respectively. Employment of the algorithm in Eqs. (5-21)-(5-24) allows for a gradually increasing time step that inflicts no unwanted numerical oscillations for integration time windows as wide as hundreds of picoseconds. It should be noted that the specific window width rendered by the algorithm is long enough for electrons and lattice to reach thermal equilibrium subject to a laser fluence, Φ , that is $0.15\text{J}/\text{cm}^2$ or lower.

Figure 5.2 shows the time evolutions of both the electrons and lattice subject to the excitation of a 500fs laser pulse that is low in fluence and small in irradiated spot size. It is seen that the electrons and lattice reach a state of identical temperature early on at the first few picoseconds after laser irradiation. The particular state remains its constancy throughout the time window considered. Such a thermal equilibrium is observed for all fluence input considered in the course of the investigation. At the equilibrium state where $T_e = T_l$, the source term dictating the diffusion of lattice heat, $C_{e-h}(T_e - T_l) / \tau_e$ in Eq. (5-20), becomes negligible. Consequently, Eq. (5-20) along with Eqs. (5-6)-(5-13) governs the physical process subsequent to the reaching of the state of thermal equilibrium. A larger integration time step can then afterwards be followed to model the generation and propagation of thermally induced stress waves at the nanoseconds scale.

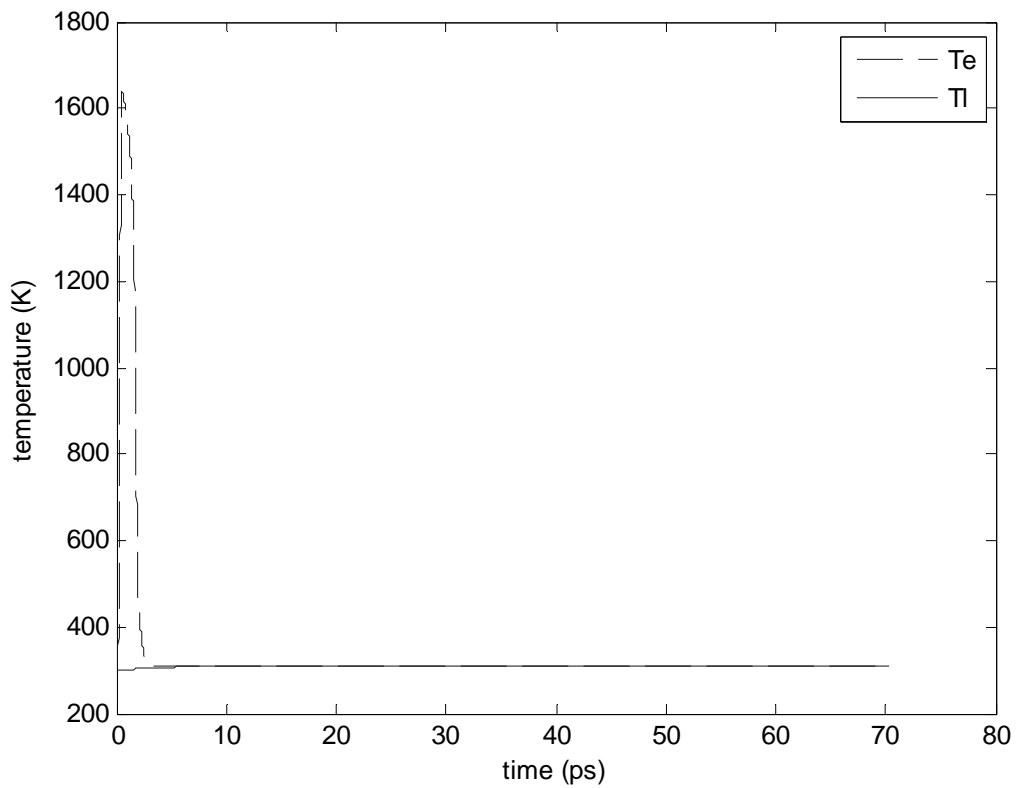


Figure 5.2 Time evolutions of electron (T_e) and lattice (T_l) temperature
(pulse duration 500fs, spot size $10\mu\text{m}$, laser fluence $0.005\text{J}/\text{cm}^2$)

5.3.3 Staggered Grid Finite Difference Model

The inherent complexity of the governing equations renders it difficult to obtain closed-form solutions to Eqs. (5-6)-(5-20). A finite difference scheme with staggered grids is introduced in the following for solving the equations numerically in the $20\mu\text{m}\times 20\mu\text{m}$ model domain. Unlike the conventional finite difference method in which primary variables are evaluated at grid points, the staggered finite difference scheme depicted in Figure 5.3 allows velocity variables (\dot{u} and \dot{w}) and the first order spatial derivative terms ($\partial/\partial r$ and $\partial/\partial z$) to be calculated at locations midway between two consecutive grid points, and shear stress (σ_{rz}) to be evaluated at the center of each element. By defining other variables, such as temperatures (T_e and T_l), normal stresses (σ_{ii}) and carrier density (n), at the grid points, a “staggered” grids model can be established with stress components being surrounded by velocity components, and vice versa. The staggered grid finite difference method has been found to be effective in suppressing numerical oscillations [31, 32].

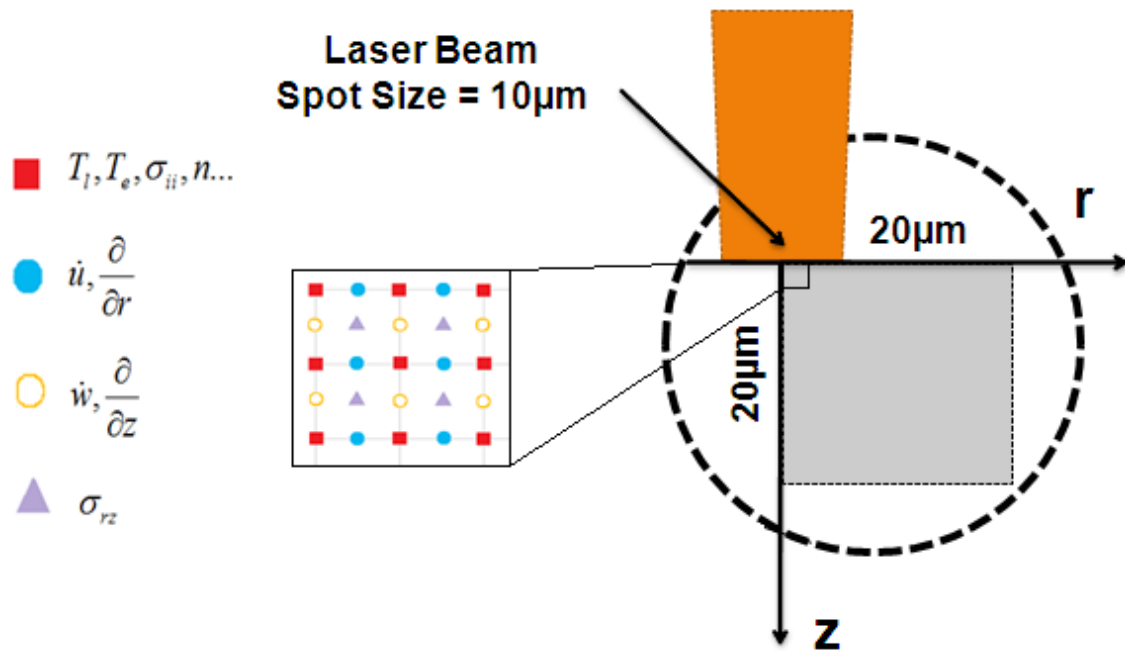


Figure 5.3 Finite difference model with staggered grids

Using the arrangement defined in Figure 5.3 and assuming a time step, Δt , temperatures, stresses and velocities are calculated by applying the forward difference scheme. As an illustration, Eqs. (5-6)-(5-13) and (5-20) without the $C_{e-h}(T_e - T_l) / \tau_e$ term can be discretized into the following finite difference equations:

$$\begin{aligned} \dot{u}(i, p + \frac{1}{2}, j + 1) = & \dot{u}(i, p + \frac{1}{2}, j) + \frac{\Delta t}{\rho} \left[\frac{\sigma_{rr}(i, p + 1, j) - \sigma_{rr}(i, p, j)}{\Delta r} \right. \\ & + \frac{\sigma_{rz}(i + \frac{1}{2}, p + \frac{1}{2}, j) - \sigma_{rz}(i - \frac{1}{2}, p + \frac{1}{2}, j)}{\Delta z} \\ & + \left(\frac{\sigma_{rr}(i, p, j) + \sigma_{rr}(i, p + 1, j)}{2} \right. \\ & \left. \left. - \frac{\sigma_{\theta\theta}(i, p, j) + \sigma_{\theta\theta}(i, p + 1, j)}{2} \right) \frac{1}{r} \right] \end{aligned} \quad (5-25)$$

$$\begin{aligned} \dot{w}(i + \frac{1}{2}, p, j + 1) = & \dot{w}(i + \frac{1}{2}, p, j) \\ & + \frac{\Delta t}{\rho} \left[\frac{\sigma_{rz}(i + \frac{1}{2}, p + \frac{1}{2}, j) - \sigma_{rz}(i + \frac{1}{2}, p - \frac{1}{2}, j)}{\Delta r} \right. \\ & + \frac{\sigma_{zz}(i + 1, p, j) - \sigma_{zz}(i, p, j)}{\Delta z} \\ & \left. + \frac{\sigma_{rz}(i + \frac{1}{2}, p - \frac{1}{2}, j) + \sigma_{rz}(i + \frac{1}{2}, p + \frac{1}{2}, j)}{2} \frac{1}{r} \right] \end{aligned} \quad (5-26)$$

$$\begin{aligned} \sigma_{rr}(i, p, j + 1) = & \sigma_{rr}(i, p, j) + \Delta t [2\mu \frac{\dot{u}(i, p + \frac{1}{2}, j) - \dot{u}(i, p - \frac{1}{2}, j)}{\Delta r} \\ & + \lambda \dot{\epsilon}_{kk}(i, p, j) - (3\lambda + 2\mu) \alpha' \dot{T}_i(i, p, j)] \end{aligned} \quad (5-27)$$

$$\begin{aligned}\sigma_{\theta\theta}(i, p, j+1) = & \sigma_{\theta\theta}(i, p, j) + \Delta t \left[2\mu \frac{1}{r} \frac{\dot{u}(i, p + \frac{1}{2}, j) + \dot{u}(i, p - \frac{1}{2}, j)}{2} \right. \\ & \left. + \lambda \dot{\varepsilon}_{kk}(i, p, j) - (3\lambda + 2\mu) \alpha' \dot{T}_i(i, p, j) \right]\end{aligned}\quad (5-28)$$

$$\begin{aligned}\sigma_{zz}(i, p, j+1) = & \sigma_{zz}(i, p, j) + \Delta t \left[2\mu \frac{\dot{w}(i + \frac{1}{2}, p, j) - \dot{w}(i - \frac{1}{2}, p, j)}{\Delta z} \right. \\ & \left. + \lambda \dot{\varepsilon}_{kk}(i, p, j) - (3\lambda + 2\mu) \alpha' \dot{T}_i(i, p, j) \right]\end{aligned}\quad (5-29)$$

$$\begin{aligned}\sigma_{rz}(i + \frac{1}{2}, p + \frac{1}{2}, j+1) = & \sigma_{rz}(i + \frac{1}{2}, p + \frac{1}{2}, j) \\ & + \Delta t \mu \left[\frac{\dot{w}(i + \frac{1}{2}, p+1, j) - \dot{w}(i - \frac{1}{2}, p, j)}{\Delta r} \right. \\ & \left. + \frac{\dot{u}(i+1, p + \frac{1}{2}, j) - \dot{u}(i, p + \frac{1}{2}, j)}{\Delta z} \right]\end{aligned}\quad (5-30)$$

$$\begin{aligned}\dot{\varepsilon}_{kk}(i, p, j) = & \dot{\varepsilon}_{rr}(i, p, j) + \dot{\varepsilon}_{zz}(i, p, j) + \dot{\varepsilon}_{\theta\theta}(i, p, j) \\ = & \frac{\dot{u}(i, p + \frac{1}{2}, j) - \dot{u}(i, p - \frac{1}{2}, j)}{\Delta r} \\ & + \frac{\dot{w}(i + \frac{1}{2}, p, j) - \dot{w}(i - \frac{1}{2}, p, j)}{\Delta z} \\ & + \frac{1}{r} \frac{\dot{u}(i, p + \frac{1}{2}, j) + \dot{u}(i, p - \frac{1}{2}, j)}{2}\end{aligned}\quad (5-31)$$

$$\begin{aligned}
\dot{T}_l(i, p, j) = & \frac{1}{C_l(i, p, j)} \left[\kappa_l(i, p, j) \frac{\partial T_l(i, p + \frac{1}{2}, j) + \frac{\partial T_l(i, p - \frac{1}{2}, j)}{\partial r}}{2} \right. \\
& + \left(\frac{\frac{\partial T_l(i, p + \frac{1}{2}, j) + \frac{\partial T_l(i, p - \frac{1}{2}, j)}{\partial r}}{2}}{2} \right)^2 \frac{\partial \kappa_l(i, p, j)}{\partial T_l} \\
& + \kappa_l(i, p, j) \frac{\frac{\partial T_l(i, p + \frac{1}{2}, j) - \frac{\partial T_l(i, p - \frac{1}{2}, j)}{\partial r}}{\Delta r}}{\Delta r} \\
& + \left(\frac{\frac{\partial T_l(i + \frac{1}{2}, p, j) + \frac{\partial T_l(i - \frac{1}{2}, p, j)}{\partial z}}{2}}{2} \right)^2 \frac{\partial \kappa_l(i, p, j)}{\partial T_l} \\
& + \kappa_l(i, p, j) \frac{\frac{\partial T_l(i + \frac{1}{2}, p, j) - \frac{\partial T_l(i - \frac{1}{2}, p, j)}{\partial z}}{\Delta z}}{\Delta z} \\
& \left. - (3\lambda + 2\mu)\alpha' T_l(i, p, j) \dot{\epsilon}_{kk}(i, p, j) \right] \tag{5-32}
\end{aligned}$$

$$T_l(i, p, j+1) = T_l(i, p, j) + \Delta t \dot{T}_l(i, p, j) \tag{5-33}$$

$$\frac{\partial T_l}{\partial r}(i, p + \frac{1}{2}, j) = \frac{T_l(i, p + 1, j) - T_l(i, p, j)}{\Delta r} \tag{5-34}$$

$$\frac{\partial T_l}{\partial z}(i + \frac{1}{2}, p, j) = \frac{T_l(i + 1, p, j) - T_l(i, p, j)}{\Delta z} \tag{5-35}$$

where i and p are the grid indices in the z - and r -directions, respectively, j denotes the index for time step, the “1/2” index indicates the “staggered” arrangement. Numerical integration is allowed to move to the next time step only when all the variables, such as

temperature, stresses and velocities, at every grid location satisfy a predefined convergence tolerance of $\pm 0.1\%$.

5.3.4 Initial and Boundary Conditions

A 0.775- μm wavelength laser pulse with a 10 μm spot size is investigated. Unless otherwise mentioned, the pulse duration is $t_p = 500$ fs and the laser fluence ranges from 0.005J/cm² to 0.15J/cm². All relevant optical properties of the laser are provided in Table 5.1; while Table 5.2 tabulates the various properties of the silicon materials considered in this study [40, 41, 59, 68, 69].

Table 5.1 Laser optical properties

Parameter	Value
α	$5.02 \times 10^3 e^{T_i/430}$ (/cm)
β	2.0 (cm/GW)
Γ	$0.37 + 5 \times 10^{-5}(T_i - T_0)$
Θ	$5.1 \times 10^{-18}(T_i / T_0)$ (cm ²)

Table 5.2 Material properties for silicon

Parameter	Value
ρ	2330 (kg/m ³)
E	150 (GPa)
ν	0.17
α'	2.6×10^{-6} (/K)
E_g	$1.16 - 7.02 \times 10^{-2} T_l^2 / (T_l + 1108) - 1.5 \times 10^{-8} n^{1/3}$ (eV)
D_0	$18(T_0 / T_l)$ (cm ² /sec)
κ_l	$1585 T_l^{-1.23}$ (W/cmK)
C_l	$1.978 + 3.54 \times 10^{-4} T_l - 3.68 T_l^{-2}$ (J/cm ³ K)
C_{e-h}	$3 n k_B$ (eV/ cm ³ K)
τ_e	$240(1 + n / 6.0 \times 10^{20})$ (fsec)
γ	3.8×10^{-31} (cm ⁶ /sec)
θ_i	$3.6 \times 10^{10} e^{-1.5 E_g / k_B T_e}$ (/sec)

The ambient temperature T_0 is set to be 300K. The initial conditions are defined as follows,

$$\begin{aligned} T_e(z, r, 0) &= T_l(z, r, 0) = T_0 \\ n(z, r, 0) &= 10^{12} \text{ cm}^{-3} \\ \sigma_{ii}(z, r, 0) \ (i = r, z, \theta) &= \sigma_{rz}(z, r, 0) = 0 \\ \dot{u}(z, r, 0) = \dot{w}(z, r, 0) &= 0 \\ u(z, r, 0) = w(z, r, 0) &= 0 \end{aligned}$$

Thus, at $t = 0$, the stress, velocity and displacement components are initially zeros; the electron and lattice temperatures are equal to the ambient temperature; and the initial carrier density is set to be 10^{12} cm^{-3} . The followings specify the boundary conditions,

$$\begin{aligned} \sigma_{zz}(0, r, t) &= \sigma_{zz}(z_{\max}, r, t) = 0 \\ \sigma_{\theta\theta}(z, 0, t) &= 0 \\ u(z, 0, t) &= u(z, r_{\max}, t) = 0 \\ \frac{\partial n}{\partial z}(0, r, t) &= \frac{\partial T_e}{\partial z}(0, r, t) = \frac{\partial T_l}{\partial z}(0, r, t) = 0 \\ \frac{\partial n}{\partial z}(z_{\max}, r, t) &= \frac{\partial T_e}{\partial z}(z_{\max}, r, t) = \frac{\partial T_l}{\partial z}(z_{\max}, r, t) = 0 \\ \frac{\partial n}{\partial r}(z, r_{\max}, t) &= \frac{\partial T_e}{\partial r}(z, r_{\max}, t) = \frac{\partial T_l}{\partial r}(z, r_{\max}, t) = 0 \end{aligned}$$

so that the top ($z = 0$) and bottom ($z = z_{\max}$) faces are stress-free; the circumference at $r = r_{\max}$ is constrained in the r-direction; displacement u and normal stress $\sigma_{\theta\theta}$ are zero along the centre line ($r = 0$) of both the silicon wafer and laser beam. Given the brief action time of the laser, the heat fluxes on all open faces including the circumference are negligible. The carrier current J and energy current W are also neglected on these faces for the same reason, thus resulting in zero gradients for the carrier density, n , according to Eqs. (5-14)-(5-17).

All terms in the governing equations that involve the reciprocal of r , i.e., $1/r$, is numerically undefined at $r = 0$. However, using the L'Hopital's rule, these terms can be expressed as differentials in the forms of $\partial/\partial r$. For example, $\lim_{r \rightarrow 0}(u/r) = \partial u / \partial r|_{r=0}$.

Finally, a total number of 50 equally-spaced grid points in the z -direction and 20 in the r -direction are found to be refined enough to ensure solution convergence. When the total elements in the model domain exceed 50×20 , results obtained are seen to show negligible differences in the time period considered. Thus, no further mesh refinement is needed. Time steps varying from 5fsec to 60fsec are used to integrate pre-thermal-equilibrium time history. A much larger time step $\Delta t = 5$ psec is followed to integrate post equilibrium evolution.

5.4 Results

Using the axisymmetric finite difference model elaborated above, a laser of $0.775\text{-}\mu\text{m}$ in wavelength and $10\mu\text{m}$ in spot size is considered. The laser pulse duration is $t_p = 500$ fs with its peak located at $t = 1.5$ ps. Results presented in the section correspond to a fluence input ranging from 0.005 to 0.15 J/cm².

5.4.1 Carrier and Lattice Temperatures

Figures 5.4 and 5.5 show, respectively, the electron and lattice temperature distributions in the model domain at four different time instances $t = 1, 1.5, 2.5$ and 5 ps. Irradiation of the silicon is initially dominated by a rigorous energy transferring from the pulse to electrons as marked by a rapid elevation of the electron temperature.

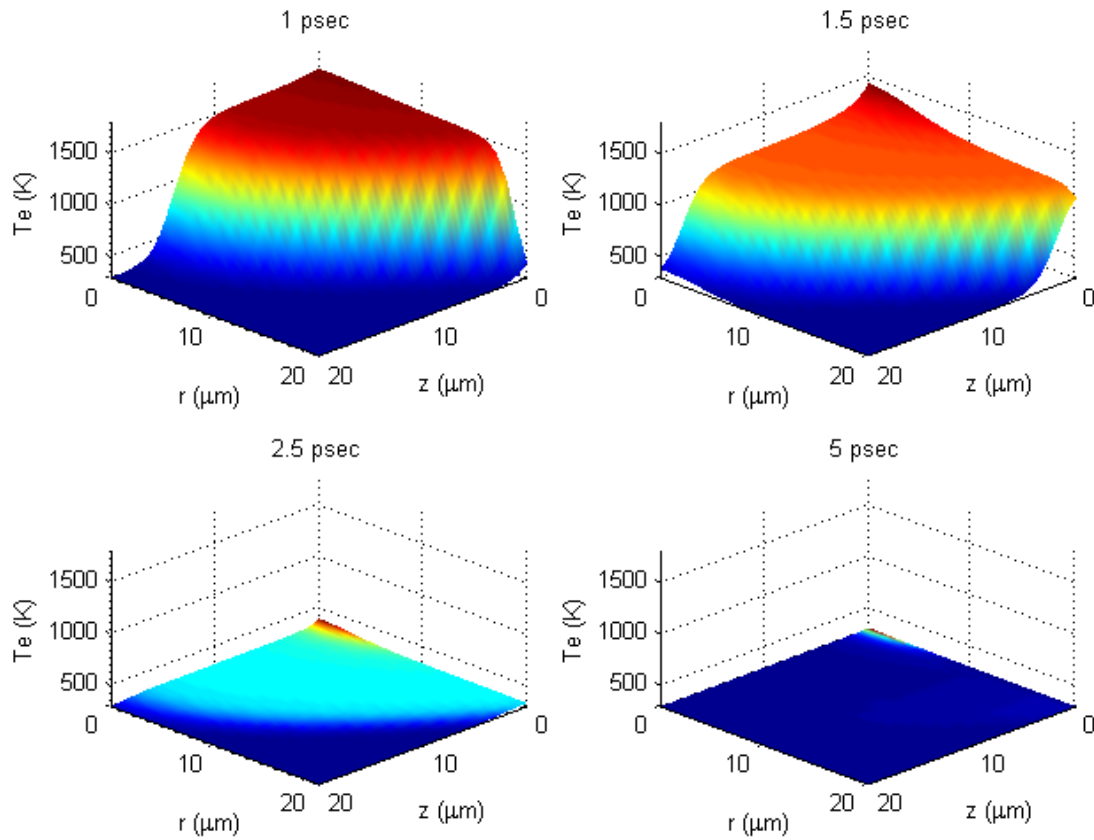


Figure 5.4 Electron temperature distribution in silicon wafer irradiated by ultrafast laser
(pulse duration 500fs, spot size $10\mu\text{m}$, laser fluence $0.005\text{J}/\text{cm}^2$)

The energy is seen to subsequently transfer to cooler lattices and diffuse further into regions that are low in temperature. Though the laser pulse does not reach its peak value till $t=1.5\text{ps}$, the electron temperature registered at $t=1\text{ps}$ in the volume bound by $r \leq 10\mu\text{m}$ and $z \leq 10\mu\text{m}$ is hundreds of Kelvins higher than that registered at $t=1.5\text{ps}$. In other words, maximum electron temperature comes ahead of the peak laser intensity. This interesting observation will be explained later. Lattice temperature keeps increasing in the model domain until it reaches thermal equilibrium with the electrons at approximately $t = 5\text{ps}$. At the center of the laser-impinged spot at $r = z = 0$, a maximum lattice temperature of 305.2K is registered in response to the $0.005\text{J}/\text{cm}^2$ fluence input.

The time histories of both the electron and lattice temperatures at $r = z = 0$ corresponding to $0.005\text{ J}/\text{cm}^2$ laser fluences are plotted in Figure 5.6. It is seen that the time taken for the electron and lattice temperatures to reach the thermal equilibrium is approximately 5ps .

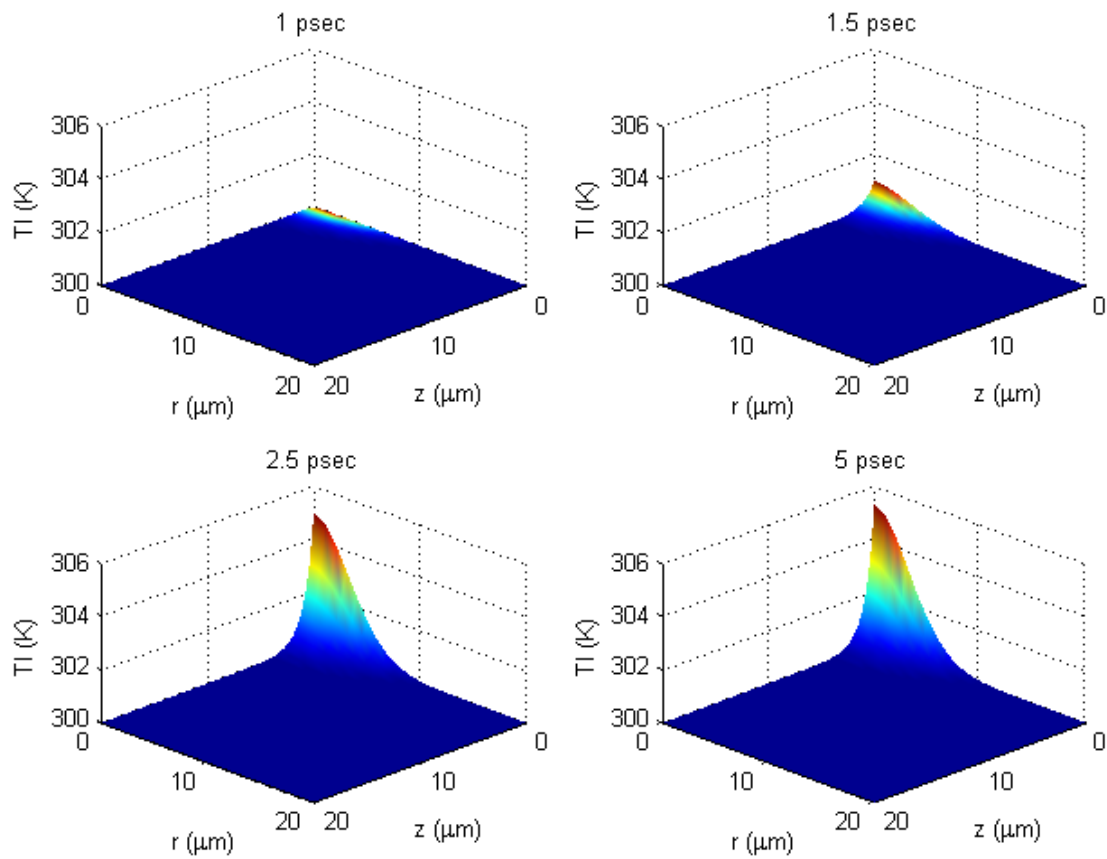


Figure 5.5 Lattice temperature distribution of silicon wafer irradiated by ultrafast laser

(pulse duration 500fs, spot size $10\mu\text{m}$, laser fluence $0.005\text{J}/\text{cm}^2$)

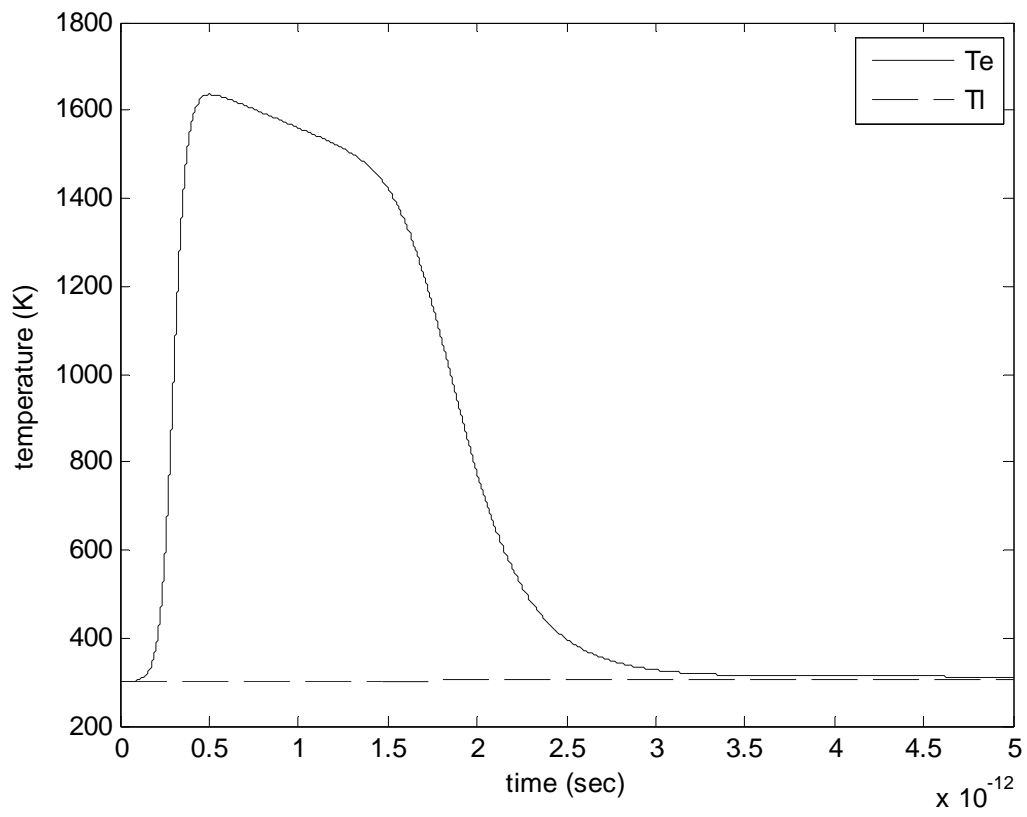


Figure 5.6 Time evolution of electron and lattice temperatures
(pulse duration 500fs, spot size 10 μ m, laser fluence 0.005J/cm²)

As stated earlier, the peak of the electron temperature occurs before the laser reaches its maximum intensity at $t=1.5\text{ps}$, which can be visualized in Figure 5.6 where 0.005J/cm^2 laser fluence is used. This can be explained using Eq. (5-19) and the definition of electron specific heat, $C_{e-h} = 3nk_B$, as follows. Although initially the laser is yet to reach its full intensity, the carrier density $n = 10^{12}\text{cm}^{-3}$ is much smaller at this early stage in time compared with its value when laser peak intensity is reached, which is of the order of 10^{19}cm^{-3} (see Figure 5.9). As the electron specific heat C_{e-h} corresponding to the initial carrier density is of seven order-of-magnitudes lower, electron temperature is therefore seeing exponential increase. After the peak temperature, electron temperature T_e begins falling down to approximately 1400K as time increases to $t=1.5\text{ps}$. This is mainly attributable to the high carrier density and the pronounced increasing rate of the carriers, $\partial n / \partial t$, which is a dominant term in Eq. (5-19) in decreasing electron temperature. Consequently, even though laser intensity is still rising, the increasing energy absorbed from the laser pulse cannot elevate T_e any higher. Since laser intensity starts to drop off after $t=1.5\text{ps}$, T_e therefore decreases with noted rate. However, there still remains a significant thermal difference between T_e and T_l for an extended amount of time before thermal balancing is eventually attained.

Figure 5.7 shows the electron and lattice temperatures obtained for a fluence input that is 3 times higher at 0.015J/cm^2 . It is seen that although the fluence is higher, the first peak of the electron temperature reaches the same level of magnitude at the same time as the lower fluence case. Nevertheless, a second T_e peak occurs right after

$t=1.5\text{ps}$ as seen in Figure 5.7. The magnitude of the second peak is around 1700K, which is slightly higher than the first one. The presence of the second peak indicates that in the competition between increasing laser intensity and high rate of change of carrier density, the former dominates the higher fluence case. Time evolutions of the electron and lattice temperatures in response to a higher laser fluence at $0.15\text{J}/\text{cm}^2$ is shown in Figure 5.8. It illustrates that for this particular laser fluence the magnitude of the second peak arises 8 times higher than the first peak. The high laser intensity is one reason behind the result. The other is the rapid reduction of the carrier density (see Figure 5.11), thus resulting in a relatively large negative value for the rate of change of the carrier density, $\partial n / \partial t$, that contributes to the rapid increasing T_e . As the effect of the thermal relaxation term, τ_e , defined in Eq. (4-60), becomes prominent subject to such a large carrier density gradient in time, the reaching of the maximum T_e is delayed as compared with Figures 5.6 and 5.7. As a result, T_e and T_l would eventually reach a significantly higher equilibrium temperature at a much later time than the two previous cases. Careful extractions place the reaching of thermal equilibrium at $t = 70\text{ps}$ for the $0.015\text{ J}/\text{cm}^2$ fluence and $t = 1\text{ns}$ for the $0.15\text{ J}/\text{cm}^2$ case.

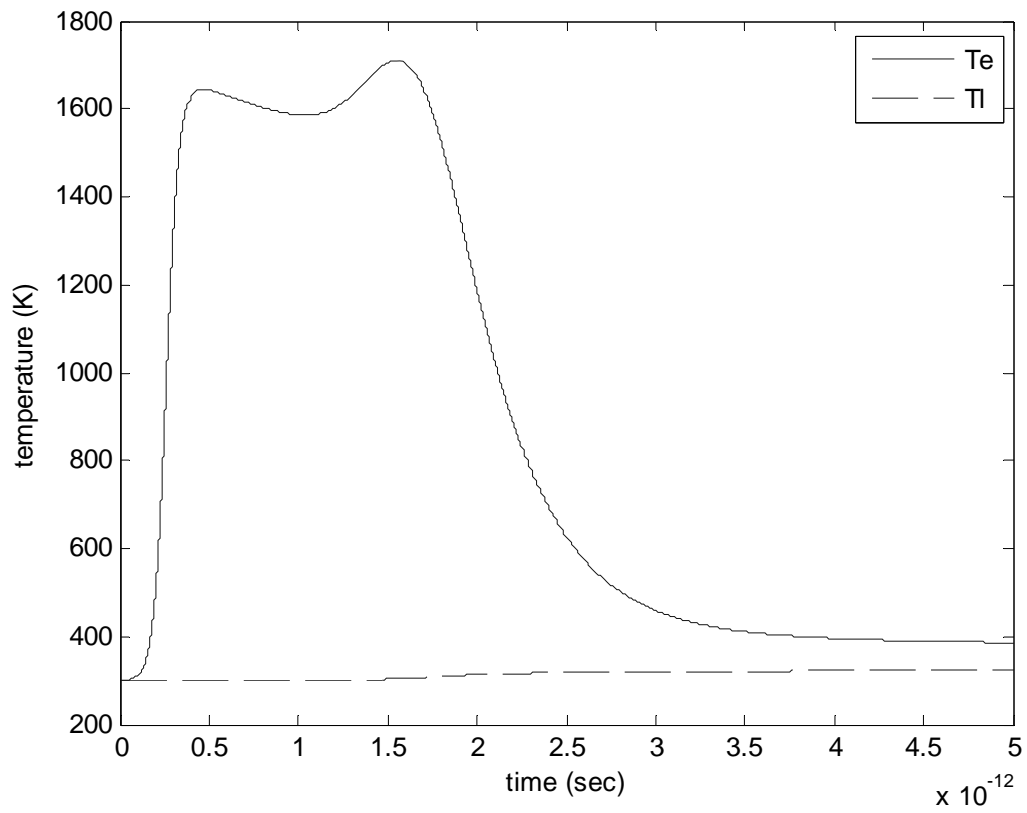


Figure 5.7 Time evolution of electron and lattice temperatures
(pulse duration 500fs, spot size 10 μ m, laser fluence 0.015J/cm²)

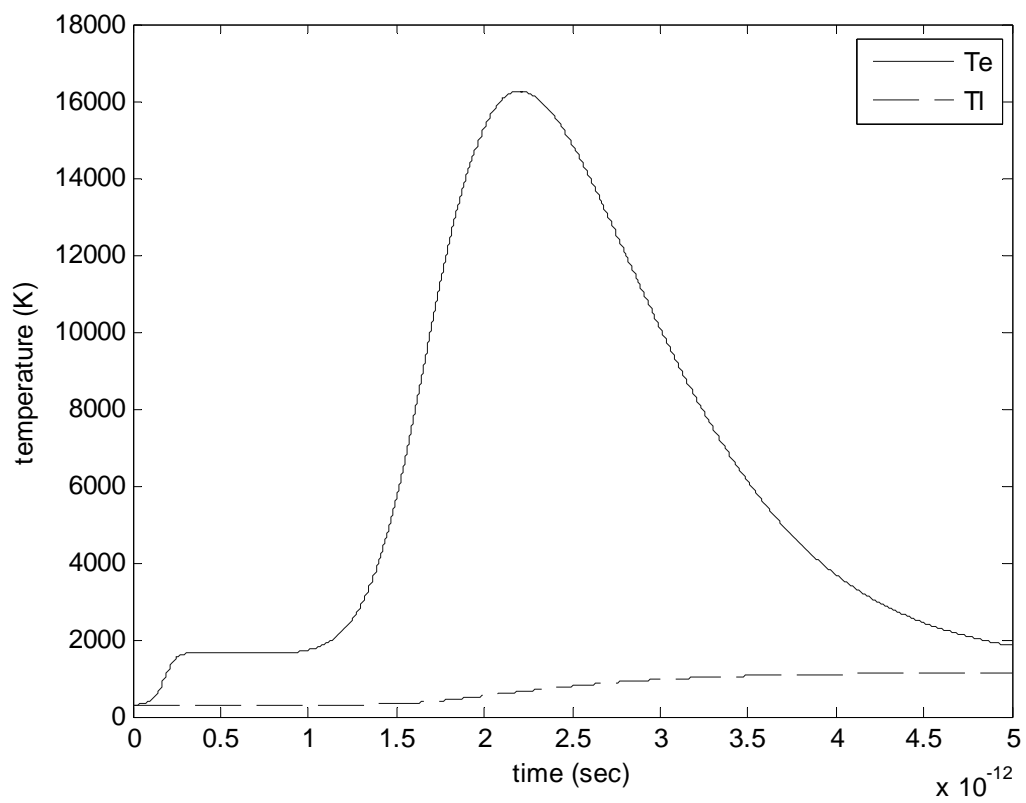


Figure 5.8 Time evolution of electron and lattice temperatures
(pulse duration 500fs, spot size 10 μ m, laser fluence 0.15J/cm²)

5.4.2 Carrier Density

Figures 5.9 to 5.11 show the variations of the carrier density n with respect to three laser fluences at three different depths at $z = 0, 2,$ and $4\mu\text{m}$. It is seen that the maximum carrier densities ($1.26 \times 10^{20} \text{cm}^{-3}$ and $3.74 \times 10^{20} \text{cm}^{-3}$) that correspond to the two lower fluences at 0.005J/cm^2 and 0.015J/cm^2 are basically proportional to the input fluence. However, as the carrier density approaches the critical value at $2.74 \times 10^{21} \text{cm}^{-3}$ for the silicon material [41], non-thermal melting would immediately ensue. At this state, n is no longer proportional to fluence input and damage to the material is eminent. Furthermore, the level of carrier density attenuates very fast at increasing depth. For example, at $z = 2\mu\text{m}$, n is 20% of that at $z = 0\mu\text{m}$ in Figure 5.11. At location $z = 4\mu\text{m}$ the drop is a steeper and miniscule 4%. Thus the carrier densities at these shallow depths are far below the critical melting threshold even though the top face at $z = 0\mu\text{m}$ is very close to being damaged. In other words, material damage inflicted by the particular laser pulse is highly localized and confined to an extremely small volume beneath the irradiated surface. By using this model, it is therefore feasible to follow the distribution of the carrier density in both time and space and track the regions experiencing non-thermal melting in silicon wafers when processed by ultrafast laser pulses.

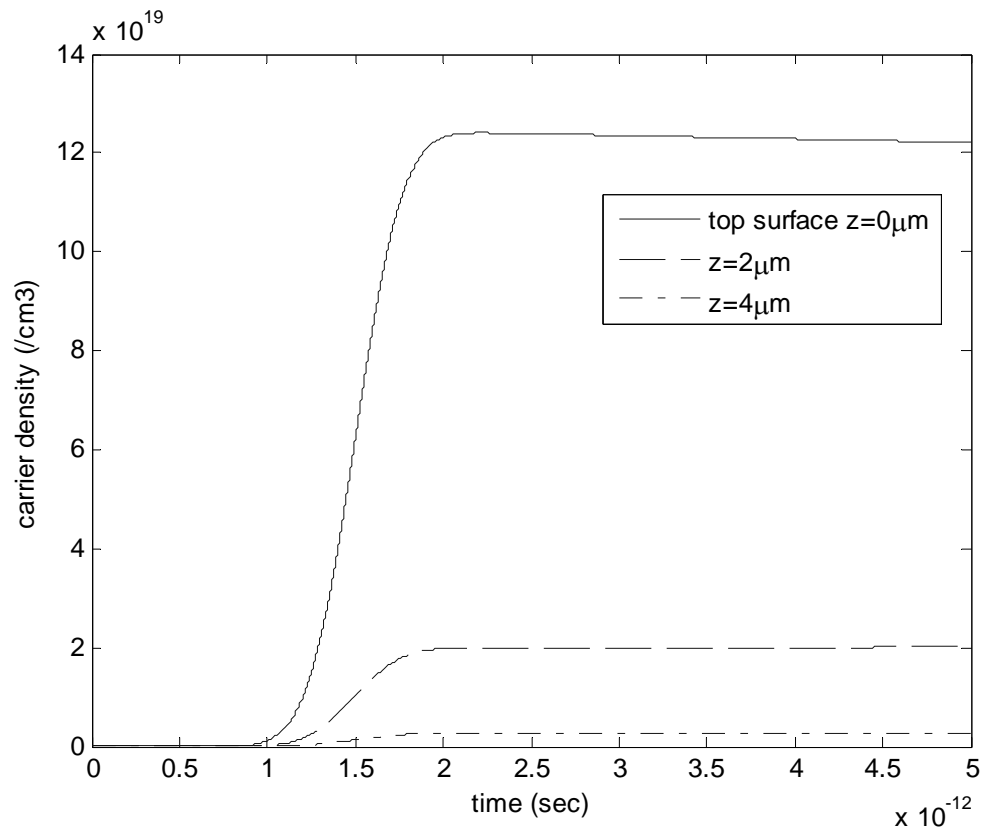


Figure 5.9 Time evolution of carrier density

(pulse duration 500fs, spot size $10\mu\text{m}$, laser fluence $0.005\text{J}/\text{cm}^2$)

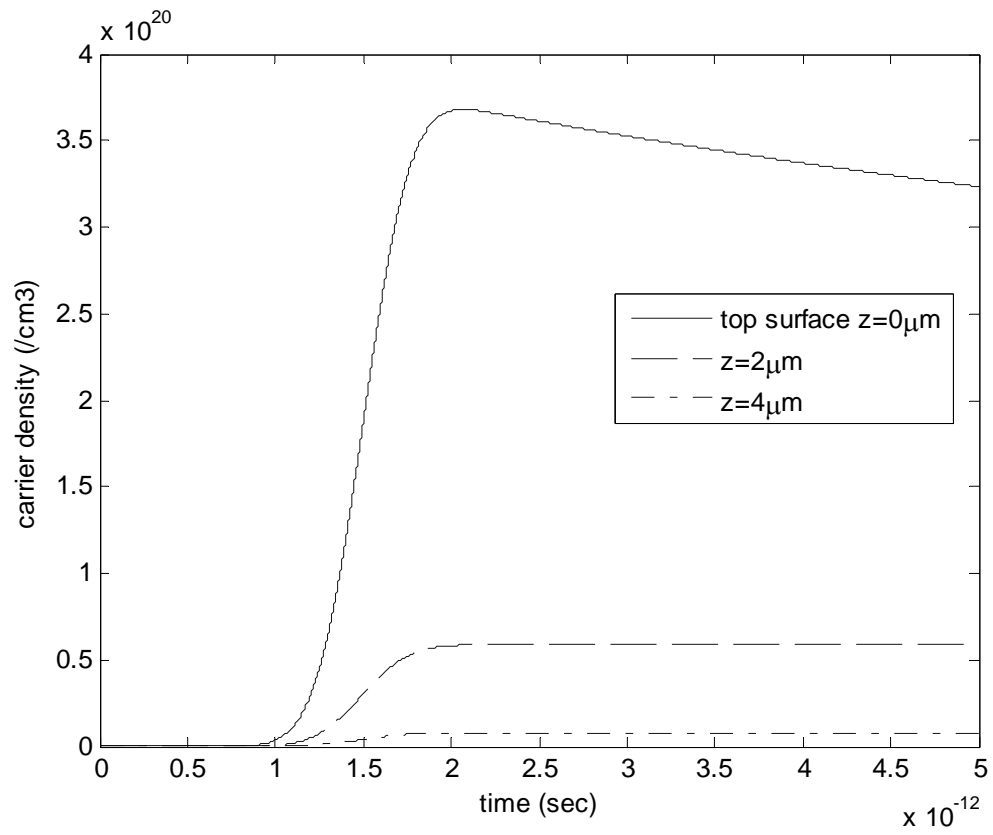


Figure 5.10 Time evolution of carrier density

(pulse duration 500fs, spot size $10\mu\text{m}$, laser fluence $0.015\text{J}/\text{cm}^2$)

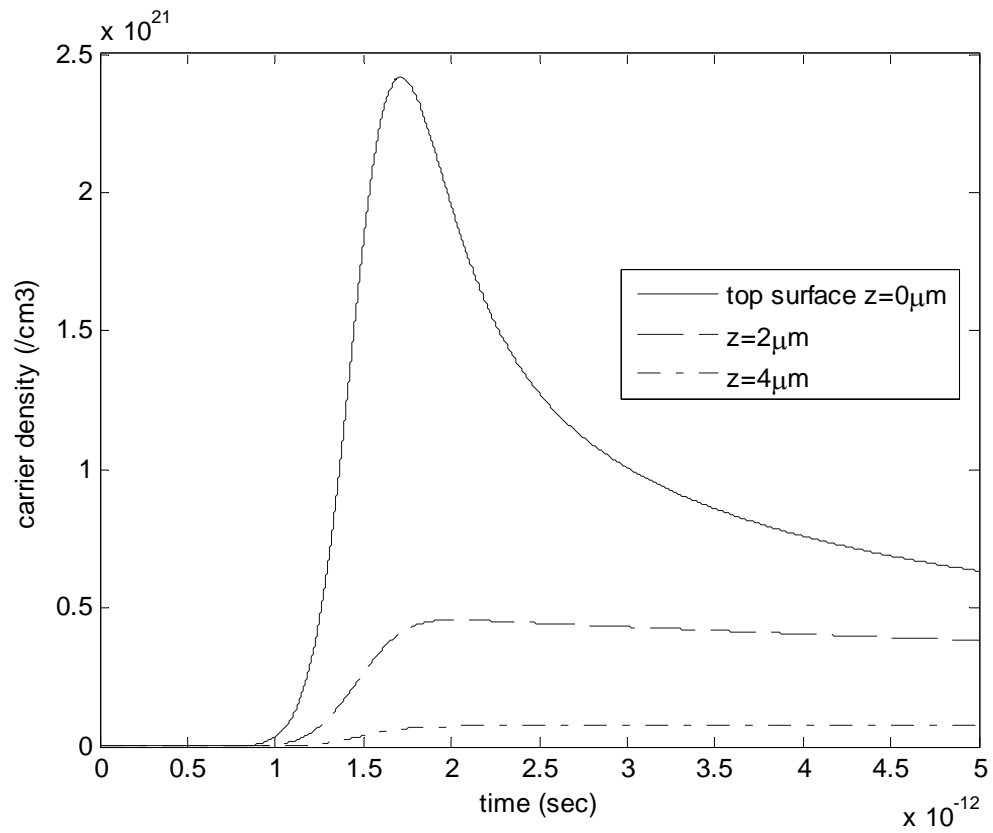


Figure 5.11 Time evolution of carrier density

(pulse duration 500fs, spot size $10\mu\text{m}$, laser fluence $0.15\text{J}/\text{cm}^2$)

5.4.3 Displacement and Velocity Fields

The displacement response of the model domain impinged by a $0.005\text{J}/\text{cm}^2$ laser pulse is presented in Figure 5.12, where w and u are displacement variables in the z - and r -direction, respectively. It is seen that the magnitudes of these mechanical responses are of the order of 10^{-12}m at time $t = 10\text{ns}$. As a fully developed wave, w wavefront covers $10\mu\text{m}$ in the z -direction and $17\mu\text{m}$ in the r -direction within the first 5ns . It then travels an additional $8\mu\text{m}$ in z -direction and another $1\mu\text{m}$ in r -direction in the next 5ns . It is clear from looking at the changing w waveforms at the two time instants that the wave is dispersive. The displacement in the other direction, u , on the other hand, does not display any feature indicative of a full-fledged wave. Since u carries a relatively large negative amplitude in the proximity of $z = 0$, all the neighboring nodes on the surface therefore are in compression. This compression state is seen to progress from $t = 5\text{ns}$ to 10ns towards the center line of the laser beam with increasing magnitudes. Though of small magnitudes, the zone affected by u , however, is seen to keep trailing and propagating in the z -direction.

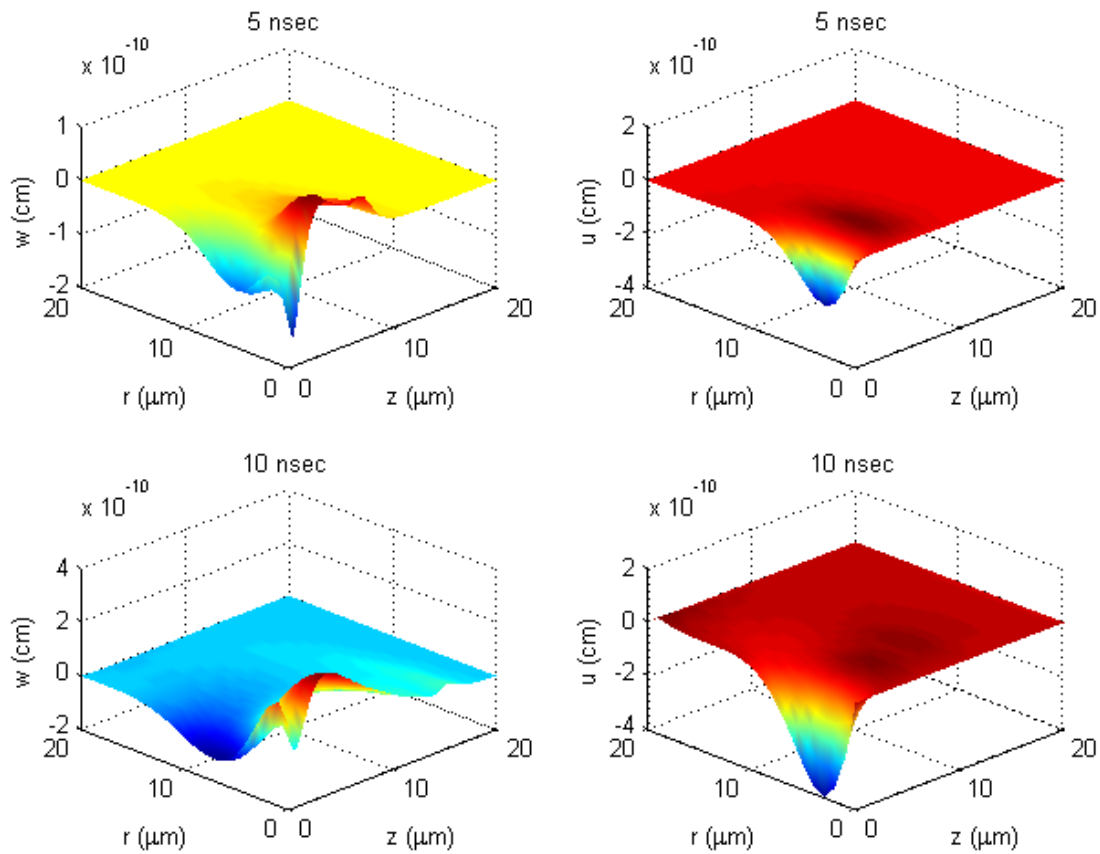


Figure 5.12 Displacement profiles of silicon wafer irradiated by ultrafast laser at two different times (pulse duration 500fs, spot size $10\mu\text{m}$, laser fluence $0.005\text{J}/\text{cm}^2$)

To visualize laser-induced motions in the silicon wafer, the positions of the grid nodes of the axisymmetric model are plotted in Figure 5.13 for two consecutive times at $t = 5\text{ns}$ and $t = 10\text{ns}$. It should be noted that (1) all empty circles in the figure are initially at where the corresponding grid nodes are located; (2) the resultant displacement is calculated for each node using its w and u displacement components; (3) as the induced motion is highly localized in space, only displacement responses within the disk bound by $z \leq 10\mu\text{m}$ and $r \leq 15\mu\text{m}$ are considered; (4) the resultant displacements shown in the figure are magnified by a factor of 3×10^5 for clarity. It can be seen by following the two snap shots taken at $t = 5\text{ns}$ and $t = 10\text{ns}$ that as if the nodes along $r = 0$ are being plucked towards the positive z -direction, and all others are rubber-banded together and move accordingly. This figure along with Figure 5.12 conveys an image not unlike dropping a pebble onto a body of water to initiate a trough and an accompanying wave crust propagating radially outwards. As the silicon considered for the study is one of thin disk that supports guided stress waves, the snap shots capture a Lamb waveguide mode in its initial burgeoning stage. The presented model therefore enables not just the generation and propagation of Lamb waves to be studied as time functions of laser input parameters and material geometry. It also allows thermal-mechanical responses induced by femtoseconds heating to be established at near-field.

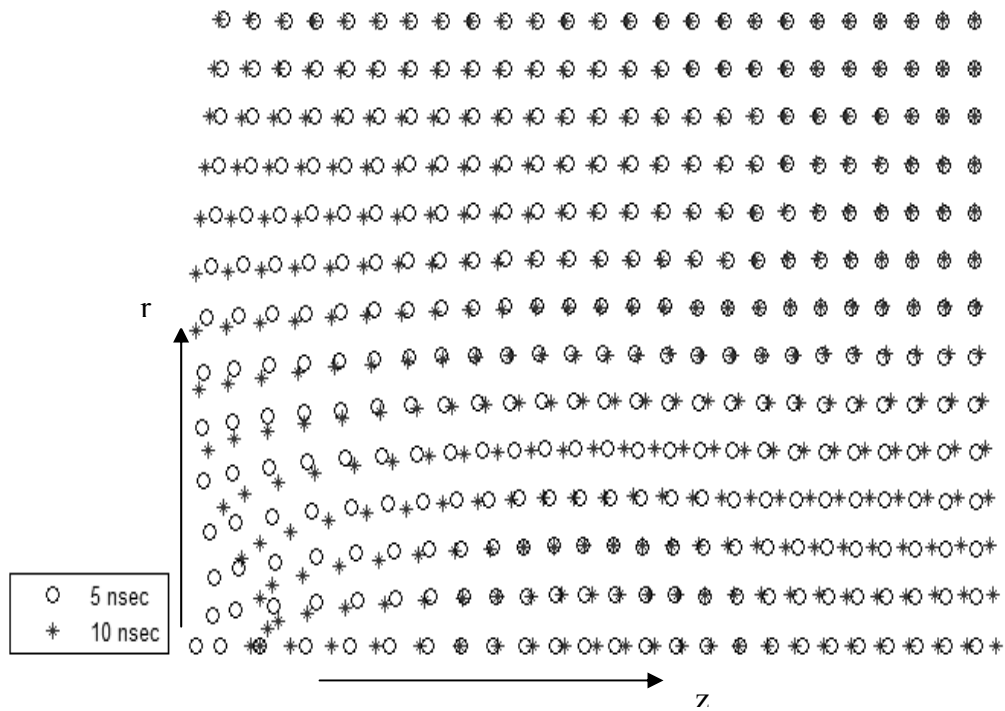


Figure 5.13 Laser induced nodal motion of silicon wafer
 (pulse duration 500fs, spot size 10 μ m, laser fluence 0.005J/cm²)

Figure 5.14 shows the time evolutions of nodal velocity over the entire model domain at $t = 5$ and 10ns . Given the relatively non-oscillating displacements in Figure 5.12, nodal velocities are seen to progress in the z -direction with high-frequency oscillations; while no such oscillating features are observed in the radial direction. As energy transport in the form of particle kinetics is indicated by the spatial gradients of the velocity shown, it can be seen in Figure 5.14 that the transport of mechanical energy is both finite and localized. It takes 10ns to cover approximately $20\mu\text{m}$ into the depth. It would have to transverse the entire thickness and reach the backside of the wafer to bring about a Lamb wave.

5.4.4 Thermal Stress Waves

Figure 5.15 shows the spatial distributions of three normal stress components (namely, σ_{zz} , σ_{rr} and $\sigma_{\theta\theta}$) along with one shear stress component (σ_{rz}) at times $t = 5$ and 10ns . The magnitudes of all the stress components are of the order of several MPa or less within the time window considered. The σ_{zz} component is in contrast to all others in that it exhibits definitive features indicative of a propagating wave. As none fulfills a complete oscillation cycle within the first 10ns window, what components σ_{rr} , $\sigma_{\theta\theta}$ and σ_{rz} each demonstrated in the figure are near-field elastodynamic responses that precede the forming of a full-fledged wave in their respective directions. Although the near-field responses are largely localized in the $10\mu\text{m} \times 10\mu\text{m}$ volume revolved about the axisymmetric axis, however, they do see their magnitudes doubled within 5ns .

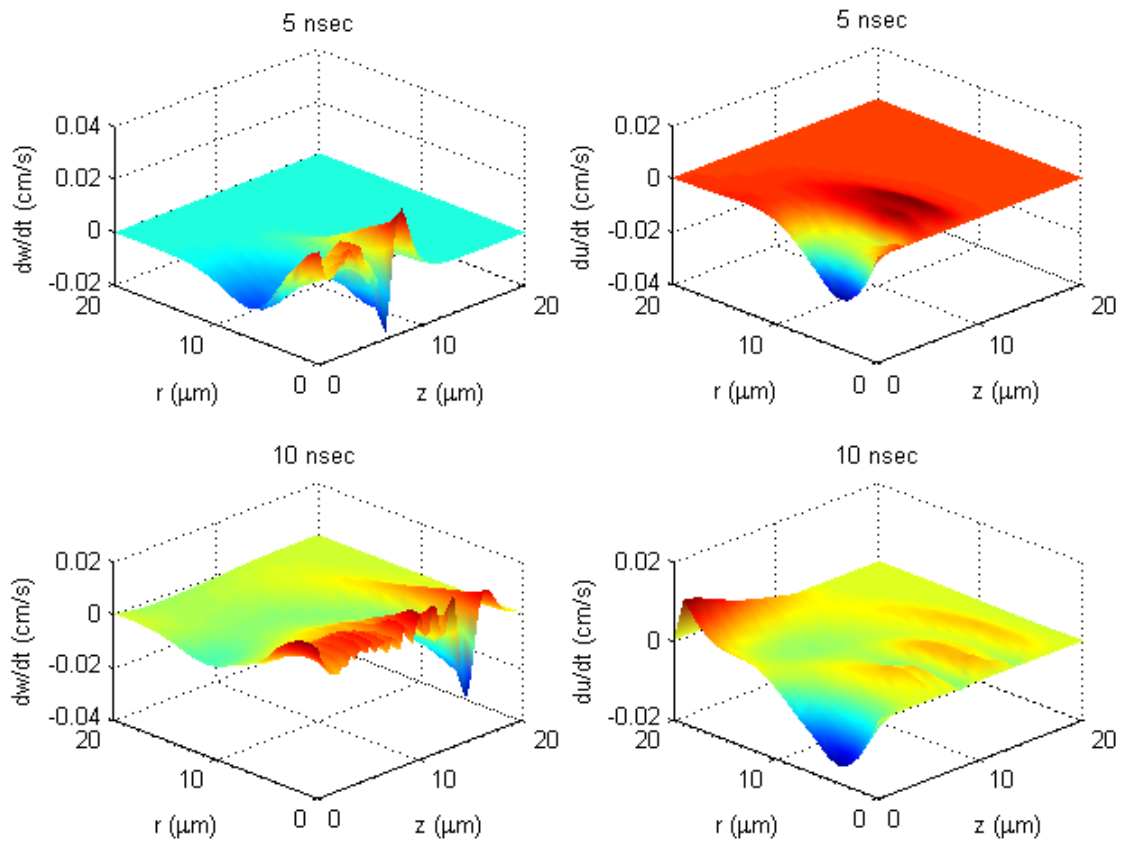


Figure 5.14 Velocity profiles of silicon wafer irradiated by ultrafast laser at two different times (pulse duration 500fs, spot size $10\mu\text{m}$, laser fluence $0.005\text{J}/\text{cm}^2$)

The σ_{zz} thermal stress wave generated by the 500fs ultrafast laser pulse is dispersive and characteristically of broadband, low amplitude and extremely high frequency. To resolve wave dispersion along with the associated frequency components, a propagation path is defined in Figure 5.16. Two sampling points, A and B, are placed along the path from which waveforms are extracted. A and B are each $2\mu\text{m}$ and $6\mu\text{m}$ from the top face, respectively, thus defining a $4\mu\text{m}$ propagation length. The two dissimilar time waveforms obtained at A and B suggest the σ_{zz} wave is dispersive with a time-varying spectrum. The Gabor Wavelet Transform (GWT) is then employed to resolve the waveforms of their respective dispersion. As an alternative to Fourier Transform, GWT has been shown to provide simultaneous time-frequency resolution optimal for resolving dispersive waves found propagating in beams and silicon wafers [10, 33]. Figure 5.17 shows the GWTs of the waveforms acquired at A and B. The σ_{zz} wave is characteristically broadband with a 0-500MHz bandwidth. It is calculated using the GWT result that the group velocity of the 50MHz frequency component is approximately 5.7km/s, and 1.6km/s for the 200MHz component. The two frequency components progressing in space with different velocities is essential to signify that the σ_{zz} wave is indeed dispersive.

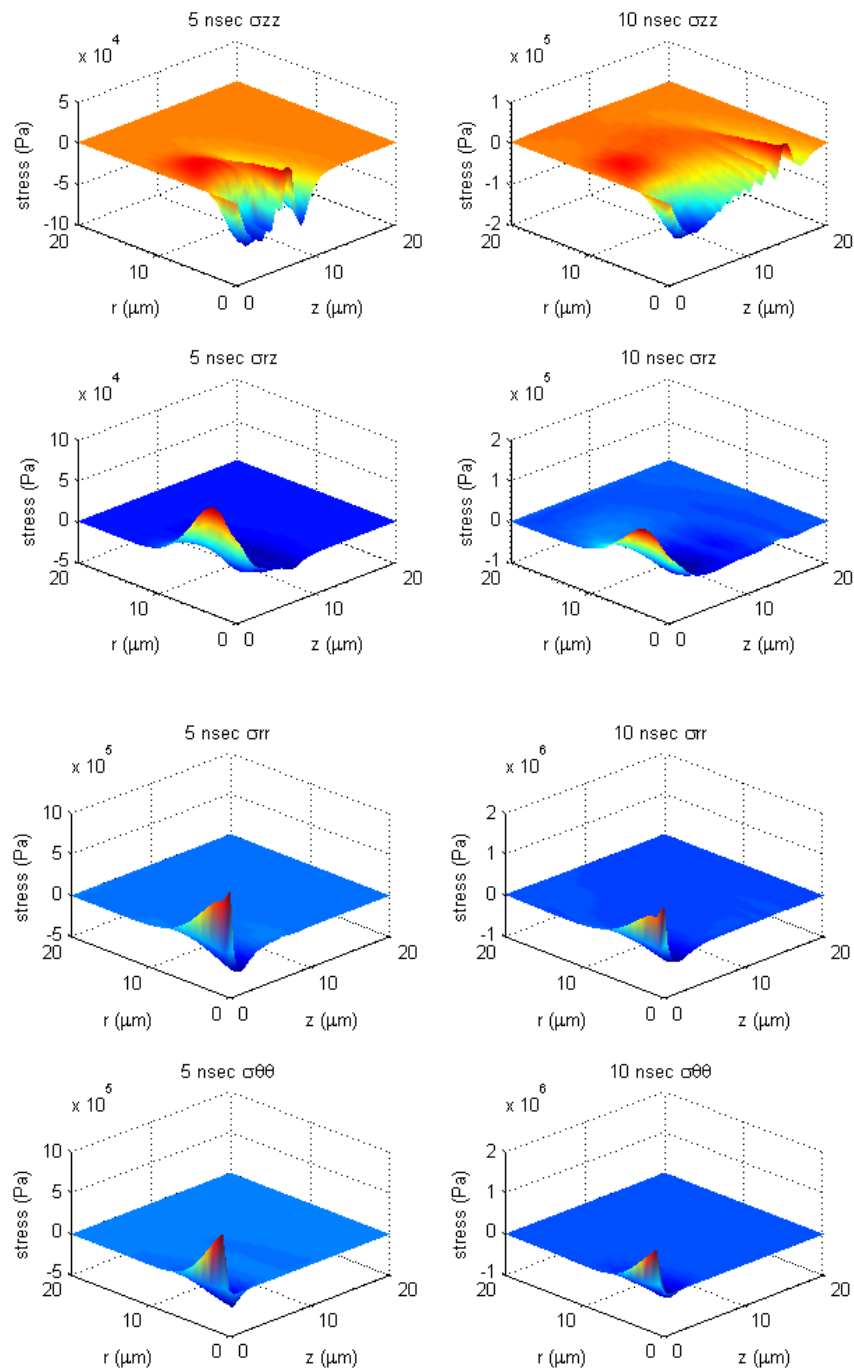


Figure 5.15 Stress distributions of silicon wafer irradiated by ultrafast laser at two different times (pulse duration 500fs, spot size $10\mu\text{m}$, laser fluence $0.005\text{J}/\text{cm}^2$)

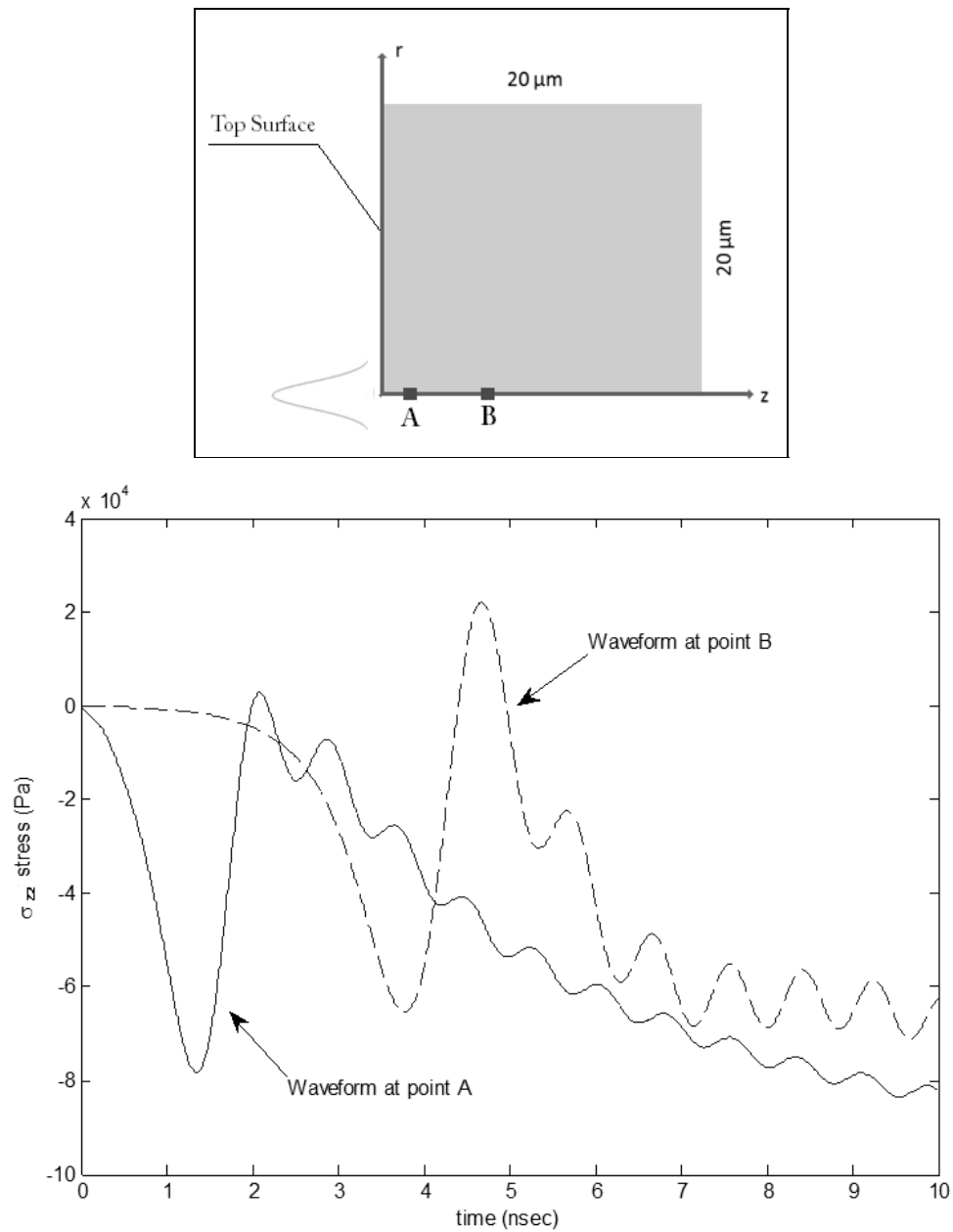
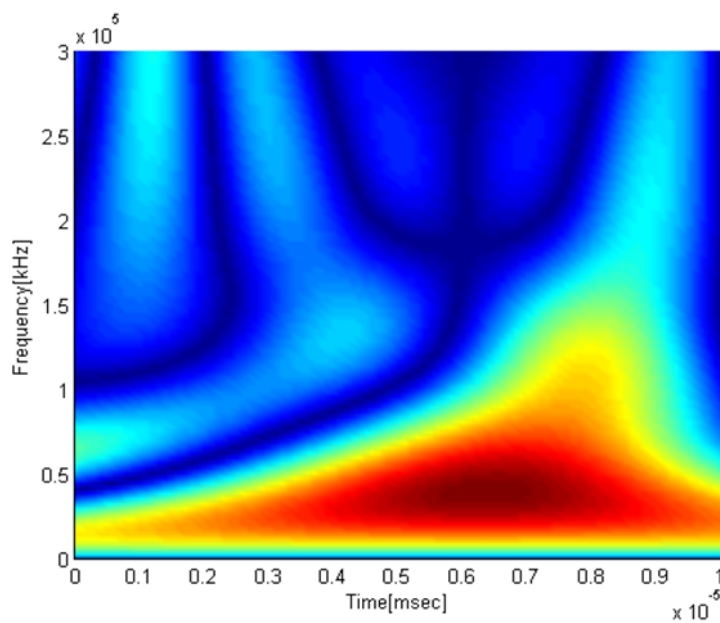
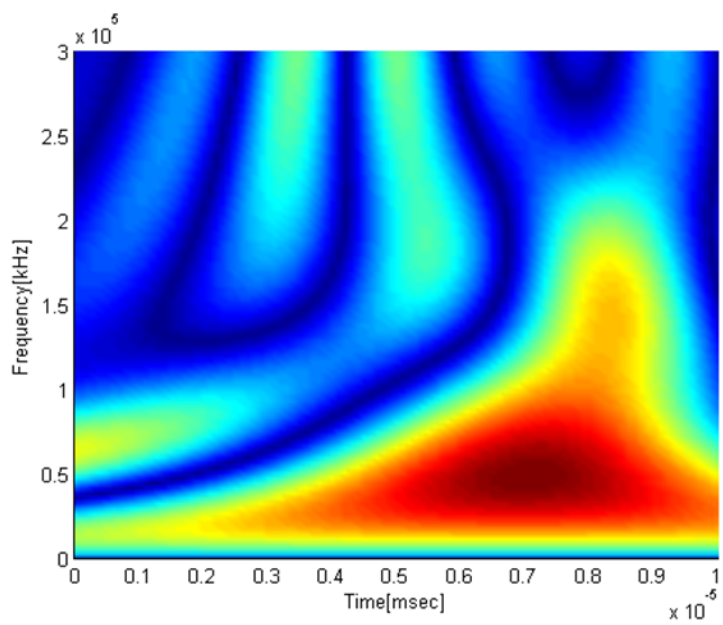


Figure 5.16 Waveforms obtained at sampling locations A and B
(pulse duration 500fs, spot size 10μm, laser fluence 0.005J/cm²)



(a)



(b)

Figure 5.17 GWT of waveforms acquired at sampling locations (a) A and (b) B
(pulse duration 500fs, spot size 10 μ m, laser fluence 0.005J/cm²)

5.4.5 Power Density and Effect of Laser Fluence

The temporal gradient of an oscillating stress has an equivalent unit that can be obtained through using the SI notations as $[N/m^2s] \equiv [W/m^3]$. With this equivalent unit, all stress variations in time can be interpreted alternatively as power per cubic volume, thus properly termed as power density. The notion of power density has been successfully applied to correlate dispersive stress waves with the development of mechanical faults and defects in microelectronic packages [46, 47]. Since thermal stress waves are dispersive with broad, time-varying spectra, the number of loading cycles exerted by each constituent frequency within any given time span is therefore difficult to be determined. The Accumulated Damage Evaluation Method developed in [46] are followed to predict if fatigue cracking is likely at a particular location for a given amount of time subject to the actions of power density.

Figures 5.18 and 5.19 plot the power densities associated with the normal stress wave σ_{zz} and the shear stress wave σ_{rz} at time $t = 5\text{ns}$. In spite of low stress magnitudes, the corresponding power densities are of the order of 10^{14} W/m^3 and 10^{13} W/m^3 for the σ_{zz} and σ_{rz} components, respectively. Maximum power densities are observed at a depth of $7\mu\text{m}$ along the axisymmetric axis. The power densities of the σ_{rr} component at times $t=5\text{ns}$ and $t=10\text{ns}$ also show similar order-of-magnitudes in Figures 5.20 and 5.21. Contrast to Figure 5.15 where σ_{rr} responses are strictly near-field and local, the σ_{rr} power density behaves like a wave and propagates both radially and axially. To evaluate if these power density waves could potentially inflict havoc, the

high cycle fatigue data found in [70] is utilized. Single crystalline silicon thin films were cycled with 40kHz and 50kHz frequencies at 6.5GPa (4.5GPa) and achieved 10^6 (10^{11}), the lowest (highest) fatigue life cycles. The corresponding power densities can then be calculated as, respectively, 3.8×10^{14} and 3.5×10^{14} W/m³. As the power densities presented in Figs. 16-17 all have a magnitude that is below the $3.5\text{-}3.8 \times 10^{14}$ W/m³ threshold, one may be deceived into thinking that stress waves of such power density level are benign and raise no concerns over the initiation of fatigue cracking.

Figures 5.22 and 5.23 show the results associated with a higher $0.015\text{J}/\text{cm}^2$ laser fluence input at $t = 10\text{ns}$. Compared with the results shown in Figures 5.12 and 5.15, it is seen that the waves share very similar spatial configurations and identical time-of-arrivals with their counterparts generated using $1/3$ of the fluence input at $0.005\text{ J}/\text{cm}^2$. The magnitudes of these mechanical responses, on the other hand, are approximately 10 times larger. The few observations made to the spatial profiles of the w displacement and σ_{zz} stress component shown in Figures 5.22 and 5.23 indicate that wave propagation characteristics are in general independent of the fluence input. By nonlinearly related to laser fluence, wave amplitude is an exception.

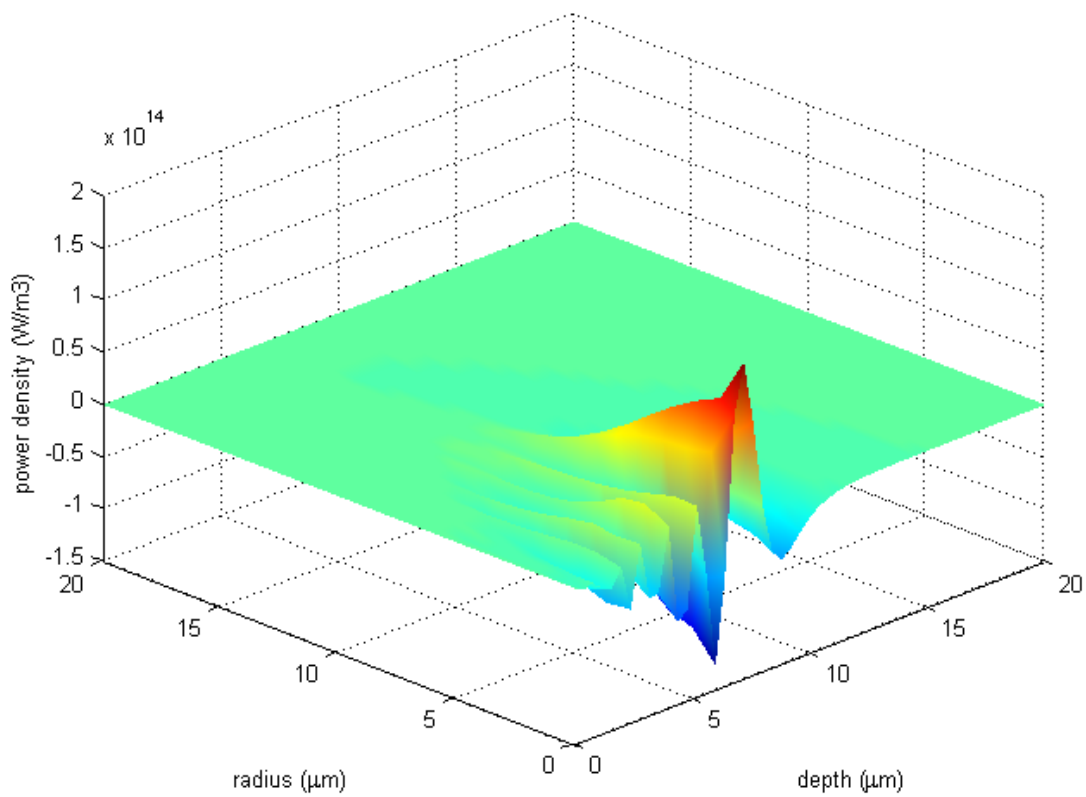


Figure 5.18 Power density of σ_{zz} at $t = 5\text{ns}$

(pulse duration 500fs, spot size $10\mu\text{m}$, laser fluence $0.005\text{J}/\text{cm}^2$)

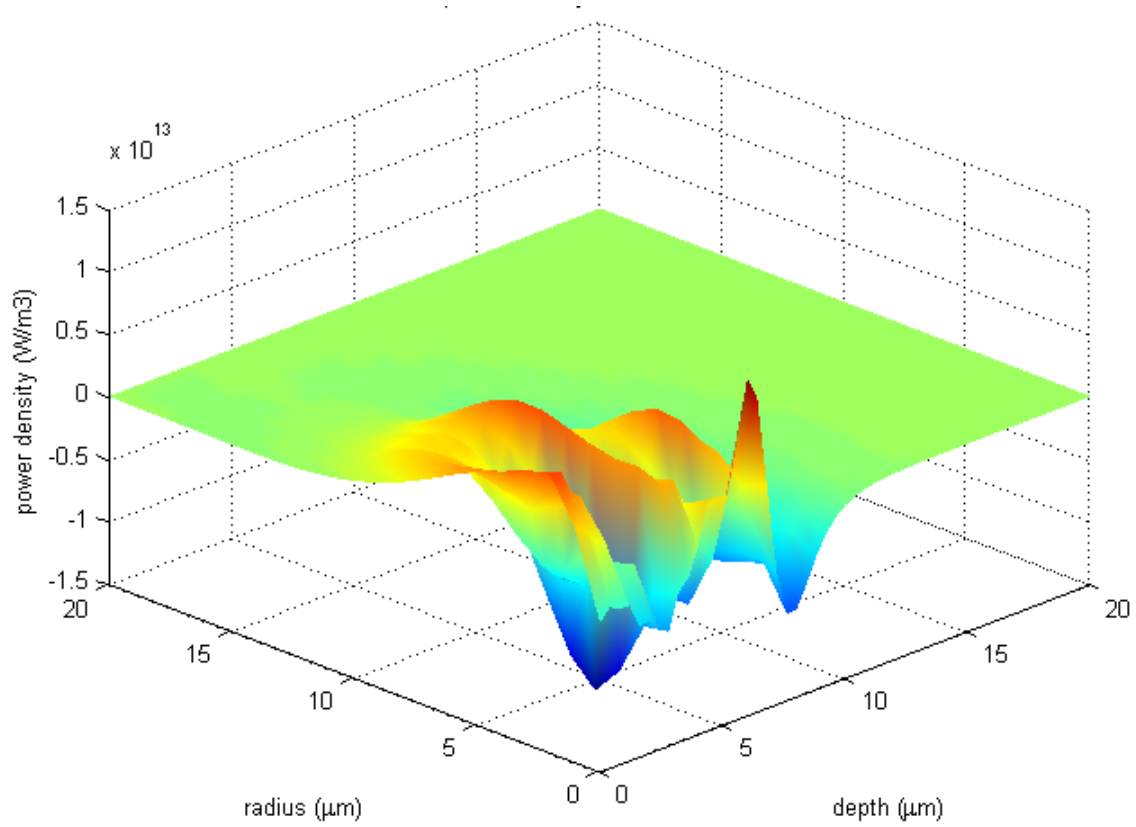


Figure 5.19 Power density of σ_{rz} at $t = 5\text{ns}$

(pulse duration 500fs, spot size $10\mu\text{m}$, laser fluence $0.005\text{J}/\text{cm}^2$)

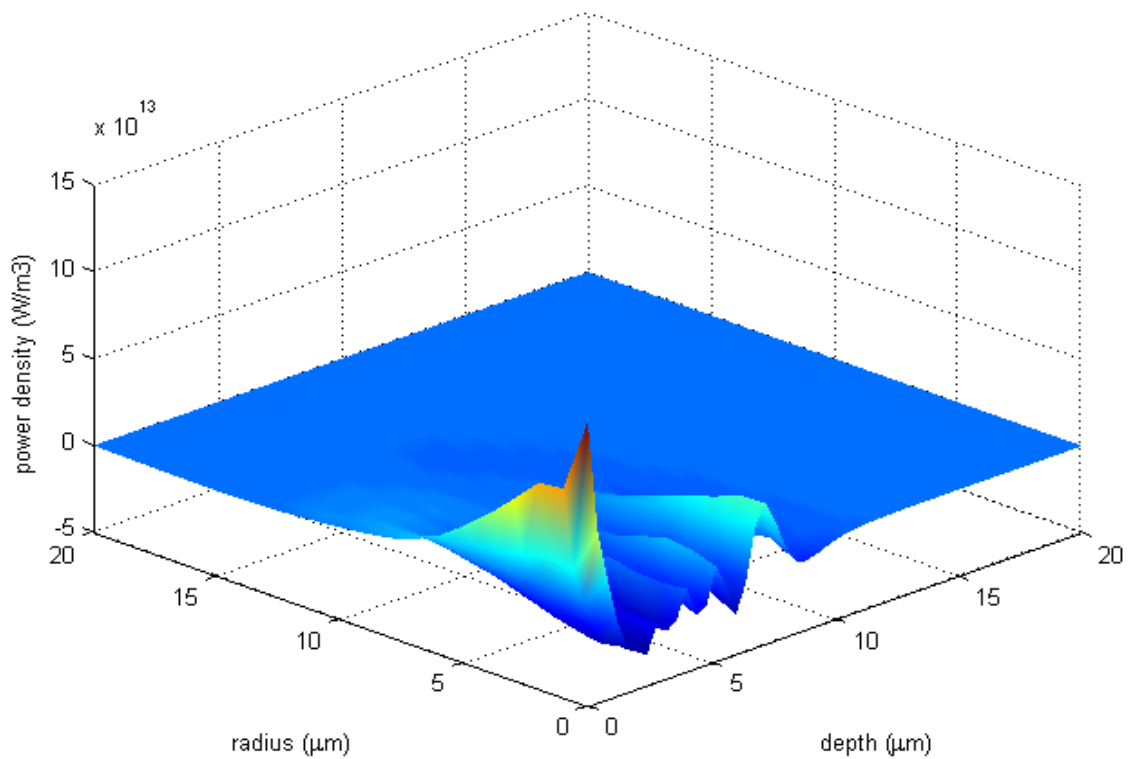


Figure 5.20 Power density of σ_{rr} at $t = 5\text{ ns}$

(pulse duration 500fs, spot size $10\mu\text{m}$, laser fluence $0.005\text{J}/\text{cm}^2$)

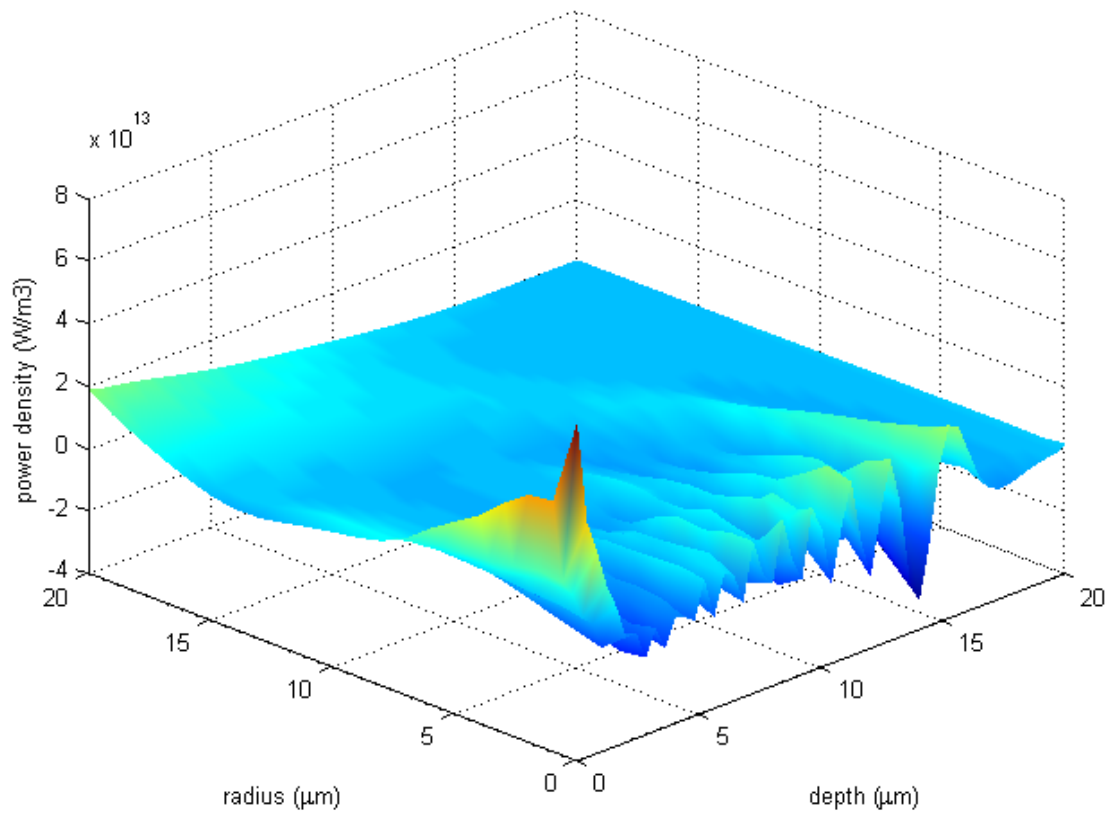


Figure 5.21 Power density of σ_{rr} at $t = 10\text{ns}$

(pulse duration 500fs, spot size $10\mu\text{m}$, laser fluence $0.005\text{J}/\text{cm}^2$)

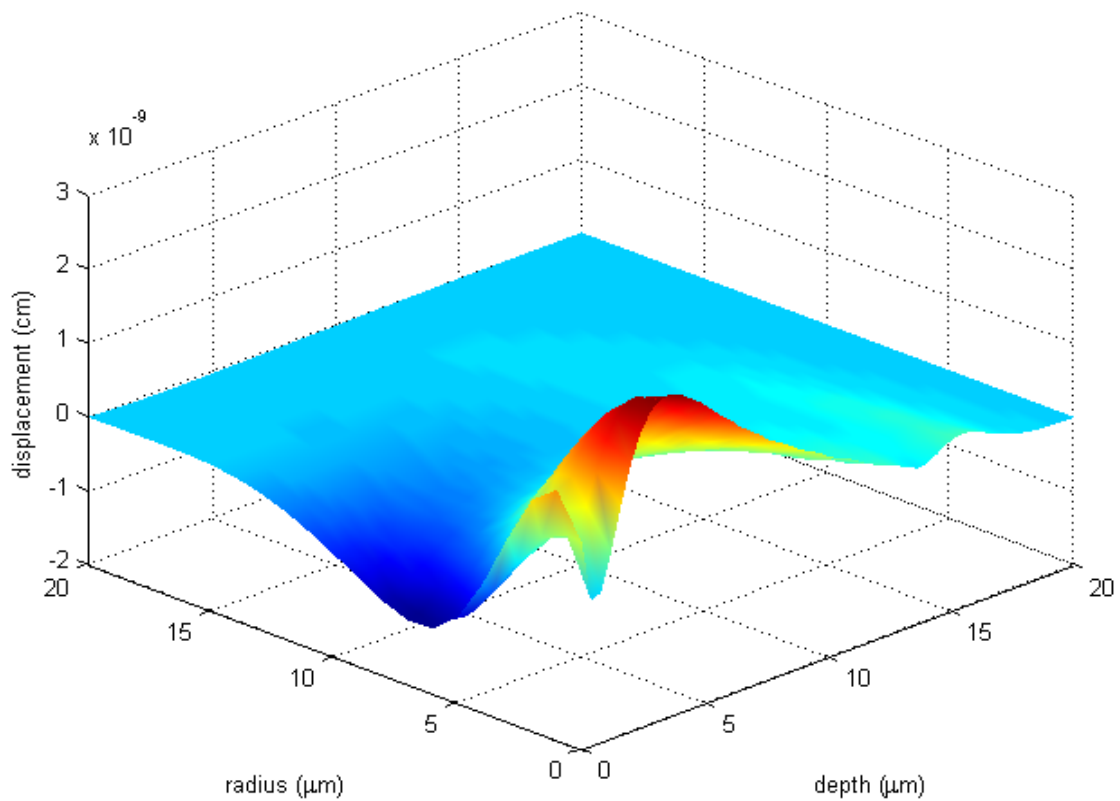


Figure 5.22 w displacement profile at $t = 10\text{ns}$ for higher laser fluence
(pulse duration 500fs, spot size $10\mu\text{m}$, laser fluence $0.015\text{J}/\text{cm}^2$)

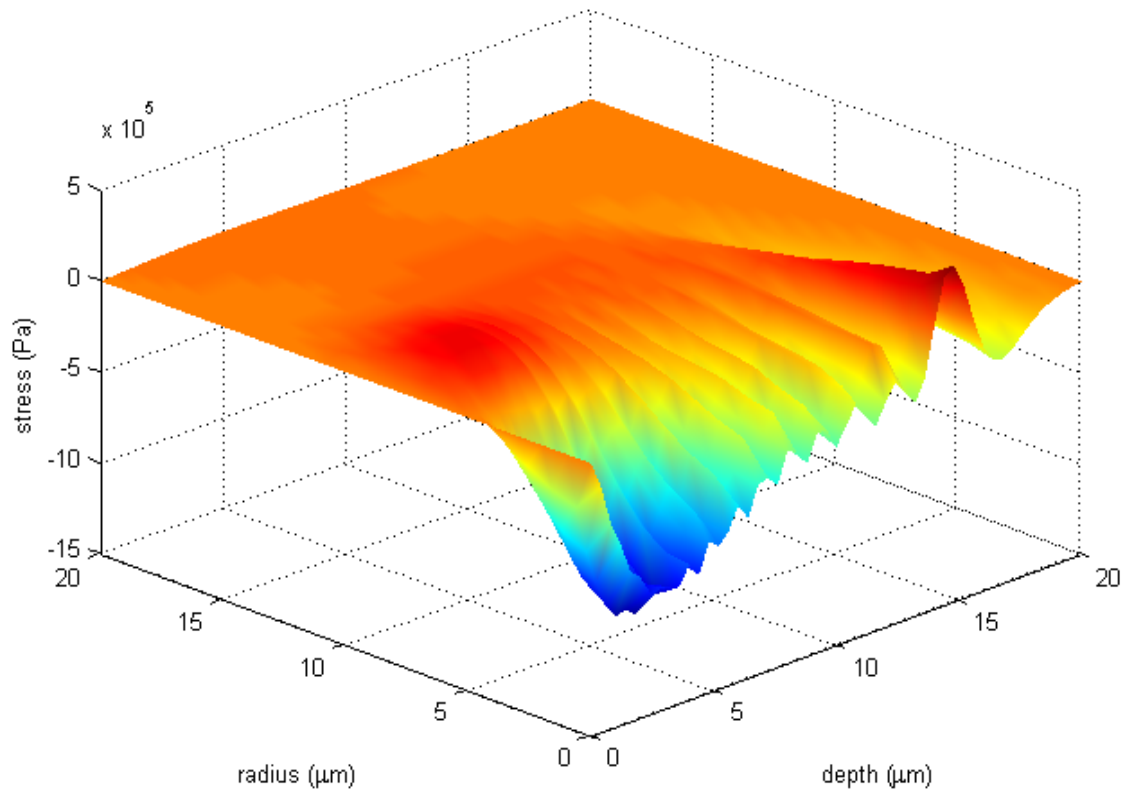


Figure 5.23 σ_{zz} stress profile at $t = 10\text{ns}$ for higher laser fluence
(pulse duration 500fs, spot size $10\mu\text{m}$, laser fluence $0.015\text{J}/\text{cm}^2$)

5.5 Summary

The femtosecond laser pulse heating formulations presented in the chapter coupled transport dynamics and classical thermoelasticity with the momentum equations in describing lattice motions in silicon material. The computational scheme developed for modeling laser-induced mechanical responses was shown to describe the evolutions of electron-lattice temperatures and electron-hole carrier density as a localized transport phenomenon both in time and space. It also allowed responses including transverse stress waves and precursors to the initiation of waveguide modes to be modeled and investigated in a window as wide as 10ns in time span.

Results presented in this chapter indicated that the path and time scale with which electrons and lattices reached thermal equilibrium varied with the laser fluence input. In addition, it was found feasible to explore the evolution of carrier density in time and determine if a given fluence and pulse duration input would induce non-thermal damages. The time scale associated with the generation of transverse stress waves along the thickness direction was on the order of nanoseconds; while it was sub-picoseconds for electron-lattice interaction and microseconds for plate wave propagation. These ultrashort laser pulse induced waves were found to be highly dispersive and characteristically of broadband, low amplitude, and extremely high frequency and power density contents. Near-field responses preceding the development of a full-blown plate wave were also found to be localized in space with a power density magnitude on the order of $10^{13} \sim 10^{14} \text{W/m}^3$.

CHAPTER VI
GENERALIZED THERMO-ELASTODYNAMICS FOR SILICON MATERIALS
SUBJECTED TO ULTRAFAST LASER HEATING

6.1 Generalized Thermoelasticity

The classical theory of thermoelasticity views heat propagation in a heat-conducting elastic body as a diffusion phenomenon dictated by a parabolic heat transport equation. As thermal disturbances diffuse with infinite speed, the corresponding thermoelastic responses therefore are to be observed instantaneously anywhere in the entire model domain regardless of how far it is from where the heat source is applied. Although it works well for problems where the duration of thermal shock is as short as $1\mu\text{s}$ [43], the classical thermoelastic theory presents a paradox nonetheless. Such a physical dilemma presents negative implications in the characterization and interpretation of near-field, sub-picoseconds responses induced by ultrafast laser pulses.

The generalized theory of thermoelasticity proposed by Green and Lindsay [72] is one based on a generalized entropy production inequality [73]. The model incorporates hyperbolic energy transport equations and was found to be satisfactory in describing laser heating problems of short pulses and high thermal gradient input. The theory retains the classical form of the entropy flux and entropy source even though it is founded on very different assumptions including two relaxation time constants that completely redefine the fundamental physics of thermoelastic process. For homogeneous isotropic materials and in the absence of body force, the theory is

constituted by four coupled partial differential equations, namely, one energy equation and three equations of motion [62]

$$\rho c_v t_2 \ddot{\theta}_l + \rho c_v \dot{\theta}_l + (3\lambda + 2\mu)\alpha' T_0 \nabla \dot{\mathbf{U}} = \kappa_l \nabla^2 \theta_l \quad (6-1)$$

$$\mu \nabla^2 \mathbf{U} + (\lambda + \mu) \nabla \nabla \cdot \mathbf{U} - (3\lambda + 2\mu)\alpha' (\nabla \theta_l + t_1 \nabla \dot{\theta}_l) = \rho \ddot{\mathbf{U}} \quad (6-2)$$

where $\theta_l = T_l - T_0$ is the field of thermal difference, t_1 and t_2 are the thermal-mechanical and thermal relaxation time constants, respectively. It is seen that the Green-Lindsay model is characterized by a system of partial differential equations in which, in comparison to the classical system, the constitutive relations for the stress tensor and the entropy are generalized by introducing two different relaxation times into considerations [74].

6.2 Lattice Energy Balance Equation and Equations of Motion

According to Eq. (6-1), for homogenous isotropic materials such as the micron-scale silicon thin structure considered for the study, the energy balance equation for lattices is therefore of the form

$$C_l t_2 \frac{\partial^2 \theta_l}{\partial t^2} + C_l \frac{\partial \theta_l}{\partial t} = \nabla \cdot (\kappa_l \nabla \theta_l) + \frac{C_{e-h}}{\tau_e} (T_e - T_l) - (3\lambda + 2\mu)\alpha' T_0 \dot{\epsilon}_{kk} \quad (6-3)$$

where $\theta_l = T_l - T_0$ is the temperature increment between lattice temperature and ambient temperature. The other parameters are defined following the classical model in Eq. (5-3). The last term on the right hand side is due to the energy transferred into the lattices. This amount of energy induces steep thermal gradient, which then in turn initiates

propagating thermal stress waves. Eq. (6-3) can be cast into the cylindrical coordinates as

$$\begin{aligned}
C_l t_2 \frac{\partial^2 \theta_l}{\partial t^2} + C_l \frac{\partial \theta_l}{\partial t} &= \frac{1}{r} \kappa_l \frac{\partial \theta_l}{\partial r} + \left(\frac{\partial \theta_l}{\partial r} \right)^2 \frac{\partial \kappa_l}{\partial \theta_l} \\
&+ \kappa_l \frac{\partial^2 \theta_l}{\partial r^2} + \left(\frac{\partial \theta_l}{\partial z} \right)^2 \frac{\partial \kappa_l}{\partial \theta_l} + \kappa_l \frac{\partial^2 \theta_l}{\partial z^2} \\
&+ \frac{C_{e-h}}{\tau_e} (T_e - T_l) - (3\lambda + 2\mu) \alpha' T_0 \dot{\varepsilon}_{kk}
\end{aligned} \tag{6-4}$$

The corresponding equations of motion expressed in the cylindrical coordinates are

$$\rho \ddot{u} = \sigma_{rr,r} + \sigma_{rz,z} + \frac{\sigma_{rr} - \sigma_{\theta\theta}}{r} \tag{6-5}$$

$$\rho \ddot{w} = \sigma_{rz,r} + \sigma_{zz,z} + \frac{\sigma_{rz}}{r} \tag{6-6}$$

where u and w are the displacement variables in the r - and z -directions, respectively. Following Eqs. (6-2), (6-5) and (6-6), the three normal stresses, σ_{ii} ($i = r, z, \theta$), and the shear stress, σ_{rz} , are defined as

$$\sigma_{ii} = 2\mu \varepsilon_{ii} + \lambda \varepsilon_{kk} - (3\lambda + 2\mu) \alpha' (\theta_l + t_1 \frac{\partial \theta_l}{\partial t}) \quad (i = r, z, \theta) \tag{6-7}$$

$$\sigma_{rz} = 2\mu \varepsilon_{rz} \tag{6-8}$$

As the lattice temperature induced by ultrafast laser pulses of the order of subpico- or femto-seconds is effectively low in magnitude, and provided that material phase transition temperature is not violated, silicon wafer can be assumed to undergo elastic deformation only at low ambient temperature. The corresponding strain-displacement relations in the cylindrical coordinates are the same as Eqs. (5-10)-(5-13).

The governing equations for describing generalized thermo-elastodynamics of silicon materials in response to ultrafast laser heating include the macroscopic electrical current equation (Eq. 4-37), macroscopic energy current equation (Eq. 4-52), balance equation of carrier number (Eq. 4-56), balance equation of carrier energy (Eq. 4-60), balance equation of lattice energy (Eq. 6-4) and equations of motion (Eqs. 6-5 and 6-8).

6.3 Computational Model

The geometric model and finite difference scheme with staggered-grids presented in Chapter V are again considered in the generalized thermo-elastodynamic model for numerical solutions. For specifics regarding the derivation and arrangement of the staggered scheme along with the modified velocity-Verlet algorithm adopted for time-integrating various responses, Chapter V is referred. Using the arrangement defined and assuming a time step, temperatures, stresses and velocities are calculated by applying the forward difference scheme. The thermal-mechanical relaxation time t_1 and thermal relaxation time t_2 are defined in Table 6.1 [42]. The remaining parameters have the same values as Tables 5.1 and 5.2.

Table 6.1 Relaxation times [42]

Parameter	Value
t_1	2.8×10^{-13} (sec)
t_2	2.8×10^{-14} (sec)

The numerical model subsequent to the reaching of the thermal equilibrium of electrons and lattice can be discretized into the following finite difference equations:

$$\theta_l(i, p, j) = T_l(i, p, j) - T_0 \quad (6-9)$$

$$\dot{\theta}_l(i, p, j) = \frac{\theta_l(i, p, j) - \theta_l(i, p, j-1)}{\Delta t} \quad (6-10)$$

$$\begin{aligned} \sigma_{rr}(i, p, j+1) = \sigma_{rr}(i, p, j) + \Delta t [& 2\mu \frac{\dot{u}(i, p + \frac{1}{2}, j) - \dot{u}(i, p - \frac{1}{2}, j)}{\Delta r} \\ & + \lambda \dot{\varepsilon}_{kk}(i, p, j) - (3\lambda + 2\mu)\alpha'(\dot{\theta}_l(i, p, j) \\ & + t_1 \frac{\dot{\theta}_l(i, p, j) - \dot{\theta}_l(i, p, j-1)}{\Delta t})] \end{aligned} \quad (6-11)$$

$$\begin{aligned}
\sigma_{\theta\theta}(i, p, j+1) = & \sigma_{\theta\theta}(i, p, j) + \Delta t \left[2\mu \frac{1}{r} \frac{\dot{u}(i, p + \frac{1}{2}, j) + \dot{u}(i, p - \frac{1}{2}, j)}{2} \right. \\
& + \lambda \dot{\varepsilon}_{kk}(i, p, j) - (3\lambda + 2\mu) \alpha'(\dot{\theta}_l(i, p, j) \\
& \left. + t_1 \frac{\dot{\theta}_l(i, p, j) - \dot{\theta}_l(i, p, j-1)}{\Delta t}) \right]
\end{aligned} \tag{6-12}$$

$$\begin{aligned}
\sigma_{zz}(i, p, j+1) = & \sigma_{zz}(i, p, j) + \Delta t \left[2\mu \frac{\dot{w}(i + \frac{1}{2}, p, j) - \dot{w}(i - \frac{1}{2}, p, j)}{\Delta z} \right. \\
& + \lambda \dot{\varepsilon}_{kk}(i, p, j) - (3\lambda + 2\mu) \alpha'(\dot{\theta}_l(i, p, j) \\
& \left. + t_1 \frac{\dot{\theta}_l(i, p, j) - \dot{\theta}_l(i, p, j-1)}{\Delta t}) \right]
\end{aligned} \tag{6-13}$$

$$\begin{aligned}
\sigma_{rz}(i + \frac{1}{2}, p + \frac{1}{2}, j+1) = & \sigma_{rz}(i + \frac{1}{2}, p + \frac{1}{2}, j) \\
& + \Delta t \mu \left[\frac{\dot{w}(i + \frac{1}{2}, p+1, j) - \dot{w}(i - \frac{1}{2}, p, j)}{\Delta r} \right. \\
& \left. + \frac{\dot{u}(i+1, p + \frac{1}{2}, j) - \dot{u}(i, p + \frac{1}{2}, j)}{\Delta z} \right]
\end{aligned} \tag{6-14}$$

$$\begin{aligned}
\dot{u}(i, p + \frac{1}{2}, j+1) = & \dot{u}(i, p + \frac{1}{2}, j) + \frac{\Delta t}{\rho} \left[\frac{\sigma_{rr}(i, p+1, j) - \sigma_{rr}(i, p, j)}{\Delta r} \right. \\
& + \frac{\sigma_{rz}(i + \frac{1}{2}, p + \frac{1}{2}, j) - \sigma_{rz}(i - \frac{1}{2}, p + \frac{1}{2}, j)}{\Delta z} \\
& + \left(\frac{\sigma_{rr}(i, p, j) + \sigma_{rr}(i, p+1, j)}{2} \right. \\
& \left. - \frac{\sigma_{\theta\theta}(i, p, j) + \sigma_{\theta\theta}(i, p+1, j)}{2} \right) \frac{1}{r} \left. \right]
\end{aligned} \tag{6-15}$$

$$\begin{aligned}
\dot{w}(i+\frac{1}{2}, p, j+1) &= \dot{w}(i+\frac{1}{2}, p, j) \\
&+ \frac{\Delta t}{\rho} \left[\frac{\sigma_{rz}(i+\frac{1}{2}, p+\frac{1}{2}, j) - \sigma_{rz}(i+\frac{1}{2}, p-\frac{1}{2}, j)}{\Delta r} \right. \\
&+ \frac{\sigma_{zz}(i+1, p, j) - \sigma_{zz}(i, p, j)}{\Delta z} \\
&\left. + \frac{\sigma_{rz}(i+\frac{1}{2}, p-\frac{1}{2}, j) + \sigma_{rz}(i+\frac{1}{2}, p+\frac{1}{2}, j)}{2} \frac{1}{r} \right]
\end{aligned} \tag{6-16}$$

$$\begin{aligned}
\dot{\varepsilon}_{kk}(i, p, j) &= \dot{\varepsilon}_{rr}(i, p, j) + \dot{\varepsilon}_{zz}(i, p, j) + \dot{\varepsilon}_{\theta\theta}(i, p, j) \\
&= \frac{\dot{u}(i, p+\frac{1}{2}, j) - \dot{u}(i, p-\frac{1}{2}, j)}{\Delta r} \\
&+ \frac{\dot{w}(i+\frac{1}{2}, p, j) - \dot{w}(i-\frac{1}{2}, p, j)}{\Delta z} \\
&+ \frac{1}{r} \frac{\dot{u}(i, p+\frac{1}{2}, j) + \dot{u}(i, p-\frac{1}{2}, j)}{2}
\end{aligned} \tag{6-17}$$

$$\begin{aligned}
\ddot{\theta}_l(i, p, j) = & \left\{ \frac{1}{C_l(i, p, j)} \left[\frac{\kappa_l(i, p, j)}{r} \frac{\frac{\partial \theta_l(i, p + \frac{1}{2}, j) + \frac{\partial \theta_l(i, p - \frac{1}{2}, j)}{\partial r}}{2}}{2} \right. \right. \\
& + \left(\frac{\frac{\partial \theta_l(i, p + \frac{1}{2}, j) + \frac{\partial \theta_l(i, p - \frac{1}{2}, j)}{\partial r}}{2} \right)^2 \frac{\partial \kappa_l(i, p, j)}{\partial \theta_l} \\
& + \kappa_l(i, p, j) \frac{\frac{\partial \theta_l(i, p + \frac{1}{2}, j) - \frac{\partial \theta_l(i, p - \frac{1}{2}, j)}{\partial r}}{\Delta r}}{\Delta r} \\
& + \left(\frac{\frac{\partial \theta_l(i + \frac{1}{2}, p, j) + \frac{\partial \theta_l(i - \frac{1}{2}, p, j)}{\partial z}}{2} \right)^2 \frac{\partial \kappa_l(i, p, j)}{\partial \theta_l} \\
& + \kappa_l(i, p, j) \frac{\frac{\partial \theta_l(i + \frac{1}{2}, p, j) - \frac{\partial \theta_l(i - \frac{1}{2}, p, j)}{\partial z}}{\Delta z}}{\Delta z} \\
& \left. \left. - (3\lambda + 2\mu)\alpha' T_0(i, p, j) \dot{\epsilon}_{kk}(i, p, j) \right] - \dot{\theta}_l(i, p, j) \right\} \frac{1}{t_2} \quad (6-18)
\end{aligned}$$

$$\dot{\theta}_l(i, p, j+1) = \dot{\theta}_l(i, p, j) + \Delta t \ddot{\theta}_l(i, p, j) \quad (6-19)$$

$$\theta_l(i, p, j+1) = \theta_l(i, p, j) + \Delta t \dot{\theta}_l(i, p, j+1) \quad (6-20)$$

$$\frac{\partial \theta_l}{\partial r}(i, p + \frac{1}{2}, j) = \frac{\theta_l(i, p+1, j) - \theta_l(i, p, j)}{\Delta r} \quad (6-21)$$

$$\frac{\partial \theta_l}{\partial z}(i + \frac{1}{2}, p, j) = \frac{\theta_l(i+1, p, j) - \theta_l(i, p, j)}{\Delta z} \quad (6-22)$$

It should be noted that the initial conditions and boundary conditions applied in this model are the same as those specified in Chapter V. A time step of 5fsec is applied, and the selected time step has to be lower than the thermal relaxation time t_2 of the silicon in order to resolve thermal waves properly.

6.4 Results

6.4.1 Carrier Density and Model Validation

Figure 6.1 shows the time evolution of the carrier density n at the center of the top surface at $z = r = 0$ corresponding to four different laser fluences; namely, 0.005, 0.015, 0.15 and 0.20 J/cm². It is seen that the peak of the carrier density occurs after the laser reaches its maximum intensity at $t = 1.5$ ps for a particular fluence. As the carrier density is governed by the carrier generation term and the recombination term in Eq. (5-19), the recombination process becomes more and more dominant after the maximum laser intensity is reached. By comparing the carrier density curves corresponding to different laser fluences, one can observe that the maximum value rises faster and is met earlier with increasing laser fluence. There is a critical carrier density value, $2.74 \times 10^{21} \text{cm}^{-3}$ (indicated by the horizontal line in Figure 6.1) for the silicon material [41] above which non-thermal melting would immediately ensue and damage in the form of immediate crystal disordering or ultimate material removal through ablation is imminent. For instance, the figure shows that the peak carrier density values is below the non-thermal melting threshold for the three lower fluences (0.005, 0.015 and 0.15J/cm²), thus there is no damage inflicted to the silicon wafer by using these laser

energy input. However, when irradiated by the 500fs laser with $0.2\text{J}/\text{cm}^2$ fluence, the material will undergo non-thermal melting process since the maximum carrier density exceeds the threshold at a certain time instance. Further calculation confirms that carrier density levels off rapidly into the thickness direction, thus the material damage inflicted by the ultrafast laser pulse is highly localized and confined to an extremely small volume beneath the irradiated surface. It is therefore probable to follow the distribution of carrier density in both time and space to subsequently identify the regions experiencing thermal melting in silicon wafer when processed by ultrafast laser pulses.

Figure 6.2 compares the computed melting thresholds with the experimental data available in [75]. The results are determined by first selecting specific pulse durations and then followed by establishing their corresponding laser fluence level at which the maximum carrier density at $z = 0$ exceeds the critical threshold level. It is found that the computational results agree well with the physical data, thus validating the modeling formulations along with the numerical procedures. Another observation with Figure 6.2 is that the discrete results roughly divide this fluence-duration plane into two parts shown as the shaded and un-shaded regions. For certain pulse duration, the silicon wafer will more or less be damaged if the laser fluence lands within the shaded region. The farther the fluence stays within the boundary of the un-shaded region, the safer the material is subject to the pulsing of the ultrafast laser.

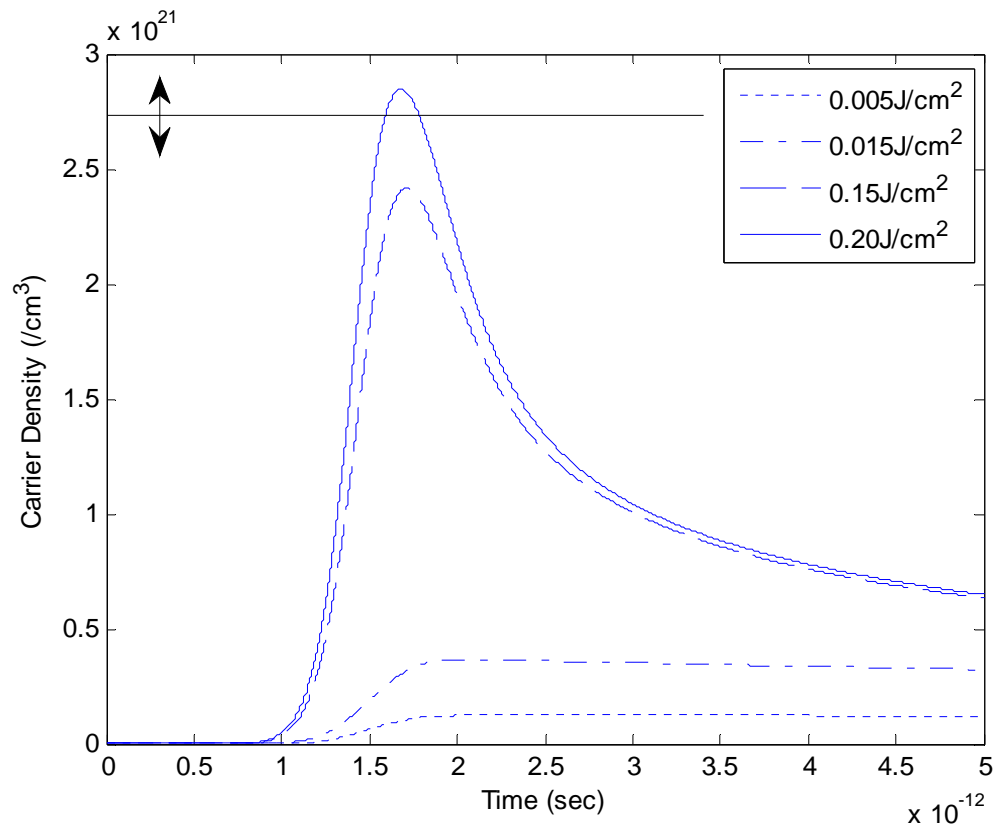


Figure 6.1 Time evolution of carrier density subject to four laser fluences
(laser pulse duration 500fs, spot size $10\mu\text{m}$)

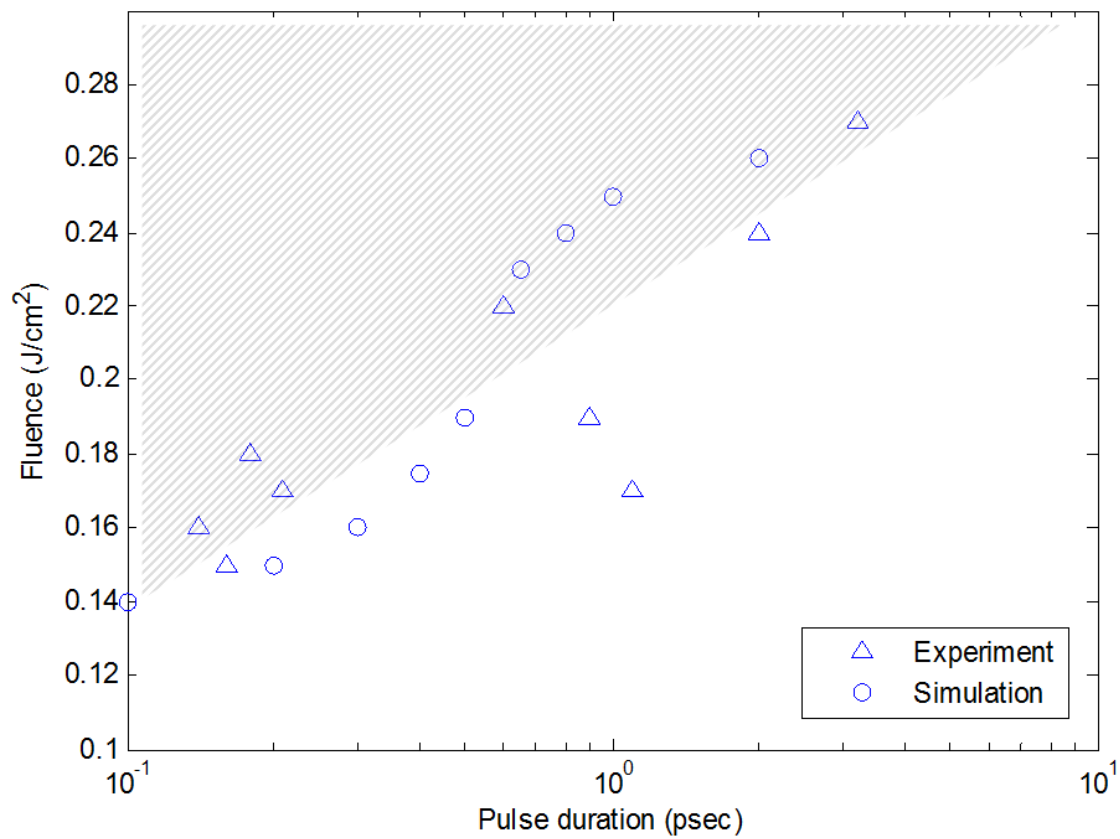


Figure 6.2 Comparison of computed non-thermal melting thresholds with experimental data

6.4.2 Lattice Temperature and Heat Flux

Figure 6.3 shows the spatial distribution of $\theta_l = T_l - T_0$ at $t = 10\text{ns}$, which is the variation of the lattice temperature, T_l , with respect to the ambient temperature, T_0 . The generalized thermo-elastodynamic formulation incorporating θ_l is explicated in Eqs. (6-1)-(6-4). The θ_l wave is seen within the 10ns time window to have propagated $10\mu\text{m}$ in the thickness (z-) direction and over $15\mu\text{m}$ in the radial (r-) direction. With the remaining model domain staying thermally undisturbed, it is observed that the heat affected zone is finite and highly localized. This is in contrast to the observation made in Chapter V where the parabolic energy equations admit thermal diffusion and permit thermal disturbances to be registered instantaneously everywhere in the model domain. The generalized formulation presented in this chapter remedies such a counter-intuitive paradox by considering energy transport as thermal waves of finite propagation speed. Another observation made with the oscillating thermal wave in Figure 6.3 is that it attenuates much faster with significantly lower amplitude than its parabolic counterpart studied in the last chapter.

Figure 6.4 presents the heat flux components along the axial (q_z) and radial (q_r) directions. It is seen that the order of magnitudes of the heat flux in both directions are low at $t = 10\text{ns}$. Generally, a high level of heat flux will cause damage to the material. Apparently this is not the case with the ultrafast laser induced heat fluxes. This is one of the prominent advantages of ultrafast lasers over lasers of nanosecond pulses or longer.

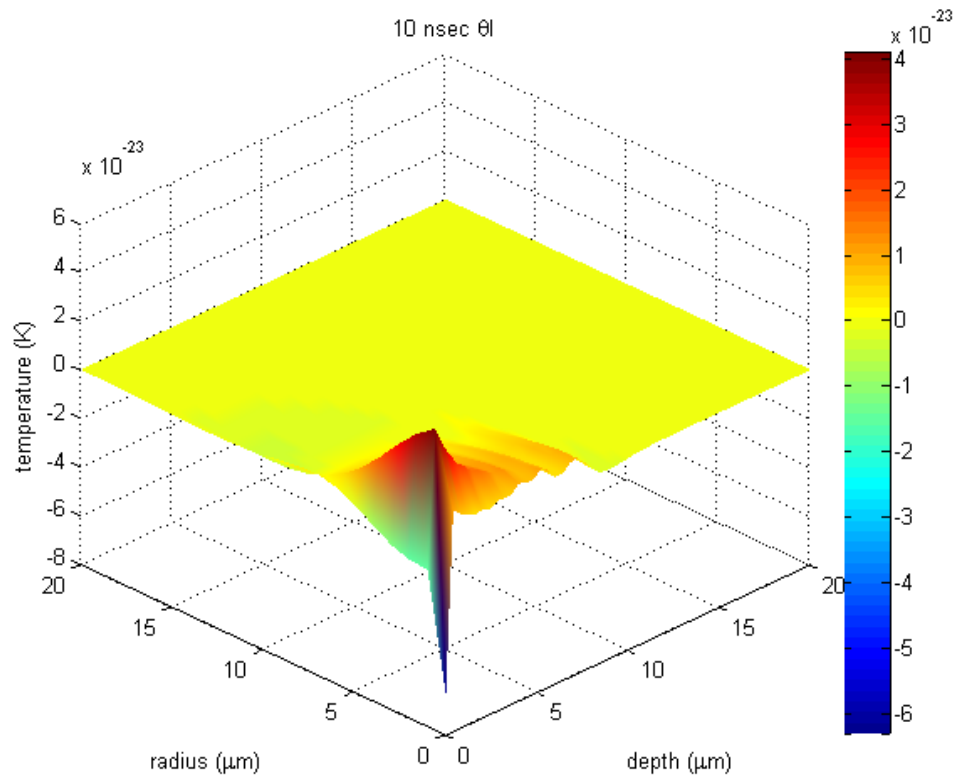


Figure 6.3 Distribution of lattice temperature oscillation θ_l at 10ns
(pulse duration 500fs, spot size $10\mu\text{m}$, laser fluence $0.005\text{J}/\text{cm}^2$)

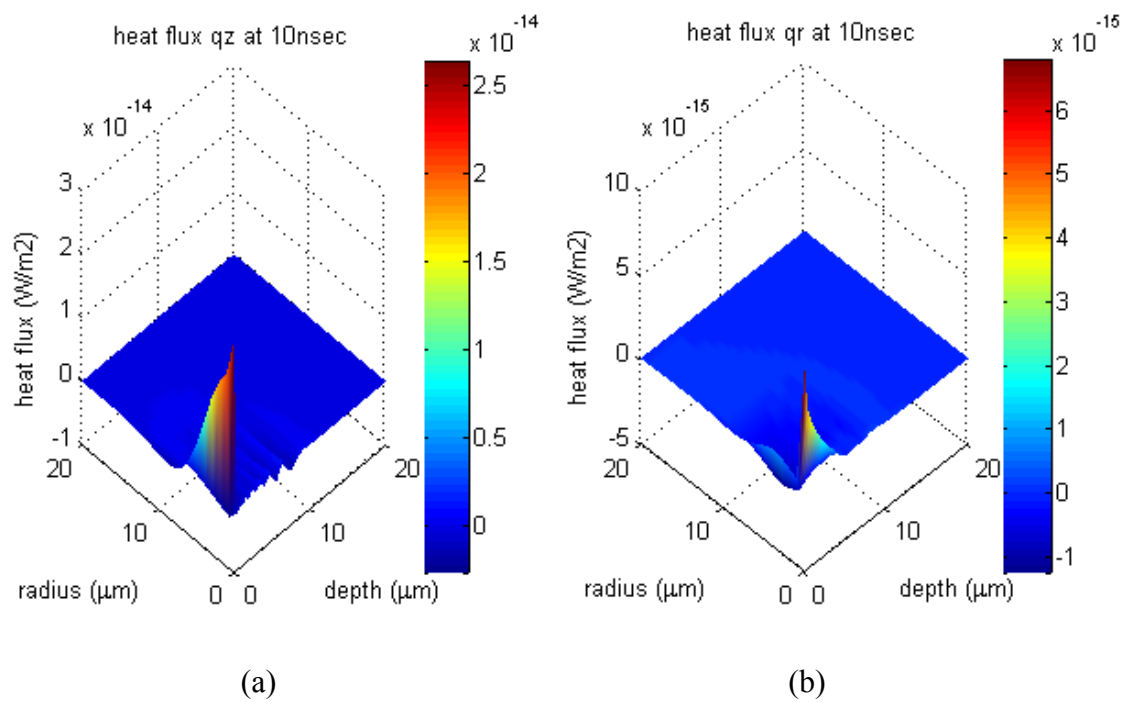


Figure 6.4 Distribution of heat flux components (a) q_z and (b) q_r , at $t = 10\text{ns}$

(pulse duration 500fs, spot size $10\mu\text{m}$, laser fluence 0.005J/cm^2)

The extremely small heat affected zone along with the small resulted heat flux is what enables precise control for laser micro-machining. Damages to silicon material by ultrafast laser pulses, if any, are therefore not the result of the induced thermal field, but rather the violation of the carrier density threshold and the exertion of the induced stress waves.

6.4.3 Displacement and Velocity Fields

Figure 6.5 shows the displacement response of the model domain impinged by the ultrafast laser pulse, where w and u are displacement variables in the z - and r -direction, respectively. It illustrates that the order of magnitude of these mechanical responses are of the order of 10^{-9} cm within 10ns, and such amplitudes increase as time elapses. The w wave covers a $5\mu\text{m}\times 10\mu\text{m}$ volume in the initial 5ns and propagates further and deeper in the next 5ns. It is clear from looking at the changing w waveforms at the two time instants that the wave is dispersive. The displacement in the other direction, u , does not have prominent oscillation features indicative of a full-blown wave. But rather all the affected nodes move toward the symmetry axis $r = 0$ in compression. This compression state is seen to progress from $t = 5\text{ns}$ to 10ns with increasing magnitudes. Compared with the displacement field obtained by the parabolic thermoelasticity (Figure 5.12) in which the infinite thermal speed is felt in both the temperature and displacement fields since the governing equations are coupled, the displacement waves affected zone associated with generalized thermoelasticity is very localized.

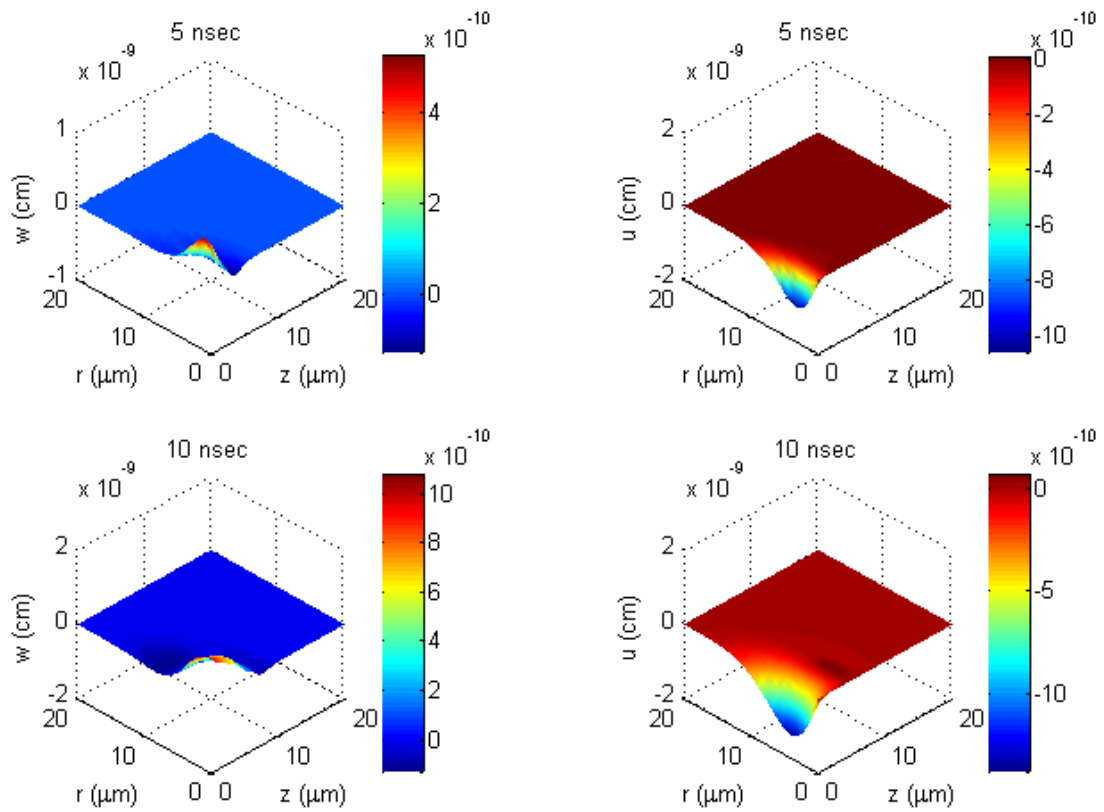


Figure 6.5 Displacement components w and u at two different times

(pulse duration 500fs, spot size $10\mu\text{m}$, laser fluence $0.005\text{J}/\text{cm}^2$)

The initial undisturbed positions of the grid nodes of the axisymmetric model at $t = 0$ (blue circles) is laid over their corresponding positions at $t = 10\text{ns}$ (red circles) in Figure 6.6 to help visualize laser-induced deformations. Resultant displacement is calculated for each node using its w and u displacement components. It should be noted that as the induced motion is highly localized in space, only displacement responses within the disk bound by $z \leq 10\mu\text{m}$ and $r \leq 15\mu\text{m}$ are considered, and the resultant displacements shown in the figure are magnified by a factor of 5×10^4 for clarity. Compared with Figure 5.13 in which the nodal motion is plotted according to the parabolic type energy equation, the nodal motion in Figure 6.6 shows the same tendency as being plucked towards the positive z -direction, and all other nodes are rubber-banded together and move accordingly. However, it is obvious that the nodes in the last column ($z=10\mu\text{m}$) is not affected by the ultrafast laser induced displacement at 10ns , which is different from the last column in Figure 5.13. The unrealistic infinite disturbance speed governed by the parabolic type energy equation indeed has a great impact on thermal-mechanical coupled field.

The developed velocity components, \dot{w} and \dot{u} , are shown in Figure 6.7. Given the relatively non-oscillating displacements in Figure 6.5, nodal velocities are seen to progress in the z -direction with high-frequency oscillations. As energy transport in the form of nodal kinetics is indicated by the spatial gradients of the velocity, it is seen that the transport of mechanical energy is both finite and localized. The remaining model domain stays undisturbed by the velocity field.

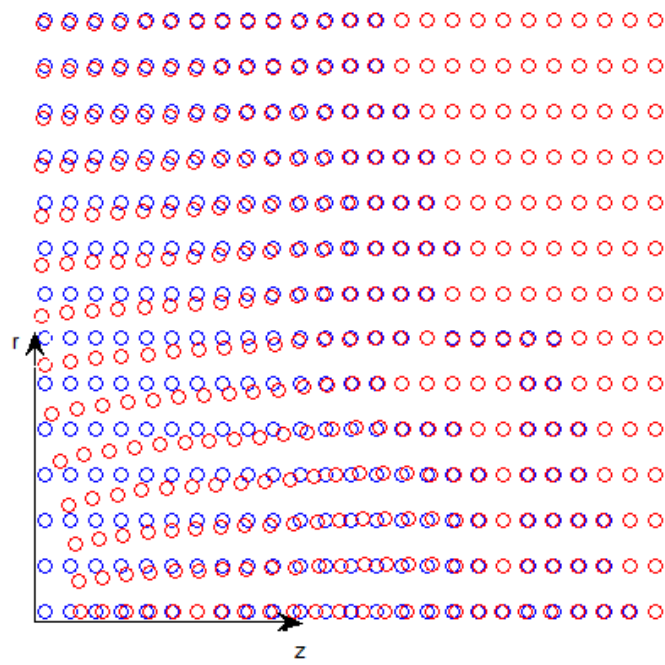


Figure 6.6 Laser induced nodal motions at 10ns
(pulse duration 500fs, spot size 10 μ m, laser fluence 0.005J/cm²)

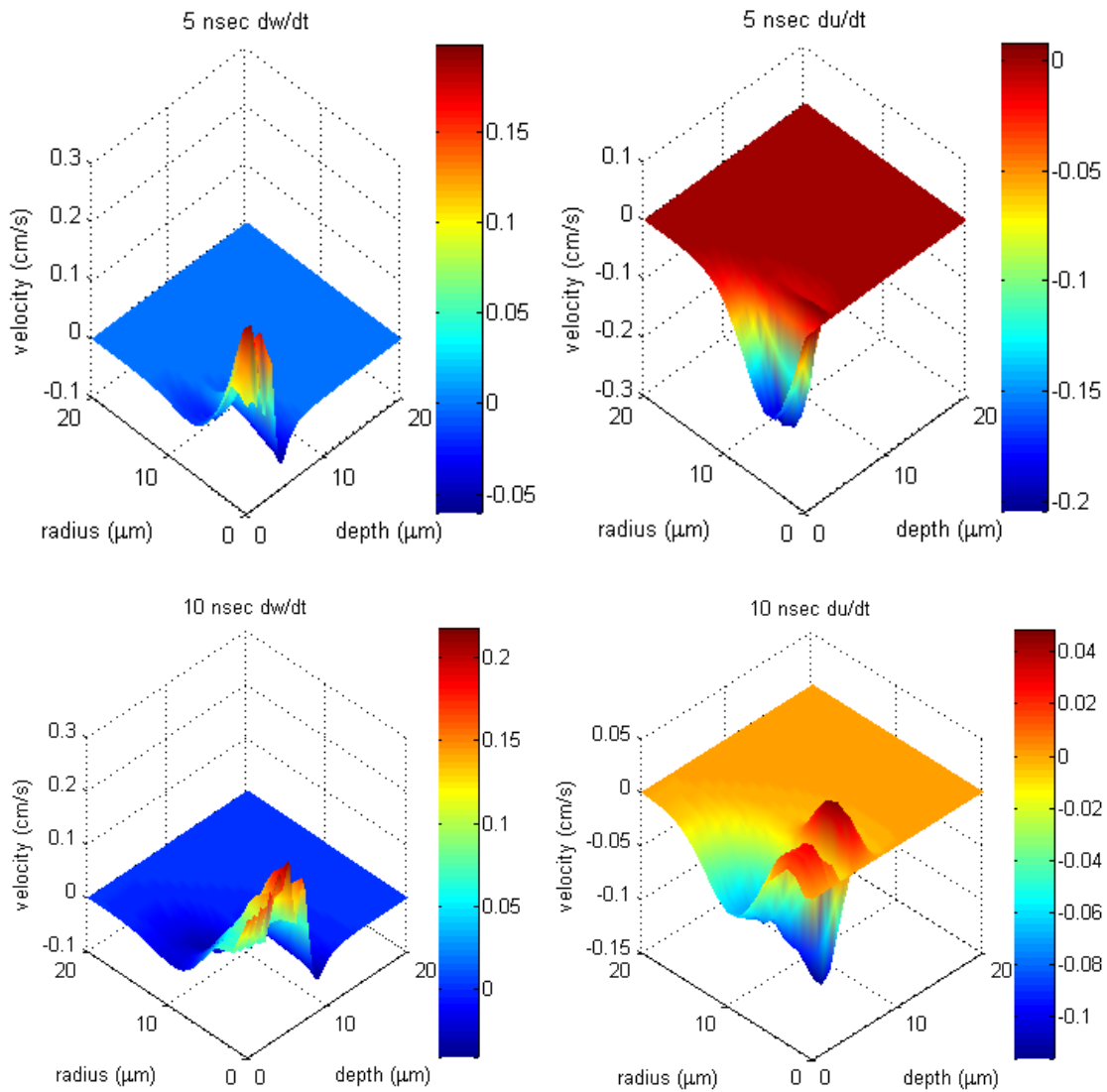


Figure 6.7 Profiles of velocity components at two different times (pulse duration 500fs, spot size $10\mu\text{m}$, laser fluence $0.005\text{J}/\text{cm}^2$)

6.4.4 Thermal Stress Waves

The distributions of the three normal stress components (σ_{zz} , σ_{rr} and $\sigma_{\theta\theta}$) along with the one shear stress component (σ_{rz}) at $t = 5\text{ns}$ and 10ns are shown in Figure 6.8. The σ_{zz} and σ_{rz} components are in contrast to the other two in that they exhibit definitive features typical of a propagating wave, i.e. σ_{zz} primarily propagates in the z -direction, and the shear stress propagates in both directions. On the other hand, the σ_{rr} and $\sigma_{\theta\theta}$ components are seen to be more localized and preceding the developing of a full-fledged wave in their respective direction. The magnitudes of all the stress components are of the order of several MPa or less within the time window considered, and increase slightly as time elapses from $t = 5\text{ns}$ to $t = 10\text{ns}$. By resolving the induced thermal stress waves σ_{zz} and σ_{rz} in the simultaneous time-frequency domain using the Gabor Wavelet Transform (GWT), it becomes clear that they are highly dispersive and characteristically of broadband, low amplitude and extremely high frequency. Compare with the corresponding stress waves described by the parabolic transport equations in Figure 5.15, the stress waves depicted in Figure 6.8 are more localized in both time and space, and also of higher oscillation amplitude.

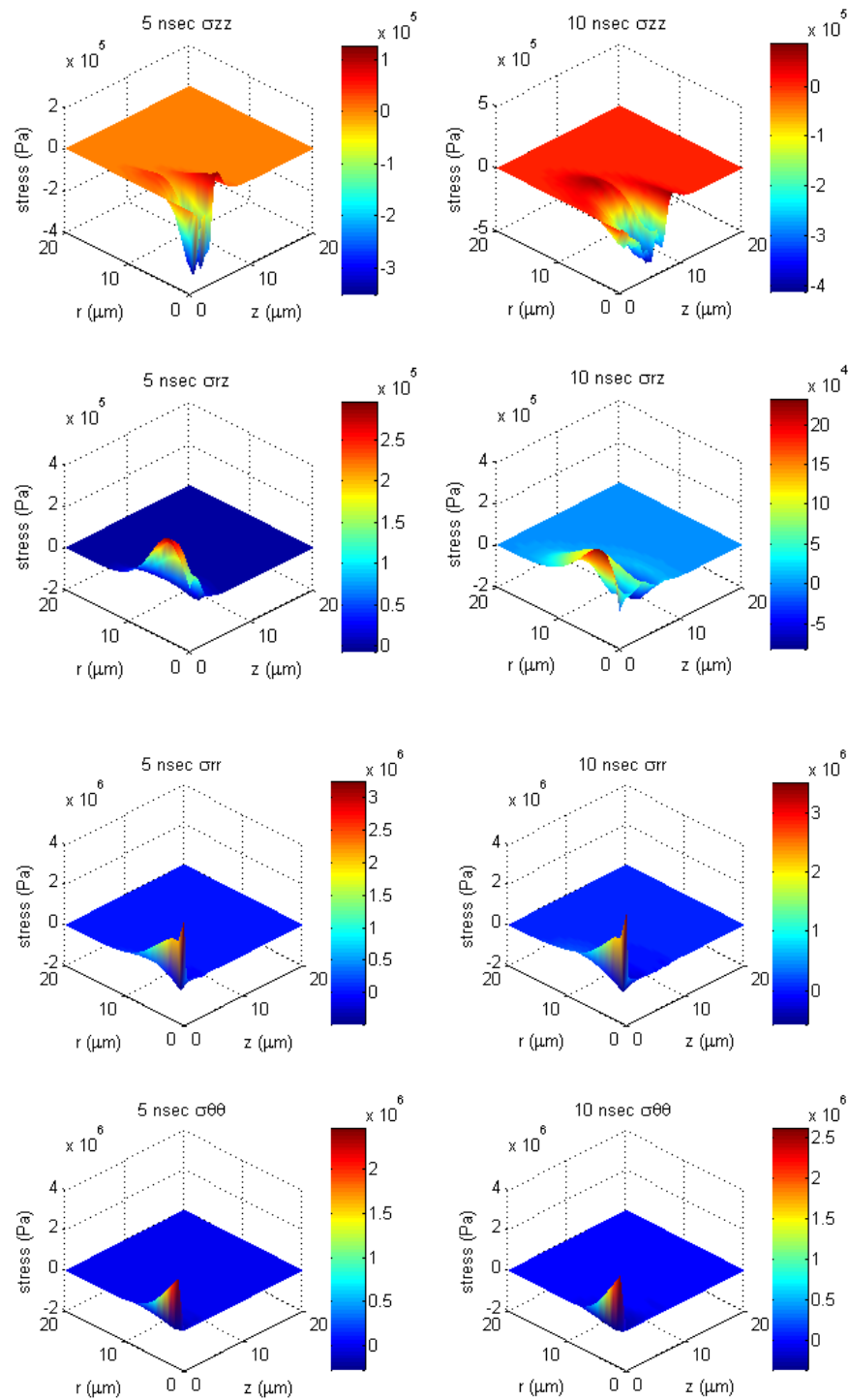


Figure 6.8 Distributions of stress component at 10ns
(pulse duration 500fs, spot size $10\mu\text{m}$, laser fluence $0.005\text{J}/\text{cm}^2$)

6.5 Damage Evaluation

As previously mentioned, non-thermal melting threshold is determined mainly by pulse duration and laser fluence. Non-thermal damage is generally in the form of immediate crystal disordering or ablation. However, as ultrafast lasers also generate short-time scale shock waves, micro-cracking is another potential damage mode that could compromise fabrication quality. In this section, the concept of power density is employed along with high cycle fatigue and joint time-frequency analysis to qualitatively evaluate the likelihood for laser induced short-time wave motions to inflict the particular damage mode.

6.5.1 Power Density

As presented in Chapter V, the temporal gradient of an oscillating stress, dS/dt , has an equivalent unit that can be obtained through using the SI notations as $[N/m^2s] \equiv [W/m^3]$. Here S represents a stress component, which could be σ_{zz} , σ_{rr} , $\sigma_{\theta\theta}$ or σ_{rz} in the study. Figure 6.9 plots the power densities associated with all stress components at $t = 10\text{ns}$. In spite of low stress magnitudes, all the corresponding power densities are of the order of 10^{13} - 10^{14} W/m^3 , oscillate and propagate like waves both radially and axially. Of the components plotted, the power density of the σ_{zz} wave has the largest oscillation magnitude, thus indicating a higher probability for the stress wave to initiate micro-cracking. Consequently, the σ_{zz} power density wave is selected to be investigated further below.

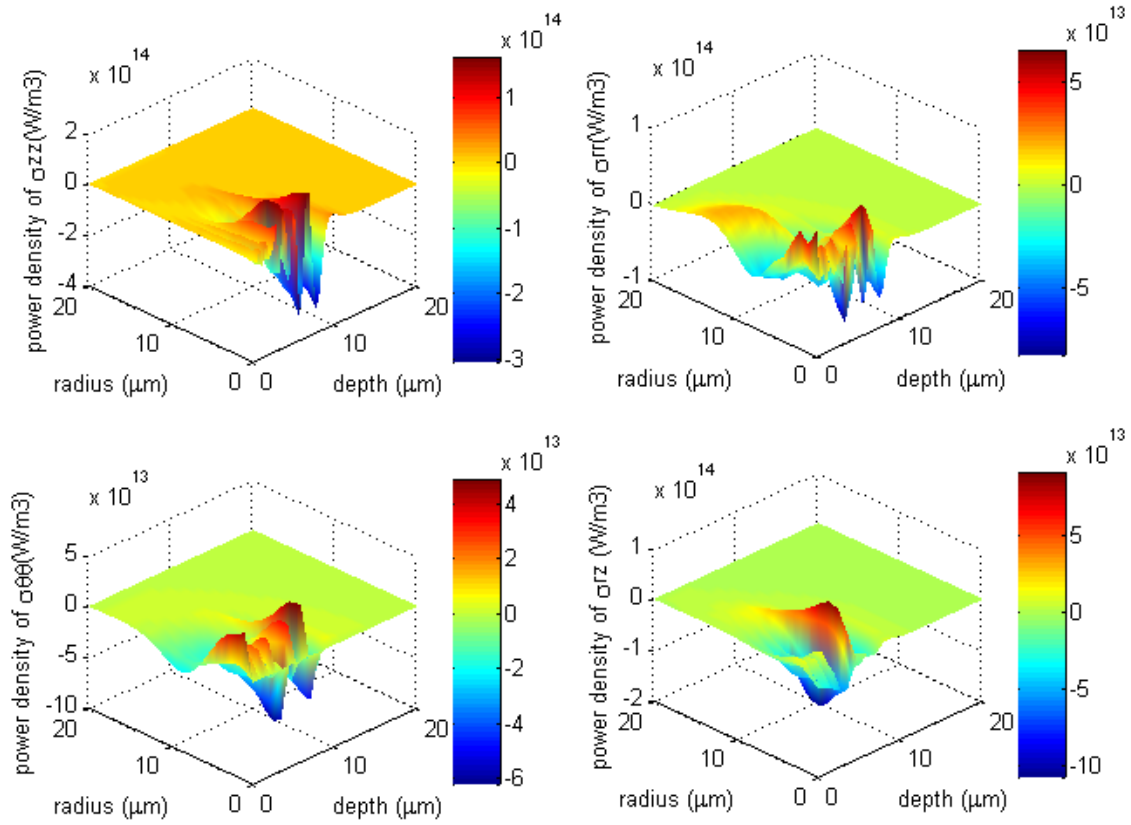


Figure 6.9 Distributions of power density components at 10ns
(pulse duration 500fs, spot size 10μm, laser fluence 0.005J/cm²)

6.5.2 Accumulated Damage Evaluation

The notion of power density in conjunction with the algorithm of accumulated damage evaluation has been applied as a viable methodology to successfully correlate high-frequency dispersive stress waves with the development of mechanical faults and defects in microelectronic packages [46, 47]. The methodology is applicable to investigating dynamic phenomena of brief presence that involve low loading stress but high loading frequency (thus high power density). It allows one to qualitatively evaluate the impact of power density waves on material reliability using the accumulated damage evaluation algorithm. In this section the evaluation algorithm is followed to determine if fatigue cracking is likely in response to the action of power density wave within the 10ns time window.

S-N curves are important tools for design against fatigue failure, with S being the reversed stress and N being the number of cycles to fatigue failure under S. There are low cycle failure and high cycle failure from which materials could be loaded to fail. In low cycle fatigue, a very high loading stress is usually applied that generates not only elastic strains but also plastic strains. The number of cycles to failure N is usually less than 10^3 . However, for the high cycle fatigue mode, much higher number of cycles ($N > 10^5$) is expected since the stress level is low enough to only produce elastic strains. As seen in Figure 6.9 that the oscillating stress waves are of relatively small amplitude, broad bandwidth and extremely high frequency, there is a concern over such waves initiating high cycle fatigue cracking in the silicon material.

To relate the ultrafast laser induced power density waves to fatigue cycles, the high cycle S-N curve for single crystalline silicon materials available in [70] is utilized. It should be noted that the silicon specimens considered in [70] did not follow the standard ASTM specifications or were subject to the standard fatigue test procedure. Ref. [70] should be consulted for specifics as to how the S-N curve was compiled. The fatigue life cycles of the single crystalline silicon specimens of 20 μ m in thickness are reported to be ranging from 10^6 to 10^{11} over a range of loading stresses between 4 and 10GPa. The S-N curve can be approximated using:

$$S = (13.4 - 0.875 \log N_f) 10^9 \text{ Pa} \quad (6-23)$$

where N_f is the number of cycles to fatigue failure under the $f = 40$ kHz loading frequency. The corresponding power density as a function of the fatigue life N_f can then be expressed as

$$\frac{dS}{dt} = 4(10^4)(13.4 - 0.875 \log N_f) 10^9 \text{ W/m}^3 \quad (6-24)$$

Thus the following equation can be used to estimate how many cycles to failure are expected under a certain power density:

$$N_f = 10^{[15.31 - 2.857(10^{-14}) \frac{dS}{dt}]} \quad (6-25)$$

Next is to determine how many cycles have been accumulated with respect to the total fatigue life N_f within the 10ns time window. To predict how much damage has been accumulated at a particular location of the silicon thin structure due to the cyclic power density waves, 8 sampling locations in the axisymmetric finite difference model

are selected to study their corresponding accumulated damage. The coordinates of the 8 locations are $(z, r) = (0.4\mu\text{m}, 0\mu\text{m}), (4.8\mu\text{m}, 0\mu\text{m}), (9.6\mu\text{m}, 0\mu\text{m}), (14.4\mu\text{m}, 0\mu\text{m}), (0.4\mu\text{m}, 1\mu\text{m}), (4.8\mu\text{m}, 1\mu\text{m}), (9.6\mu\text{m}, 1\mu\text{m})$ and $(14.4\mu\text{m}, 1\mu\text{m})$, as numbered in Figure 6.10.

To estimate the accumulated damage due to the exertion of the power density waves, it is necessary to examine the time evolution of the power density at every sampling location. Figure 6.11 shows the power density time history acquired at the 8 selected locations. The order of magnitudes of the power density at locations 1 and 5 are much higher in the first 5ns. Located closest to the top face, the power density waves corresponding to locations 1 and 5 are also fast-attenuating. Furthermore, one sees that the power density at location 5, which is $1\mu\text{m}$ away from the center line of the laser beam, displays lower oscillation amplitude. With its relatively larger power density magnitude, location 1 is most susceptible to accumulated damage. Should location 1 be determined to be damage-free, the material could then be considered intact subject to the rapid heating of short laser pulses.

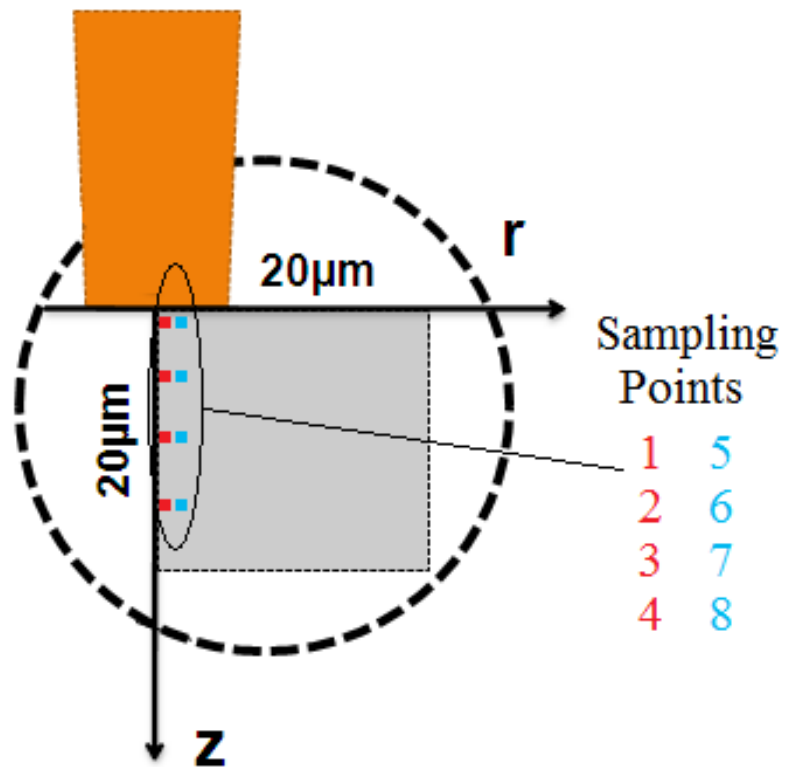


Figure 6.10 Sampling locations from which power density waves are acquired

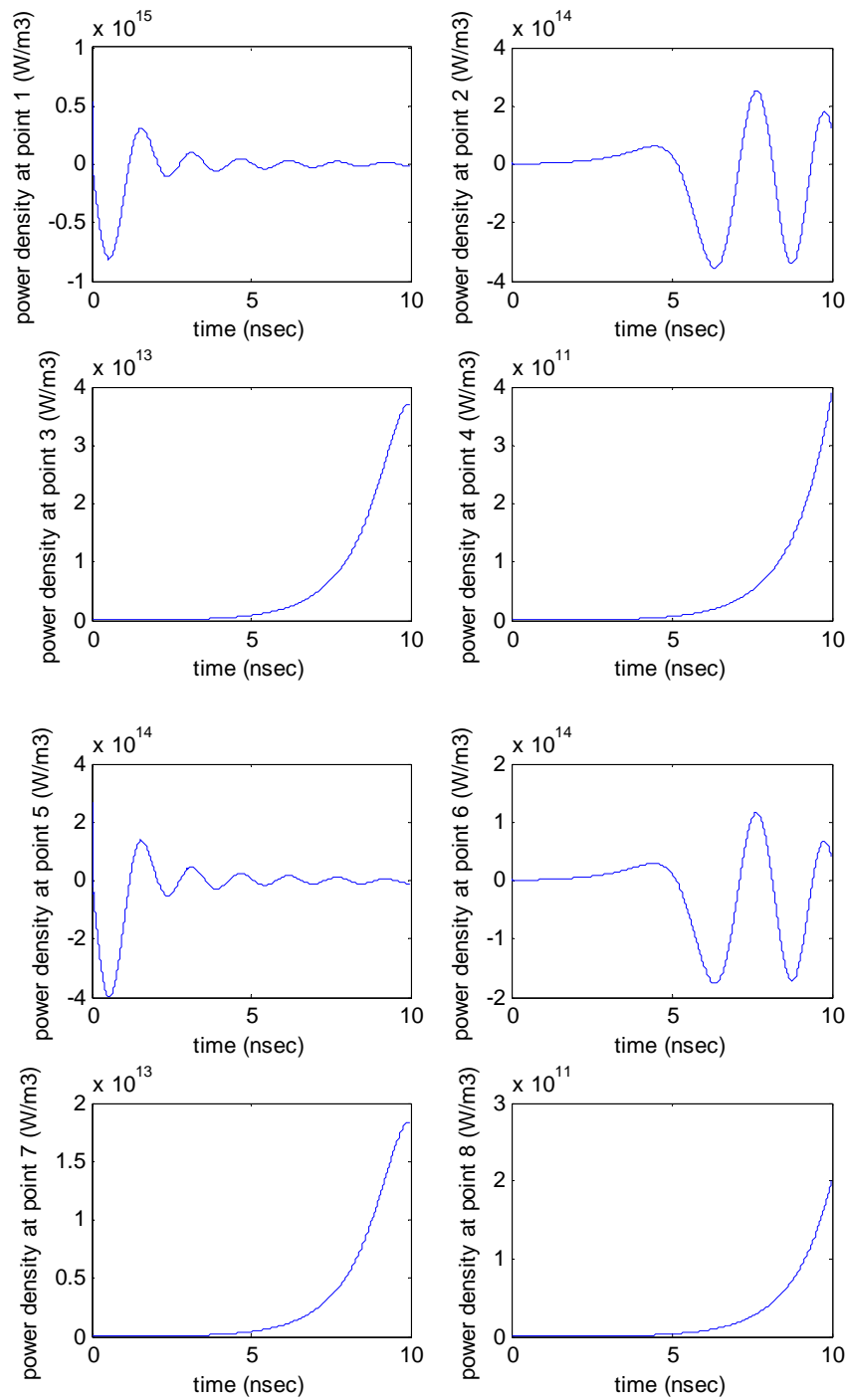
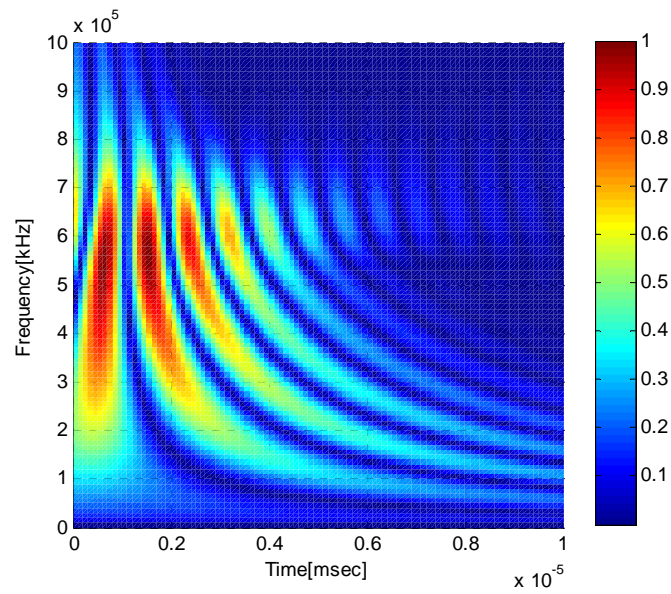


Figure 6.11 Time histories of power density at 8 sampling locations
(pulse duration 500fs, spot size 10 μ m, laser fluence 0.005J/cm²)

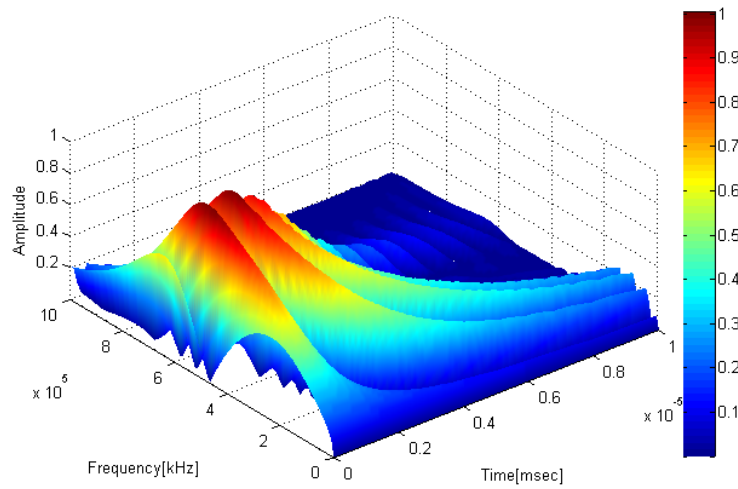
Figure 6.12 exhibits the time-frequency distribution of the power density wave acquired at location 1. It shows that the frequency ranges from 0 to 1GHz which is extremely broadband within the first 5ns. Also, the dominant frequencies constantly vary with time, thus indicating a characteristic dispersive wave. The normalized amplitude in the time-frequency plot indicates the dominant frequency components. For example, the 500-600MHz frequencies have higher magnitude than all other components in the first 2ns, thus this range of frequencies dominates. This can be better visualized by the accompanying 3D plot. By selecting a particular time instant, one can obtain a corresponding frequency spectrum along with its associated dominant frequencies.

The next step is to determine the number of cycles corresponding to each dominant frequency component. Since power density wave is dispersive with broad, time-varying spectra, the number of loading cycles exerted by each constituent frequency within any given time span therefore also vary with time. At any given time $t = t_0$, it is straightforward to first read off the corresponding power density $(dS/dt)_{t=t_0}$ from Figure 6.11 and then extract the corresponding frequency spectrum by slicing the time-frequency plane in Figure 6.12 at $t = t_0$. Using the sliced-off spectrum, one can obtain the amplitude A_i corresponding to a particular frequency harmonics, F_i . Accordingly, the relation between the power density at $t = t_0$ and frequency components can be expressed as

$$\left(\frac{dS}{dt}\right)_{t=t_0} = A \sum_i A_i \cos(F_i \Delta t) \quad (6-26)$$



(a)



(b)

Figure 6.12 Time-frequency distribution of power density wave acquired at location 1

(a) 2D view (b) 3D view

(pulse duration 500fs, spot size 10 μ m, laser fluence 0.005J/cm²)

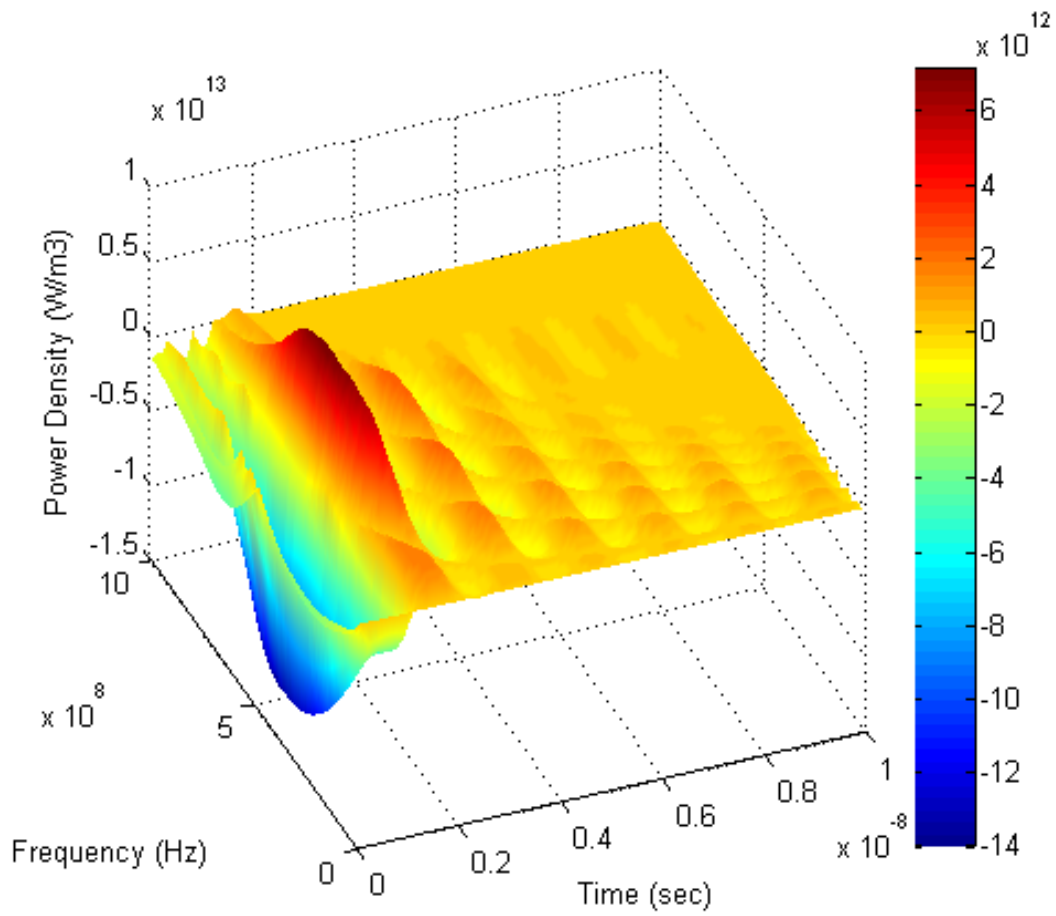


Figure 6.13 Power density vs. time-frequency at sampling location 1
(pulse duration 500fs, spot size 10 μ m, laser fluence 0.005J/cm²)

In Eq. (6-26) Δt is the time interval between t_0 and the subsequent time instant of interest, and A is a coefficient whose value can be uniquely determined. Each term on the right hand side of Eq. (6-26), $AA_i \cos(F_i \Delta t)$, computes the contribution of power density made by frequency F_i to the total power density at $t = t_0$. Apply similar calculations to all time instants of interest, the power density can be plotted as a function of frequency components and time, as shown in Figure 6.13 which corresponds to location 1. It should be noted that integrating Figure 6.12 along the frequency axis would faithfully restore the power density time history associated with location 1 as found in Figure 6.11.

Using Figure 6.13 and substituting the power density $(dS/dt)_{i,j}$ calculated at each time t_j and frequency F_i into Eq. (6-25), the total number of cycles until fatigue failure $(N_f)_{i,j}$ can be determined. Meanwhile, the number of cycles each frequency undergone $N_{i,j}$ within the time interval Δt can be determined through the following relation

$$N_{i,j} = \Delta t F_i \quad (6-27)$$

For example, the Δt selected for this study is 0.1ns, thus the 500MHz component completes 0.05 cycles within this Δt . The estimated accumulated damage in the time interval between $t = t_j$ and $t = t_{j+1}$ for frequency F_i is determined as $N_{i,j} / (N_f)_{i,j}$. For instance, as the $(N_f)_{i,j}$ calculated for the 500MHz component between $t = 1.9\text{ns}$ and $t = 2.0\text{ns}$ is 1.5×10^{15} , the accumulated damage for the frequency in this time interval is therefore $0.05 / (1.5 \times 10^{15}) = 3.3 \times 10^{-17}$. Consequently, the total accumulated damage in the 10ns time interval/window for all frequencies can be expressed as

$$T.A.D. = \sum_j \sum_i \frac{N_{i,j}}{(N_f)_{i,j}} \quad (6-28)$$

When $T.A.D. \geq 1$ (i.e. exceeding 100% probability), an ultimate fatigue failure would occur. Therefore, using the notion of “accumulated damage by fatigue cycle” that relates power density waves with fatigue failure, one can estimate how much damage has been accumulated at a particular location over a specific time period. The algorithm provides a qualitative estimate for locations that could probabilistically initiate micro-cracking. In this investigation, the total accumulated damage in the silicon within the first 10ns subject to the ultrafast laser irradiation is $T.A.D. = 2.6 \times 10^{-13}$ as shown in Figure 6.14. Given the fact that the power density wave at location 1 is both dispersive and fast-attenuating, the increasing of $T.A.D.$ in time beyond 10ns is expected to be slow and negligible. As the laser fluence considered in this study ($0.005\text{J}/\text{cm}^2$) is extremely low for a 500fs laser, the total accumulated damage is thus significantly below the critical threshold at which micro-cracking could be initiated. In summary, this fluence level can neither induce non-thermal melting (Figure 6.2 shows that the non-thermal melting threshold for a 500fs laser is $0.19\text{J}/\text{cm}^2$) nor initiate micron flaws.

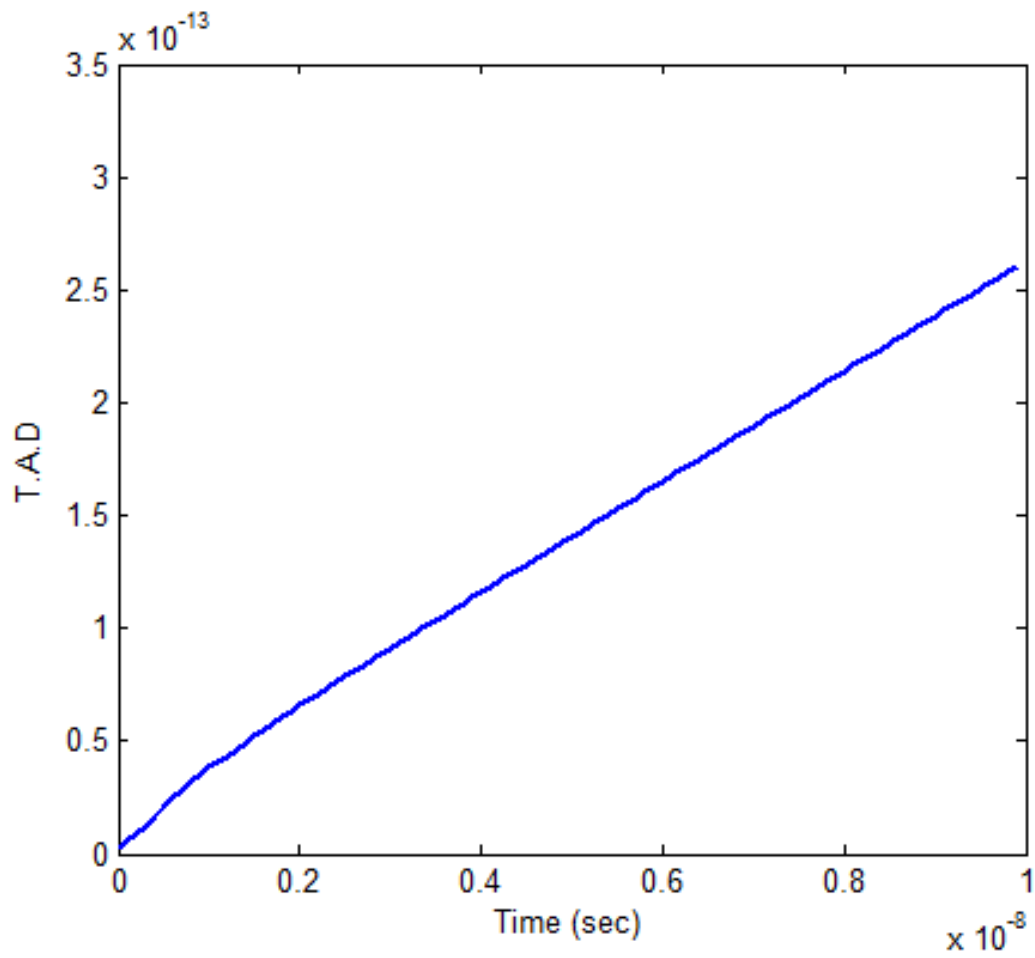


Figure 6.14 Total accumulated damage at sampling location 1 within 10ns
(pulse duration 500fs, spot size 10 μ m, laser fluence 0.005J/cm²)

6.6 Summary

The generalized ultra-short laser pulse heating formulations coupled transport dynamics and hyperbolic-type energy transport equations along with the momentum equations in describing thermo-elastodynamic response in silicon thin structure. By introducing the thermal-mechanical relaxation time and thermal relaxation time to the heat equations, the model formulation imparted a finite nature to the propagation of thermal disturbance. The computational scheme developed for modeling laser-induced mechanical responses was shown to produce carrier density and non-thermal melting threshold that were in excellent agreement with real-world data.

Near-field responses and wave dispersion described by the presented model formulation were found to be characteristically different from those investigated in Chapter V where parabolic governing equations were considered for the same laser input parameters. Results presented in this chapter indicated the thermal and mechanical waves propagate with finite speed. These ultrashort laser pulse induced waves were highly dispersive and characteristically of broadband, low magnitude, and extremely high frequency. Near-field responses preceding the development of stress waves were also found to be localized in space with a power density magnitude on the order of 10^{14} W/m³. The algorithm of accumulated damage evaluation was applied to qualitatively estimate the potential for the induced stress waves to initiate fatigue cracking. It was shown that the high power density waves generated by the 500fs ultrafast laser of 0.005J/cm² in fluence and 10 μ m in spot size were insufficient to inflict non-thermal damage or mechanical flaws.

CHAPTER VII

**GENERALIZED THERMO-ELASTO-VISCO-PLASTODYNAMICS FOR
SILICON MATERIALS SUBJECTED TO ULTRAFAST LASER HEATING**

In Chapters V and VI, the parabolic and generalized thermo-elastodynamics for silicon material subject to the irradiation of femtosecond lasers were considered for elastic deformations only. The reasons that the silicon was not considered for elasto-visco-plastodynamical responses was that the lattice temperature induced by the ultrafast laser pulses of the order of subpico- or femto-seconds was too low in magnitude to allow for material phase transition. Additionally the 300K ambient temperature modeled in Chapters IV and V was low enough to only induce elastic deformations. However, as ambient temperature increases, the silicon wafer will no longer behave elastically, but rather elasto-viscoplastically. In order to study the feasibility of employing femtosecond laser in LISWT, the thermo-elasto-visco-plastodynamic behaviors of the silicon wafer at elevated temperature need be investigated. This chapter aims at combining the constitutive law described by the Haasen-Sumino model in Chapter II with the generalized model of Chapters IV and VI to establish the knowledge base needed for modeling femtosecond laser induced thermo-elasto-visco-plastodynamics in silicon wafer.

7.1 Lattice Energy Balance Equation and Equations of Motion

The balance equation of lattice energy and equations of motion derived in the section follow from Eqs. (6-1) and (6-2) in which a generalized thermoelasticity was formulated by Green and Lindsay. The lattice energy balance equation retains the same form as Eq. (6-4) in the cylindrical coordinates

$$\begin{aligned}
 C_l t_2 \frac{\partial^2 \theta_l}{\partial t^2} + C_l \frac{\partial \theta_l}{\partial t} &= \frac{1}{r} \kappa_l \frac{\partial \theta_l}{\partial r} + \left(\frac{\partial \theta_l}{\partial r} \right)^2 \frac{\partial \kappa_l}{\partial \theta_l} \\
 &+ \kappa_l \frac{\partial^2 \theta_l}{\partial r^2} + \left(\frac{\partial \theta_l}{\partial z} \right)^2 \frac{\partial \kappa_l}{\partial \theta_l} + \kappa_l \frac{\partial^2 \theta_l}{\partial z^2} \\
 &+ \frac{C_{e-h}}{\tau_e} (T_e - T_l) - (3\lambda + 2\mu) \alpha' T_0 \dot{\epsilon}_{kk}
 \end{aligned} \tag{7-1}$$

According to the constitutive law described in Chapter II, the total strain rate of a body undergoing elasto-plastic deformation can be defined as the summation of the elastic strain rate and the plastic strain rate as

$$\dot{\epsilon}_{ij} = \dot{\epsilon}_{ij}^{(e)} + \dot{\epsilon}_{ij}^{(p)} \tag{7-2}$$

with u and w being the total displacement variables, including both the elastic and plastic displacements, in the r - and z -directions, respectively. The total strain rate $\dot{\epsilon}_{ij}$

can be expressed alternatively using the followings in the cylindrical coordinates

$$\dot{\epsilon}_{rr} = \frac{\partial \dot{u}}{\partial r} \tag{7-3}$$

$$\dot{\epsilon}_{zz} = \frac{\partial \dot{w}}{\partial z} \tag{7-4}$$

$$\dot{\epsilon}_{\theta\theta} = \frac{\dot{u}}{r} \tag{7-5}$$

$$\dot{\epsilon}_{rz} = \frac{1}{2} \left(\frac{\partial \dot{u}}{\partial z} + \frac{\partial \dot{w}}{\partial r} \right) \quad (7-6)$$

The plastic strain rate in Eq. (7-2) can be expressed the same as Eq. (2-3),

$$\dot{\epsilon}_{ij}^{(p)} = f S_{ij} \quad (7-7)$$

where S_{ij} is the deviatoric stress tensor. The dislocation density related coefficient f are defined in Eqs. (2-4)-(2-6).

The corresponding equations of motion in the r- and z-directions expressed in the cylindrical coordinates are

$$\rho \ddot{u} = \sigma_{rr,r} + \sigma_{rz,z} + \frac{\sigma_{rr} - \sigma_{\theta\theta}}{r} \quad (7-8)$$

$$\rho \ddot{w} = \sigma_{rz,r} + \sigma_{zz,z} + \frac{\sigma_{rz}}{r} \quad (7-9)$$

Substituting Eq. (7-2) into the Hooke's law with $[C]$ being the stiffness matrix, we have

$$[\dot{\sigma}_{ij}] = [C][\dot{\epsilon}_{ij} - \dot{\epsilon}_{ij}^{(p)}] \quad (7-10)$$

Following Eqs. (6-2), and (7-3)-(7-10), one can obtain the rates of three normal stress components, $\dot{\sigma}_{ii}$ ($i = r, z, \theta$), and the shear stress component, $\dot{\sigma}_{rz}$, as

$$\begin{aligned} \dot{\sigma}_{ii} = & 2\mu(\dot{\epsilon}_{ii} - fS_{ii}) + \lambda(\dot{\epsilon}_{kk} - fS_{kk}) \\ & - (3\lambda + 2\mu)\alpha'(\dot{\theta}_l + t_1\ddot{\theta}_l) \quad (i = r, z, \theta) \end{aligned} \quad (7-11)$$

$$\dot{\sigma}_{rz} = 2\mu(\dot{\epsilon}_{rz} - fS_{rz}) \quad (7-12)$$

Therefore, the governing equations for describing generalized thermo-elasto-viscoplastodynamics in silicon material include macroscopic electrical current equation (Eq.

4-37), macroscopic energy current equation (Eq. 4-52), balance equation of carrier number (Eq. 4-56), balance equation of carrier energy (Eq. 4-60), balance equation of lattice energy (Eq. 7-1) and equations of motion (Eqs. 7-8, 7-9, 7-11 and 7-12).

7.2 Computational Model

The computational model still utilizes the axisymmetric model and the staggered-grid finite difference scheme presented in Chapter V for solving the generalized thermo-elasto-viscoplastic model numerically. For specifics regarding the derivation and arrangement of the staggered scheme, Chapter V is again referred. Parameter values used in the model are provided in Tables 1.1, 5.1, 5.2 and 6.1. The initial and boundary conditions specified for the model are the same as those used in Chapter V except that the ambient temperature T_0 is no longer constant at 300K, but rather ranging from 300K to 1100K as needed. The initial value of the dislocation density is set at $N_m = 2 \times 10^4$ (/cm²) [48] (See Eq. 2-4).

The numerical model subsequent to the reaching of the thermal equilibrium of electrons and lattice can be discretized into the following finite difference equations:

$$N_m(i, p, j) = N_m(i, p, j-1) + \Delta t K V_0 N_m(i, p, j-1) (\sqrt{J_2} - D \sqrt{N_m(i, p, j-1)})^{p+\xi} \quad (7-13)$$

$$f(i, p, j) = \frac{bV_0 N_m(i, p, j)(\sqrt{J_2} - D\sqrt{N_m(i, p, j)} - \tau_d)^p}{\sqrt{J_2}} \quad (7-14)$$

$$\theta_l(i, p, j) = T_l(i, p, j) - T_0 \quad (7-15)$$

$$\dot{\theta}_l(i, p, j) = \frac{\theta_l(i, p, j) - \theta_l(i, p, j-1)}{\Delta t} \quad (7-16)$$

$$\begin{aligned} \sigma_{rr}(i, p, j+1) = & \sigma_{rr}(i, p, j) \\ & + \Delta t [2\mu \left(\frac{\dot{u}(i, p + \frac{1}{2}, j) - \dot{u}(i, p - \frac{1}{2}, j)}{\Delta r} \right. \\ & - f(i, p, j)S_{rr}(i, p, j)) \\ & + \lambda(\dot{\varepsilon}_{kk}(i, p, j) - f(i, p, j)S_{kk}(i, p, j)) \\ & - (3\lambda + 2\mu)\alpha'(\dot{\theta}_l(i, p, j) \\ & \left. + t_1 \frac{\dot{\theta}_l(i, p, j) - \dot{\theta}_l(i, p, j-1)}{\Delta t} \right)] \end{aligned} \quad (7-17)$$

$$\begin{aligned} \sigma_{\theta\theta}(i, p, j+1) = & \sigma_{\theta\theta}(i, p, j) \\ & + \Delta t [2\mu \left(\frac{1}{r} \frac{\dot{u}(i, p + \frac{1}{2}, j) + \dot{u}(i, p - \frac{1}{2}, j)}{2} \right. \\ & - f(i, p, j)S_{\theta\theta}(i, p, j)) \\ & + \lambda(\dot{\varepsilon}_{kk}(i, p, j) - f(i, p, j)S_{kk}(i, p, j)) \\ & - (3\lambda + 2\mu)\alpha'(\dot{\theta}_l(i, p, j) \\ & \left. + t_1 \frac{\dot{\theta}_l(i, p, j) - \dot{\theta}_l(i, p, j-1)}{\Delta t} \right)] \end{aligned} \quad (7-18)$$

$$\begin{aligned}
\sigma_{zz}(i, p, j+1) = & \sigma_{zz}(i, p, j) \\
& + \Delta t [2\mu \left(\frac{\dot{w}(i+\frac{1}{2}, p, j) - \dot{w}(i-\frac{1}{2}, p, j)}{\Delta z} \right. \\
& - f(i, p, j) S_{zz}(i, p, j)) \\
& + \lambda (\dot{\epsilon}_{kk}(i, p, j) - f(i, p, j) S_{kk}(i, p, j)) \\
& - (3\lambda + 2\mu) \alpha'(\dot{\theta}_l(i, p, j)) \\
& \left. + t_1 \frac{\dot{\theta}_l(i, p, j) - \dot{\theta}_l(i, p, j-1)}{\Delta t} \right)]
\end{aligned} \tag{7-19}$$

$$\begin{aligned}
\sigma_{rz}(i+\frac{1}{2}, p+\frac{1}{2}, j+1) = & \sigma_{rz}(i+\frac{1}{2}, p+\frac{1}{2}, j) \\
& + \Delta t \mu \left[\frac{\dot{w}(i+\frac{1}{2}, p+1, j) - \dot{w}(i-\frac{1}{2}, p, j)}{\Delta r} \right. \\
& + \frac{\dot{u}(i+1, p+\frac{1}{2}, j) - \dot{u}(i, p+\frac{1}{2}, j)}{\Delta z} \\
& \left. - 2f(i, p, j) S_{rz}(i+\frac{1}{2}, p+\frac{1}{2}, j) \right]
\end{aligned} \tag{7-20}$$

$$\begin{aligned}
\dot{u}(i, p+\frac{1}{2}, j+1) = & \dot{u}(i, p+\frac{1}{2}, j) + \frac{\Delta t}{\rho} \left[\frac{\sigma_{rr}(i, p+1, j) - \sigma_{rr}(i, p, j)}{\Delta r} \right. \\
& + \frac{\sigma_{rz}(i+\frac{1}{2}, p+\frac{1}{2}, j) - \sigma_{rz}(i-\frac{1}{2}, p+\frac{1}{2}, j)}{\Delta z} \\
& + \left(\frac{\sigma_{rr}(i, p, j) + \sigma_{rr}(i, p+1, j)}{2} \right. \\
& \left. - \frac{\sigma_{\theta\theta}(i, p, j) + \sigma_{\theta\theta}(i, p+1, j)}{2} \right) \frac{1}{r} \left. \right]
\end{aligned} \tag{7-21}$$

$$\begin{aligned}
\dot{w}(i + \frac{1}{2}, p, j+1) &= \dot{w}(i + \frac{1}{2}, p, j) \\
&+ \frac{\Delta t}{\rho} \left[\frac{\sigma_{rz}(i + \frac{1}{2}, p + \frac{1}{2}, j) - \sigma_{rz}(i + \frac{1}{2}, p - \frac{1}{2}, j)}{\Delta r} \right. \\
&+ \frac{\sigma_{zz}(i+1, p, j) - \sigma_{zz}(i, p, j)}{\Delta z} \\
&\left. + \frac{\sigma_{rz}(i + \frac{1}{2}, p - \frac{1}{2}, j) + \sigma_{rz}(i + \frac{1}{2}, p + \frac{1}{2}, j)}{2} \frac{1}{r} \right]
\end{aligned} \tag{7-22}$$

$$\begin{aligned}
\dot{\epsilon}_{kk}(i, p, j) &= \dot{\epsilon}_{rr}(i, p, j) + \dot{\epsilon}_{zz}(i, p, j) + \dot{\epsilon}_{\theta\theta}(i, p, j) \\
&= \frac{\dot{u}(i, p + \frac{1}{2}, j) - \dot{u}(i, p - \frac{1}{2}, j)}{\Delta r} \\
&+ \frac{\dot{w}(i + \frac{1}{2}, p, j) - \dot{w}(i - \frac{1}{2}, p, j)}{\Delta z} \\
&+ \frac{1}{r} \left[\frac{\dot{u}(i, p + \frac{1}{2}, j) + \dot{u}(i, p - \frac{1}{2}, j)}{2} \right]
\end{aligned} \tag{7-23}$$

$$\begin{aligned}
\ddot{\theta}_l(i, p, j) = & \left\{ \frac{1}{C_l(i, p, j)} \left[\frac{\kappa_l(i, p, j)}{r} \frac{\partial \theta_l(i, p + \frac{1}{2}, j) + \partial \theta_l(i, p - \frac{1}{2}, j)}{2} \right. \right. \\
& + \left(\frac{\frac{\partial \theta_l(i, p + \frac{1}{2}, j) + \partial \theta_l(i, p - \frac{1}{2}, j)}{2}}{2} \right)^2 \frac{\partial \kappa_l(i, p, j)}{\partial \theta_l} \\
& + \kappa_l(i, p, j) \frac{\frac{\partial \theta_l(i, p + \frac{1}{2}, j) - \partial \theta_l(i, p - \frac{1}{2}, j)}{\Delta r}}{\Delta r} \\
& + \left(\frac{\frac{\partial \theta_l(i + \frac{1}{2}, p, j) + \partial \theta_l(i - \frac{1}{2}, p, j)}{2}}{2} \right)^2 \frac{\partial \kappa_l(i, p, j)}{\partial \theta_l} \\
& + \kappa_l(i, p, j) \frac{\frac{\partial \theta_l(i + \frac{1}{2}, p, j) - \partial \theta_l(i - \frac{1}{2}, p, j)}{\Delta z}}{\Delta z} \\
& \left. \left. - (3\lambda + 2\mu)\alpha' T_0(i, p, j) \dot{\epsilon}_{kk}(i, p, j) \right] - \dot{\theta}_l(i, p, j) \right\} \frac{1}{t_2} \quad (7-24)
\end{aligned}$$

$$\dot{\theta}_l(i, p, j+1) = \dot{\theta}_l(i, p, j) + \Delta t \ddot{\theta}_l(i, p, j) \quad (7-25)$$

$$\theta_l(i, p, j+1) = \theta_l(i, p, j) + \Delta t \dot{\theta}_l(i, p, j+1) \quad (7-26)$$

$$\frac{\partial \theta_l}{\partial r}(i, p + \frac{1}{2}, j) = \frac{\theta_l(i, p+1, j) - \theta_l(i, p, j)}{\Delta r} \quad (7-27)$$

$$\frac{\partial \theta_l}{\partial z}(i + \frac{1}{2}, p, j) = \frac{\theta_l(i+1, p, j) - \theta_l(i, p, j)}{\Delta z} \quad (7-28)$$

7.3 Results

7.3.1 Temperature Increment of Lattice Temperature

The increment of the lattice temperature is defined as the variation of the lattice temperature T_l with respect to the ambient temperature T_0 , i.e. $\theta_l = T_l - T_0$. The spatial distributions of the temperature increment corresponding to four different ambient temperatures, 300K, 600K, 800K and 1100K, within a 10ns time window are shown in Figure 7.1. It is seen that the thermal disturbance travels in the form of a wave with finite speed. In contrast to the observations made in Chapter V where the parabolic energy equations admitted thermal diffusion and permitted thermal disturbances to be registered instantaneously everywhere in the model domain, the θ_l wave is seen to have propagated less than 10 μm in the thickness (z-) direction and approximately 15 μm in the radial (r-) direction. Since the thermo-elasto-viscoplastic model is also based on the generalized thermoelasticity, the thermal wave has the same characteristics described in Chapter VI.

As the ambient temperature increases from room temperature to over 1000K, the dynamic behavior of the silicon wafer is no longer elastic but rather dominantly elasto-viscoplastic. The propagation speed of the thermal wave at 1100K decreases approximately 10% compared with the wave speed at 300K at $t=10\text{ns}$. Furthermore, the augment of such an elasto-viscoplastic behavior modifies the thermal waveform, especially in the thickness direction. Instead of oscillating along the thickness direction and propagating deeper into the region, as the wave corresponding to 300K ambient

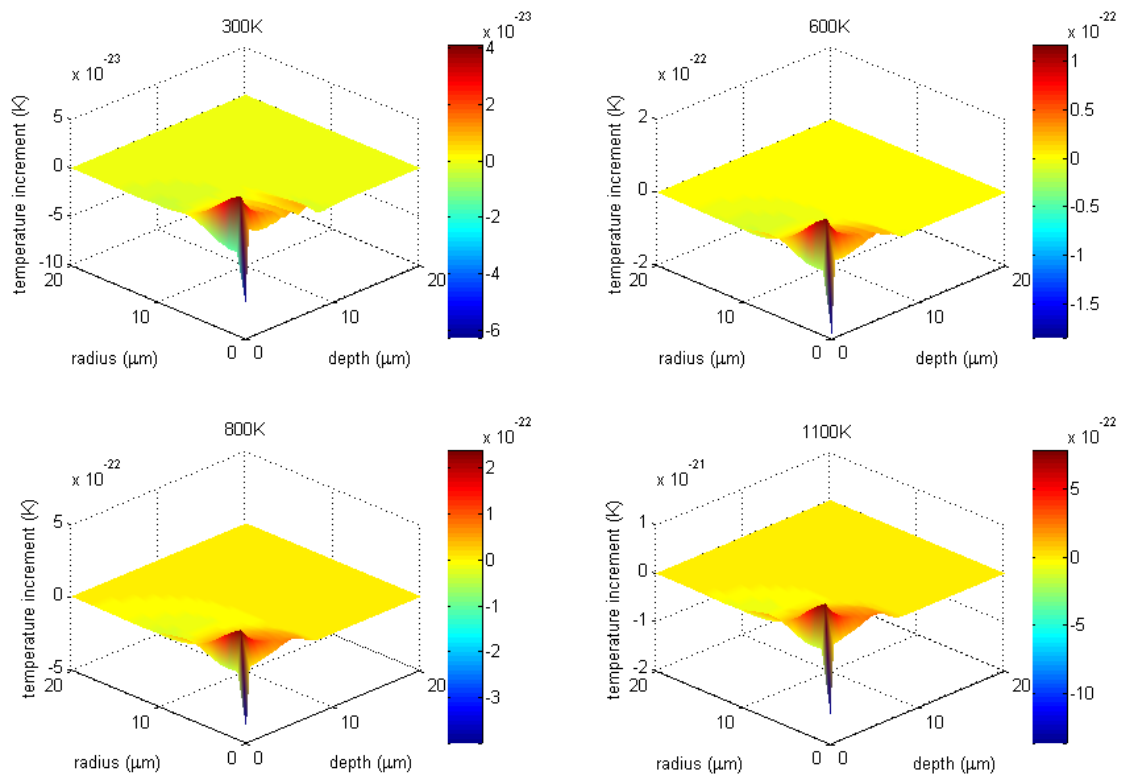


Figure 7.1 Temperature increment of lattice temperature at $t=10\text{ns}$ corresponding to four different ambient temperatures: 300K, 600K, 800K and 1100K (pulse duration 500fs, spot size $10\mu\text{m}$, laser fluence $0.005\text{J}/\text{cm}^2$)

temperature, the thermal wave is seen to oscillate less as the ambient temperature increases.

7.3.2 Displacement Fields as Temperature Indicators

The ultra-short laser pulse induced displacement fields corresponding to 300K and 1100K ambient temperatures are presented in Figure 7.2. As aforementioned, w and u are displacement variables in the z - and r -direction, respectively. By comparing the elasto-viscoplastic displacement at 1100K with the elastic response at 300K, it is seen that the amplitudes of these displacements in both directions increase nearly one order of magnitude within the time window considered. Similar to the thermal field, the waveforms of these mechanical responses are smoothed when the silicon material goes into the elasto-viscoplastic range. For instance, as highlighted in the figure, the elasto-viscoplastic behavior of the silicon wafer at high ambient temperature eliminates the high frequency components that are seen appearing at 300K. In addition, the displacement waves are seen to travel 10% slower for the 1100K case. The displacement in the radial (r -) direction, u , has a negative and relatively large amplitude near the top surface, all laser affected nodes enclosed in this region move toward the symmetry axis $r = 0$ in compression.

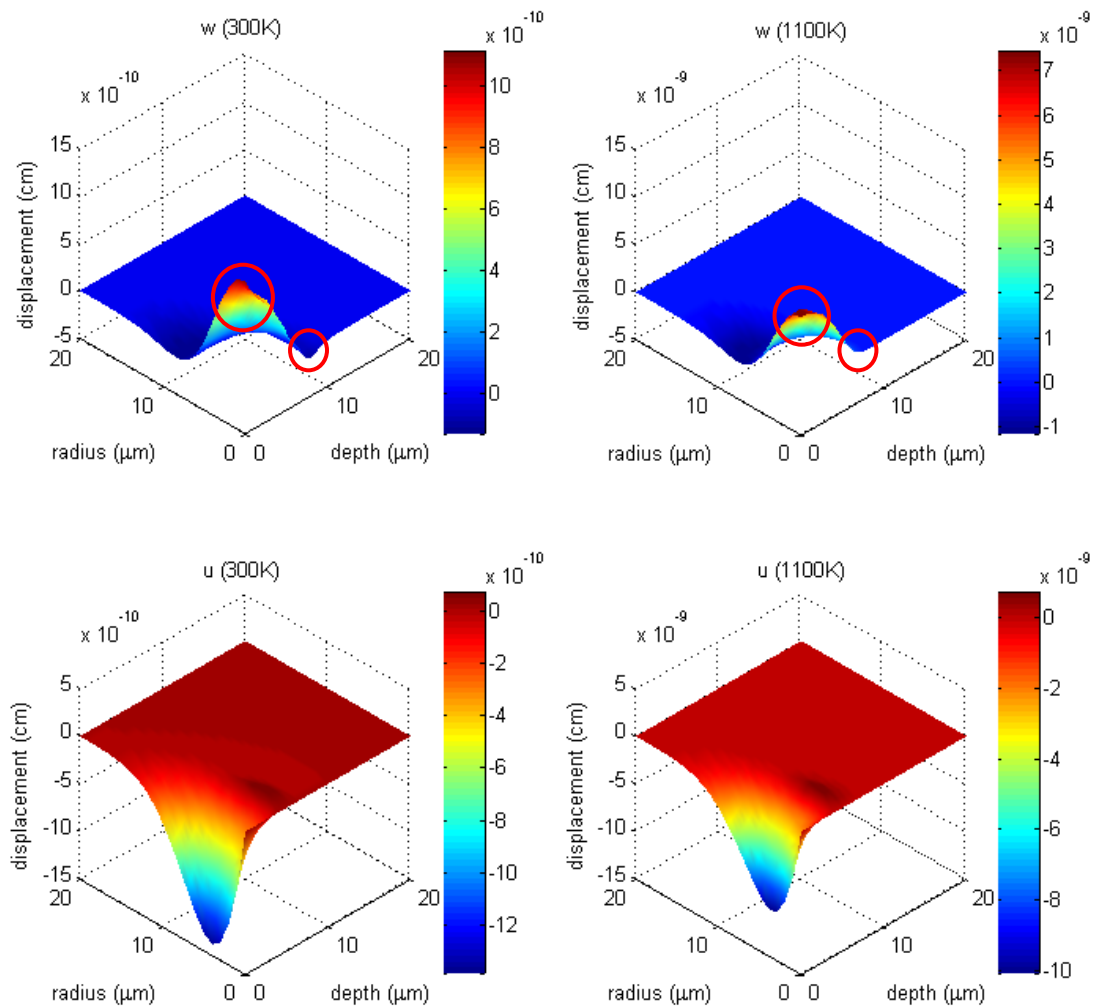


Figure 7.2 Displacement fields at 10ns corresponding to two different ambient temperatures: 300K and 1100K

(pulse duration 500fs, spot size $10\mu\text{m}$, laser fluence $0.005\text{J}/\text{cm}^2$)

The nodal motion can be further studied by determining the resultant displacement of w and u at each node. Deformations induced by the ultra-short laser pulse at two different ambient temperatures, 300K and 1100K, are shown in Figure 7.3. It should be noted that as the induced motion is highly localized in space, only the results within the disk bound by $z \leq 6\mu\text{m}$ and $r \leq 12.5\mu\text{m}$ are considered, and the resultant displacements shown in the figure are magnified by a factor of 10^4 for clarity. The positions of the grid nodes are taken at $t=10\text{ns}$. It can be seen by comparing the results corresponding to 300K and 1100K that the nodal motion becomes more prominent as the ambient temperature increases. Given the relatively small amplitude of motion compared with the atomic and lattice dimensions, the nodal motions can be interpreted as atomic or lattice vibrations. Due to the increasing dislocation density generated by plastic flow, silicon atoms will vibrate with much larger amplitudes when ambient temperature rises. It is thus probable that the femtosecond laser induced lattice displacements could be a viable thermal indicator.

Figure 7.4 exhibits the displacement w at $t=10\text{ns}$ as a function of ambient temperature ranging from 300K to 1100K. The displacement is taken at a sampling location on the top face of the silicon wafer where $z=0$, $r=4\mu\text{m}$. It is seen that the amplitude of the nodal motion at the sampling location considered increases with temperature. The relationship between the displacement w and temperature, though nonlinear, is obviously well-defined. The data in the figure is perfectly curve-fitted using third-order polynomials as

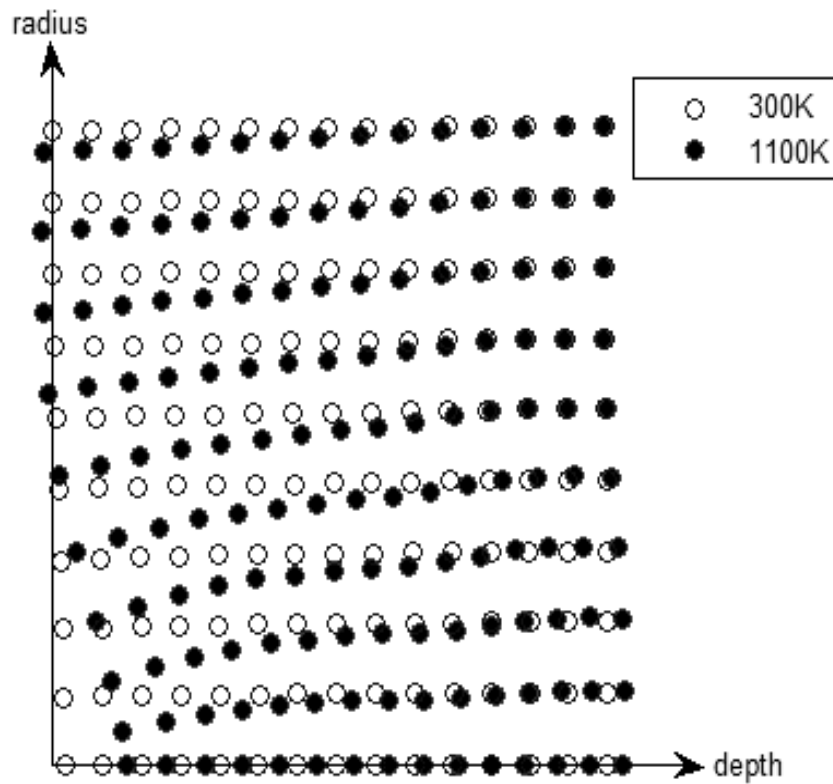


Figure 7.3 Comparison of nodal motions at $t=10\text{ns}$ corresponding to two different ambient temperatures: 300K and 1100K
(pulse duration 500fs, spot size $10\mu\text{m}$, laser fluence $0.005\text{J}/\text{cm}^2$)

$$w = 7.2 \times 10^{-8} T^3 - 7.6 \times 10^{-5} T^2 + 0.034 T + 2.2 \quad (7-29)$$

It should be noted that the unit of displacement w in Eq. (7-29) is pico-meters, and temperature T is in Kelvin. Therefore, as can be seen in Figure 7.4, as long as the out-of-plane displacement w at the selected sampling location is measured at the particular time instance ($t=10\text{ns}$ in this example), the temperature of the silicon wafer can be determined within the investigated temperature range. However, a relevant question to ask is if such a small displacement (atomic vibration) could be observed by any means? Harb, Miller and co-workers [76-78] have demonstrated the feasibility for using femtosecond electron diffraction (FED) to resolve laser induced atomic motions in single crystalline silicon wafer. The time resolution of FED is found to be as small as 300fs. In other words, the FED method is capable of monitoring the atomic positions every 300fs. As the coherent atomic vibrations modulate the optical properties of the silicon film (e.g. reflectivity), the electron diffraction changes correspondingly can be probed by a CCD camera. There are also a few other techniques, such as X-ray diffraction [79-81], that provide a direct mapping of the lattice structure. Consequently, the measurement of femtosecond laser induced displacements at $t=10\text{ns}$ is theoretically and practically feasible.

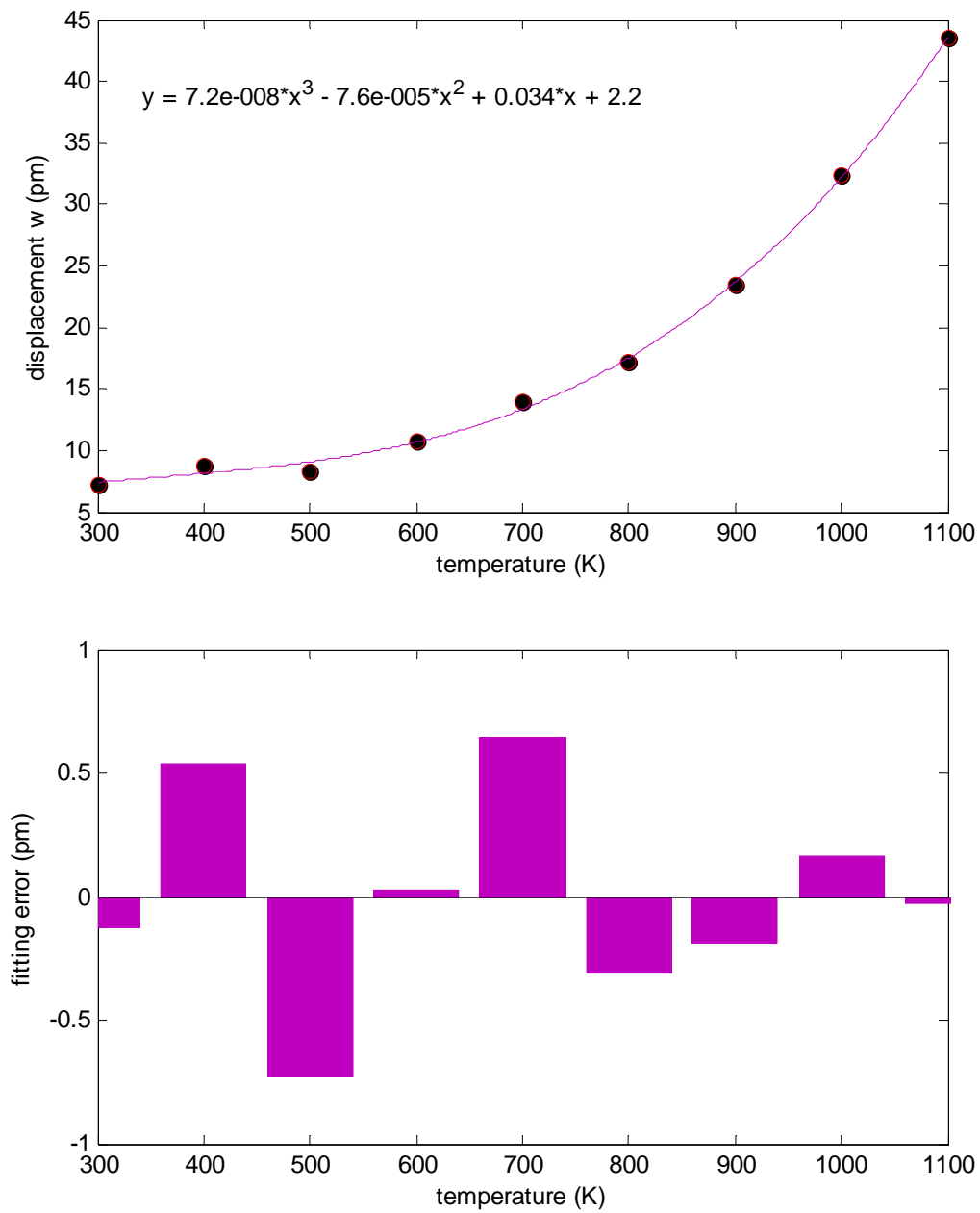


Figure 7.4 Displacement w vs. temperature at $t=10\text{ns}$ with fitting error; sampling location at $z=0$, $r=4\mu\text{m}$ (pulse duration 500fs , spot size $10\mu\text{m}$, laser fluence $0.005\text{J}/\text{cm}^2$)

Figure 7.5 shows the changes of displacement u at $t=10\text{ns}$ at various temperatures. The displacement is taken at the same sampling location as w . The negative magnitude of u is subject to the compressive nodal motion towards the center of the laser beam. Similar to the transverse displacement w , the longitudinal displacement u also has larger amplitudes at higher temperatures. The well-defined relationship between the displacement u and temperature is nonlinear, and the nonlinearity is seen to be significantly more prominent for elasto-viscoplastic behavior. The third-order polynomials used to fit the u - T relation can be expressed as

$$u = -1.7 \times 10^{-7} T^3 + 1.8 \times 10^{-4} T^2 - 0.092 T + 2.4 \quad (7-30)$$

Even though the longitudinal displacement u associates with comparatively poor signal-to-noise ratios, the FED method was proved to be able to gauge both the transverse and longitudinal acoustic waves [76], indicating that the displacement u could be temperature indicator as well. Compared with w , displacement u is seen to be relatively more sensitive to temperature increment. This is more evident in Figure 7.6. To differentiate 301K from 300K, one would need to differentiate approximately 0.01pm in w -displacement. Figure 7.6 shows the differentiating w -displacements needed to discern 401K from 400K, 501K from 500K, ..., and 1101K from 1100K. It is seen that the corresponding $\pm 1\text{K}$ resolution using u -displacement is approximately twice that of the w 's, implying that transverse atomic motions could provide better differentiation resolution. Another observation is that thermal resolution becomes better with increasing temperature. For instance, to tell 1100K apart from 1101K, one would only need to be able to differentiate approximately 0.13pm in the w displacement.

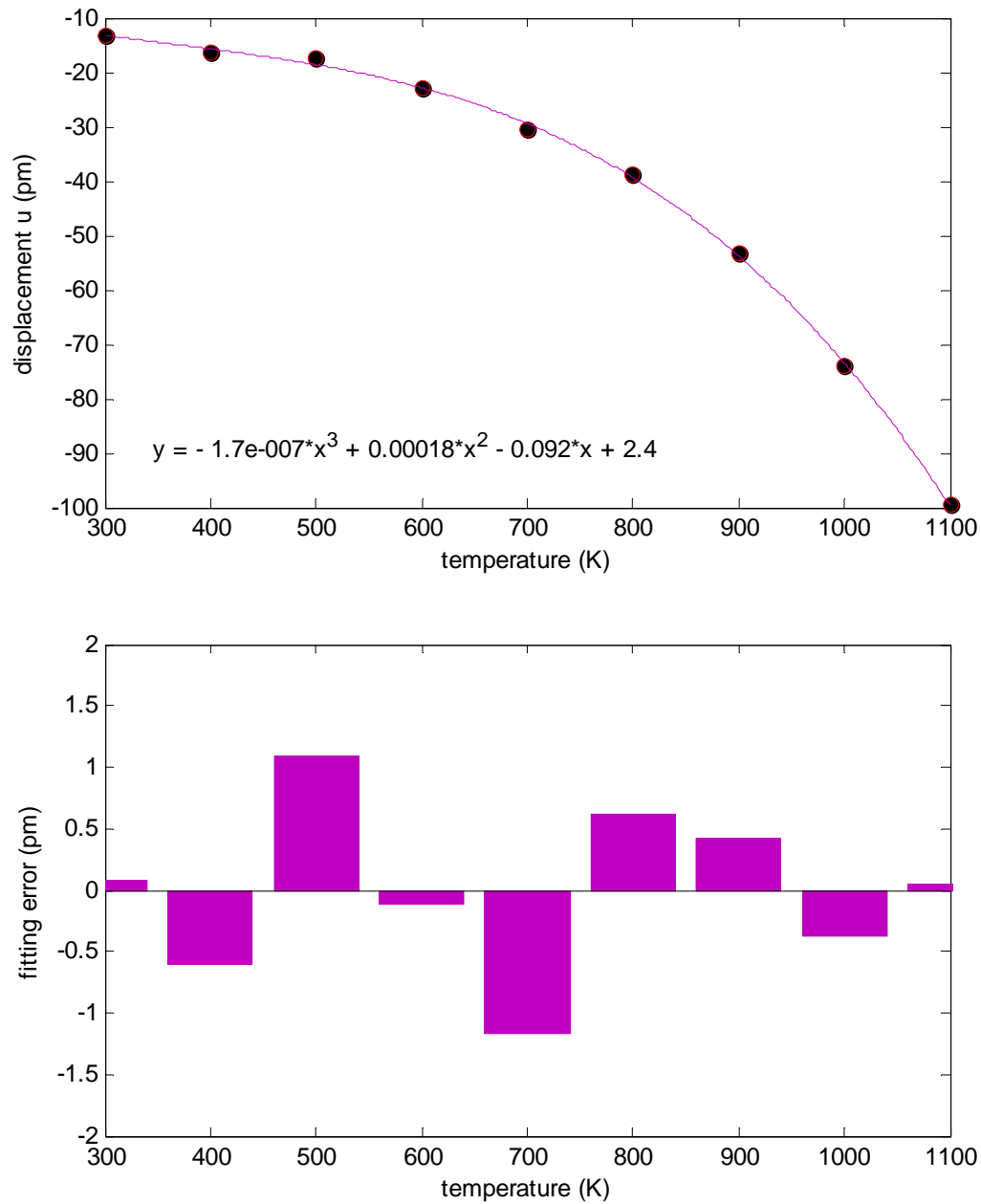


Figure 7.5 Displacement u vs. temperature at $t=10\text{ns}$ with fitting error; sampling location at $z=0$, $r=4\mu\text{m}$ (pulse duration 500fs , spot size $10\mu\text{m}$, laser fluence $0.005\text{J}/\text{cm}^2$)

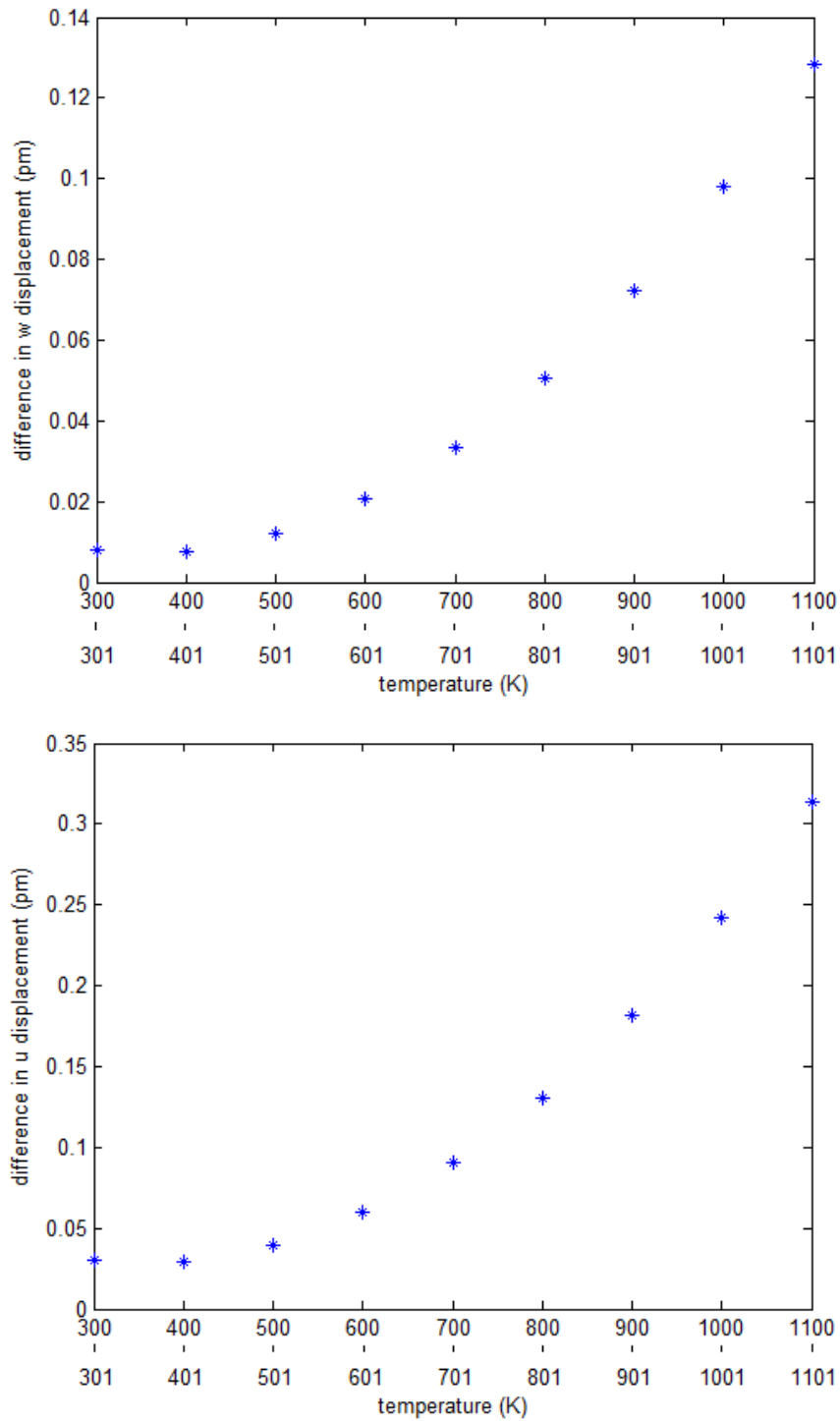


Figure 7.6 Using displacements w and u to differentiate 1K temperature

(pulse duration 500fs, spot size $10\mu\text{m}$, laser fluence $0.005\text{J}/\text{cm}^2$)

7.3.3 Stress Fields as Temperature Indicators

The distributions of the three normal stress components (σ_{zz} , σ_{rr} and $\sigma_{\theta\theta}$) along with the one shear stress component (σ_{rz}) at 300K and 1100K are shown in Figure 7.7. Compared the elasto-viscoplastic thermal stresses at 1100K with the corresponding elastic response at 300K, it is observed that the amplitudes of these stress components increase nearly one order of magnitude within 10ns. The normal component σ_{zz} displays similar traits as do the displacement w and thermal field in that the waves are modified in response to the elasto-viscoplastic constitutive law. Other than this, the distributions of the four stress components do not exhibit much difference in wave profiles.

To investigate the impact of temperature on the dispersion of the stress wave, a propagation path needs be defined first. The center line of the laser beam, $r=0$, is selected as the path. Two sampling locations, 1 and 2 shown in Figure 6.10, are placed along the path. The coordinates of these locations are $(z, r) = (0.4\mu\text{m}, 0\mu\text{m})$ and $(4.8\mu\text{m}, 0\mu\text{m})$. The propagating length between them is therefore $4.4\mu\text{m}$. The σ_{zz} waveforms acquired at locations 1 and 2 corresponding to 300K and 1100K are plotted in Figure 7.8. It is seen that the influence of temperature on the waveforms is significant. The oscillating elastic thermal stress wave is completely modulated due to the elasto-viscoplastic behavior. The amplitude of the propagating σ_{zz} stress wave does not vary too much at 300K. However, it increases approximately one order of magnitude traveling from location 1 to location 2 at 1100K.

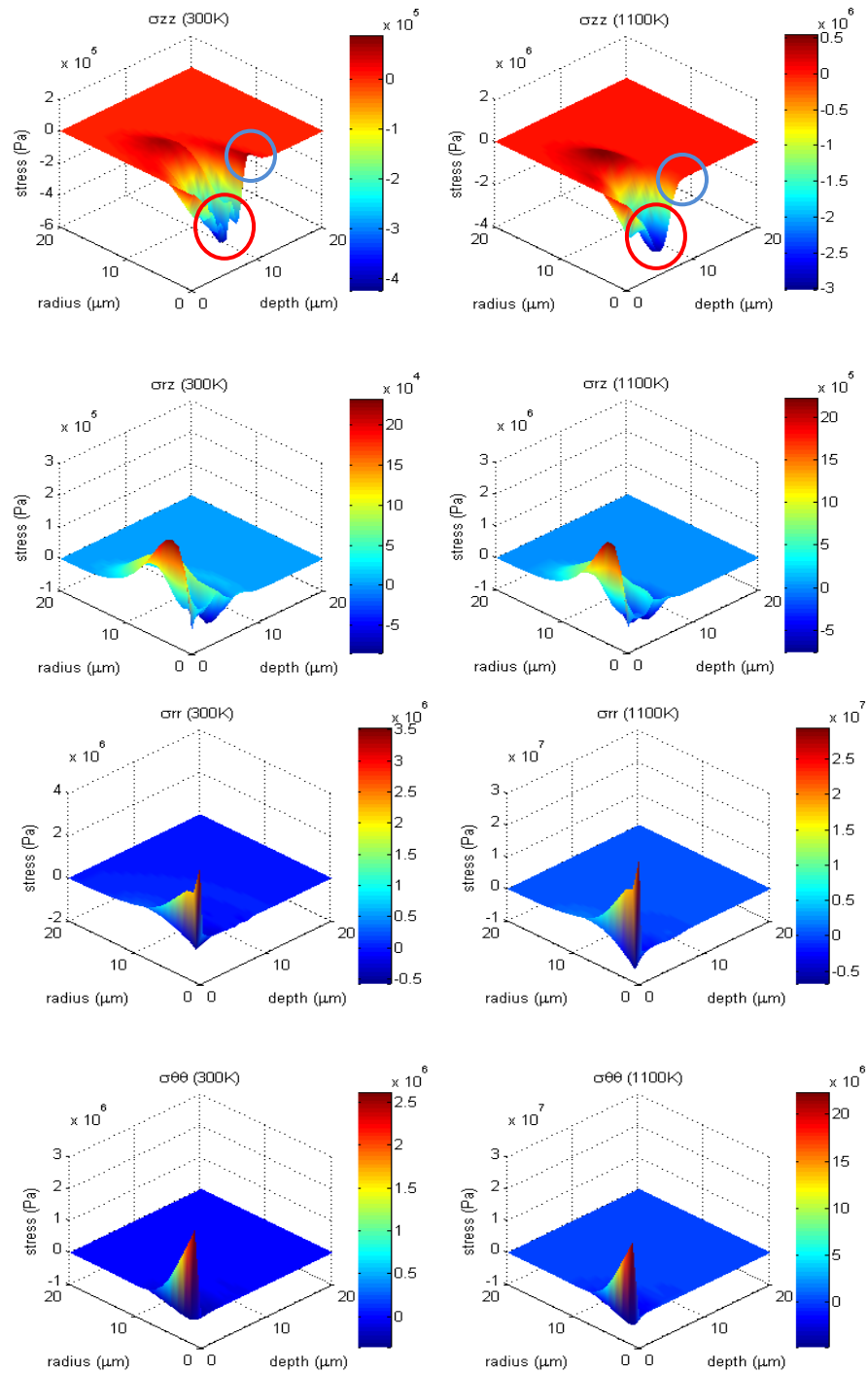


Figure 7.7 Stress fields at $t=10\text{ns}$ corresponding to two different ambient temperatures:

300K and 1100K (pulse duration 500fs, spot size $10\mu\text{m}$, laser fluence $0.005\text{J}/\text{cm}^2$)

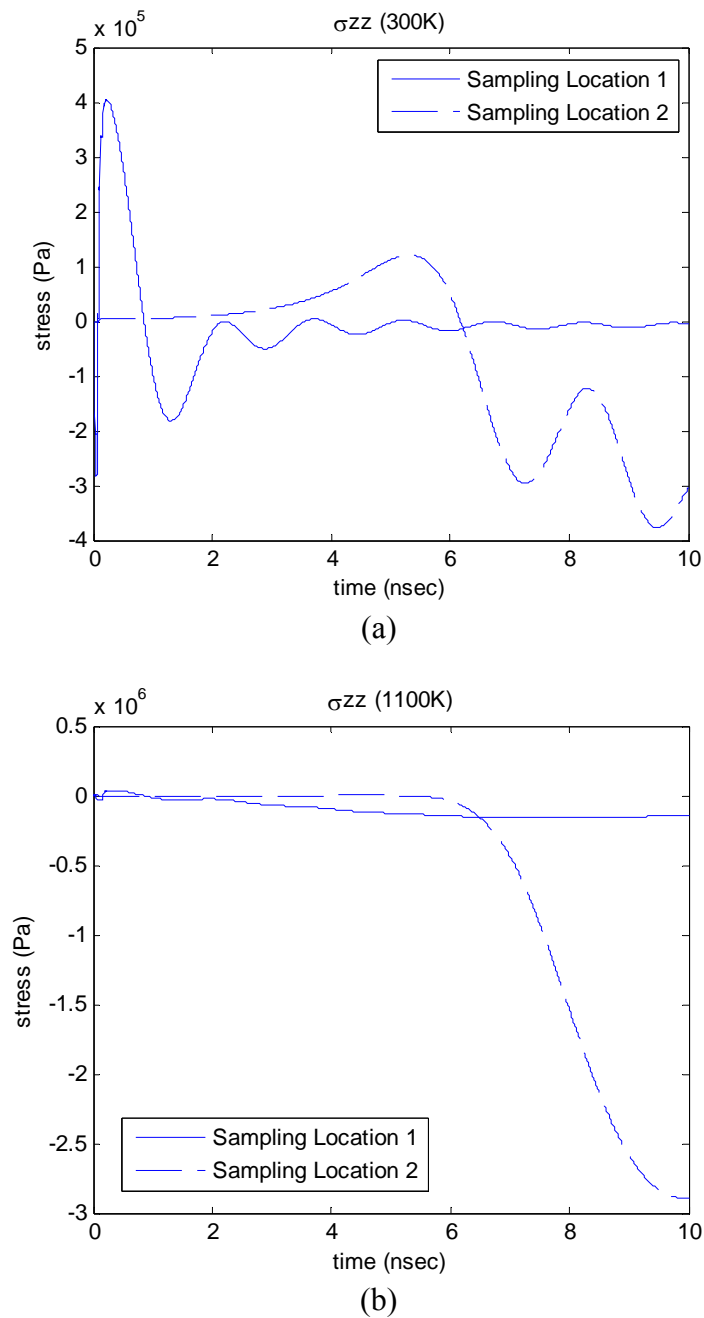


Figure 7.8 Waveforms obtained at sampling locations 1 and 2 corresponding to two different ambient temperatures: (a) 300K and (b) 1100K (pulse duration 500fs, spot size 10 μ m, laser fluence 0.005J/cm²)

To investigate the two dissimilar waveforms of time-varying spectra obtained at locations 1 and 2, the Gabor Wavelet Transform (GWT) is employed to resolve the time-frequency information. As mentioned in Chapter III, GWT has been shown to provide simultaneous time-frequency resolution optimal for resolving dispersive waves found propagating in silicon wafers. Figure 7.9 shows the GWTs of the waveforms acquired at locations 1 and 2 corresponding to 300K and 1100K. For the 300K case, where the silicon wafer undergoes only elastic deformations, the majority frequency components at location 1 are approximately 400-800MHz. As the wave propagates to location 2, the high frequencies can barely be observed. Instead the lower frequency components at 100-200MHz become dominant. The high frequency components, on the other hand, do not exist at both locations for the 1100K case, thus indicating the same observation made previously that the plastic flow greatly dampens high frequencies in the elasto-viscoplastic response.

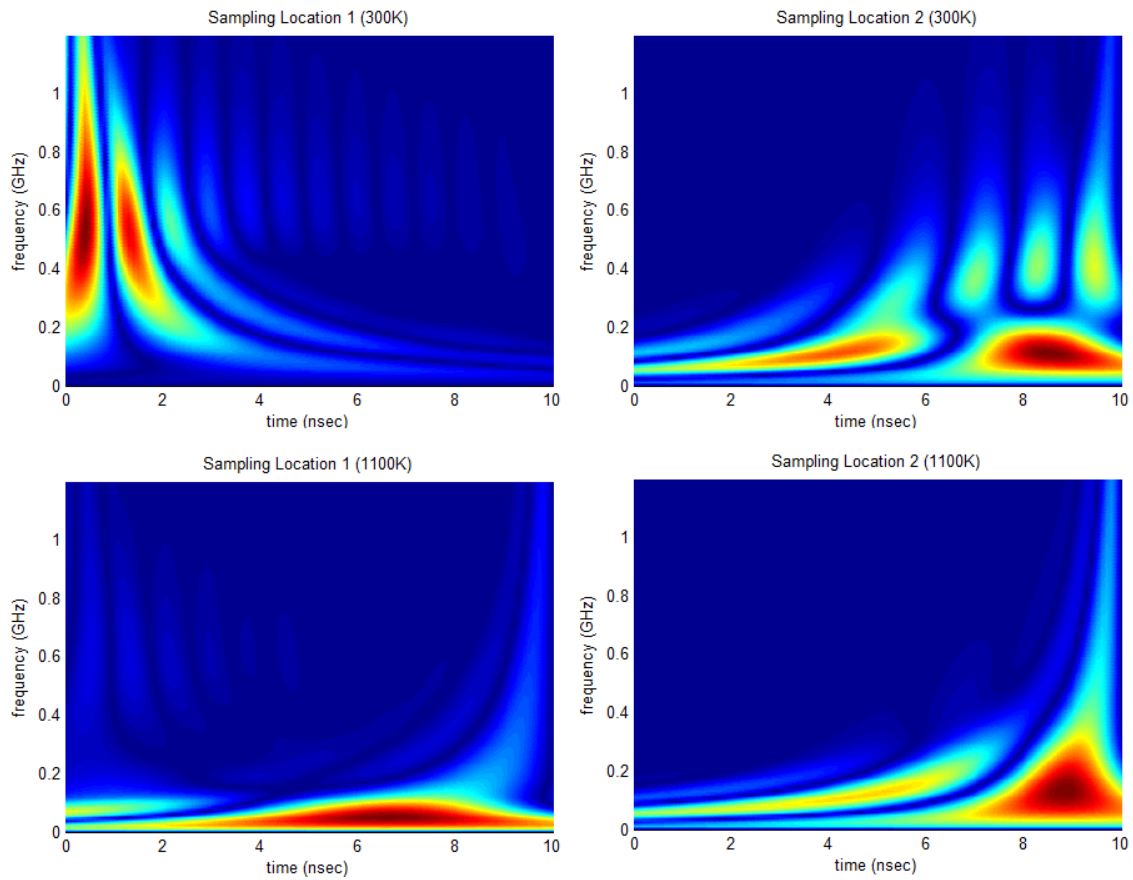


Figure 7.9 GWT of waveforms obtained at sampling locations 1 and 2 corresponding to two different ambient temperatures: 300K and 1100K
(pulse duration 500fs, spot size $10\mu\text{m}$, laser fluence $0.005\text{J}/\text{cm}^2$)

Stress variations as a function of ambient temperatures is discussed in the followings. The stress-free boundary condition specified in Chapter V where $\sigma_{zz} = 0$ on the top surface of the silicon wafer at $z=0$, renders σ_{zz} infeasible for resolving temperature variation. Instead the stress component, σ_{rr} , is explored. Figure 7.10 displays the change of σ_{rr} at $t=10\text{ns}$ at various temperatures. The data is taken at the same finite different grid as displacements w and u . The amplitude of σ_{rr} is seen to increase as temperature increases. The well-defined relationship between σ_{rr} and temperature can also be well fitted using a third-order polynomials as

$$\sigma_{rr} = 2.4 \times 10^{-8} T^3 - 2.7 \times 10^{-5} T^2 + 0.014 T - 0.73 \quad (7-31)$$

It should be noted that the unit of σ_{rr} in Eq. (7-31) is MPa. Therefore, as can be seen in Figure 7.10, the stress generated by femtosecond laser is extremely sensitive to temperature variations. This can be better concluded by studying Figure 7.11 in which a 1K thermal variation results in at least a 5,000Pa changes in stress amplitude. This 1K temperature resolution becomes even better when the silicon undergoes elasto-viscoplastic response. For instance, the thermal resolution of σ_{rr} is over 40KPa at 1100K. Harb has demonstrated that the atomic strain waves can be measured by FED [76], indicating that the determination of stresses in such a nano-scale region is practical. Consequently, it is probable to explore the femtosecond laser induced stresses using LISWT to achieve the desired $\pm 1\text{K}$ thermal resolution.

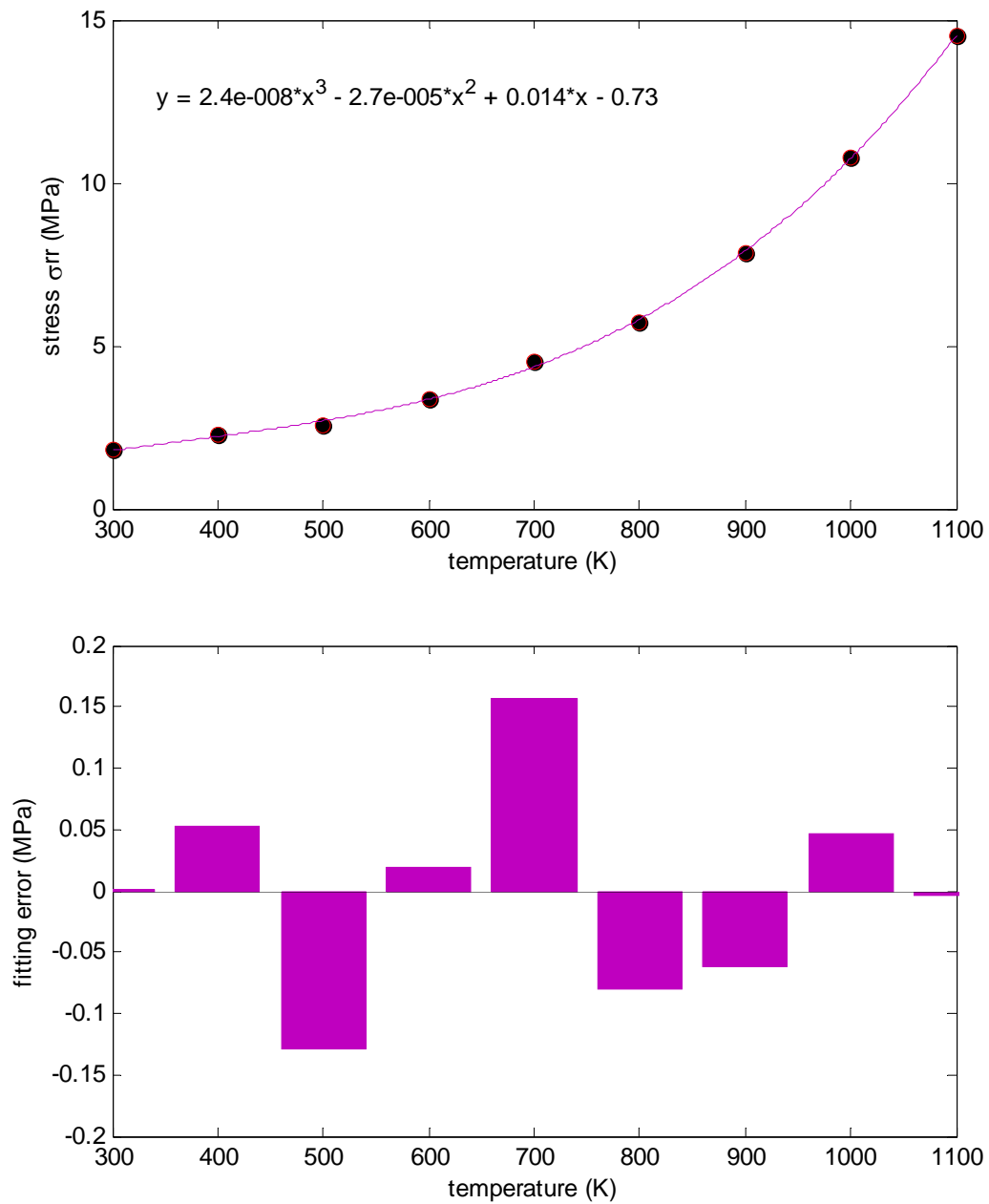


Figure 7.10 Stress σ_{rr} vs. temperature at $t=10\text{ns}$ with fitting error; sampling location at

$$z=0, r=4\mu\text{m}$$

(pulse duration 500fs, spot size $10\mu\text{m}$, laser fluence $0.005\text{J}/\text{cm}^2$)

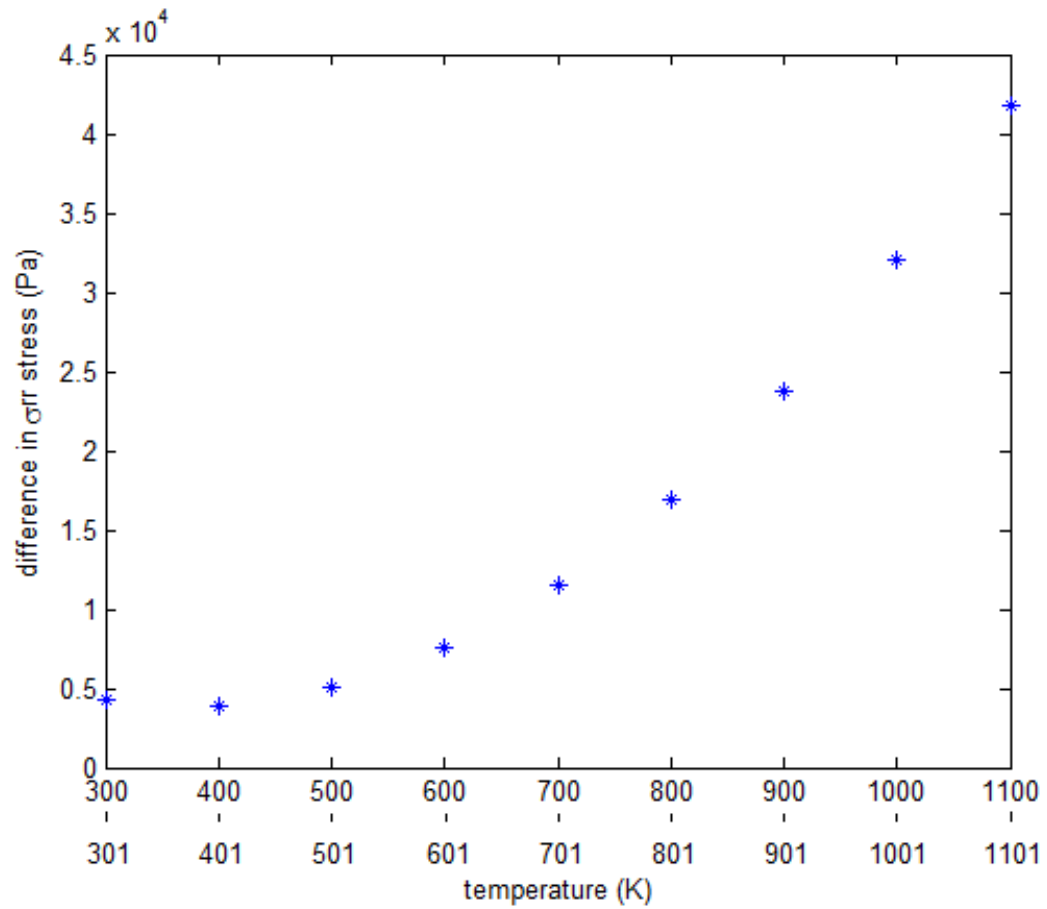


Figure 7.11 Using stress component σ_{rr} to differentiate 1K temperature

(pulse duration 500fs, spot size 10 μ m, laser fluence 0.005J/cm²)

7.4 Summary

The femtosecond laser induced thermo-elasto-visco-plastodynamics in silicon wafer was investigated in this chapter. The governing formulation incorporated the generalized thermodynamic model and the Haasen-Sumino constitutive law for single crystalline silicon. The presented computational algorithm allowed the thermo-elasto-viscoplastic responses to be investigated at elevated ambient temperatures ranging from 300K to 1100K. Results presented in this chapter admitted thermomechanical near-field responses that were inherently elasto-visco-plastodynamic subject to the wide thermal ranges considered. The propagation speeds of the thermal and mechanical waves at 1100K reduced approximately 10% compared with the corresponding wave speeds at 300K within 10ns time window. The high frequency components seen to associate with the elastic response at low temperature were found to be eliminated, and waveforms modified, as the silicon wafer underwent elasto-viscoplastic deformations. The amplitudes of the mechanical responses, including displacements and thermal stresses, were observed to increase with elevating temperature, indicating that they could be employed as viable temperature indicators. Transverse displacement w , longitudinal displacement u and normal stress σ_{rr} all established well-defined relations with temperatures. Employing electron diffraction and X-ray diffraction, it is probable to explore femtosecond laser induced w , u and σ_{rr} fields for the thermal profiling of silicon wafer undergoing RTP with the desired ± 1 K thermal resolution.

CHAPTER VIII

CONCLUSIONS

The primary goal of this research was to formulate a comprehensive model for describing the fundamental mechanism dictating the interaction of ultrafast laser pulses with single crystalline silicon thin structure. The need for establishing the feasibility of employing femtosecond laser for silicon wafer processing using Laser Induced Stress Waves Thermometry (LISWT) motivated the work. The dissertation addressed the need for understanding and interpreting the thermomechanical responses in single crystalline silicon when irradiated by lasers of subpico- and nano-seconds pulse width. The comprehensive physical model developed for the study was of hyperbolic type capable of characterizing non-thermal melting and elasto-viscoplastic deformation as functions of laser input parameters and ambient temperature.

The plastic constitutive law described by the Haasen-Sumino model was followed to consider the kinematics of elasto-plastic deformation of the silicon material subject to nanosecond laser pulses, which resulted in the formulation of a system of nine first-order hyperbolic equations applicable to describing 3-D elasto-viscoplastic wave motions in silicon wafer. The formulation allowed both velocities and stresses be simultaneously determined without having to solve for displacements. Numerical results showed that the elasto-viscoplastic characteristics of the single crystalline silicon were accurately realized at temperatures ranging from room temperature to exceeding 1000°C. A staggered finite difference model was developed to execute the solution strategy for

obtaining converged solutions without unwanted numerical oscillations. Compared with conventional finite difference methods in which primary variables were evaluated at grid points, the staggered finite difference scheme defined primary variables at spatial locations midway between two consecutive grid points and the center of each element. The group velocity and attenuation factor of certain selected frequency components were correlated with temperature to study the feasibility of exploiting nanosecond laser induced propagating stress waves to the high resolution thermal profiling of silicon wafers undergoing rapid annealing. Frequency- and temperature-dependent group velocity and wave attenuation were calculated using the time-frequency Gabor Wavelet Transform (GWT). Extensive numerical simulations demonstrated good agreements with published physical data. The group velocities of the 30~70kHz frequency components were recommended for the extraction of thermal information with the desired $\pm 1^\circ\text{C}$ resolution. Wave attenuation factor was found to have unsatisfactory thermal resolution, thus not recommended for performing thermometric functions in nanosecond laser induced stress wave thermometry.

Femtosecond laser induced transport dynamics in semiconductor material was formulated based on the relaxation-time approximation of the Boltzmann equation. The underlying governing equations that included the macroscopic electrical current equation, macroscopic energy current equation, balance equation of carrier number and balance equation of carrier energy were comprehensively reviewed along with the key assumptions made for the legitimate application of the Boltzmann equation to describing physical domains that are of macroscopic scale. Temperature-dependent multi-phonons,

free-carrier absorptions, and the recombination and impact ionization processes governing the laser model and carrier numbers were considered. The balance equation of lattice energy and the equations of motion that are of both parabolic and hyperbolic types were derived to describe the complex thermo-elasto-plastodynamic behaviors of the silicon material in response to ultrafast laser pulsing.

The parabolic femtosecond laser heating formulation allowed responses including the evolutions of electron-lattice temperatures, electron-hole carrier density, displacement and stress fields and precursors to the initiation of waveguide modes to be modeled and investigated. Unlike the many one-dimensional models reported in the literature that considered semi-infinite half-space, an axisymmetric model of finite geometry was employed to better understand the effects of multi-dimensionality on thermal and mechanical wave generations. A novel scheme incorporating varying time steps ranging from 5fs to 5ps was implemented with the velocity-Verlet multi-time scale algorithm to allow for time-integrating various thermal-mechanical responses up to 10ns. The time evolution and spatial distribution of electron-lattice temperatures varied with the laser fluence input. The femtosecond laser generated non-thermal damages were also found to be functions of laser fluence and pulse duration. The induced mechanical responses including displacement and stress waves were highly dispersive and characteristically of broadband, low amplitude, and extremely high frequency. The near-field responses preceding the development of stress waves were seen to generate propagating power densities with high magnitudes on the order of $10^{13}\sim 10^{14}\text{W/m}^3$.

The dilemma that thermal disturbances propagate with infinite speed was properly remedied by considering energy transport as finite and local. The hyperbolic femtosecond laser heating formulation incorporated hyperbolic-type energy transport equations derived following the Green-Lindsay's generalized theory of thermoelasticity, in which the finite nature of both the thermal and mechanical responses was facilitated through considering thermal-mechanical relaxation and thermal relaxation. It also permitted the variations of temperature, displacement and thermal stress in both time and space to be established as functions of the non-melting laser input parameters. The time evolution of the carrier density in conjunction with the non-thermal melting fluence at which no physical damage was inflicted subject to a given pulse duration was favorably examined against published experimental data, thus validating the model formulation. Femtosecond pulse induced waves described by the hyperbolic formulation were also dispersive and broadband in frequency. The algorithm of accumulated damage evaluation was applied to qualitatively estimate the potential for the induced stress waves to initiate fatigue cracking. It was seen that the high power density waves generated by the 500fs ultrafast laser of $0.005\text{J}/\text{cm}^2$ in fluence and $10\mu\text{m}$ in spot size, although on the order of $10^{14}\text{W}/\text{m}^3$, was insufficient to inflict mechanical flaws.

Lastly the Haasen-Sumino constitutive model was incorporated into the hyperbolic femtosecond laser heating formulation to describe the thermo-elasto-viscoplastic behaviors of the silicon wafer at elevated ambient temperature ranging from 300K to 1100K. The elasto-visco-plastodynamic responses of the material at 1100K were characterized by thermal-mechanical waves devoid of high frequency components

that were observed propagating in the corresponding elastic responses at 300K. The propagation speed of the thermo-elasto-visco-plastodynamic responses was found to be approximately 10% slower than their elastic counterparts. Displacement responses including the transverse (w) and longitudinal (u) components showed well-defined relations with various wafer temperatures. The relations could be fitted by third-order polynomials with negligible errors. The normal stress component, σ_{rr} , also established a similar affection on temperature. Thermal resolution improved as silicon became elasto-viscoplastic in response. With proven atomic motion tracing technologies such as electron diffraction and X-ray diffraction, performing femtosecond laser induced thermal-mechanical responses in thermometry technique of silicon wafer annealing would be feasible with desired thermal resolution.

REFERENCES

- [1] M. S. Amer, M. A. El-Ashry, L. R. Dosser, K. E. Hix, J.F. Maguire, et al., Femtosecond Versus Nanosecond Laser Machining: Comparison of Induced Stresses and Structural Changes in Silicon Wafers, *Applied Surface Science*, vol. 242, pp.162–167, 2005.
- [2] T. Matsumura, T. Nakatani, and T. Yagi, Deep Drilling on a Silicon Plate with a Femtosecond Laser: Experiment and Model Analysis, *Applied Physics A*, vol.86, pp.107–114, 2007.
- [3] E. Coyne, J. P. Magee, P. Mannion, G. M. O'Connor and T. J. Glynn, STEM (Scanning Transmission Electron Microscopy) Analysis of Femtosecond Laser Pulse Induced Damage to Bulk Silicon, *Applied Physics A*, vol. 81, pp. 371–378, 2005.
- [4] M. S. Rogers, C. P. Grigoropoulos, Andrew M. Minor and Samuel S. Mao, Absence of Amorphous Phase in High Power Femtosecond Laser-ablated Silicon, *Journal of Applied Physics*, vol. 94, Article Number: 011111, 2009.
- [5] M. Guillermin, F. Garrelie, N. Sanner, E. Audouard and H. Soder, Single- and Multi-pulse Formation of Surface Structures Under Static Femtosecond Irradiation, *Applied Surface Science*, vol. 253, pp. 8075–8079, 2007.
- [6] D. P. Korfiatis¹, A. Th. Thoma, and J. C. Vardaxoglou, Conditions for Femtosecond Laser Melting of Silicon, *Journal of Physics D: Applied Physics*, vol. 40, pp. 6803–6808, 2007.

- [7] E. G. Gamaly, A. V. Rode, B. Luther-Davies, and V. T. Tikhonchuk, Ablation of Solids by Femtosecond Lasers: Ablation Mechanism and Ablation Thresholds for Metals and Dielectrics, *Physics of Plasmas*, vol. 9, no. 3, pp. 949-957, 2002.
- [8] N. N. Nedialkov, P. A. Atanasov, S. Amoroso, R. Bruzzese and X. Wang, Laser Ablation of Metals by Femtosecond Pulses: Theoretical and Experimental Study, *Applied Surface Science*, vol. 253, pp. 7761–7766, 2007.
- [9] A. M. Lomonosov, P. Hess, R. E. Kumon and M. F. Hamilton, Laser-generated Nonlinear Surface Wave Pulses in Silicon Crystals, *Physical Review B*, vol. 69, p. 035314, 2004.
- [10] G. A. Rabroker, C. S. Suh, R. Chona, Laser-induced Stress Waves Thermometry Applied to Silicon Wafer Processing: Modeling and Experimentation, *Experimental Mechanics*, vol. 45, no.1, pp. 3-8, 2005.
- [11] C. S. Suh, G. A. Rabroker, C. E. Burger, and R. Chona, Ultrasonic Time-Frequency Characterization of Silicon Wafers at Elevated Temperatures, *Symposium on Applications of Experimental Mechanics to Electronic Packaging, ASME International Mechanical Engineering Congress and Exposition*, Dallas, TX, pp. 37-44, 1997.
- [12] V. Vedantham, In-Situ Temperature and Thickness Characterization for Silicon Wafers Undergoing Thermal Annealing, M.S. Thesis, Texas A&M University, College Station, TX, 2003.
- [13] Semiconductor Industry Association (SIA), *The National Technology Roadmap for Semiconductors*, San Jose, 1998.

- [14] F. L. Degertekin, and B. T. Kuri-Yakub, Lamb Wave Excitation by Hertzian Contacts With Applications in NDE, *IEEE Transactions on Ultrasonic Ferroelectric Frequency Control*, vol. 44, pp. 769-778, 1997.
- [15] F. L. Degertekin, J. Pei, B. T. Kuri-Yakub, and K. C. Saraswat, In Situ Acoustic Temperature Tomography of Semiconductor Wafers, *Applied Physics Letters*, vol. 64, pp. 1338-1340, 1994.
- [16] C. Schietinger, B. Adams, and C. Yarlring, Ripple Technique: A Novel Non-Contact Wafer Emissivity and Temperature Measurement Method for RTP, *Mat. Res. Symp. Proc.*, vol. 224, pp. 23-31, 1991.
- [17] D. H. Chen, D. P. DeWitt, B. K. Tsai, K. G. Kreider, and W. A. Kimes, Effects of Wafer Emissivity on Rapid Thermal Processing Temperature Measurement, *10th IEEE International Conference on Advanced Thermal Processing of Semiconductors*, pp. 59-67, 2002.
- [18] B. K. Tsai, Traceable Temperature Calibrations of Radiation Thermometers for Rapid Thermal Processing, *11th IEEE International Conference on Advanced Thermal Processing of Semiconductors*, pp. 101-106, 2003.
- [19] C. Burger, N. A. Schumacher, C. E. Duffer, and E. D. Knab, Fiberoptic Techniques for Generating and Detecting Ultrasonic Waves for Quantitative NDE, *Optics and Lasers in Engineering*, vol. 19, pp. 121-140, 1993.
- [20] E. H. Lee and D. T. Liu, Finite-Strain Elastic-Plastic Theory with Application to Plane-Wave Analysis, *Journal of Applied Physics*, vol. 38, no. 1, pp. 19-27, 1967.

- [21] G. Giese and M. Fey, High-Order Simulation of the Elastic-Plastic Wave Equation in Two Space Dimensions, *Wave Motion*, vol. 38, pp. 327-343, 2003.
- [22] H. Alexander, and P. Haasen, Dislocation and Plastic Flow in the Diamond Structure, *Solid State Physics*, vol. 22, pp. 28-156, 1968.
- [23] M. Suezava, K. Sumino, and I. Yonenaga, Dislocation Dynamics in the Plastic Deformation of Single Silicon Crystals, II. Theoretical Analysis of Experimental Results, *Phys. Stat. Sol. (a)*, vol. 51, pp. 217-226, 1979.
- [24] C. T. Tsai, O. Dillon, and R. Angelis, The Constitutive Equation for Silicon and Its Use in Crystal Growth Modeling, *Journal of Engineering Materials and Technology*, vol. 112, pp. 183-187, 1990.
- [25] C. T. Tsai, M. W. Yao, and A. Chait, Prediction of Dislocation Generation During Bridgman Growth of GaAs Crystals, *Journal of Crystal Growth*, vol. 125, pp. 69-80, 1992.
- [26] C. T. Tsai, On the Finite Element Modeling of Dislocation Dynamics During Semiconductor Crystal Growth, *Journal of Crystal Growth*, vol. 113, pp. 499-507, 1991.
- [27] J. Virieux, P-SV Wave Propagation in Heterogeneous Media: Velocity-stress Finite-difference Method, *Geophysics*, vol. 51, no.4, pp. 889-901, 1986.
- [28] J. Robertson, J. Blanch, and W. Symes, Viscoelastic Finite-difference Modeling, *Geophysics*, vol. 59, no. 9, pp. 1444-1456, 1994.
- [29] E. Saenger, N. Gold, S. Shapiro, Modeling the Propagation of Elastic Waves Using a Modified Finite-difference Grid, *Wave Motion*, vol. 31, pp. 77-92, 2000.

- [30] J. Represa, C. Pereira, M. Panizo, F. Tadeo, A Simple Demonstration of Numerical Dispersion Under FDTD, *IEEE Transactions on Education*, vol. 40, no.1, pp. 98-102, 1997.
- [31] E. Weinan, and J.-G. Liu, Projection Method III: Spatial Discretization on the Staggered Grid, *Mathematics of Computation*, vol. 237, pp. 27-47, 2001.
- [32] Y. Morinishi, T. S. Lund, O. V. Vasilyev, and P. Moin, Fully Conservative Higher Order Finite Difference Schemes for Incompressible Flow, *Journal of Computational Physics*, vol. 143, pp. 90-124, 1998.
- [33] K. Kishimoto, H. Inoue, M. Hamada, and T. Shibuya, Time Frequency Analysis of Dispersive Waves by Means of Wavelet Transform, *Journal of Applied Mechanics*, vol. 62, pp. 841-846, 1995.
- [34] B. Pecholt, M. Vendan, Y. Dong and P. Molian, Ultrafast Laser Micromachining of 3C-SiC Thin Films for MEMS Device Fabrication, *Int. J. Adv. Manuf. Technol.*, vol. 39, pp. 239–250, 2008.
- [35] M. Shinoda, R. R. Gattass, and E. Mazur, Femtosecond Laser-induced Formation of Nanometer-width Grooves on Synthetic Single-crystal Diamond Surfaces, *Journal of Applied Physics*, vol. 105, Article Number: 053102, 2009.
- [36] R. A. Murdick, R. K. Raman, Y. Murooka, and C.-Y. Ruan, Photovoltage Dynamics of the Hydroxylated Si(111) Surface Investigated by Ultrafast Electron Diffraction, *Physical Review B*, vol. 77, Article Number: 245329, 2008.

- [37] S. Alimpiev, A. Grechnikov, J. Sunner, V. Karavanskii and Ya. Simanovsky, et al., On the Role of Defects and Surface Chemistry for Surface-assisted Laser Desorption Ionization from Silicon, *Journal of Chemical Physics*, vol. 128, Article Number: 014711, 2008.
- [38] E. Koudoumas, O. Kokkinaki, and M. Konstantaki, Nonlinear Optical Response of Silicon Nanocrystals, *Optical Materials*, vol. 30, pp. 260–263, 2007.
- [39] J. S. Van Vechten, R. Tsu, and F. W. Saris, Nonthermal Pulsed Laser Annealing of Si: Plasma Annealing, *Physics Letters*, vol. 74A, pp. 422-426, 1979.
- [40] H. M. van Driel, Kinetics of High-density Plasmas Generated in Si by 1.06- and 0.53- μm Picosecond Laser Pulses, *Physical Review B*, vol. 35, pp. 8166-8176, 1987.
- [41] J. K. Chen, D. Y. Tzou, and J. E. Beraun, Numerical Investigation of Ultrashort Laser Damage in Semiconductors, *International Journal of Heat and Mass Transfer*, vol. 48, pp. 501-509, 2005.
- [42] M. Nagaraj, and C. S. Suh, On Short Time Scale Stress Wave Phenomena and Initiation of Mechanical Faults in Flip Chip Configurations, *IEEE Transactions on Device and Materials Reliability*, vol. 5, no. 2, pp. 224-230, 2005.
- [43] T. Roznowski, *Moving Heat Sources in Thermoelasticity*, Ellis Horwood, Chichester, United Kingdom, 1989.
- [44] A. Abdulle, and E. Weinan, Projection Method III: Finite Difference Heterogeneous Multi-scale Method for Homogenization Problems, *Journal of Computational Physics*, vol. 191, no. 1, pp. 18-39, 2003.

- [45] H. Tal-Ezer, Spectral Methods in Time for Hyperbolic Problems, *SIAM Journal on Numerical Analysis*, vol. 23, pp. 11-26, 1986.
- [46] Y. Oh, C. S. Suh, and H.-J. Sue, On Failure Mechanisms in Flip Chip Assembly – Part 1: Short-time Scale Wave Motion, *Journal of Electronic Packaging*, vol. 130, Article Number: 021008, 2008.
- [47] Y. Oh, C. S. Suh, and H.-J. Sue, On Failure Mechanisms in Flip Chip Assembly – Part 2: Optimal Underfill and Interconnecting Materials, *Journal of Electronic Packaging*, vol. 130, Article Number: 021009, 2008.
- [48] L. Liu, Elasto-viscoplastic Wave Propagation in a Single Crystallographic Silicon Thin Structure, M.S. Thesis, Texas A&M University, College Station, TX, 2005.
- [49] M. Yasutake, M. Umeno, and H. Kawabe, Mechanical Properties of Heat-treated CZ-Si Wafers From Brittle to Ductile Temperature Range, *Japan Journal of Applied Physics*, vol. 21, pp. L288-90, 1982.
- [50] M. Noriyuki, U. Hitoshi, M. Tsuyoshi, F. Kazumasa, and S. Yuji, Dislocation Density Analysis of Bulk Single Silicon Crystal Growth Using Dislocation Kinetics Model, *Mechanics and Materials for Electronic Packaging, vol. 1- Design and Process Issues in Electronic Packaging, ASME* , vol.195, pp. 59-64, 1994.
- [51] G. A. Rabroker, Laser-induced Stress Wave Thermometry Applied to Silicon Wafer Processing, M.S. Thesis, Texas A&M University, College Station, TX, 2000.
- [52] J. C. Goswami, and A. K. Chan, *Fundamentals of Wavelets: Theory, Algorithms, and Applications*. John Wiley & Sons, Inc., New York, 1999.

- [53] K. Kishimoto, Wavelet Analysis of Dispersive Stress Waves, *JSME International Journal Series A*, vol. 38, pp. 416-423, 1995.
- [54] C. K. Chui, *An Introduction to Wavelets*. Academic Press, San Diego, 1992.
- [55] K. Huang, *Statistical Mechanics*. John Wiley & Sons, Inc., New York, 1987.
- [56] J. R. Drabble, and H. J. Goldsmid, *Thermal Conduction in Semiconductors*, Pergamon Press, New York, 1961.
- [57] H. M. van Driel, Transport Properties of Laser-generated Non-equilibrium Plasmas in Semiconductors, *Proceedings of the NATO Advanced Study Institute on Interfaces Under Laser Irradiation*, Acquafredda di Maratea, Italy, July 14-25, 1986.
- [58] Y. L. Klimontovich, *Kinetic Theory of Nonideal Gases and Nonideal Plasmas*, Pergamon Press, New York, 1985.
- [59] H. K. Henisch, *Semiconductor Statistics*, Pergamon Press, New York, 1962.
- [60] M. C. Biot, Thermoelasticity and Irreversible Thermodynamics, *J. Appl. Phys.*, vol. 27, pp. 240–253, 1956.
- [61] H. Parkus, *Thermoelasticity*, Blaisdell Publishing Company, Waltham, MA, 1968.
- [62] C. S. Suh and C. P. Burger, Thermoelastic Modeling of Laser-induced Stress Waves in Plates, *Journal of Thermal Stresses*, vol. 21, pp. 829-847, 1998.
- [63] N. C. Chattopadhyay and M. Biswas, Study of Thermal Stress Generated in an Elastic Half-Space in the Context of Generalized Thermoelasticity Theory, *Journal of Thermal Stresses*, vol. 30, no. 2, pp. 107-124, 2007.

- [64] C. K. Jones, and A. Khibnik, *Multiple-Time-Scale Dynamical Systems*, Springer, New York, 2000.
- [65] P. J. Hoogerbrugge, and J. M. Koelman, Simulating Microscopic Hydrodynamic Phenomena with Dissipative Particle Dynamics, *Europhys. Lett.*, vol. 19, pp. 155, 1992.
- [66] P. Español, and P. Warren, Statistical Mechanics of Dissipative Particle Dynamics, *Europhys. Lett.*, vol. 30, p. 191, 1995.
- [67] M. P. Allen and D. J. Tildesley, *Computer Simulation of Liquids*, Clarendon, Oxford, 1987.
- [68] C. M. Bhandari, and D. M. Rowe, *Thermal Conduction in Semiconductors*, John Wiley, New York, 1988.
- [69] H. F. Wolf, *Silicon Semiconductor Data*, Pergamon Press, New York, 1969.
- [70] C. L. Muhlstein, S. B. Brown, and R. O. Ritchie, High-Cycle Fatigue of Single-Crystal Silicon Thin Films, *Journal of Microelectromechanical Systems*, vol. 10, no. 4, pp. 593-600, 2001.
- [72] A. E. Green and K. A. Lindsay, Thermoelasticity, *J. Elasticity*, vol. 2, pp. 1-7, 1972.
- [73] A. E. Green and N. Laws, On the Entropy Production Inequality, *Archive for Rational Mechanics and Analysis*, vol. 45, pp. 47-53, 1972.
- [74] R. B. Hetnarski, and J. Ignaczak, Nonclassical Dynamical Thermoelasticity, *International Journal of Solids and Structures*, vol. 37, pp. 215-224, 2000.

- [75] P. Allenspacher, B. Huttner, and W. Riede, Ultrashort Pulse Damage of Si and Ge Semiconductors, *SPIE*, vol. 4932, pp. 358-365, 2003.
- [76] M. Harb, W. Peng, et al., Excitation of Longitudinal and Transverse Coherent Acoustic Phonons in Nanometer Free-standing Films of (001) Si, *Physical Review B*, vol. 79, p. 094301, 2009.
- [77] M. Harb, R. Ernstorfer, G. Sciaini, C. T. Hebeisen, R. Ernstorfer, et al., Electronically Driven Structure Changes of Si Captured by Femtosecond Electron Diffraction, *Physical Review Letters*, vol. 100, Article Number: 155504, 2008.
- [78] M. Harb, R. Ernstorfer, T. Dartigalongue, C. T. Hebeisen, R. Ernstorfer, et al., Carrier Relaxation and Lattice Heating Dynamics in Silicon Revealed by Femtosecond, *Journal of Physics and Chemistry B*, vol. 110, pp. 25308-25313, 2006.
- [79] A. Rousse and C. Rischel, Non-thermalmelting in Semiconductors Measured at Femtosecond Resolution, *Nature (London)*, vol. 410, pp. 65-67, 2001.
- [80] A. Lindenberg, J. Larsson, K. Sokolowski-Tinten, K. J. Gaffney, C. Blome, et al., Atomic-scale Visualization of Inertial Dynamics, *Science*, vol. 308, pp. 392-395, 2005.
- [81] A. Cavalleri, C. Siders and C. Rose-Petruck, Ultrafast X-ray Measurement of Laser Heating in Semiconductors: Parameters Determining the Melting Threshold, *Physical Review B*, vol. 63, p. 193306, 2001.

VITA

Xuele (Ryan) Qi was born in Chengde, Hebei Province, People's Republic of China. He received a Bachelor of Engineering degree in automotive engineering from Tsinghua University, Beijing, P. R. China in July 2003 and a Master of Science degree in mechanical engineering from Tsinghua University in January 2006. He entered the Department of Mechanical Engineering at Texas A&M University in August 2006 and joined Photomechanics Lab. He received his Ph.D. in December 2009. His research interests include ultrafast laser induced elasto-plastodynamics, time-frequency signal analysis, computational modeling of physical system, and structural health monitoring. His permanent address is Maliandao Street #80, Ou Yuan Building #4, Room 1615, Beijing, P. R. China. He can be reached by email at qixuele99@gmail.com.